8-23-2017

A Materials Genome Approach to the Design, Synthesis, and Testing of High Energy Density Dielectric Materials for Capacitor Applications

Gregory Treich
University of Connecticut - Storrs, gregory.treich@uconn.edu

A Materials Genome Approach to the Design, Synthesis, and Testing of High Energy Density Dielectric Materials for Capacitor Applications

Gregory Martin Treich, PhD

University of Connecticut, 2017

The rapid implementation and improvement of renewable energy technologies require advanced dielectric materials to enable capacitive energy storage under high fields. Since capacitors are among the most pervasive electronic device in many of these systems, my search for improved dielectrics focused on the application of film capacitors. To overcome these current problems, new polymers need to be developed that can serve as the dielectric material in electronic devices. Such a comprehensive search requires careful prior planning to ensure that effort is not needlessly wasted and thus a rational co-design approach was developed. Through this approach, high-throughput computational predictions are used to guide experimental synthesis so that the most likely candidates can be made and characterized first. Through a feedback loop, these real-world results are returned to the computationalists to improve their search to yield better informed suggestions. The result of this approach is the selection of several polymers as candidates for dielectric materials. Those polymer candidates were then studied in-depth to understand how various polarization mechanisms would influence their dielectric response. Computational methods such as molecular dynamics, density functional theory, and machine learning were used to gather deeper insight and help understand experimental results. Ultimately, by exploiting these polarization mechanisms, polymers with high dielectric constants, breakdown strengths, and energy densities could be produced.

A Materials Genome Approach to the Design, Synthesis, and Testing of High Energy Density Dielectric Materials for Capacitor Applications

Gregory Martin Treich

B.S. Rensselaer Polytechnic Institute, 2013

A Dissertation

Submitted in Partial Fulfillment of the

Requirements for the Degree of

Doctor of Philosophy

at the

University of Connecticut

2017

APPROVAL PAGE

Doctor of Philosophy Dissertation

A Materials Genome Approach to the Design, Synthesis, and Testing of High Energy Density Dielectric Materials for Capacitor Applications

Presented by

Gregory Martin Treich, B.S.

Major Advisor _____
Gregory A. Sotzing

Associate Advisor _____
Yang Cao

Associate Advisor _____
Ramamurthy Ramprasad

Associate Advisor _____
Douglas H. Adamson

University of Connecticut
2017

Acknowledgements

It would be insane to say that anyone could earn a Ph.D. alone, and I have many people to thank for both setting me on the right path and helping me to realize my dream of becoming a scientist who could, hopefully, contribute positively to society. First, I want to thank my major advisor, Prof. Gregory A. Sotzing, for giving me more advice and knowledge throughout my Ph.D. than I realized at the time. He has taught me how to be both an independent researcher, contemplating and carrying out my own experiments, and a collaborative member of a multi-university and multi-disciplinary research effort where coordination between numerous research groups was essential to meet our goals. Prof. Yang Cao and JoAnne Ronzello also deserve special thanks for listening to hours upon hours of my questions and crazy ideas as I expanded my work deeper into electrical engineering despite having their own students who kept them both incredibly busy. Towards the end of my research I would often times spend more time in their lab carrying out tests than I would in my own lab. I would also like to thank my other associate advisors, Prof. Ramamurthy Ramprasad and Prof. Douglas H. Adamson, for their helpful discussions and guidance, which allowed me to think about my research in new ways.

I also want to thank my undergraduate research advisor Prof. Chang Y. Ryu at Rensselaer Polytechnic Institute (RPI), who first raised my interest in Polymers. Prof. Ryu would often meet with me one-on-one to teach me the fundamentals of polymer physics that had not yet been covered in my coursework. I am forever

grateful to the late Prof. James V. Crivello who taught me Polymer Chemistry at RPI and helped lead me to get my Ph.D. in Polymer Science instead of Chemistry, which opened up many exciting possibilities for me.

My thesis work on a Navy Funded Multidisciplinary University Research Initiative (MURI) required many people to run effectively, and I would like to thank them all for their work, discussions, and suggestions. Dr. Arun Kumar Mannodi Kanakkithodi has been especially close, as both a researcher and a friend, allowing us to have late night discussions about our work that would sometimes lead to novel ideas. Mattewos Tefferi, Zongze Li, Dr. Huan Tran, Prof. Sanat Kumar and Dr. Mayank Misra from Columbia, Prof. Mukerrem Cakmak and Dr. Ido Offenbach from Akron, among many others, were very helpful throughout my research.

Sotzing Lab members, both current and past were of great help including my mentors Dr. Aaron Baldwin and Dr. Rui Ma as well as all my coworkers, especially Shamima Nasreen and Sneh Sinha. My undergraduate students, Sydney Scheirey and James Flynn, both worked alongside me in the lab for years and carried out numerous experiments whose results are reported in this Thesis. Thanks to their help, I was able to work on more projects simultaneously than I would have alone.

Finally, I would like to thank my friends and family for their endless support of me throughout my journey, especially my parents, Martin and Debbie Treich. To my wife, Melissa Treich, who I married during my Ph.D., I certainly would not be completing this without your help, encouragement, and love. Thanks.

TABLE OF CONTENTS

Chapter 1

1. Introduction

This introduction covers some fundamentals and theories that are necessary to understand and discuss the contents of this thesis, most importantly, the theory of dielectrics. A brief overview of the uses of dielectrics and origins are outlined to give a historical perspective. In addition, a survey is carried out on the strategies being employed by other research groups around the world as the community strives to improve and expand the dielectric materials available. Finally, the strategy that was followed in this thesis, the rational co-design approach between computational predictions, experimental synthesis, and electrical characterization is discussed. This section covers both the overall strategy and early successes that helped guide the work presented in this thesis.

1.1 Theory of Dielectrics

Throughout this thesis, there will be numerous references to and mentions of dielectrics, an area of electrical engineering that may not be as familiar to the readers of this as the chemistry presented here. Due to this fact, the introduction attempts to cover some of the basics of the theory of dielectrics as well as introducing some applications for them. Also included are some common materials for dielectrics, which

will serve as benchmarks throughout this thesis to compare newly synthesized materials to what is currently being used in the industry as well a brief history on how dielectric materials have progressed over the years. While not complete, this introduction on dielectrics should give the reader enough knowledge to understand the experiments that were performed and the reasoning behind them as they read the later chapters.

1.1.1 Polarization and Permittivity

Dielectric materials can be thought of, most basically, as an insulator, such as the polyethylene coating around high voltage cables. If a conductive material were placed in an electric field, electrons would flow through the material as it does in a metal wire. When a dielectric material is placed in an electric field, the electrons instead alter their equilibrium positions through a process called polarization. Dipoles in materials are also moved through shifts in electron positions caused by polarization, and even the orientations of materials can move. An example of polarization is shown in **Figure 1.1** where a dielectric material is placed between two conductive plates with an area (A) and distance (d) with an applied electric field (**E**). The relative permittivity of a material has a large dependence on several factors as the Clausius-Mossotti relationship in **Equation 1.1** demonstrates below.

$$\frac{\varepsilon_r - 1}{\varepsilon_r + 2}\frac{M_W}{\rho} = \frac{N_A \alpha}{3\varepsilon_0} \qquad \textbf{(1.1)}$$

Here, M_W is the molecular weight of the molecule, ρ is density, N_A is Avogadro's number (6.022×10^{23}), and α is the constant of molecular polarizability. The Clausius-

Mossotti relationship shows that while polarization is fundamental in determining relative permittivity, other aspects should not be ignored. An equivalent but simpler equation, the Lorentz-Lorenz **Equation 1.2** is also used. This equation instead uses N which is the number of molecules per cubic meter, also referred to as number density.[1]

$$\frac{\varepsilon_r - 1}{\varepsilon_r + 2} = \frac{N\alpha}{3\varepsilon_0} \qquad \textbf{(1.2)}$$

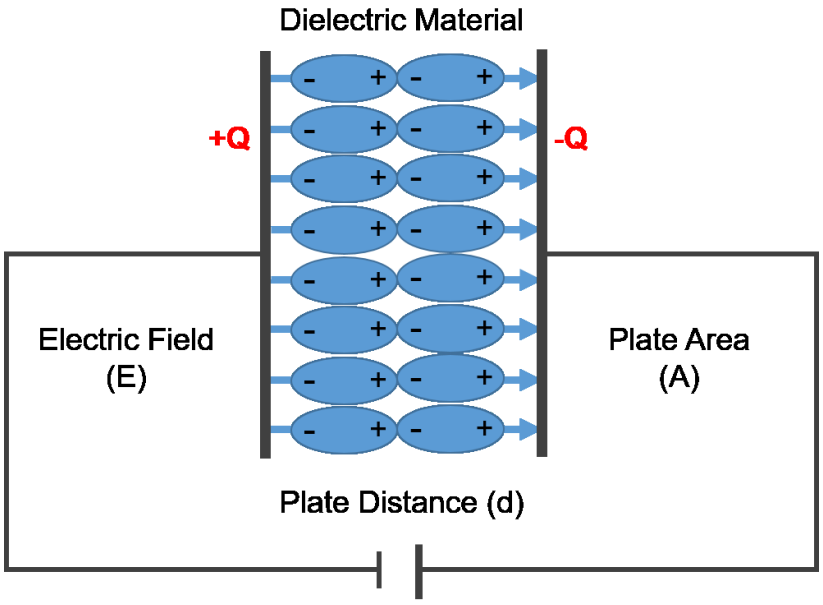

Figure 1.1 Representation of a dielectric material in an applied electric field (E) across a plate distance (d) with plate area (A) and the internal polarization in the material denoted by positive (+) and negative (-) charges.

In a basic capacitor, the charges (Q) that are accumulated on both of the conductive plates throughout the experiment storage electrical energy and can later be released. The ability for the dielectric material to store this charge is based on

numerous properties but fundamentally relies on polarization. There are numerous types of polarization that can occur inside polymer dielectrics, which are considered in this thesis. They are electronic polarization (P_e), atomic polarization (P_{at}), orientational or dipolar polarization (P_{dip}), ionic polarization (P_{ion}), and interfacial polarization (P_{int}). An illustrative depiction of the three types of polarizations mechanisms important for parallel plate capacitors is shown below in **Figure 1.2**. It should be noted that the Clausius-Mossotti relationship only applies to electronic, atomic, and dipolar polarizations as they are the simplest to predict and mathematical representations of other polarizations are outside the scope of this thesis.

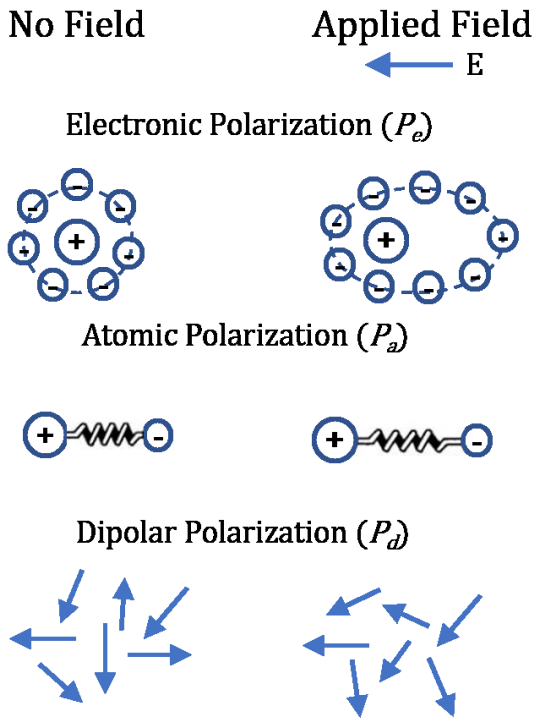

Figure 1.2 An illustrative depiction of five types of polarization mechanisms that can be present in a dielectric material.

Electronic polarization (P_e) shown in **Figure 1.2** is the most fundamental type of polarization and occurs in every atom with both a nucleus and at least one electron orbiting that nucleus. In the absence of an electric field, the electron(s) will orbit the nucleus consistent with the Electron Cloud Model per Schrodinger's equation. When an electric field is applied, even in the case of a neutral atom such as argon, the electron cloud will be polarized and distorted, so the negatively charged electrons will orbit with a bias towards the positively charged side of the applied field. While electronic polarization occurs in every atom, the effect will be stronger in sulfur than in carbon due to the larger electron cloud allowing the electrons more freedom to shift.

Atomic polarization (P_{at}) shown in **Figure 1.2** and sometimes referred to as vibrational polarization occurs in molecules as they require electron bonds between atoms. The vibrations of interest are the same vibrations studied by infrared spectroscopy such as stretching, bending, rocking, wagging, and twisting modes. In vibrational polarization, the nuclei of the atoms will polarize and adjust its position relative to other nuclei. This polarization occurs on a longer timescale than atomic polarization as atoms move significantly slower than electrons and at high frequencies, the atomic nuclei would effectively remain stationary while the electrons surrounding them would continue to be polarized.

Orientational or dipolar polarization (P_{dip}) shown in **Figure 1.2 C** exists only in molecules where there is a permanent dipole moment. When an electric field is

applied, the dipoles are oriented in the field, hence the name dipolar polarization. In molecules such as water, the speed of this orientation is relatively quick and the magnitude of polarization high. However, for polymeric materials that are the focus of this thesis the speed of orientation is much slower due to chain entanglements and inter-molecular interactions. The relative magnitude and frequency of all these polarizations are shown in **Figure 1.3.**

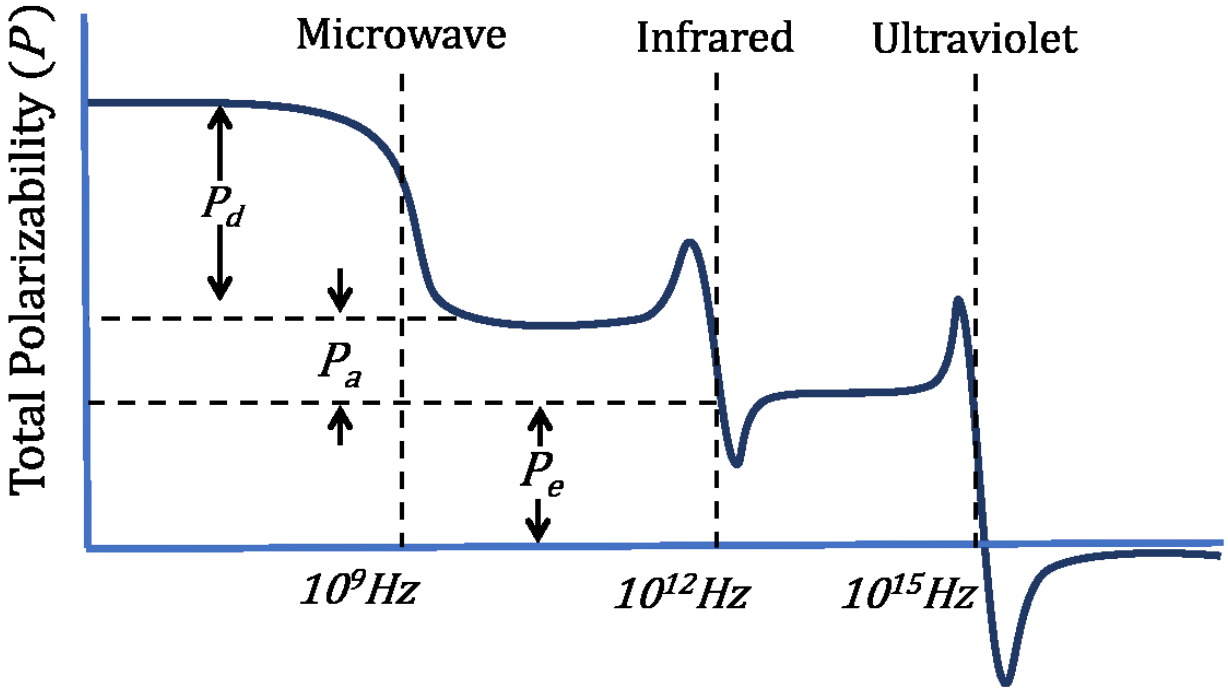

Figure 1.3 A cartoon graph showing different types of polarization as a function of relative frequency in polymers for the polarization mechanisms relevant to this study.

Ionic polarization (P_{ion}) involves ions that can move freely in response to electric fields, it is primarily found in supercapacitors and not of much importance to traditional capacitors.[2,3] The last remaining important polarization is Interfacial polarization (P_{int}), and can also be called Maxwell–Wagner–Sillers polarization.

Interfacial polarization is due to charge carrier buildup at an interface such as between a polymer and a nanoparticle.[4] These two processes typically operate at frequencies below 10 Hz and are less important for the polymer systems discussed in this thesis; however, they remain an important aspect of dielectric physics.

1.1.2 Dielectric Constant and Loss

The orientation of molecular dipoles is a relatively slow process if compared to electronic transitions or molecular vibrations. Only when sufficient time is allowed after the application of an electric field for the orientation to attain equilibrium will the maximum polarization be achieved in the material. Therefore, under an alternating field: $\boldsymbol{E} = \boldsymbol{E_0}\cos\omega t$, one should observe a lag behind the applied field. It can be described by a phase lag in the electric displacement:

$$\boldsymbol{D} = \boldsymbol{D_0}\cos(\boldsymbol{\omega t} - \boldsymbol{\delta}). \tag{1.3}$$

It can be written as

$$\boldsymbol{D} = \boldsymbol{D_1}\cos\boldsymbol{\omega t} + \boldsymbol{D_2}\sin\boldsymbol{\omega t}, \tag{1.4}$$

where $\boldsymbol{D_1} = \boldsymbol{D_0}\cos\omega t$ and $\boldsymbol{D_2} = \boldsymbol{D_0}\sin\omega t$. This made it easy to define dielectric constant as a complex function:

$$\boldsymbol{\varepsilon^*} = \boldsymbol{\varepsilon'} - \boldsymbol{i\varepsilon''} \tag{1.5}$$

where the real part of dielectric constant $\varepsilon' = \frac{D_1}{\varepsilon_0 E_0}$ and imaginary part of dielectric constant $\varepsilon'' = \frac{D_2}{\varepsilon_0 E_0}$. The ratio of the two parts $\varepsilon'/\varepsilon''$ is termed the dissipation factor, tan δ. The frequency dependence of the real and complex parts are describe with Debye's equations:

$$\boldsymbol{\varepsilon_r'(\omega) = n^2 + \frac{\varepsilon_s - n^2}{1+\omega^2\tau^2}} \quad \textbf{(1.6)}$$

$$\boldsymbol{\varepsilon_r''(\omega) = \frac{\varepsilon_s - n^2}{1+\omega^2\tau^2}\omega\tau} \quad \textbf{(1.7)}$$

where $n^2 = \varepsilon_\infty$ is the dielectric constant at very high frequency, ε_s is the static dielectric constant, and τ is called dielectric relaxation time. In practice, the dielectric constant and loss are determined by measuring the capacitance of a material in farads and the dissipation as tanδ. The dielectric constant (ε) is related to the capacitance (C) of a polymer by

$$\boldsymbol{\varepsilon = \frac{C(F)d(m)}{\varepsilon_0(F/m)A(m^2)}} \quad \textbf{(1.8)}$$

where d is the thickness of the material in meters, ε_0 is the permittivity of a vacuum in farads per meter, and A is the area of the electrode in square meters.

1.1.4 Dielectric Breakdown

The point of breakdown, or failure, in dielectric polymers is of increased interest as materials are sought out with ever-increasing energy densities. The energy density (U_e) of a material is given by

$$\boldsymbol{U_e(J/cc) = \frac{1}{2}K\varepsilon_0 E^2} \quad \textbf{(1.9)}$$

where K is the dielectric constant, ε_0 is the permittivity in a vacuum and E is the applied electric field. Dielectric materials that have a higher breakdown strength are able to be safely and repeatedly used at higher operation voltages. Due to the squared dependence on the electric field, any increase in operating voltages leads to a larger increase in the overall energy density than a similar increase in dielectric constant.

The intrinsic breakdown strength in a material can either be considered as the breakdown strength in an absolute defect free and 100% pure sample or, as the highest breakdown field ever recorded for a given material, which, is more practical to determine. Typically, impurities can impact a material by either being mobile and conductive or an interface at which a charge buildup could occur.[5]

The intrinsic breakdown strength mainly depends on the electronic band structure of the dielectric material. An insulating material has two electronic bands of interest, the valance band where electronic sit in atomic orbitals, and the conduction band, which is comprised of empty atomic orbitals. When enough energy is present to excite an electron from the valance band to the conduction band, a chain reaction is set off resulting in a catastrophic breakdown event. Therefore, polymers with high band gaps such as polyethylene and polypropylene have been widely used as dielectric materials.[6] Polymer dielectrics benefit from graceful failure mode which occurs at the point of breakdown in polymer films. When a breakdown event happens, the polymer film and nearby thin aluminum electrode are vaporized to prevent future shorting and remain operational.[7]

1.2 Applications for Dielectrics

1.2.1 Capacitors for DC Link Grid Connects

Film capacitors have an integral role in the electrified future promised by the green energy revolution. As traditional industries, such as power generation and

vehicular transportation, the shift from fossil fuels towards renewable energies electronic devices are needed to interface between energy generation, storage, and use. For power generation in wind turbines, DC-Link capacitors are used to stabilize voltage in intermediate circuitry and require the ability to operate at high voltages. Solar inverters also use DC-Link capacitors in parallel, either with the source or between the batteries. Since solar panels are typically placed in sunny locations that can reach high temperatures and elevated safe operational temperature is required for their reliable operation. On the power consumption side, DC-Link capacitors are used in electricity driven trains where the AC grid power is converted to DC power to drive the motors. These capacitors are again used to interface between regenerative breaking technologies and the power system.[8,9]

1.2.2 Embedded Capacitors (PCB)

Embedded capacitors are a type of embedded component in which the parts of the device are integrated into the printed circuit board (PCB). Such components are typical in computer circuit boards such as the motherboard and daughterboard in personal computers. Embedded components have an advantage over discrete components due to an increased electrical performance, greater efficiency, and a higher density of components leading to reduced device cost. The improvements in electrical performance come with higher reliability as embedded components eliminate solder points, which are a major point of failure in systems. The shortened leads and compact design give the device a greater efficiency due to reduced parasitic loss As in all film capacitors, a high dielectric constant allows for increased energy

density and increasing the dielectric constant allows for the same energy to be stored in a smaller space, saving room and improving the device.[10]

1.2.3 Pulse-Powered Applications

The United States Military, following the discovery of the pulse-powered radar by Robert Page at the Office of Naval Research in 1934, originally spearheaded large-scale implementation of pulse-powered devices. Radar technology proved to be crucial to the allied victory in World War II and continued to progress in both land and airborne implantations afterwards. Research into pulse-powered systems expanded greatly after the war and had continued to be pursued by the Office of Naval Research to this day.[11] New research focuses include high-speed railguns, high-energy lasers, and modernized aircraft launch systems instead of the steam catapults used since their inception.

One of the most crucial components of an aircraft carrier is the launching catapult that is required to accurate aircraft to takeoff speeds. Historically, this has been powered by steam driven catapults, which were first used in 1912, and over 100 years later their old design is beginning to show. The systems take up 1133 m^3 of volume and weigh in at 486 metric tons, most of which is above water destabilizing the ship, and are limited to an energy limit of around 95 mega joules (MJ). These new Gerald R. Ford class super carriers are being designed with a new Electromagnetic Aircraft Launch System (EMALS), which will take stored energy on rotary disk alternators and release it in a 2-3 second pulse. The system requirements are less than 425 m^3 and less than 225 metric tons or about half the mass and volume of the

current launch system while delivering up to 122 MJ of launch energy. While these are currently being implanted on new ships out of necessity, the Navy desires a move away from mechanical energy storage to a capacitor driven system which would reduce weight, volume, and maintenance.[12,13]

The Navy is also looking to the future of combat by developing long-range electromagnetic rail guns with distances exceeding 200 miles to strike a target well before the ship is vulnerable. Attacks at these distance from the sea are typically carried out with tactical guided missiles with are cost prohibitive for large volume barrages. With an electromagnetic rail gun, a 10-20 kg projectile is shot between 2000-3000 m/s, allowing for a cheaper munition to more rapidly respond to a threat. Since rail guns do not have any explosive propellant, they are naturally safer but need up to 60 MJ of energy to launch. While currently large capacitor banks are used to test rail guns, they are typically used as a single shot since a large amount of heat is produced with each firing. Besides kinetic rail guns, high-energy laser weapons are also being developed which would concentrate a 1-4 MW laser at a point target for several seconds. The point target would be trained on incoming missiles to neutralize them before they come within striking distance of sensitive targets. With improved energy densities, these laser systems could be integrated into aircraft effectively shielding them from attack. Any system designed for rapid, repeated fire must have a cooling system integrated to keep the system at the operation temperature of the capacitors. This is especially difficult since capacitors are good dielectric insulators; they are naturally very good thermal insulators as well. By increasing the operational

limit of the capacitors, a reduced cooling system would be required to keep the capacitor bank in operation.[14,15]

1.2.4 Inertial Confinement Fusion

Inertial Confinement Fusion (ICF) is one of the most promising methods currently being studied to carry out a sustainable fusion reaction for power generation. The approach entails taking a fuel pellet, typically on the order of milligrams, consisting of deuterium and tritium and compressing it while heating. The easiest way to accomplish that is by concentrating numerous high-powered lasers all at the same point and pulsing them simultaneously. Previous designs have used electrons or ions; however, lasers are now regarded as the best path forward. The French Laser Megajoule facility is designed with capacitor banks to power the lasers with a capacity of 480 MJ to power the flash lamps. In total 176 beams will be powered by these capacitors. The United States' National Ignition Facility is also conducting research using laser pulses powered by capacitors banks. However, much of the research there is focused on nuclear weapons research and simulating bomb confinement since the comprehensive test ban treaty prohibits direct testing of nuclear weapons. By improving capacitor technology, the size and cost of these massive capacitor banks needed to power the ICF experiments, and someday, commercial reactors should drastically decrease. More importantly, if capacitor efficiency at operational electric fields and temperatures is improved the amount of power needed to be drawn from the grid would be reduced, allowing the experiments to become more sustainable.[16–18]

1.3 Common Dielectric Materials

1.3.1 History of Capacitor Dielectrics

Capacitors have been traced back to the earliest forms around 1745 starting with a Leyden jar of water with an inner electrode and foil on the outside of the jar by Ewald Georg von Kleist.[19] Benjamin Franklin removed the water and made a capacitor using foil as electrodes on either side of a glass sheet forming a matching schematic to a modern day capacitor.[20] In 1876 Fitzgerald used wax-impregnated paper, still with foil electrodes while other variations used oil-impregnated paper depending on the applications.[21] Later, William Dubliner invented mica capacitors in 1909, which became heavily used due to their low losses. The elimination of airgaps gave greater capacitance per volume while airtight enclosures prevented any microstructure and performance change due to oxidation or corrosion that could happen between metal plates. The third main iteration of ceramic capacitors after glass and mica came about from barium titanate ($BaTiO_3$) which has a dielectric constant of about 1,000, and they are used to this day in multilayer ceramic capacitors (MLCC).[7] Today barium titanate is being rigorously studied for use as a nanoparticle filler in dielectric composites to drastically boost the dielectric constants of organic polymers as discussed later in **Section 1.4.2**. Modern film capacitors first started in 1900 when the paper was metallized to produce a self-clearing capacitor but was impractical to use. This was followed by paper coated in lacquer in the 1940s, and finally, in 1954, Bell Labs produced a lacquer film, metallized it, and made the first metallized film capacitor.[22,23] Polymer film capacitors then rapidly took off as

polyethylene terephthalate (PET), polyethylene (PE), polystyrene (PS), and polycarbonate (PC) were all investigated and used in capactiors.[24] Biaxially-oriented polypropylene (BOPP) was developed an served as the industrial standard for metallized film capacitors into the present and will be talked about, along with other materials used today and novel materials being developed to replace these materials in the following sections.[25]

1.3.2 Biaxially-Oriented Polypropylene (BOPP)

Biaxially-Oriented Polypropylene (BOPP) has been called the most important polymer film for capacitors and is often referred to as the state of the art material by which all recent innovations and works are compared to. One of the main benefits that BOPP has over other polymers is it's low cost, being synthesized directly from propene gas which itself is low cost makes the reaction simple and clean to produce the bulk feedstock. While other commodity polymers such as polyethylene (PE) and polystyrene (PS) are similarly cheap, their properties are not close to BOPP, and thus they are less desirable. BOPP also has the benefit of being melt processable in the bulk, this allows for a solvent free process to extrude continuous films. While continuous films can also be solvent cast, the high mobility of solvent molecules within a film can lead to increased conductivity and dielectric loss in a capacitor film and must be carefully processed to remove nearly all residual solvent. Bulk processes the polymer from the melt help to alleviate these steps. One of the largest benefits of BOPP that is also found in PE is that their chains consist almost entirely of hydrocarbons, which drastically lowers their hysteresis loss and allows for high

energy efficiency capacitors. Due to statically chances, there will be some oxidation that occurs along these polymer chains, specifically where disproportionation leaves an unsaturated double bond. However the concentration of these would be low. The real benefit that PP has over PE is that the addition of the side group allows PP films to be a stretch in ways that drastically enhance the crystallinity. After films are extruded, they can be passed through rollers and expanded along both the x and the y-axis, with the z-axis being the film's thickness, resulting in biaxially-oriented polypropylene (BOPP). This crystallinity in non-polar polymers helps to increase the breakdown strength and in the case of BOPP brings it to upwards of 640 MV/m and in some cases as high as 730 MV/m. Despite having a low dielectric constant due the hydrocarbon chain of 2.2, this high breakdown strength gives BOPP a maximum energy density of 5 J/cm^3, with the energy density typically being closer to 3 J/cm^3 at electric fields used in practice.[25–28]

1.4 Strategies for Enhancing Dielectric Constant

Besides the coveted BOPP, many other polymers have been invested for use in dielectric films for capacitors.[7] Polyethylene (PE) has a low operational temperature and could never match the high breakdown strength that BOPP has with a similar dielectric constant. Polyester, specifically polyethylene terephthalate (PET), has also been widely used in specialty capacitors and has a higher maximum operational temperature of 125 °C compared to between 85 °C and 105 °C for BOPP. Despite a lower breakdown voltage of about 570 MV/m, PET has a similar energy density as

BOPP due to an increased dielectric constant at 3.3. Along with PET, polycarbonate (PC) was also used for some capacitors but has an increased cost over BOPP and is more likely to have defects throughout the structure that could prove detrimental to operation along with increased loss. Poly(vinylidene fluoride) (PVDF) showed a great dielectric constant an order of magnitude higher at around 12 but to get this high of a dielectric constant through polarization came with an equally high loss at about two magnitudes higher than that of BOPP, rendering it ineffective for most capacitor applications.[26] Several polymers were also investigated for use as high temperature polymers in poly(ether imide) (PEI) with a dielectric constant of 3.2, poly(ether ether ketone) (PEEK) at 3.1, and poly(phenylene sulfide) (PPS) also at 3.1. For high temperature applications, up to 150 °C it was clear that the commercially available PPS was sufficient. However, conductivity increased past that point and PEEK, but more impressively PEI, were found to be preferred choices. Despite PEEK having a glass transition temperature (Tg) of 149 °C the film still proved operational and until 200 °C, the highest temperature measured.[29] As has been discussed in section 1.2, there is a growing desire to find new polymers to replace these initial film capacitors that have been in production since the 1960s with materials that have a higher energy density with improved operation at elevated temperatures. Through utilizing the now better understood polarization mechanisms and phenomena that affect dielectric constant and breakdown in polymers, laboratory scale materials are being developed with improved dielectric constants and subsequent energy densities to take dielectric materials into the next generation.

1.4.1 Polyvinylidene Fluoride (PVDF)

One strategy used to achieve high dielectric constants in polar polymers is to rely on the previously mentioned orientational polarization mentioned in **Section 1.1.1**. The viability of such polarizations in dielectric applications has to do with the frequency at which they relax and whether this overlaps with the usage window of the application. While this is true for all types of polarizations, including electronic which is present in all materials, orientational polarization can typically occur in the use window. When the relaxation occurs in that regime, it will impart significant dielectric loss which manifests itself as heat, making the material less than desirable for most applications as there is typically a desire to remove heat and have efficient charging and discharging of the electric field.[30] PVDF is a well-known polar polymer which is ferroelectric in nature resulting in wide D-E hysteresis loops which large losses.[31] While it would appear that PVDF would be a poor material for high energy density dielectrics, it has been found that the crystalline structure of PVDF is strongly correlated to its dielectric loss.[32,33] In order to control the crystalline structure, copolymers and terpolymers of PVDF with other monomers such as trifluoroethylene (TrFE), chlorotrifluoroethylene (CTFE), and hexafluoropropylene (HFP).[34–38]

The copolymer p(VDF-HFP) in a 96/4 (mol/mol) ratio was synthesized and the processing methods were studied to enhance the dielectric constant from about 6 to 12 by hot pressing and stretching the films to give a crystal structure parallel to the chain axis. This was compared to a solution cast sample, which was oriented in a

perpendicular crystal structure to the chain axis. The orientation of the hot pressed and stretched films were able to have reduced loss as the relaxation peak was shifted from about 10 Hz to roughly 10^6 Hz.[30] By blending a copolymer p(VDF-CTFE) with a similar polymer that had a low dielectric loss, poly(ethylene-chlorotrifluoroethylene) p(ECTFE), a high dielectric constant of 7 with a loss as low as 1% was able to be achieved, which was remarkable for a PVDF based material at the time. The high field hysteresis loss was also able to be drastically reduced when the blends were crosslinked together to impede any ability to phase segregate at high fields.[32] Besides fluorinated polymers, PVDF has also been blended with aromatic polythiourea achieving energy densities around 10.8 J/cc with an efficiency above 83%.[39] By expanding beyond the homopolymer PVDF and experimenting with co/terpolymerizations and blends the dielectric relaxation can be pushed to higher frequencies, which successfully removes much of the hysteresis loss from the typical use window of high energy density applications.

1.4.2 Nanocomposites

The other commonly used strategy to increase the dielectric constant of polymers is to add metallic fillers to them in order to increase the polarization. Typically these fillers are sub-micron in size or even a little larger and are typically referred to as nanocomposites.[40] Beginning in the 1940s when the ceramic barium titanate ($BaTiO_3$) was discovered to have a dielectric constant over 1000 it was evident that these ceramics would have a much higher dielectric constant than polymers probably ever could achieve. With further study, it was revealed that the

grain size of $BaTiO_3$ played a large role in the dielectric constant and that coarse grains (20-50 μm) were responsible for the now relatively low dielectric constant of 1000 and fine grains (1 um) were found to have permittivity's as high as 5000 at room temperature.[41] Despite these high dielectric constants, pure ceramics are not ideal for some dielectric applications such as capacitors due to their catastrophic failure and other reasons discussed in the previous sections. Instead, researchers have tried to combine these ultra-high dielectric ceramics with a polymer matrix in order to get the benefits of a film capacitor with the high dielectric constants and subsequent high energy densities of ceramic. The size of the particle filler becomes increasing important with these polymer composites as the applications require thin polymers films on the order of several microns, therefor the fillers have to be at least an order of magnitude smaller than that as to not cause issues.[42] The reduction in the size of these fillers from the 1 um $BaTiO_3$ to 10s of nanometers causes the dielectric constant to drop considerably to a few hundred.[41,43] Besides $BaTiO_3$, numerous other nano-fillers have been investigated for dielectric applications including TiO_2 (80) ZrO_2 (25) HfO_2 (25) as well as numerous other cheap metal oxides and ceramics.[44]

In order to achieve high dielectric constants in stable nanocomposites that can withstand high electric fields several considerations need to be taken into account when during processing. Small nanoparticles have an incredibly high surface area which causes them to want to agglomerate together.[45] To overcome this, high shear mixing is required to get a fully dispersed composite. Without uniform dispersion, the capacitive properties would suffer, and in the worse cases, conductivity could actually

increase. To further improve dispersion and reduce the potential for agglomeration researchers attempt to modify the surface of the nanoparticles. In one such study, researchers modified the BZCT [$(Ba_{0.7}Ca_{0.3})$ $(Zr_{0.2}Ti_{0.8})$-O_3] nanoparticle with methoxysilanes to improve the interface with a thiol-ene ink, PTD3 [pentaerythritol tetrakis (3-mercaptopropionate) (PEMP, P), 1,3-diisopropenylbenzene (DPB, D), 2,4,6-triallyloxy-1,3,5-triazine (TOTZ, T)] polymer matrix. The results were a threefold increase in the energy density from 13 J/cc to 36 J/cc by increasing the breakdown strength and moderately increasing the dielectric constant.[46] Other studies have focused on reducing the amount of polymer nanoparticles needed to achieve percolation, typically known to be around 30% by weight for a spherical particle.[45] One approach has been to increase the aspect ratio of $BaTiO_3$ nanowires from 9.3 to 45.8 boosting the dielectric constant about 30% at the same concentration or allowing similar dielectric constants with reduced weight of filler.47 PVDF and its copolymers has also been a growing area of research with nanocomposites from traditional BaTiO3 to novel reduced graphene oxide sheets.[34,48–51] Boronitride nanosheets have also been studied as a means of increasing the breakdown field both as a traditionally nanofiller and as layered sheets to block charge flow through the film to recent success.[52–55]

1.5 Rational Co-Design Process

This work followed an emerging rational co-design process to rapidly screen potential polymers for synthesis and characterization as described in the introduction

of my Advanced Materials Progress Report titled "Rational Co-Design of Polymer Dielectrics for Energy" and reproduced here.[56]

1.5.1 Rational Co-Design Introduction

Scientific discoveries and technological innovations have benefitted enormously from seemingly "trial and error" practices, and serendipity. A classic example that is often quoted in this context is the work of Thomas Edison surrounding the discovery of suitable materials for the light bulb filament.[57,58] Although the "Edisonian Approach" has been replicated time and time again in materials science and related fields by systematically (and laboriously) experimenting with several candidate materials,[59–61] recent materials discovery efforts approach this problem in a more rational manner using computations in the first screening stage (and in subsequent steps as required).[62] The initial down-selection effort based on advanced computations, when combined with targeted additional computations, materials synthesis, testing, and validation, is referred to here as "co-design". This emerging rational material co-design paradigm can significantly reduce costs, provide enormous insights, and speed up the materials design process.

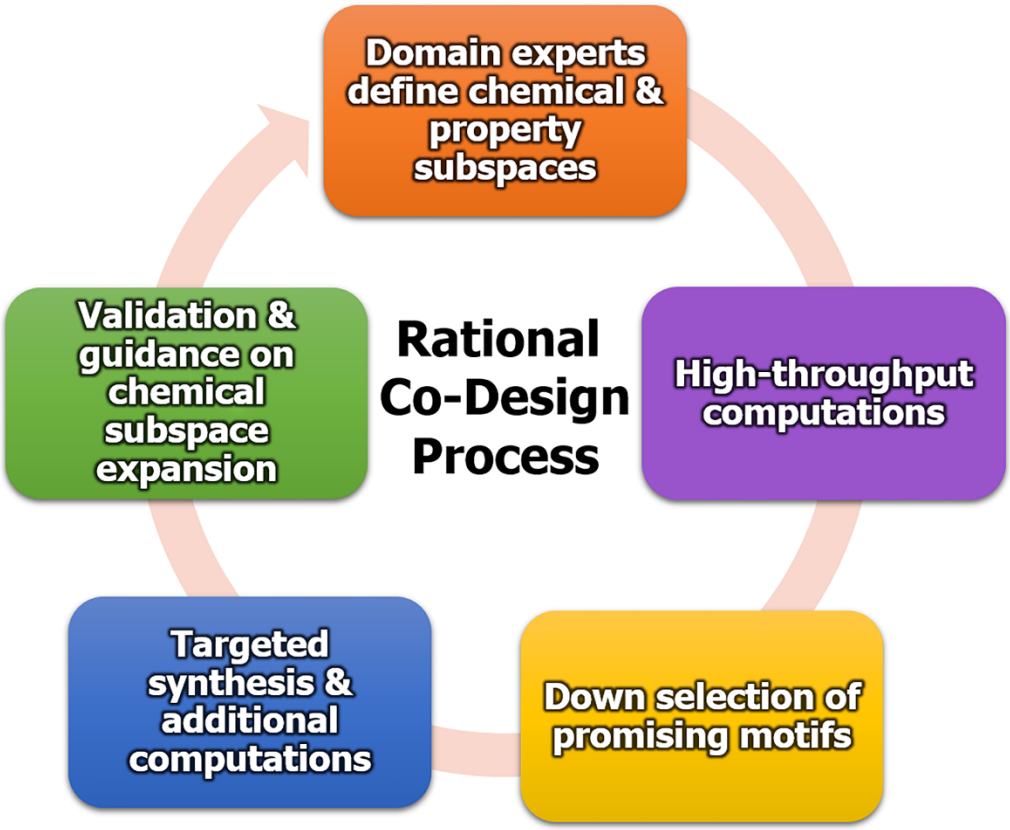

Figure 1.4. The primary steps involved in a rational co-design approach. Reproduced with permission from[56], Copyright (2016) John Wiley and Sons, Inc.

For the rational computation-guided co-design approach to work—at least in the manner practiced in the recent past—the problem has to be amenable to rapid high throughput computations, and it should be possible to state the (initial) screening criteria in terms of calculable properties. If such is the case, the "domain experts" of the materials and applications subfields frame the chemical subspace to be explored defined by the atoms/structural units and the framework in which such units may be placed; this will lead to a list of combinatorial possibilities. Additionally, the domain experts specify computable properties that are relevant to the desired

application. High throughput computations are then performed on these systems, at a chosen acceptable level of theory, to determine the properties deemed important in the initial screening step, leading to a shortlist of potentially useful candidate materials. Following this, the materials synthesis specialist further reduces the shortlist by determining which cases would be amenable to synthesis considering both availabilities of starting materials and cost of production. Only at this point are any benchtop experiments done, and attempts are made to produce the few selected materials. Those successfully synthesized undergo in-depth computations to include additional details previously ignored during the initial high-throughput screening step (such as the actual crystal structure or morphology, the requirement of a higher level of theory for some properties, etc.). The computed results are then compared with measurement results for validation, and the results are analyzed. Further in-depth studies are planned that may lead to an alteration of the initially chosen chemical subspace, and the process may continue in an iterative manner. A possible workflow that captures these notions is portrayed in Figure**.4.**

Notable examples of recent successes of such efforts include the identification of new cathode materials for Li-ion batteries,[63] design of Li-doped Cr_2MnO_4 as a new p-type conducting oxide material,[64] realizing the suitability of a host of previously unknown 18 electron ABX compounds for topological insulators, thermoelectric and piezoelectrics,[65] the rational co-design of Co_2-based Heusler compounds for spintronics applications,[66] the creation of advanced catalysts,[67] and the rational design of new organic and organometallic polymer dielectrics,[68–74] the subject of this

article. The past successes and future potential of the rational co-design approach has been recognized in terms of initiatives such as the Materials Genome Initiative[75,76] and the Integrated Computational Materials Engineering[77] framework, as well as in terms of the emergence of several useful materials databases.[78–82]

The primary focus of this article is the application of such a rational co-design process for the identification of entirely new polymer dielectrics options for high energy density and electrostatic energy storage applications. The demand for high energy density capacitors has gone up in recent years, courtesy the on-going electrification of land[83,84] and sea[85] transportation, and other military and civilian systems[85,86]. Whereas ceramics could conceivably be used as dielectrics in capacitive energy storage applications, polymers provide a clear advantage as they display "graceful failure" at high electric fields. Since the energy stored in a capacitor is proportional to the dielectric constant and the square of the electric field, dielectric polymers of interest should display a high dielectric constant and high electrical breakdown field. Low dielectric loss and resistance to high field degradation of the polymer itself are other important requirements. Biaxially oriented polypropylene (BOPP), with a high breakdown field of about 700 MV/m and a dielectric constant of about 2.2, is the current state-of-the-art polymer dielectric in high energy density (metalized) film capacitors. Attempts to improve upon BOPP have been based on poly(vinylidene fluoride) (PVDF) and its copolymers,[31,39,87–91] polymer nanocomposites,[45,92,93] multilayers,[94–98] and so on. All such potential replacements have suffered from one or the other weakness, like high loss or low parallel plate

breakdown field. The history of capacitor materials, including recent advances and persistent challenges underlying new materials development, has been recently reviewed.[99]

Clearly, strategies are needed to identify new promising polymers. Given the vastness of the polymer chemical (and configurational) space, it is safe to assume that significant untapped opportunities exist and that several new polymer dielectrics are waiting to be discovered. As pointed out above, the availability of modern computational methods, used within a co-design paradigm, provides the opportunity to perform rational and targeted searches for novel dielectrics at reasonable cost;[100] this can extend significantly the reaches of purely empirical Edisonian attempts. The present contribution reviews recent such successful attempts at chemical space searches that have resulted in the co-design of new organic and organometallic polymer dielectrics appropriate for high energy density applications.

1.5.2 Strategy for Initial Rational Computation-Guided Search

With respect to exploring large polymer chemical spaces for dielectric capabilities, the historical work has generally featured a few limited subclasses/families of polymers. The staggeringly large number of chemical unit possibilities, and the various kinds of possible connectivity sequences of the units giving rise to different polymer repeat units (Figure provides a flavor) make an experimental examination of a substantial number of these systems impractical.

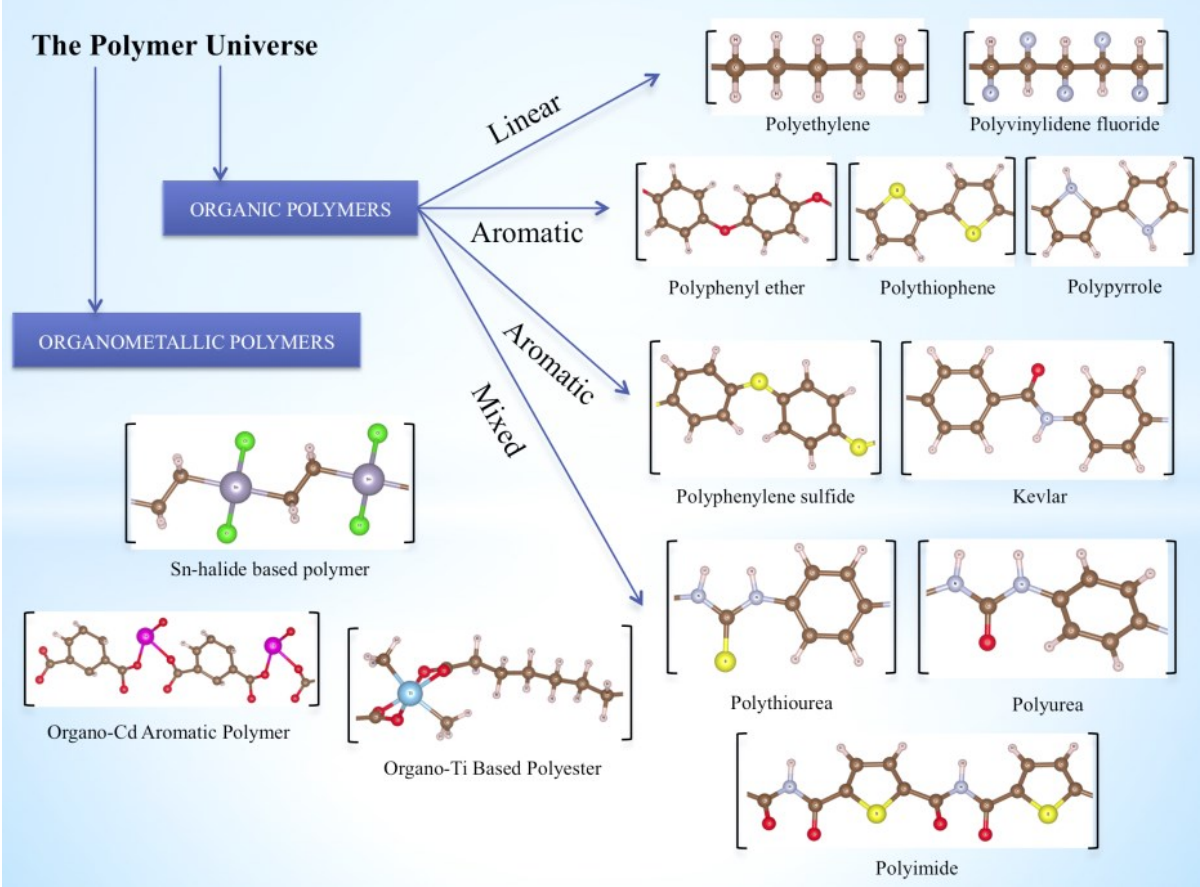

Figure 1.5. The vast chemical space spanned by a variety of polymer building blocks. Reproduced with permission from[56], Copyright (2016) John Wiley and Sons, Inc.

However, a controlled subspace selected out of this vast expanse could be a dataset of polymers that is ripe for high-throughput computational study. This was recently attempted in a study by Sharma *et al.*,[68] in which the chemical subspace contained the following 7 building blocks: CH_2, CO, NH, C_6H_4, C_4H_2S, CS and O. Such a set of building blocks was chosen based on their presence in well-known polymer systems, and was deemed suitable for performing a controlled computational-experimental study of organic polymers. The different polymers were generated by linearly connecting randomly chosen blocks out of the set of 7, as shown in **Figure**

1.6. This led to the possibility of hundreds of different symmetry-unique polymers, assuming that the repeat units were composed of 4 blocks.

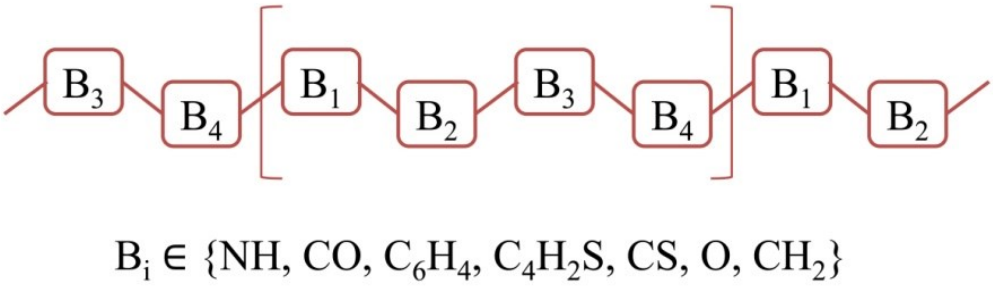

Figure 1.6. The organic polymer chains selected for high throughput computations. Reproduced with permission from[56], Copyright (2016) John Wiley and Sons, Inc.

First principles computations using density functional theory (DFT)[101,102] was then performed on all such polymers in a high-throughput manner, resulting in the band gap and the electronic and ionic dielectric constants, denoted by ε_{elec} and ε_{ion}. In the terminology used here, ε_{ion} includes all non-electronic contributions to the dielectric response, including bond stretching and bond (dipole) rotations allowed within a crystalline lattice. The sum of these two quantities, namely, ε_{elec} and ε_{ion}, typically computed within the perturbation formalism of DFT,[103] is the total dielectric constant ε_{tot}, which is relevant for comparison with measurements. For dielectric polymers to maximize the amount of energy stored in a capacitor the dielectric constant as well as the dielectric breakdown field should be high (and the dielectric loss should be low). Given the difficulty in computing the breakdown field (especially the true engineering breakdown field) and the dielectric loss at the low frequencies

(kHz) of interest from first principles, the band gap (known to be correlated with the breakdown field and dielectric loss[99,104] was used as the proxy instead. Thus, an initial screening criterion of "high dielectric constant" and "large band gap" was used to down-select suitable polymers. It should be noted that DFT is used here because computing the band gap and dielectric constant are "solved problems", that is, DFT is widely used to accurately estimate these properties. In **Figure 1.7**, we provide a comparison of the DFT computed band gaps and dielectric constants with the corresponding experimentally measured values. We show some inorganic compounds, some known polymers and some new polymers (that we cover in this review), and see that DFT does indeed estimate the properties accurately.

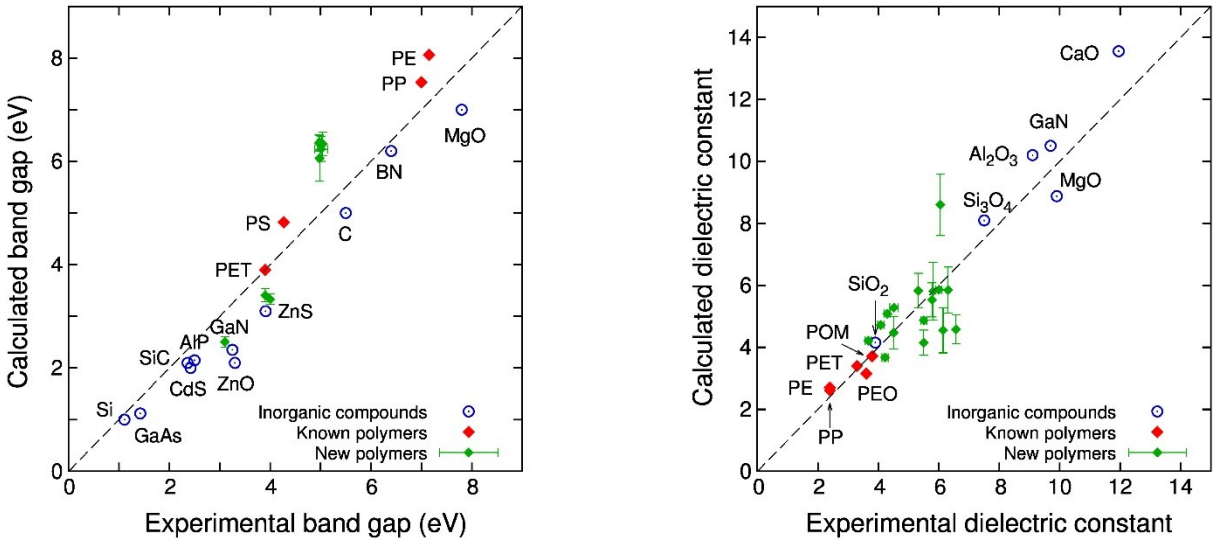

Figure 1.7. DFT computed band gaps and dielectric constants compared with experimental measurements. Reproduced with permission from[56], Copyright (2016) John Wiley and Sons, Inc.

1.5.3 Initial Computational Guidance

In the investigation by Sharma *et al.*,[68] hundreds of polymers in their single-chain form, each with a repeat unit made out of 4 building blocks, were considered (see **Figure 1.6** for an illustration). The possible van der Waals and other interactions between chains were ignored at this initial stage for ease and speed of computations. While the band gap was computed directly using DFT (using the hybrid Heyd-Scuseria-Ernzerhof (HSE)[105] electronic exchange-correlation functionals) for these single chains, the dielectric constant estimates had to be made by combining DFT with dielectric mixing rules based on effective medium theory.[106] The latter was required as the dielectric constant computed for the single-chain computational setup included a contribution due to an artificial vacuum region that needs to be subtracted out.

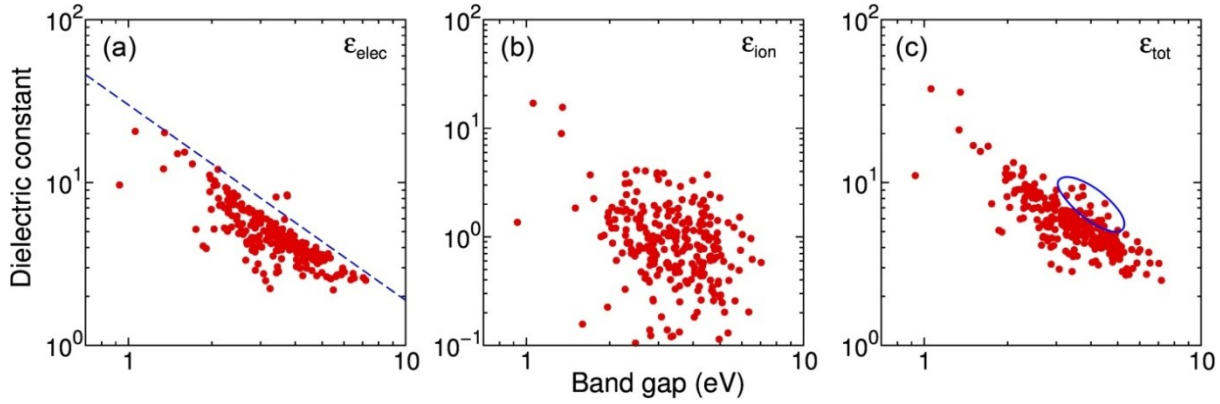

Figure 1.8. DFT computed values of (a) electronic, (b) ionic and (c) total dielectric constants plotted respectively against the computed band gap values for the 267 4-block polymers. The dashed line in (a) represents the theoretical limit of the form $\varepsilon_{elec} \leq CE_g^{-1}$ (C is a constant). The small oval in (c) encloses the most promising points with the best tradeoff between the dielectric constant and the band gap. Reproduced with permission from[68], Copyright (2014) Nature Publishing Group

With the idea of selecting promising polymer units for high energy density applications, the dielectric constants (the electronic component, the ionic component, and the total) were plotted against the electronic band gaps, as shown in **Figure 1.8**. Several important insights emerged from this analysis (as well as actual guidance for synthesis). These include:

1. The electronic part of the dielectric constant is inversely correlated to the band gap [**Figure 1.8** (a)]; hence, large electronic part of the dielectric constant, although desirable (owing to the short timescales of this response) is not safe, as it will lead to poor insulators.
2. The ionic part of the dielectric constant is immune to the above trend, i.e., it is uncorrelated, or only weakly correlated, to the band gap [**Figure 1.8** (b)]; this contribution to the dielectric constant should thus be exploited.
3. The best polymers for energy density applications are those with the best tradeoff between the total dielectric constant and the band gap. These are indicated using an oval in **Figure 1.8** (c), and include systems predominantly composed of at least one of the polar units, namely -NH-, -CO- and -O-, and at least one of the aromatic rings, namely -C_6H_4- and -C_4H_2S-. -NH-, -CO- and -O- tend to enhance the ionic part of the dielectric constant, while the aromatic groups boost the electronic part.

The last point above immediately provided the experimentalists their first vital leads.

1.5.4 Synthetic Validation of Initial Recommendations

To limit the large amount of data to a sample size that could be analyzed by the experimentalists, a threshold for dielectric constant was set at 4 and the lower limit for band gap was set at 3 eV. While a number of polymers (and a number of chemical groups/combinations of groups) were seen to be promising avenues to pursue, three polymers in particular were recommended for synthesis and characterization: -NH-CO-NH-C_6H_4-, -CO-NH-CO-C_6H_4- and -NH-CS-NH-C_6H_4-. As a synthetic starting point, these three polymers were ideal as they represented three different polymer classes, namely polyureas, polyimides, and polythioureas while maintaining the same aromatic unit, namely, C_6H_4.

A number of synthetic routes had to be considered here, as it was not possible to synthesize all the predicted structures by currently known chemistry. To fit the criteria of using only 4 structural units, monomers were chosen to obtain repeat-structural units as shown in **Figure 1.9**. Polymerizations to create all three down-selected candidates proceeded in a stepwise mechanism leading to condensation polymers, which limits the number of byproducts and side reactions that would ultimately become impurities and interfere with dielectric spectroscopy measurements.

Traditional polymer characterization techniques were employed to study the synthesized polymers. Fourier Transform Infrared Spectroscopy (FTIR) was used to confirm chemical structure, X-ray Diffractions (XRD) to determine the crystalline structure, and Ultraviolet-visible spectroscopy (UV-Vis) to estimate the band gap.

Further, Time Domain Dielectric Spectroscopy (TDDS) was employed to study the dependence of dielectric properties on the frequency. Meanwhile, the crystal structures, morphologies, and relevant properties were studied in greater detail and with more accuracy using computations. The isolated chain model was discarded in favor of polymer chains stacked next to each other in a unit cell, and the respective ground state 3-dimensional structural arrangements of the polymers were determined using two complementary and different approaches: a structure prediction algorithm (USPEX) using the DFT energies,[107,108] and a molecular dynamics based melt-and-quench approach using empirical force fields. Once the most stable crystal structures were obtained, the band gap and dielectric constant were calculated with DFT, specifically using the HSE functional[105] for the band gap and density functional perturbation theory (DFPT)[103] for the dielectric constant calculations. While the dielectric constants were found to range from 4 to 6, which is double that of PE or PP, the band gaps were seen to be greater than 3 eV. A comparison of DFT computed band gaps and dielectric constants with the corresponding experimentally measured values have been shown to largely yield property values close to experiments.[56]

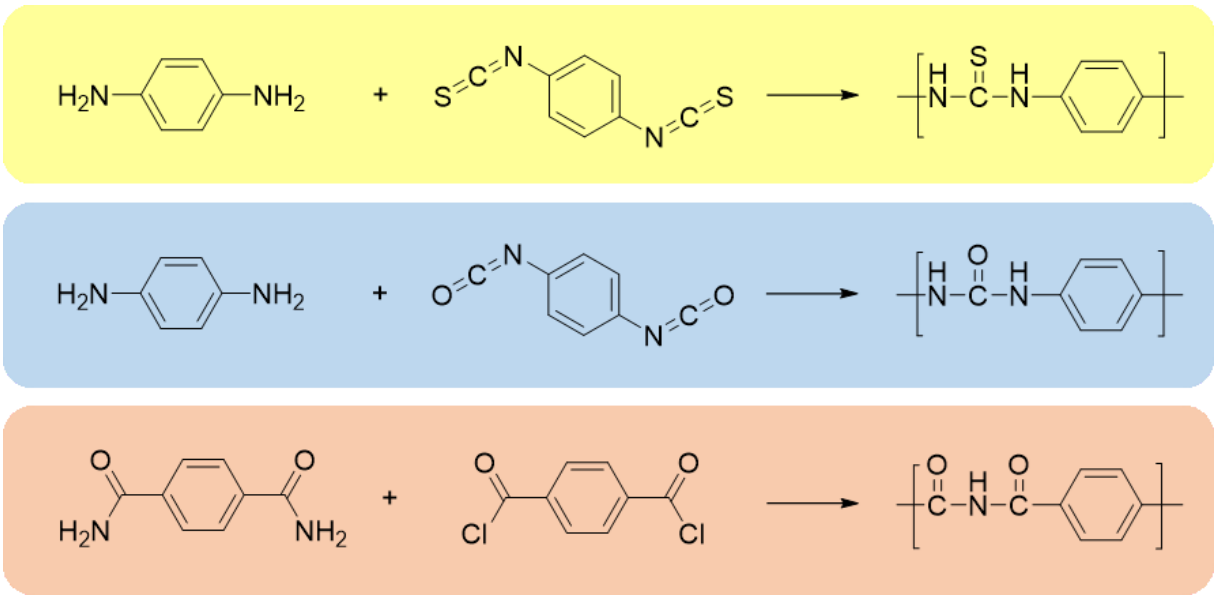

Figure 1.9. Synthetic scheme for the three down-selected organic polymers. Reproduced with permission from[68], Copyright (2014) Nature Publishing Group.

All computed values were close to experimentally measured values. Because of the consistency of the DFT results with the melt-and-quench approach, the DFT predicted ground state structures are expected to be stable at elevated temperatures as well, and thus, these computed property values are expected to stand at higher temperatures. Despite the fact that all predictions are made for purely crystalline structures, and the synthesized polymers are largely semi-crystalline or amorphous, the measured dielectric constant ranges matched up very well with predictions for the three polymers. Thus, a "computations → experiments → computations" synergistic loop was successfully pursued in the design of new organic polymer dielectrics.

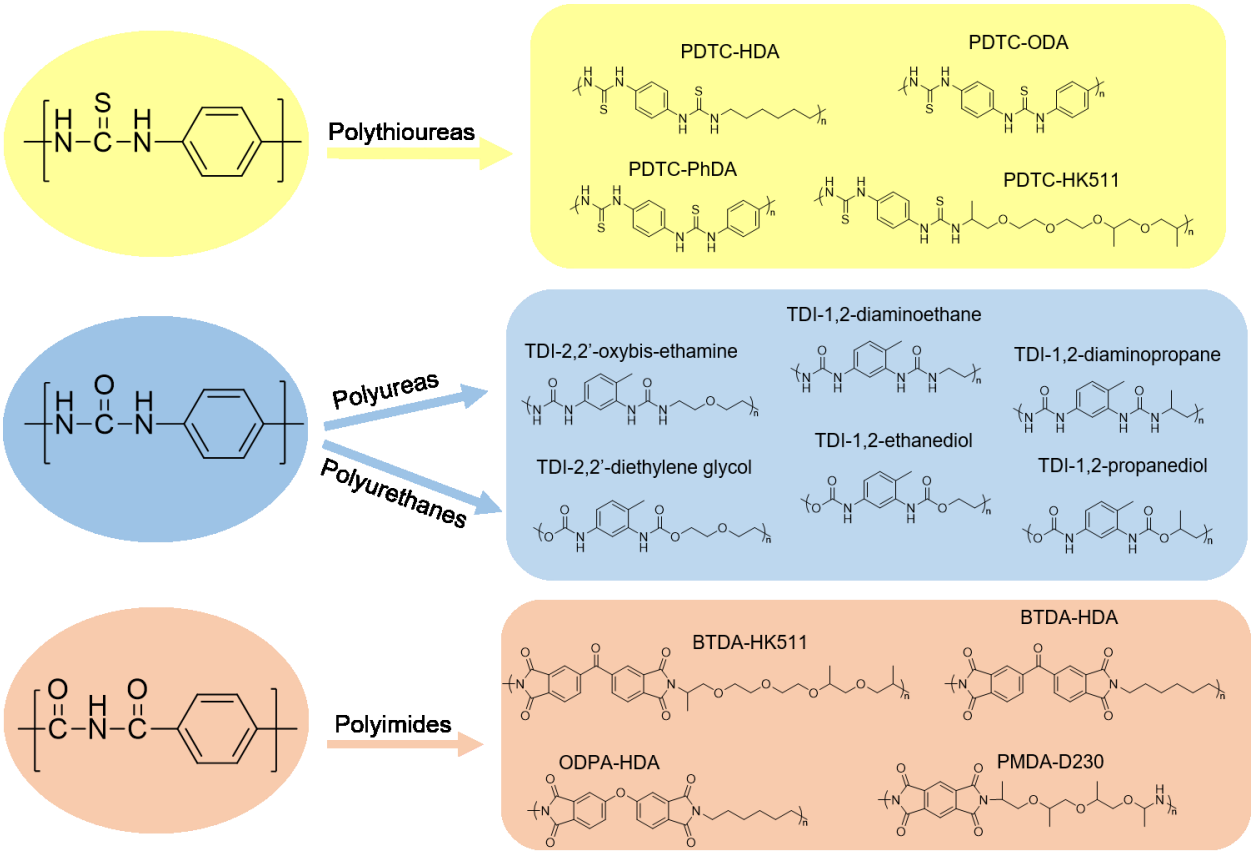

Figure 1.10. Extensions to new polythioureas, polyureas, polyurethanes, and polyimides. Reproduced with permission from[56], Copyright (2016) John Wiley and Sons, Inc.

The success of the initial mating between DFT calculations and synthetic efforts for dielectric studies gave way to more possible systems to be developed using the same initial computational data. The synthetic efforts branched into three different studies, each involving a different polymer class to further understand the theoretical and experimental properties of proposed organic dielectrics. As shown in **Figure 1.10**, the three polymers studied at first and discussed above gave way to the study of a number of a) polythioureas, b) polyureas and urethanes, and c) polyimides. The following chapters give an overview of the collaborative work that was done based

on the initial DFT predictions to generate a database of next generation dielectric polymers. The chapters also go into detail on a new approach to understand the different polarization mechanisms being measured when the experimental dielectric constant is taken by coupling low temperature dielectric spectroscopy with several methods of computational modeling and prediction. **Chapter 2** discusses some of the instruments and methods used throughout this body of work to serve as an overview and reference for readers unfamiliar with certain aspects. **Chapters 3, 4, and 5** discuss work done on polyureas, polythioureas, and polyimides respectively as a continuation of the organic polymers initially studied in this rational co-design process. **Chapters 6 and 7** detail the expansion of chemical space into novel metal containing polymers along with computational predictions that show the metal atoms give an increased ionic dielectric constant over pure organic polymers. **Chapter 8** provides a conclusion for the thesis as well as a look into the Materials Genome Initiative and how this work has focused on the creation of a Polymer Genome, which is facilitated through the website Khazana, currently found at Khazana.uconn.edu.

Chapter 2

2. Instrumentation and Characterization Methods

This chapter contains a summary of all the experimental instrumentation used to characterize the polymers throughout this thesis. This chapter is laid out in a semi-chronological order representative of the experimental process. First, the polymer structures are analyzed to verify the target polymer has been synthesized. From there, thermal measurements are done to understand and develop safe processing and handling temperatures for the polymers. Finally, electronic characterization takes place to determine the properties of interest, including dielectric constant, band gap, and energy density. This chapter concludes with a discussion of the various processing techniques used as well as a list of the materials used to carry out this work.

2.1 Structural characterization

2.1.1 Fourier Transform Infrared Spectroscopy

To determine the structure of the polymers synthesized Fourier Transform Infrared (FTIR) spectra were collected on all samples. FTIR works by passing an infrared light across a wide range of wavelengths through a sample and detecting the amount that passed through. This is then to be plotted as either percent transmission through the sample or percent absorbance of the sample verse wavenumber.

Wavenumber for FTIR is given in inverse centimeters (cm^{-1}) and is defined as in **Equation 2.1**.

$$\tilde{\nu} = 1/\lambda \quad (2.1)$$

All bond between atoms stretch, vibrate and bend at different characteristic frequencies that absorb in the infrared spectra. After decades of careful analysis, most common chemical bonds have carefully been analyzed by this method, are tabulated in literature along with wavenumber, and offer a point of comparison to help identify spectra for new polymers. FTIR is used over traditional infrared spectroscopy in most current systems as it enables all wavelengths to be collected simultaneously, giving a much higher signal to noise ratio for the same scan time. In addition, FTIR has been reported to have a higher sensitivity, known as the Jacquinot advantage, and higher accuracy, known as the Connes advantage, due to advanced detectors and internal calibration respectively.[109] In this work, all FTIR spectra's were collected on a Nicolet Magna 560 FTIR spectrometer with two different accessories where the wavelengths analyzed are between 2.5 µm or 4000 cm^{-1} and 25 µm or 400 cm^{-1}. Powder samples were analyzed using a Nicolet Magna 560 FTIR spectrometer with a Specac Quest Diamond Attenuated Total Reflectance (ATR) accessory (resolution 0.35 cm-1) as seen in **Figure 2.1**, while films samples were measured using the instrument in transmission mode through the films.

Figure 2.1. Film and pellet FTIR (A) and Diamond ATR (B).

2.1.2 Nuclear Magnetic Resonance Spectroscopy

Verification of polymer chemical structure was characterized by Nuclear Magnetic Resonance (NMR) spectroscopy on a Bruker DMX 500 MHz NMR Spectrometer shown in **Figure 2.2**. While FTIR uses the vibrations, stretches, and rotations in chemicals bonds to deduce structure, NMR investigation probes the magnetic properties of atomic nuclei. Only certain elemental isotopes are able to be probed by NMR with the most common being ^{1}H and ^{13}C due to their abundance in almost all chemical compounds. An NMR scan consists of the instrument exciting the nuclei in the sample through a radio frequency pulse and the sample nuclei relax back to their ground states while a very sensitive radio receiver picks up the frequency induced decay or FID signal. This signal, in the time domain, is converted with a Fourier transform to the frequency domain for analysis. Typically, 16 to 32 successive scans are necessary to produce and adequate signal in small molecules while polymer samples may require more due to their added complexity. Due to the drastically lower abundance of ^{13}C in most samples compared to ^{1}H, investigation of

^{13}C typically requires many times more scans than ^{1}H and experiments can last hours instead of minutes.

While NMR only looks at single nuclei instead of bonds between atoms the chemical structure is able to be determined by the effect that nearby nuclei have on the one being probed. The electronic environment of the nuclei including electrons from neighboring atoms will have a local magnetic field that is opposite of the magnetic field being induced by the NMR partially 'shielding' the nuclei from the field. The opposite effect can be seen when electron-withdrawing groups are attached to a nucleus being investigated where the local electron density is lowered to partially 'deshielded' the nuclei. This effect is manifested in the resulting NMR spectra which show nuclei peaks of varying intensity depending on the number of similar species in the compound while being separated based on their electron environment 'shifts' and represented in terms of the shift in parts per million (ppm).

Solution-based NMR spectroscopy was employed for this research. For solution based NMR the sample is dissolved at a low concentration in an 'invisible' solvent such as chloroform-d, dimethyl sulfoxide-d^6, or acetic acid-d^4. By using these deuterated solvents, there are no NMR active nuclei to interfere with the FID spectra. Typically, tetramethylsilane in very small quantities is used as a reference peak where all 12 hydrogens exist at the same point in an intense singlet and are typically set as 0 ppm. Solution-based NMR has an advantage over solid-state NMR where can be carried out orders of magnitude faster than solid-state due to the mobility of molecules in a solution. While high-resolution solution based NMR can be carried out

in a matter of minutes, a similar resolution on a solid-state NMR could take days or be unachievable even when using ^{1}H, with ^{13}C sometimes requiring up to a week of run-time. Despite this drawback, sometimes, especially in polymer chemistry it is impossible to solvate the final product in a solvent suitable for solution based NMR, and solid-state NMR is the only method available.

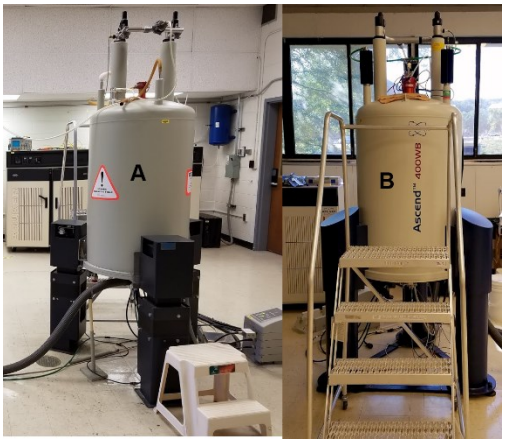

Figure 2.2. 500 MHz solution NMR (A) and 400 MHz solid-state NMR (B).

2.1.3 X-Ray Diffraction

X-ray diffraction (XRD) was used to determine the crystal structure of materials. Qualitatively, XRD was used in this thesis to see a change in crystallinity as different synthetic and processing conditions were used, with the goal of creating amorphous polymer films. XRD spectra were collected on a Bruker D2 Phaser as shown in **Figure 2.3A** and a Xcalibur X-ray Diffraction System from Rigaku Oxford Diffraction in **Figure 2.3B** both with a Cu-Kα (λ = 1.54184 Å) source beam. The Xcalibur was used to investigate free standing films while powder samples were studied using the D2 Phaser. The periodic structures in a given sample must be on

the same order of magnitude as the radiation to cause diffraction, in XRD this is limited to angstroms. By knowing both the angle of diffraction from the instrument position and the wavelength of X-rays emitted from the copper source, Bragg's law shown in **Equation 2.2** can be used to calculate the spacing between crystalline planes also known as the d-spacing.

$$n\lambda = 2d(sin\emptyset) \quad \textbf{(2.2)}$$

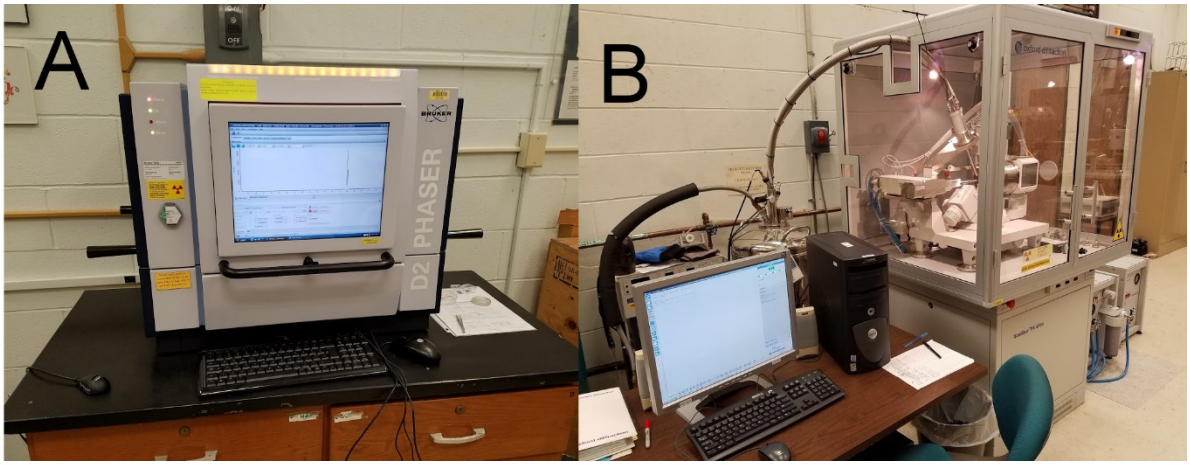

Figure 2.3. D2 Phaser (A) and Oxford Excalibur (B)

2.2 Thermal characterization

2.2.1 Thermogravimetric Analysis

When a new polymer is synthesized, it is important first to understand the thermal properties of that material before any processing or testing occurs above room temperature. Thermogravimetric analysis (TGA) is a straightforward method for thermal analysis which, while being destructive, only requires a small amount of

sample, typically on the order of milligrams. The instrument consists of an extremely precise balance, in this case, +/- 0.01%, a furnace that heats up to 1000 °C, and air flow to control the environment.[110] The TGA system used here was also equipped with an auto sampler for ease of sample loading and a computer with TA Instruments Universal Analysis for data analysis. In this work, TGA was performed using a TA Instruments TGA Q500 with a heating rate of 10 °C per minute under a nitrogen atmosphere as shown in **Figure 2.4**. In a typical run, the sample pan is first tared in the furnace and then released to be loaded with the polymer. The sample is then placed back in the furnace, and a nitrogen environment is pumped in to exclude any oxygen. The furnace is then heated at a constant rate well past the expected degradation temperature of the metal, and the mass is measured through the experiment. The final result is a plot that shows the percentage of mass remaining per temperature.

Figure 2.4. TGA Q500 with nitrogen and oxygen gas cylinders.

The first few points of weight loss are typically small molecules that come off first and can be found in a similar range to their boiling points. Typically, solvents, both organic and water will come off first, followed by larger chemicals such as plasticizers and higher boiling solvent, including some liquid monomers. Depending on the number and amount of each of these small molecules there could be several stepwise losses in mass around 1% or 2% for dried samples. In a typical run, the next area of weight loss will be a large decrease in mass where half the material or more degrades and leaves the sample holder. This area is useful for roughly determining the decomposition temperature of a material, which can be determined in a few ways. If the percent weight loss has been constant throughout the run, then the onset temperature can be taken as the initial point that the material begins to lose weight. In most situations presented in this thesis, there is initial weight loss from solvents and other molecules and the onset of decomposition is taken at a set weight loss percent. The onset of decomposition is then used as a guide for the extreme upper limit that the polymer can be handled at, and typically a temperature much lower than that is the highest the polymer will be heated. In certain circumstances, TGA can be used to understand a chemical reaction. In the case of polyimides, polyamic acid is first produced and converted to polyimides through heating and water is released. The imidization can then be monitored by taking the TGA of several films cured at different temperatures and tracking the amount of water lost as the system ramps up in heat. TGA can also be used to monitor the thermal stability of a sample

at a certain temperature by holding it there for several hours. This can be done before a long cure or anneal to be sure that the polymer will not degrade over that time.

2.2.2 Differential Scanning Calorimetry

Differential Scanning Calorimetry (DSC) is a form of thermal analysis in which two pans, one with a sample inside and the other empty as a reference, are heated and cooled in unison. The furnace chamber is filled with a gas, either air, oxygen, or nitrogen depending on the desired conditions to be tested. The instrument maintains both samples at close to the same temperature as each other throughout the experiment, and the heat flow required to maintain that is recorded. The end result is a plot of heat flow verse temperature. The change in heat flow can indicate thermal transitions such as a melt or crystallization where a downwards or upwards spike will show where the end of the spike returns to almost the same heat flow position as the start of the spike. When the heat flow decreases as the temperature increases in a downward slope and then stays at that lower value, it is indicative of a glass transition temperature of the polymer, a change from a brittle glass like the state to a rubbery state. For this thesis, DSC was performed on a TA Instruments DSC Q20 and DSC Q100 connected to a TA Refrigerated Cooling System 90 while some extreme low-temperature measurements were done on a DSC 2920 with an attach liquid nitrogen Dewar as shown in **Figure 2.5**.[111]

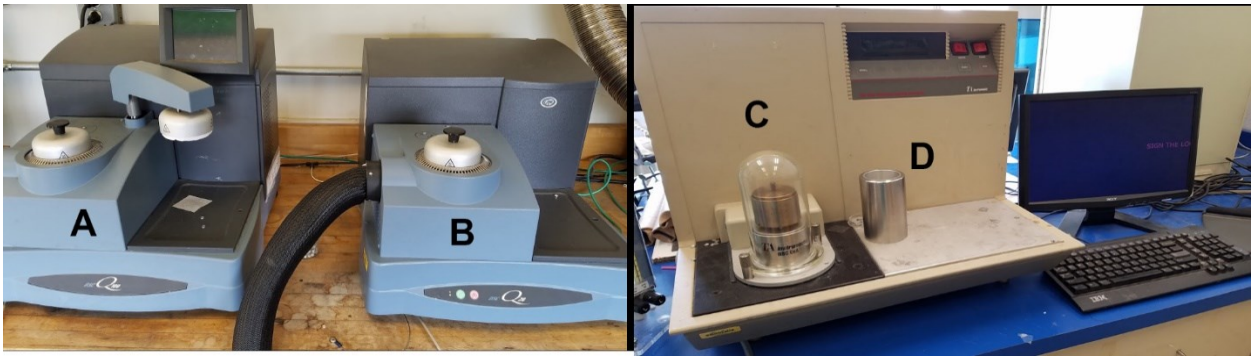

Figure 2.5. DSC Q100 (A) and DSC Q20 (B) both connected to a chiller with DSC 2920 (C) for extreme temperature analysis with a liquid nitrogen dewar (D) for low-temperature analysis.

In a typical run, around 10 milligrams of the polymer is put into the sample pan and sealed with a crimper, an empty reference pan is also crimped closed, and both are put into the furnace. Using the attached computer, the experimental run conditions are set up using the TGA results to set the upper limit, typically around 5-10 °C below the decomposition temperature. For a new polymer material that has recently been precipitated and dried the sample is normally cycled once up to the upper limit and down to the lower limit to remove any thermal history the sample may have accumulated. However, for polymer films that have been carefully cast and annealed this initial cycle holds valuable data on how those conditions affected the thermal transitions and crystallinity. DSC run will then usually have one or two more cycles to verify the results and note any changes. When a melt transition is being investigated, the sample is typically run at 40 °C min^{-1} while when the Tg is being investigated a heating rate of 20 °C is often used. A higher heat ramp will give a sharper peak than a slower heat ramp. Sometimes the final cycle can be taken up to

the decomposition temperature to analyze the material characteristics at failure however if the sample escapes the crimped pan it can cause damage to the furnace.

2.2.3 Dynamic Mechanical Thermal Analysis

Polymer relaxations were investigated using a TA Instruments DMA 2980 or dynamic mechanical analyzer (DMA) also referred to as a dynamic mechanical, thermal analyzer (DMTA) when a change in temperature is involved as shown in **Figure 2.6**. The instrument involves taking a homogenous piece of material about 2 mm wide and 40 mm long to be placed between two clamps. The thickness of the material can vary. However, a thicker sample on the order of 100 µm was found to be favorable. There are numerous tests this instrument can carry out and only a basic test was used for this thesis. Here, the film is placed between two clamps, the bottom of which freely floats initially and the sample oven covers the entire holding apparatus. The bottom clap then begins to oscillate at a specified frequency while and the force required to stretch the sample to a specific length is recorded. As the temperature is raised through electrical heat, a softening of the polymer will be evident by a drop in required force to deform the sample, indicating the material has passed the glass transition temperature (Tg). As the sample is chilled to much lower temperatures through the use of an attached liquid nitrogen dewar, secondary transitions may be seen by small changes in the force required for deformation.

Figure 2.6. TA Instruments DMA 2980 to carry out DMTA analysis on polymer films.

2.2.4 Film GC/MS

In order to analyses the composition and residual solvent or chemicals in polymer films a GC/MS modified by IMS laboratory manager Gary Lavigne was used. An Agilent 6890 gas chromatograph attached to an Agilent 5972A mass spectrometer is attached to a custom film sample holder for this analysis as shown in **Figure 2.7**. The polymer film sample is put in the modified sample holder and heated to a specified temperature, which is typically right under the degradation temperature as determined by TGA, for two minutes. A carrier gas passes over the film and transports the chemicals that are vaporized onto the column where they are immobilized by liquid nitrogen. After two minutes the liquid nitrogen is removed and the column oven slowly heated up to the specified temperature allowing the chemicals to separate and be identified by the mass spectrometer.

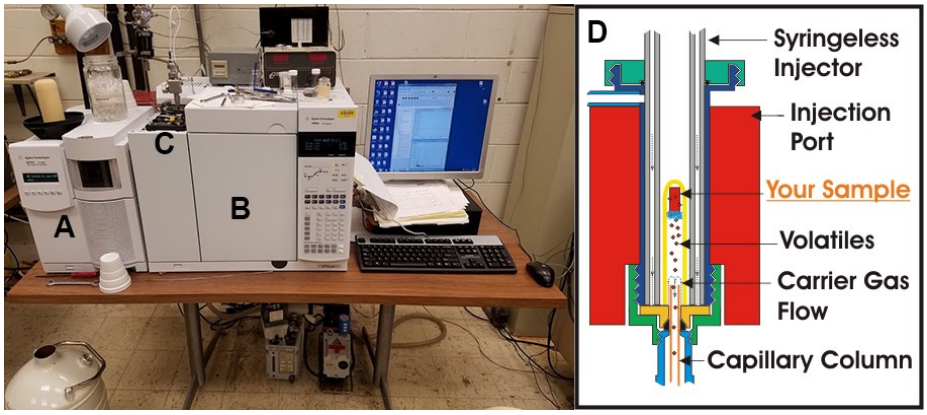

Figure 2.7. Mass spectrometer (A) gas chromatograph (B) film sample holder (C) and diagram of the custom sample holder (D).

2.2.5 Elemental Analysis

To verify the composition of new polymers produced an Elementar Vario MICRO Cube was used to perform elemental analysis as shown in **Figure 2.8**. The system has the ability to digest samples with temperatures exceeding 1200 °C through the use of an oxygen jet to breakdown the compounds and analyze their composition. The Elementar can detect levels of carbon, hydrogen, nitrogen, and sulfur in the compound for comparison to empirical formulas. The chemical composition serves as another verification that the proposed structure of the polymers and their repeat units are correct.

Figure 2.8. Elementar Vario MICRO Cube

2.2.6 Density Measurements

The density of a polymer is an important property to be reported whenever a new one is produced. However the importance increased when molecular dynamics simulations were run on these systems. The density can be predicted and is used as in indication that the simulations are being run on a polymer with comparable free volume and amorphous structure. To carry out density measurements a small 2 cm x 2 cm piece of film is cut and placed in a distilled water containing large test tube and the tube is sonicated to remove any air bubbles on the film surface to allow the film to sink to the bottom. Sodium iodide salt is slowly added to the water, followed by vortex stirring and sonication to homogenous disperse the salt and agitate the film. This process is repeated until the film is suspended for several minutes in the

solution. If too much salt is added some DI water is added to dilution the solution, and the process starts again. Once the film is suspended, the density of the solution can be taken as the density of the film and several 5 ml portions are volumetrically pipetted off, massed, and divided by the volume to give density as shown in **Figure 2.9**. This process is repeated several times to ensure an accurate reading.

Figure 2.9. Test tube containing a polymer film, distilled water, and a solution of sodium iodide to modify the solution volume to be the same as the film.

2.3 Electronic Characterization

To measure the electronic properties of the materials being produced for this thesis several instruments and apparatuses were required. A sample holder was fabricated to uniformly hold the samples during both frequency and time dependent dielectric spectroscopy. An ultraviolet – visible spectrometer was used to determine the band gap of the material using the built-in sample holder while the samples

refractive index was determined via refractive index. In addition, several high-field measurements were also carried out including high field breakdown and conduction as well high field polarization through a charge and discharge cycles.

2.3.1 Dielectric Material Sample Holder

To carry out dielectric spectroscopy measurements, a sample holder was developed in house by the Electrical Insulation Research Center (EIRC) in the Institute of Materials Science (IMS) at the University of Connecticut as shown in **Figure 2.10** below. The holder consists of two thick insulating plastic boards connected by aluminum posts on the outer corners. On the outside, there is a screw to adjust the height of the electrodes with the ability to tighten down to ensure a good connection with the sample material. The inside of the holder is modular to allow varying size electrodes to be switched in and out depending on the sample being studied, in addition, the use of both guarded and unguarded electrodes are possible. The sample holder uses metal electrodes; however, to ensure maximum contact between the electrodes and the polymer samples electrically conductive silicone sheets with carbon black were used as an intermediate between the metal electrodes and the sample. For the purposes of this thesis, the positive electrode was 1 cm in diameter resulting in 0.78 cm^2 of conductive area for purposes of calculating the dielectric constant. The positive electrode was guarded with the same conductive silicone to minimize the fringe fields while the back side of the polymer was also attached to the holder with the same silicone of a larger size to encompass both the positive electrode and the guard.

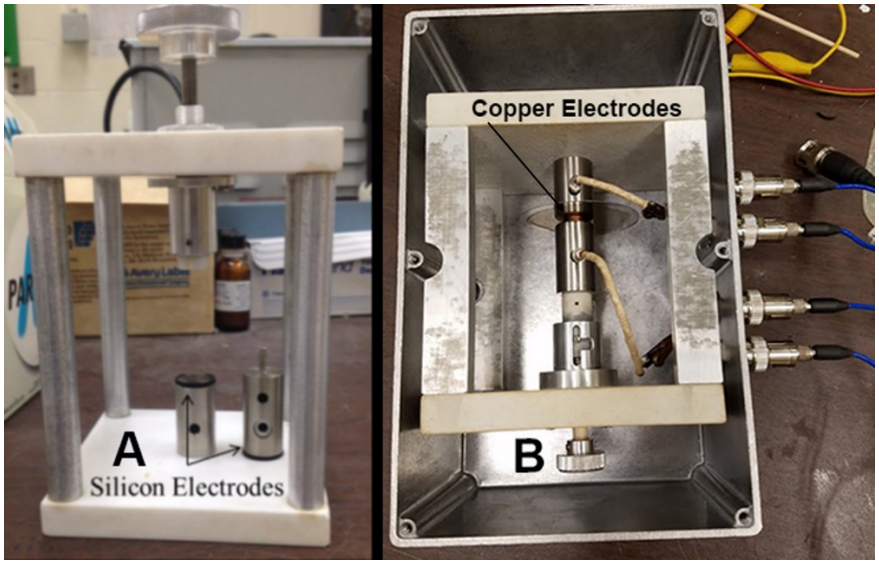

Figure 2.10. Sample holders for dielectric spectroscopy designed by the EIRC and custom made in the IMS machine shop for room temperature and above (A) as well as below zero measurements (B).

For measurements below freezing (0 °C) a new sample holder had to be developed by the EIRC to deal with condensation on the electrodes which would lead to high conductivity values, and the silicone electrodes lose their conductive properties. To accommodate this, a spring-loaded sample holder was devised which replaced the silicone electrodes with smooth copper, and the spring ensured a strong connection. The contact areas of the films were also metalized using the sputter coater as detailed in **Section 2.4.9** to keep the sample area consistent. To eliminate condensation from covering the sample with cryogenic gases and measurement noise from the gas flow an aluminum case was built for the sample holder that tightly screws down to block airflow. Teflon coated electrodes were passed through the aluminum exterior with coaxial connections to isolate the sample from the environment further. Due to this extensive shielding, the sample is required to be

held at each temperature for 30 minutes to equilibrate the temperature of the sample oven to that of the film inside.

2.3.2 Inductance, Capacitance, and Resistance Meter

One method employed to determine the dielectric constant of materials is to probe the response of the material in the frequency domain using an inductance, capacitance, and resistance (LCR) meter, specifically the Agilent 4284A Precision LCR meter, as shown below in **Figure 2.11**.[112] The electrode wires for the LCR meter we placed inside an insulated Delta 9023 oven to allow for both thermal and electrical shielding. The oven itself was connected to a liquid nitrogen tank to allow both for rapid cooling to room temperature and for low-temperature measurements to be taken. To assist in multiple samples runs at different temperatures, an undergraduate, Justin Delarm, wrote a LabVIEW program to automate the process as well as outputting a display graph while the run was under operation. His software allowed for the input of each temperature that was going to be measured, the length of time the sample was held at each temperature before the measurement was taken, and a number of measurements that were to be taken and averaged at each temperature as shown in **Figure 2.12**. Justin's contribution to the instrument setup proved to be very important and hundreds of hours were saved due to this automated procedure.

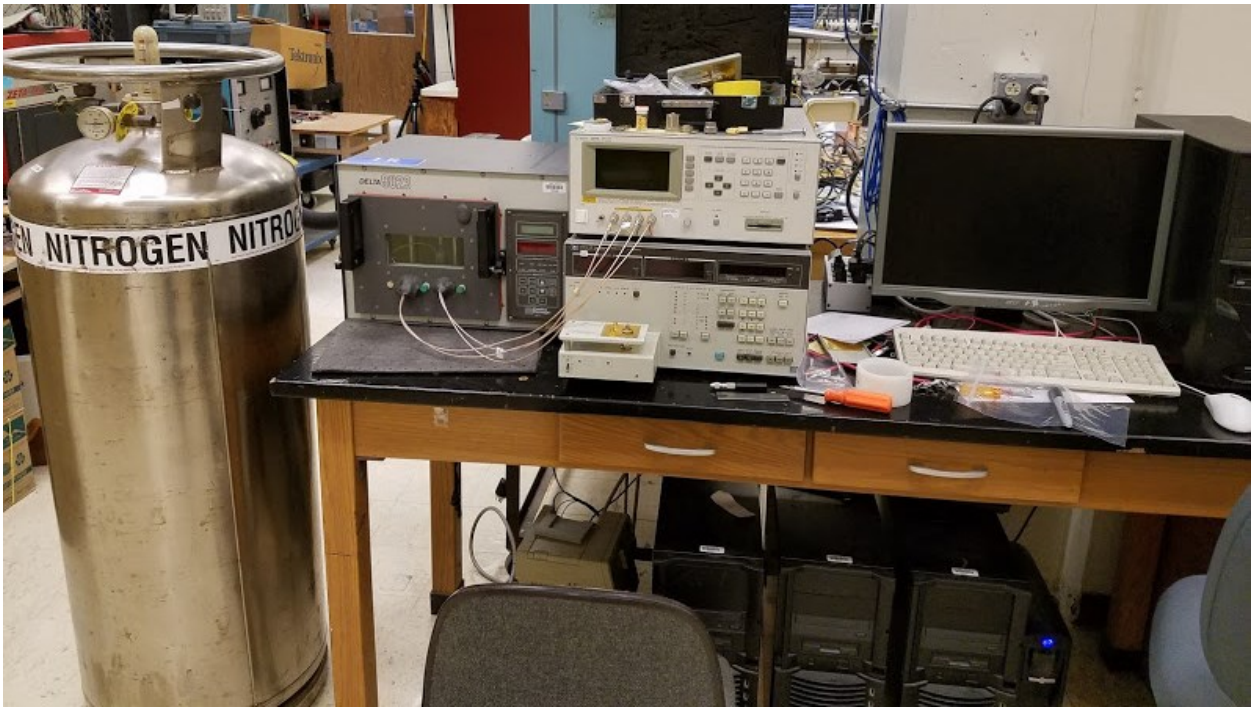

Figure 2.11. Agilent 4284A Precision LCR meter hooked, up to a computer for data analysis, with leads extending into a Delta 9023 oven for temperature control and attached liquid nitrogen.

The LCR meter itself is able to measure capacitance and loss (along with a large array of other parameters not mentioned here) versus frequency over the range of 20 Hz to 10^6 Hz and is carried out in either air or a nitrogen flushed oven when using the attached tank. The measured capacitance is then converted to dielectric constant through **Equation 1.8** and plotted either as a two-dimensional plot of a single temperature or a three-dimensional mesh when multiple temperatures are used.

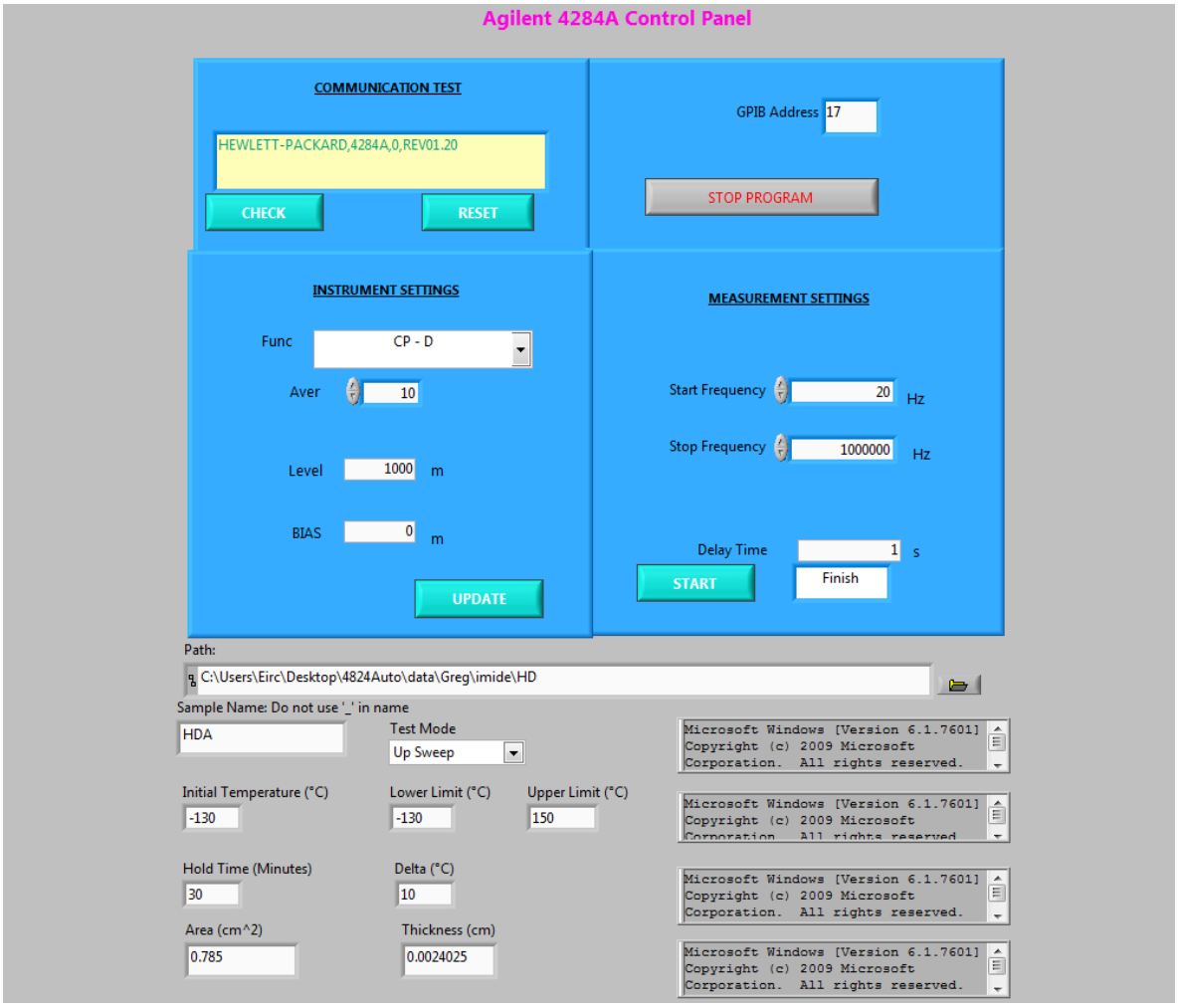

Figure 2.12. Modified LabView software developed by Justin Delarm for automated dielectric measurements and data analysis.

2.3.3 Time Domain Dielectric Spectroscopy

The second method used to investigate the dielectric constant is known as Time Domain Dielectric Spectroscopy (TDDS) and was discovered by Mopsik in 1984, the schematic he drew in his paper is shown below in **Figure 2.13**[113] The advantage to using TDDS is that a large frequency range could be covered in a relatively short amount of time. This would occur by applying a voltage step and recording the

polarization current. A computer would then carry out Fourier transforms to covert this data into complex frequency response allowing the dielectric constant to be determined. Initially, this conversion process took several minutes but as computers have advanced, the time required has become negligible.

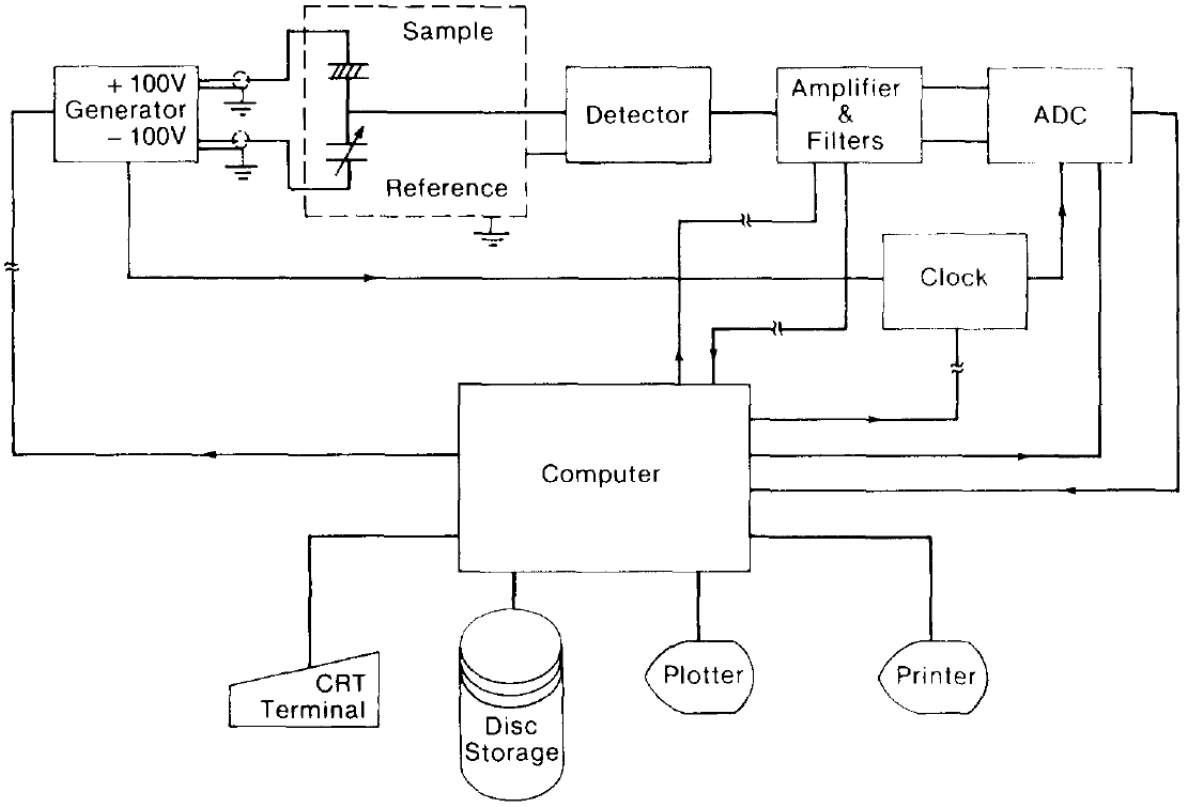

Figure 2.13. Block Diagram depicting Mopsik's Time Domain Dielectric Spectrometer from Mopsik's 1984 paper. Reproduced with permission from[113], Copyright (1984) American Institute of Physics.

The instrument used for this work was an IMASS TDDS and was set up in a similar manner to the LCR meter. The TDDS had a Delta 9023 oven, liquid nitrogen tank, and computer with LabVIEW for control and recording of data as shown in **Figure 2.14.** An important aspect of TDDS is that it is capable of achieving much a

lower frequency than traditional dielectric spectroscopy; in this case, a frequency range of 10^{-3} to 10^{4} Hz is possible. This also comes with it excellent loss resolution in tan δ to 10^{-5}. However, samples with relatively high conduction will saturate the detector and are unable to be measured while they would still be measurable on an LCR meter. JoAnne Ronzello of the EIRC was invaluable in maintaining and operating the TDDS for the duration of the work involved in this thesis.

Figure 2.14. IMASS Time-Domain Dielectric Spectrometer hooked, up to a computer for data analysis, with leads extending into a Delta 9023 oven for temperature control and attached liquid nitrogen.

2.3.4 Ultraviolet–Visible Spectroscopy

The band gaps of the polymers synthesized in this thesis were determined using ultraviolet-visible spectroscopy. Band gap measurements were taken by scanning the UV-visible spectra from 800-200 nm and measuring the wavelength of absorption onset. This onset relates to the energy of the band gap through planks relation in **Equation 2.3.**[114] The onset of absorption is determined by placing a straight line through the slope of absorbance and a line through the background spectrum at higher nm wavelengths, the intersection was then taken as the onset wavelength.

$$E_g = hc/\lambda \qquad \textbf{(2.3)}$$

Figure 2.15. UV-Vis Spectrometer

2.3.5 Refractive Index

Refractive index is taken by measuring with a J. A. Woolman Co. M-2000 Spectroscopic Ellipsometer shown in **Figure 2.16**. Access to the ellipsometer was provided by Dr. Brian Willis at UConn's Chemical and Biomolecular Engineering department. The refractive index was taken over the wavelength of 350 nm to 1497 nm with the reported refractive index from 546 nm.

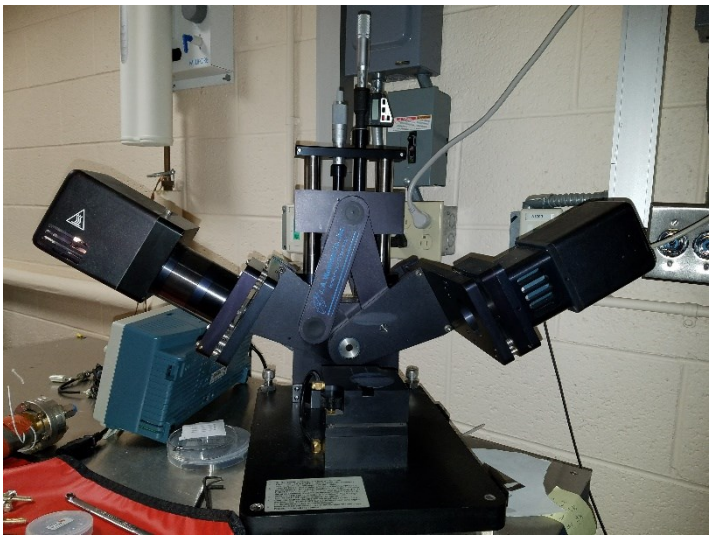

Figure 2.16. Ellipsometry

2.3.6 High Field Breakdown

To determine the maximum field that can be applied to the sample the breakdown strength was measured using a linear voltage ramp of 300 V/s. Two different sample setups are used throughout this thesis to carry out high field measurements. Typically, measurements were carried out in silicone oil on samples

3 mm in diameter in a technique known as ball to plane where the top electrode consisted of a ball bearing pressed against the metallized film and the bottom electrode being the conductive metal oil bath which contacts the opposite side of the film which is also metallized to the same dimensions. The electrodes were sputter coated onto the film with 80/20 Pd/Au by weight as outlined in **Section 2.4.9**. The ball to plane sample setup is shown in **Figure 2.17**. Another sampling technique used is called film to film and shown in **Figure 2.18** where the first layer is a film electrode placed with the conductive side facing up. On top of that, the sample to be tested is placed and covered with a Kapton mask where a 2 cm^2 hole was cut out to expose the sample. The last layer placed is another film electrode with the conductive side facing down. Due to electrostatic interactions between the conductive electrode films and the polymer test film, a good interface is formed between all layers in the setup.

Figure 2.17. Ball to plane setup used to conducted polarization measurements in oil.

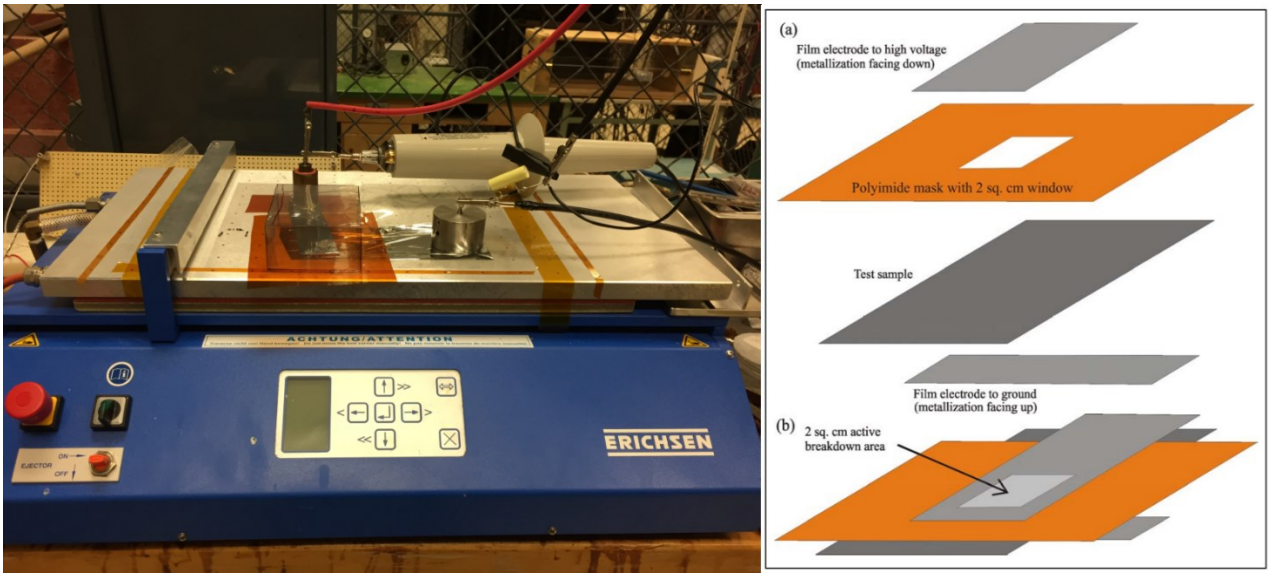

Figure 2.18. Film to film setup used to measure polymer breakdown with the experimental setup on the left and a schematic for breakdown on the right showing (a) exploded view of all four components and (b) stacked view showing setup in use.[29]

To calculate the breakdown strength, the sample thickness and the electric field at breakdown is required to end up with a value of unit's megavolts per meter (MV/m). The thickness was measured as per **Section 2.4.7** below. Typically, throughout this thesis 25 to 30 measurements were taken, each with a new section of the polymer film. After all the measurements were taken a Weibull distribution function, F(x), was used to find the Weibull characteristic breakdown field as in **Equation 2.4**[115]**.** Here, x is the electric field, η is the scale or Weibull characteristic breakdown field where there is a 63.2% probability of failure, ß is the shape parameter, which measures how much variation there is in the data, and c is the threshold field, which is the lower limit of breakdown in the sample.

$$\begin{cases} F(x)=1-\exp\left[-\left(\frac{x-c}{\eta}\right)^{\beta}\right] & \text{for } x\geq c \\ F(x)=0 & \text{for } x<c \end{cases} \quad (2.4)$$

2.3.7 D-E Hysteresis Loop

Polarization measurements were conducted with a modified Sawyer-Tower circuit, employing a Trek Model 10/40 10 kV high voltage amplifier and an OPA541 operational amplifier based current to voltage converter. The sample holder is a ball to plane measurement carried out in an oil bath as shown in **Figure 2.17**. Samples were roughly 10 μm thick polymer films with metallized electrodes 3 mm in diameter on both sides. A half-wave rectified sinusoidal wave was applied at 100 Hz, and consecutive high voltage half-sine pulses were applied with increased amplitude until the sample broke down.

2.6.8 High Field Conduction Measurements

High field conduction measurements were used to understand the nature of the loss in the polymer dielectric film at high fields using the electronic setup shown in **Figure 2.19** which is used for all three high field characterization techniques. Both polarization and conduction loss are measured in the loss of a D-E hysteresis loop. Ideally, conduction loss can be reduced by removing impurities such as unreacted monomer, low molecular weight oligomers, and residual solvent or absorbed water in the polymer film. Conduction loss can also be reduced by optimizing the processing method used in the fabrication of the film. The measurement is carried out by

applying a voltage ramp of 300 V/s while the capacitive charging current was dynamically canceled to give the resistive current. An in-depth discussion of this procedure can be found in the article by Zongze Li et al.[116]

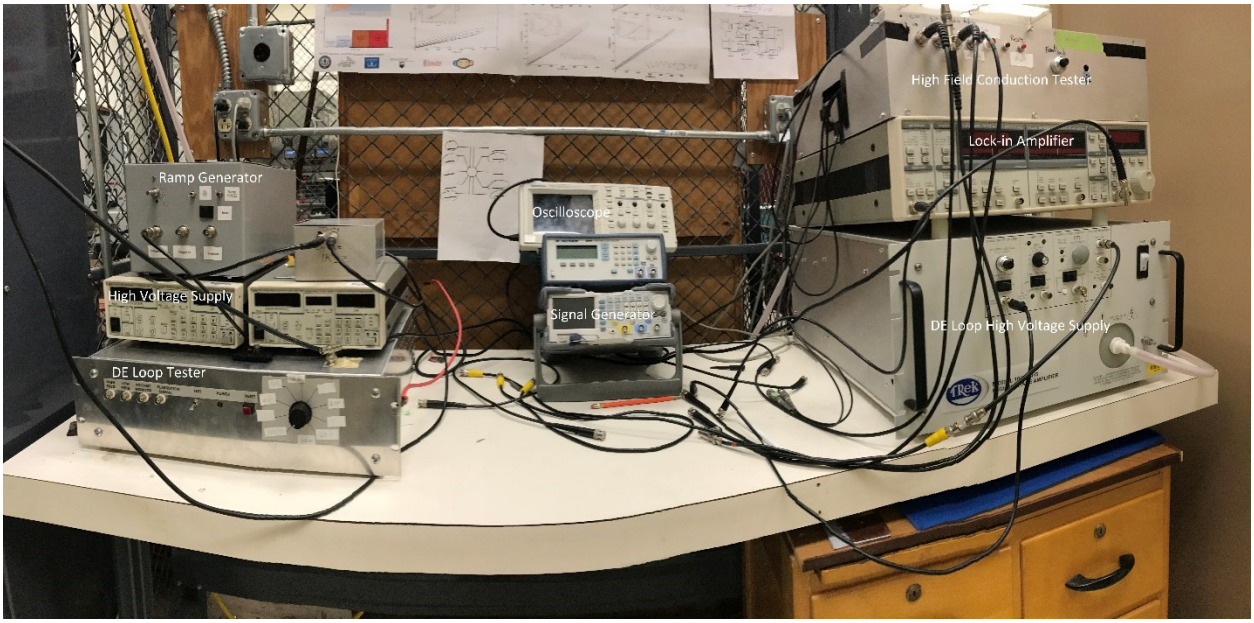

Figure 2.19. Electrical setup used to measure breakdown, polarization, and pre-breakdown high field conduction in UConn's EIRC.

2.4 Processing Techniques

In the area of dielectric materials, the way a polymer was processed can have as much of an impact on the properties of the final sample as a variation in the chemical composition. Numerous factors need to be considered when decided how to prepare a sample including solubility, melt transition, glass transition, film forming capability, and thickness of the desired final sample.

2.4.1 Plasma Treatment

In order to ensure that thin films on the order of 10 microns and below are as smooth as possible, it is important to clean off the substrate as much as possible. While a jet of dry nitrogen is able to clean the majority of dust particles off a substrate, some applications require more intensive cleaning. For films cast under clean room conditions to be only a couple micron thick a more intensive cleaning procedure is required and carried out in the IMS clean room. Silicon wafers are used to get a near-atomically flat substrate and are first cleaned off by the dry nitrogen jet. Afterwards, the wafers are placed in a PS 210 Microwave Gas Plasma System, and the atmosphere is evacuated from the chamber as seen in **Figure 2.20**. A small amount of argon is added to the chamber, and an electric field is applied to charge the argon particles. The surface of the substrate is then cleaned by the ion bombardment for three minutes, and the surface chemistry of the silicon wafer is left intact. This procedure has been shown to remove almost all traces of carbon from the surface of a silicon wafer.[117] The surface integrity is kept intact after cleaning by minimizing the time between removal of the silicon wafer from the vacuum chamber and coating the surface with the polymer through any number of processing methods, mainly spin coater and drop cast as described later.

Figure 2.20. PS 210 Microwave Gas Plasma System to prepare substrates for films.

2.4.2 Carver Laboratory Press

For some initial dielectric measurements, a thin film was unable to be produced by other means outlined here, but the electronic properties were still of interest. To overcome this challenge, a pellet was pressed from dried polymer powder, which could then be placed inside the LCR and TDDS instruments for analysis. A Carver Laboratory Press was used along with a 1-inch diameter stainless steel die as seen in **Figure 2.21**. After loading the polymer powder into the die, a pressure of around 20,000 PSI was applied via a hydraulic press at room temperature. Afterwards, the polymer pellet was removed and vacuum dried to remove any moisture before testing. Some polymer powders were found to have an affinity towards the stainless steel, which caused difficulty in removal without breaking the fragile pellets. For these situations, thin films of Teflon were used on either side of the die, and the pressed pellet was easily removed.

Figure 2.21. Carver Laboratory Press used to make polymer pellets.

2.4.3 Drop Cast

Solvent soluble polymers were able to undergo initial dielectric and band gap characterization along with X-Ray analysis by using the drop cast method. In this, a leveled hot plate was used as a platform upon which stainless steel shim stock discs and microscope slides were placed. In addition, a leveled glass plate was used as a drop cast platform in the IMS clean room for solvents such as THF, DMAc, and DMF which were evaporated slowly at room temperature and shown in **Figure 2.22**. Pre-dissolved polymer solutions of concentrations ranging from 1% to 15% were drop cast onto the substrates from a syringe with a 0.45 µm syringe filter attached to the end to remove any dust particles. The samples are then partially covered with a glass petri dish to keep dust off while allowing evaporation to occur and solvent to leave the air around the film. For low boiling point solvents with a high vapor pressure

such as THF, no heat is necessary however, for films cast from meta-cresol the substrates are gradually heated to facilitate faster evaporation and drying. After the films become sufficiently dry that they leave no residue on a Kimwipe, the films on their substrates are transferred to a vacuum oven to be dried further. The films will then either be removed from the substrate or be characterized while remaining attached.

Figure 2.22. Leveled glass sample surface assembled in the IMS clean room to drop cast.

2.4.4 Spin Coat

Thin film samples with target thicknesses from hundreds of nanometers to a few microns in thickness were produced using a Spincoater Model P6700 in the IMS clean room as seen in **Figure 2.23**. The system operates by pulling a vacuum and holding a sample substrate on the platform disk in the center. Dissolved polymer in solution is then evenly applied to the substrate, and the spin recipe is started. A typical recipe includes one to two minutes of spin at a relatively low RPM of around

600 rpm in order to thin out the solution and aid in solvent evaporation. After that cycle, a higher spin rate of 1000 rpm is carried out for 1 second to flatten out the film and remove any edge effects. The film then undergoes a drying procedure consistent with the class of polymer being produced.

Figure 2.23. Spin coater in IMS clean room to produce thin films with minimal impurities for high field measurements.

2.4.5 Dr. Blade Coater

To produce uniform, free standing films were produced using an Erichsen Dr. Blade Film Applicator, called a Dr. Blade for short seen in **Figure 2.24**. The setup consists of a staging platform that is able to be leveled through adjustment of feet prior to use and an arm that slides across to coat a substrate with solution evenly. In a typical setup, a 10 inch by 12-inch glass plate is put on top of the sample stage and vacuum is applied from underneath to prevent movement. Then a blade is chosen from 4 sizes, 150, 250, 380, and 500 microns thick and placed in front of the sliding

arm. The polymer solution is then poured in a line about an inch in front of the blade so that as it spreads, it does not touch the blade. The arm is then set in motion by the automation program which sets the speed and distance that the blade travels. Typically, the amount of solution used is such that it will all be spread before the blade reaches the end of the plate to ensure no solution falls onto to the sample stage. The sample stage can also be preheated before coating or heated in a drying procedure after a film has been applied up to a maximum temperature of 140 °C and as low as room temperature.

Figure 2.24. Erichsen Doctor Blade Film Applicator

2.4.6 Drying Ovens

To remove all solvents from polymer powder precipitates and cast films, a Fisher ISOTEMP vacuum oven Model 281 was used seen in **Figure 2.25**. The oven was powered by a Welch Duo-seal vacuum pump attached to a dry ice solvent trap to ensure no solvents or other chemicals harmed the pump during operation. The oven temperature dial was calibrated using an internal thermometer, and the values were

recorded while under vacuum. At full vacuum strength, the pump was able to reach 8.1 Torr.

Figure 2.25. Vacuum oven, dry ice solvent trap, and mechanical oil pump.

2.4.7 Point to point thickness measurement

For film thickness measurements, a Measure-It-All LE1000-2 point to point gauge was used seen in **Figure 2.26**. The gauge has an accuracy greater than 0.2 um and an LCD display to output the result. For a typical sample, an area of 0.78 cm^2 is used for dielectric spectroscopy. To accurately measure the thickness over that area, 5 points are chosen within the 1 cm diameter circle and averaged together. During this process, care is taken to ensure that the sample area being investigated is as uniform and defect free as possible through both measurements and visual analysis.

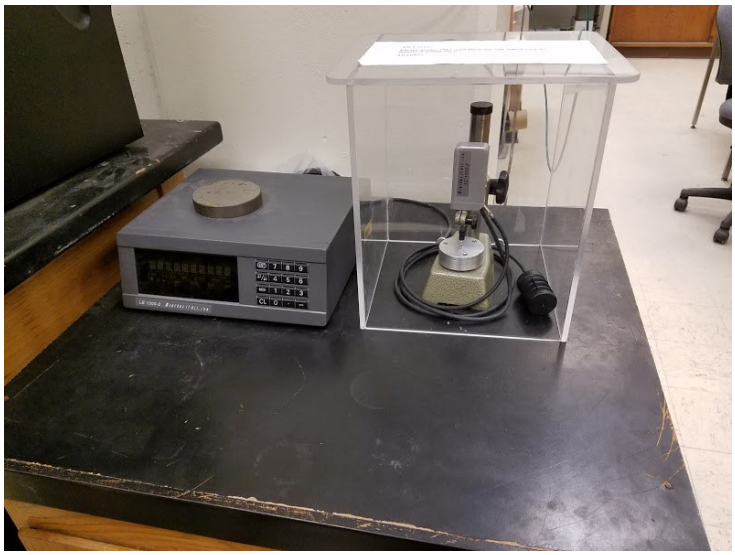

Figure 2.26. Measure-It-All LE1000-2 thickness gauge to measure films and pellets.

2.4.8 Daktek stylus thickness and roughness measurement

For precision thickness and surface roughness measurements, a Veeco Dektak 150 was employed in the controlled environment of the IMS clean room shown in **Figure 2.27**. For system operation, the first step is a calibration check against a known standard to ensure that all measurements are made accurately due to the delicate nature of the Dektak stylus probe. When used to measure surface roughness the probe is lowered onto the film and run over a sample of length about 1000 μm allowing a large area to average the roughness. Typically, this measurement is carried out several times across the film surface for accurate characterization. To measure sample thickness, a small portion of the sample is removed from the substrate after being cast to reveal clean substrate. The stylus then starts its path on the clean substrate and finishes on the polymer film. The area of the substrate is

averaged for the base, and the area of the film is averaged for the sample thickness and roughness. Typically, a peak is seen at the interface between the substrate and the sample due to polymer build-up and lasts only a few nm, that region is typically ignored for film thickness measurements however it does give insight into have the film was processed.

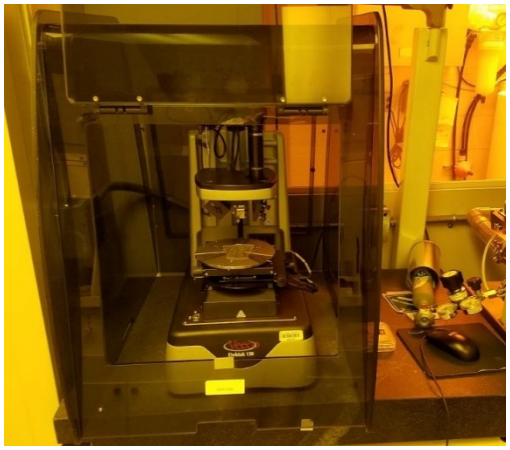

Figure 2.27. Veeco Dektak 150 inside a protective case residing in the IMS clean room.

2.4.9 Sputter Coating

Metallization of polymer films was carried out on a Polaron E5100 SEM Coating Unit seen in **Figure 2.28.** The polymers are placed in the sample chamber with a stainless-steel mask covering the films or wafers. The mask typically has cut outs that are 3 mm in diameter which is the area used for the D-E polarization measurements. A larger 1 cm^2 mask is used to metalize films for low-temperature dielectric spectroscopy. The films are then placed under a vacuum, purged with argon,

and then bathed in a steady stream of argon from a leak valve. A current is then applied to sputter coat metal onto the polymer films with an 80/20 Pd/Ag composition.

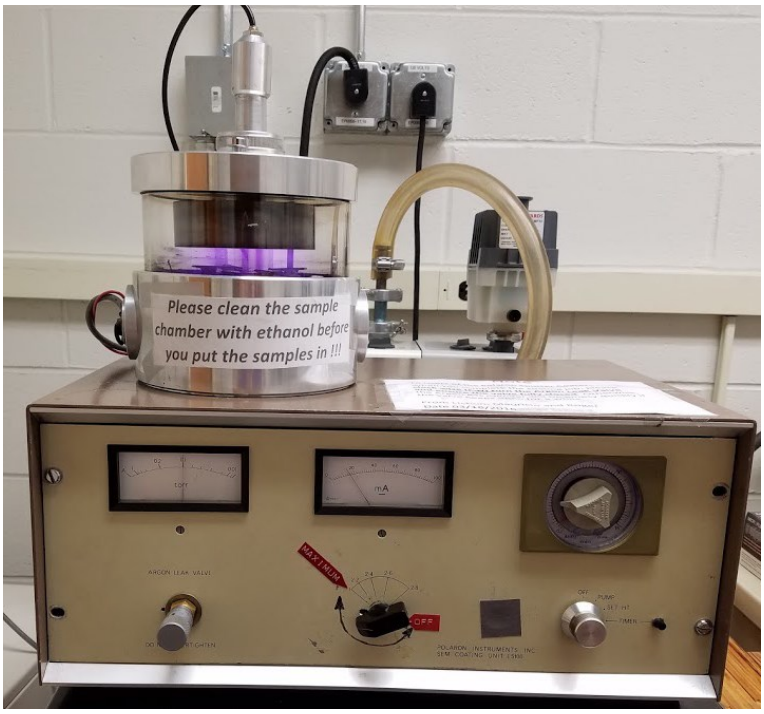

Figure 2.28. Polaron E5100 SEM Coating Unit

Chapter 3

3. Synthesis, Characterization, and Modeling of Polyureas for Dielectric Applications

3.1 Polyureas as Dielectric Materials

During the initial screening process outlined in Section 1.5 on the Rational Co-Design Process a polymer with the repeat unit of -NH-CO-NH-C5H4- was identified as having a dielectric constant greater than 5 and a band gap above 3 eV.[68] My Advanced Materials Progress Report details the preliminary work that lead to this finding as well as some early polyureas tested and is reitterated here.[56] This structure is the simplified model for polyureas with an included benzene ring which made sense from a chemical perspective due to the polar functional groups in urea. Due to the similarity of the polymer synthesis reactions between polyureas and polyurethanes both classes of polymers were studied together to see the effect of changing out a nitrogen for an oxygen in similar structures.[56] To give a large data set for initial exploration, five diamines, and five diols were used to make the polyureas and polyurethanes respectively with 2,4-tolune diisocyanate (TDI), a common industrial diisocyanate used in large quantities around the world.[70] A select amount of the polyureas and polyurethanes synthesized are shown in **Figure 1.10**. The reactions were carried out at 60 °C for 2 hours in dimethyl sulfoxide (DMSO), and for the polyurethanes, a small amount of dibutyl tin dilaurate was added as a catalyst. The

polymers were all precipitated in methanol, purified, and dried prior to use. Characterization was carried out by GPC, NMR, TGA, and DSC to understand the polymers before carrying out electrical measurements on the Time Domain Dielectric Spectroscopy (TDDS) instrument shown in **Table 3.1**. The polymers were named by the alkyl or ether chain they contained varying the number from 1-5 and the polyureas as A with polyurethanes being B.

Table 3.1. The measured dielectric constant and loss values for the polyureas (A) and polyurethanes (B) from TDDS.[70]

Polymer	1A	2A	3A	4A	5A	1B	2B	3B	4B	5B
	5.18	4.29	3.47	2.08	6.19	6.35	6.74	5.81	4.09	10.5
(%)	0.758	0.889	1.73	3.12	4.29	1.26	1.54	1.39	1.56	1.88

In general, the polyurethanes showed a higher than their corresponding polyurea cousins, which can be explained by the higher electronegativity of the urethane group compared to the urea group. Also following the same electronegativity argument is the fact that more carbon atoms in the backbone decreased across the board, as carbon has a diluting effect on the urea and urethane linkages as shown in previous studies.[118,119] The increase in seen in polymers 5A and 5B shows the beneficial effect of adding ethers into the backbone of polymers on dielectric constant, and agree with previously reported values for polyether urethanes.[120] In summary, this study confirmed that the best ways to increase the dielectric constant in aromatic polyurea and polyurethanes involve maximizing polarizability through

electronegative atoms such as oxygen, and decreasing carbon in the backbone to maximize the contribution from the functional groups.

Dr. Q. M. Zhang et al., at Penn State have also explored polyureas for dielectric applications.[121–123]. These studied went in a separate direction as the previous work done by Lorenzini et al., by focusing on polyureas with increased aromatic content, creating rigid systems that lead to no reported glass transition temperature and the ability to operate up until 200 °C. Another polymer made by their group called poly(arylene ether urea) also didn't show any transition below its degradation temperature of 300 °C.[124] All of these polyureas showed dielectric constants between 4 and 6 that were stable over a wide temperature range with losses below 2%. The high dielectric constants were attributed to keeping a high dipole moment by keeping the repeat unit small. As discussed by Dr. Zhang the orientational polarization, also known as the dipolar polarization is the dominant polarization mechanism.[124]

This chapter, and the subsequent organic **Chapters 3, 4, and 5** attempts to further understand the role and magnitude of dipolar polarization that occurs in these highly polar systems. The polymer made from TDI and JEFFAMINE® EDR148 (EDR148), (TDI-EDR148), was chosen for this study due to its high molecular weight leading to a mechanically strong film as well as its promising electrical properties during initial characterization. By maintaining the use of TDI a continued structure property relationship can consciously be updated as new data arrived, this time with a polyurea with a more flexible backbone continuing and additional ether than polyurea 5A.

3.2 Synthesis and Processing of TDI-EDR148

TDI-EDR148 was synthesized under a flow of argon to reduce the chance of side reactions with TDI. TDI was massed out into a clean and dried 100 ml 3-neck flask filled with argon and a magnetic stir bar. Dry DMSO was then added to the 3-neck flask to dilute the TDI to 10% by weight. In a separate flask, EDR148 was added in an equal molar amount to the TDI and was diluted with dry DMSO. A portion of dry DMSO was put aside so the total volume of DMSO would reduce the concentration of EDR148 to 10% by weight, the second portion was used for rinsing out the flask containing EDR148. The solution of EDR148 was added to the stirring solution of TDI and then the flask was rinsed and poured into the TDI 3-neck flask as well. Argon was continually purged over the reaction mixture throughout the addition to ensure any air that entered was immediately displaced. The reaction heated up as the polymers went towards completion and an oil bath was used to hold the reaction at 60 °C for 6 hours. After the reaction was complete, the polymer was precipitated out of solution using a 10x volume of isopropanol and then dried under vacuum. The reaction scheme is outlined in **Scheme 3.1**. The elemental analysis of the polyurea powder was found to be in accordance with the predicted values with percent concentrations of carbon at 53.1%, nitrogen at 6.5%, hydrogen at 12.9%, and oxygen at roughly 20% due to some uncertainty from the instrument incorrectly detecting sulfur in samples. The residuals calculated by Chemdraw are carbon at 55.89%, nitrogen at 6.88%, hydrogen at 17.38%, and oxygen at 19.85%.

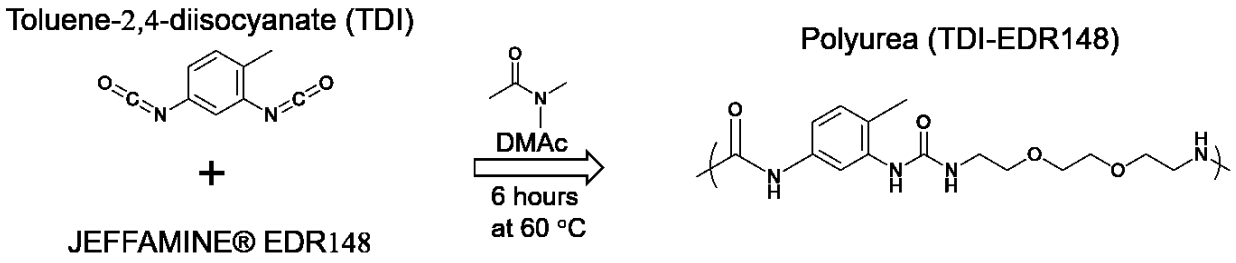

Scheme 3.1 Reaction of TDI and EDR148 to produce TDI-EDR148

To produce films of TDI-EDR148 several solvents, concentrations, and processing conditions were tested to optimize for a uniform film in the range of 8 – 12 µm while retaining minimal solvent. TDI-EDR148 was dissolved in dimethylformamide (DMF) to a 10% concentration by weight and filtered through a 0.45 m poly(tetrafluoroethylene) PTFE syringe filter. The ideal conditions were blade cast with an Erichsen CoatMaster film applicator using a blade height of 380 µm traveling at 10 mm/s on a glass substrate and a drying temperature of 70 °C for 6 hours. A film roughly 6 inches by 6 inches square was produced on the glass substrate which was then cut down to remove the edges that were not uniform. The reduced film was then placed in a Teflon frame and dried under vacuum in an oven at 110 °C for 24 hours to ensure complete removal of the solvent. A 4 x 4-inch free-standing film was ultimately produced that had a thickness of 10-12 µm. The film can be seen in **Figure 3.1** where it is overlaid on the periodic table to demonstrate its transparency.

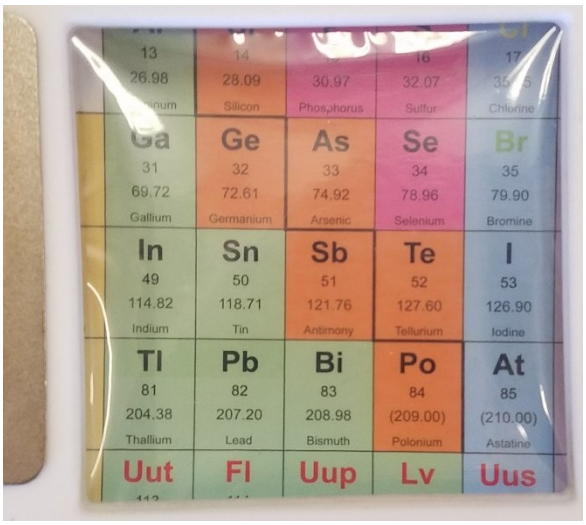

Figure 3.1 4 x 4 inch 10-12 µm film of TDI-EDR148 overlaid on the periodic table

3.3 Structural Characterization

3.3.1 Gel Permeation Chromatography of TDI-EDR148

Gel permeation chromatography (GPC) was run on the two polymer systems to determine their molecular weights. TDI-EDR148 was dissolved in dimethylacetamide (DMAc) at a concentration of 0.1 % by weight, filtered through a 0.45 µm syringe filter, and injected into the GPC column. TDI-EDR148 was found to have a weight averaged molecular weight of roughly 99,000 g/mol compared to a calibration standard from monodisperse poly(methyl methacrylate) (PMMA) which correlates to roughly 300 repeat units in the polymer backbone which should be sufficient for chain entanglements. The estimated number average molecular weight from GPC was 68,000 g/mol resulting in a poly dispersity index (PDI) of 1.45. The full GPC trace can be seen in **Figure 3.2** below.

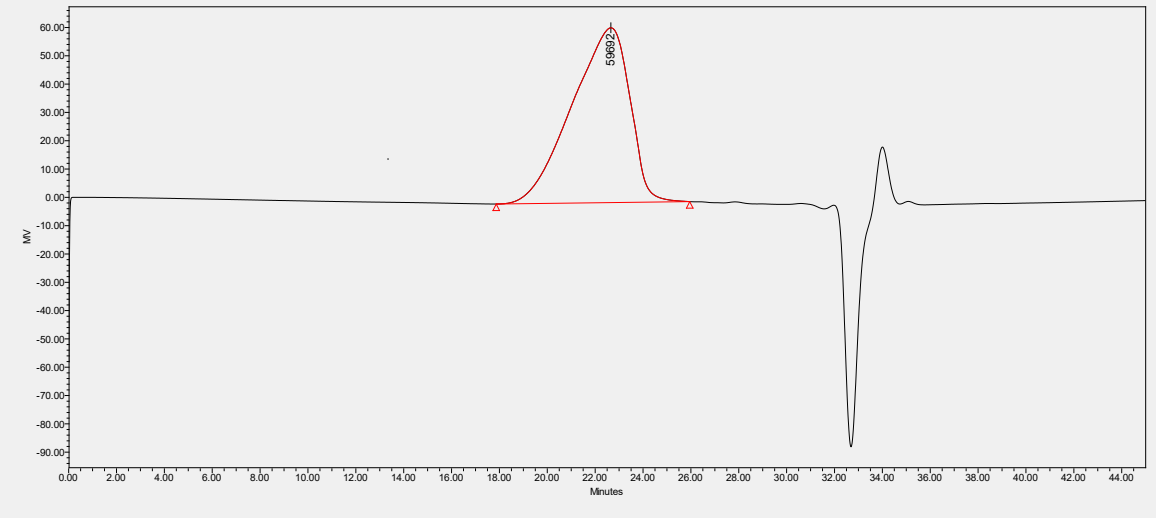

Figure 3.2 GPC trace of TDI-EDR148 in DMAc

3.3.2 Fourier Transform Infrared Spectroscopy of TDI-EDR148

Fourier transform infrared (FTIR) spectroscopy was then run on thin films cast from DMF and vacuum dried using the transmission mode. **Figure 3.3** shows the spectrum for TDI-EDR148.

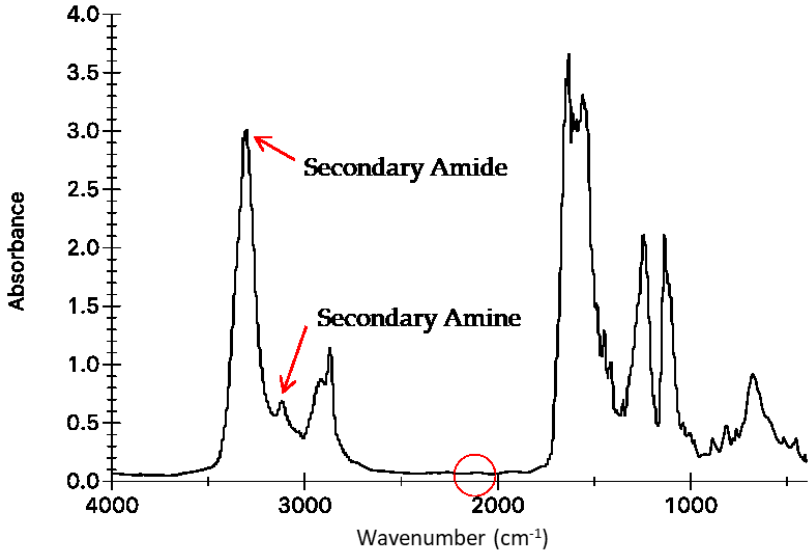

Figure 3.3 FTIR of TDI-EDR148 where the arrows point to where the secondary amide, secondary amine, and the absent isocyanate peak circled.

In this spectrum, the arrow pointing to the peak at about 3500 cm^{-1} shows the amide peak of the urea linkage. The amine peak at 3500 to 3200 shows that the monomer subunit is fully polymerized as a primary amine of EDR148 would show two peaks, whereas single peak here is indicative of a secondary amine. The circle around 2200 cm^{-1} corresponds to where an isocyanate peak would be if it were present in the sample. The purpose of pointing out these three features is to demonstrate that peaks characteristic of the monomers is not present while peaks corresponding to the polymers are present. This FTIR spectra, therefore, support the notion that the monomers have fully polymerized into their polymeric units.

3.3.3 Band Gap Determination by UV-Visible Spectroscopy

The band gap for TDI-EDR148 was determined optically by scanning the UV-Vis spectrum from 1600 nm down to 200 nm and observing the onset of UV absorption. Through the Maxwell equation, the optical band gap can be found from taking $1240/\lambda_{onset}$. The UV-Vis spectra are plotted in **Figure 3.4** with the onset overlaid graphically. The onset is 315 nm correlating to a band gap of 3.9 which is above the threshold of 3 eV initially set up as a screening criterion for high breakdown materials. TDI-EDR148 was predicted by DFT to have a higher band gap of 4.7 eV which would have made it an even more promising candidate for an insulator. However, DFT has shown to over predict the band gaps in the past, and this result is not unexpected.

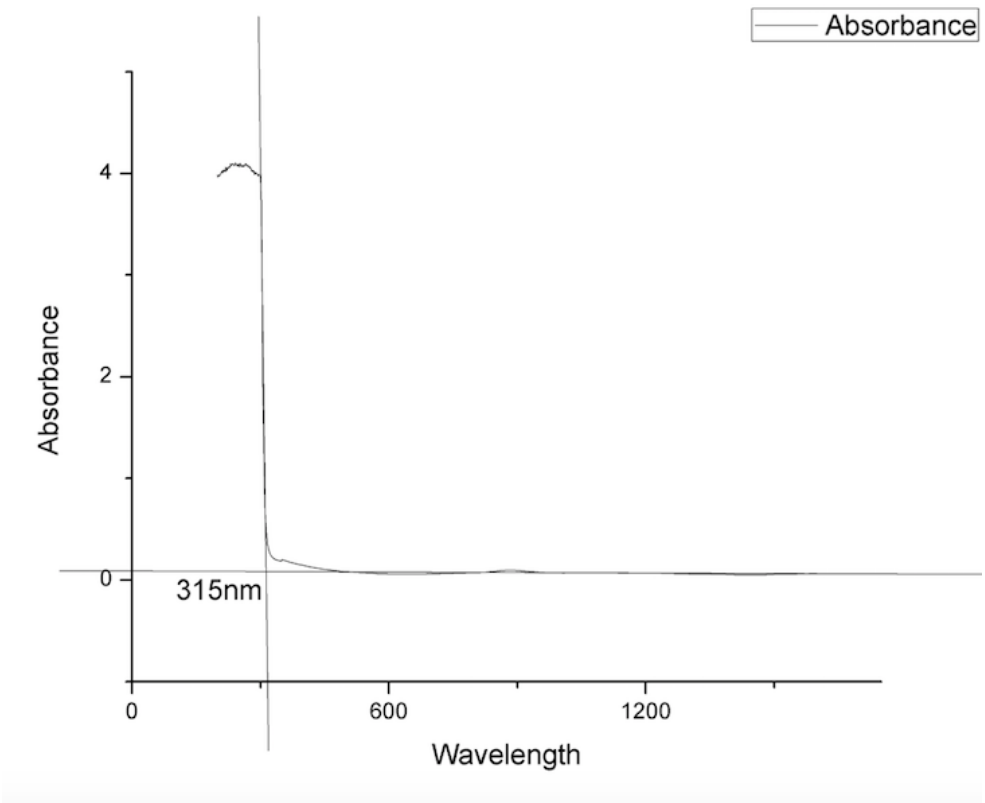

Figure 3.4. TDI-EDR148 UV/Vis spectrum used to determine band gap.

3.4 Thermal Characterization: TGA, DSC

Thermogravimetric analysis (TGA) and differential scanning calorimetry (DSC) measurements were run on the polymer film to determine its degradation and glass transition (T_g) temperatures. TDI-EDR148 was found to degrade at 262.19°C (**Figure 3.5**) and had undergone its glass transition at 125.35°C (**Figure 3.6**). A melt transition (T_m) was also observed at 211.98°C. This melt transition is significant as it shows that this polymer system is capable of undergoing melt processing where it will no longer be dependent on a solvent system.

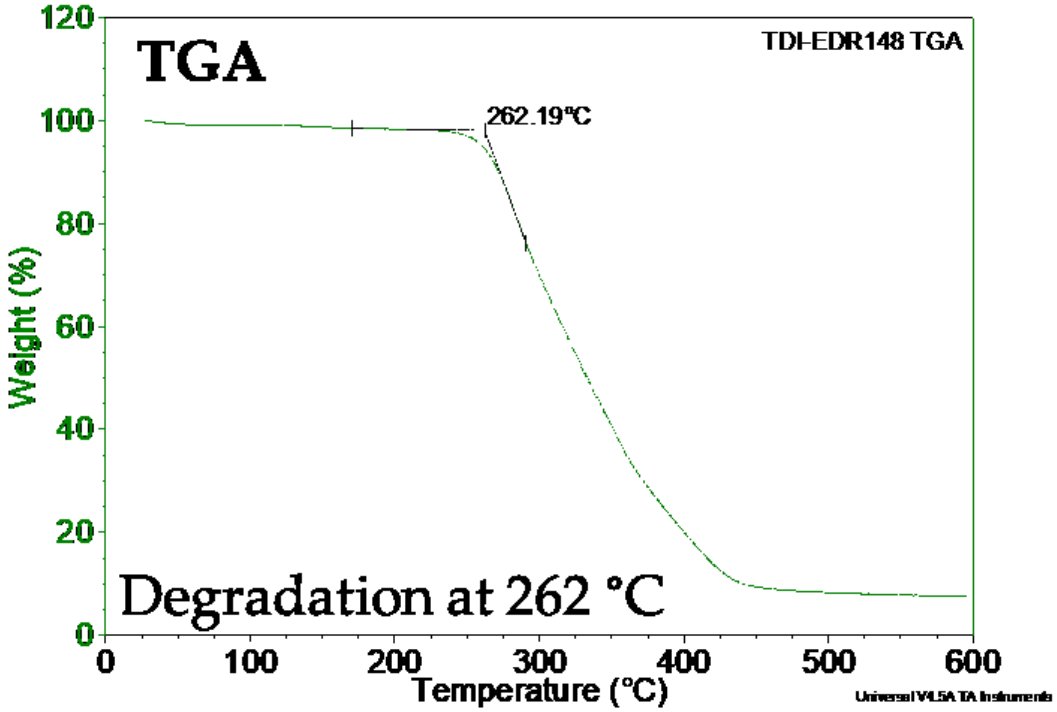

Figure 3.5. TGA of TDI-EDR148 where the degradation is found to be at 262.19°C

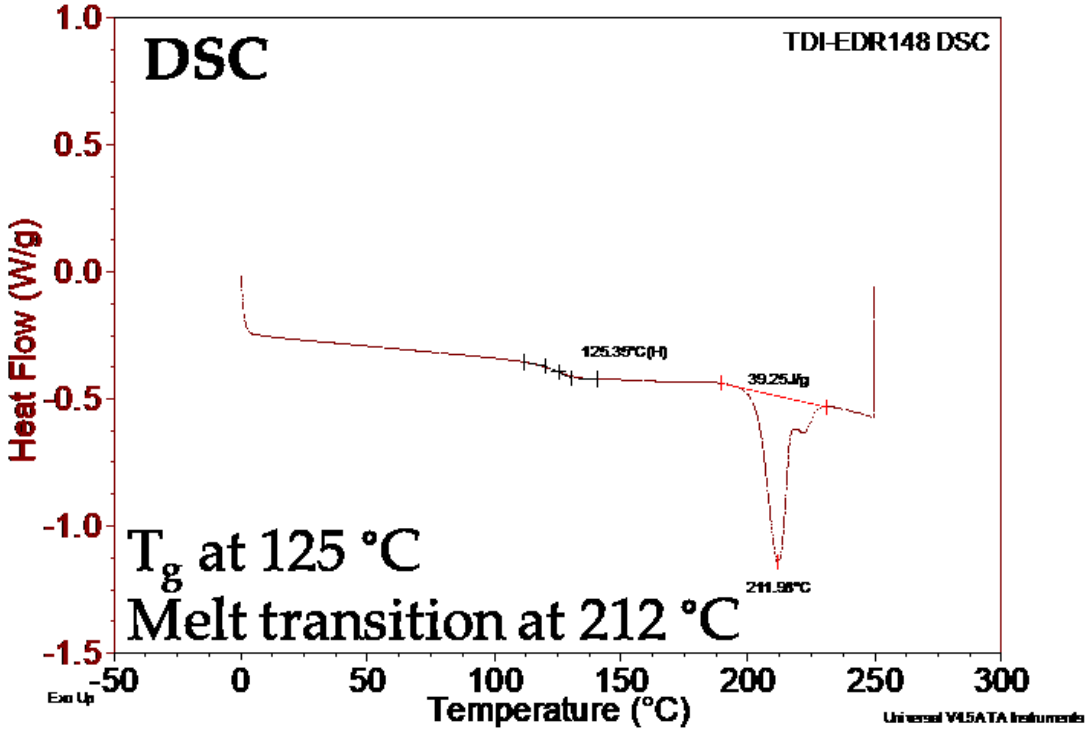

Figure 3.6. DSC of TDI-EDR148 where the glass transition was found to be 125 °C and a melt transition at 212 °C

3.5 Dielectric Spectroscopy

Dielectric spectroscopy was carried out on TDI-EDR148 at both General Electric Global Research Center in Schenectady NY and at the Electrical Insulation Research Center (ERIC) at the University of Connecticut. General Electric had access to a Novocontrol dielectric spectrometer which is an industrially produced complete system that combines a time domain dielectric spectrometer (TDDS) with a frequency domain dielectric spectrometer (LCR meter) and a temperature controlled environment to scan from 10^{-2} Hz up until 10^{6} Hz with a temperature range of -130 °C to above 200 °C which is higher than needed for this experiment. **Figure 3.7** shows the dielectric constant and dissipation verse temperature at 20 °C, 50 °C, and 100 °C. TDI-EDR148 was shown to have a high dielectric constant at around 6 and a low loss below 2% until the temperature started approaching the glass transition temperature at which both the dielectric constant and loss increased as is expected.

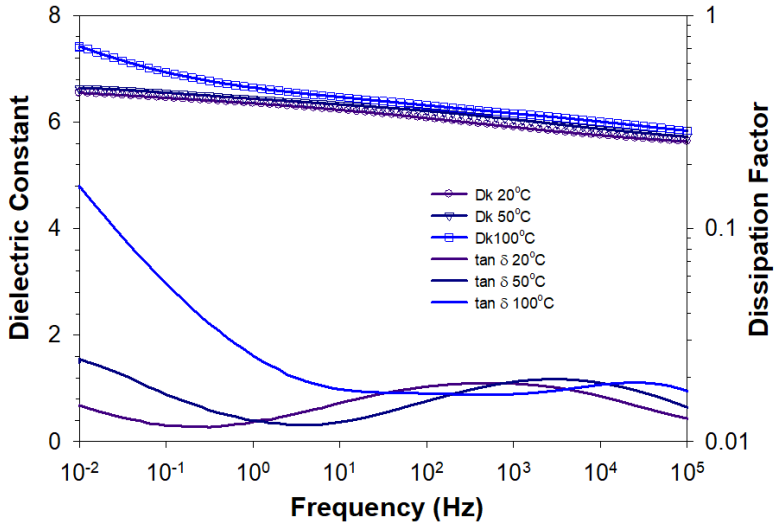

Figure 3.7. Dielectric spectroscopy of TDI-EDR148 at room temperature and above.

The Novocontrol at General Electric's Global Research Center was used to investigate the temperature dependence of the dielectric constant and loss as well as the frequency dependence. This experiment was unable to be conducted at the EIRC at the time. The three-dimension plots with gradient coloring are shown in **Figure 3.8** with a) showing the dielectric constant and b) showing the dissipation factor. The broadband dielectric spectroscopy analysis was conducted to understand the polarization mechanism. The measurement was conducted over the frequency range from 0.01 Hz up to 1 MHz and a temperature range from -90 ºC to 120 ºC with a 10 ºC step between each measurement and a hold time sufficient to allow the sample to equilibrate before the next measurement took place.

The complex dielectric spectra, as a function of angular frequency and temperature, involves several different processes. Each of the processes has specific features in the frequency and temperature dependence of the real and imaginary parts of the complex dielectric function. **Figure 3.8** shows the 3D plots of the complex dielectric spectroscopy of TDI-EDR148 with (a), the real part, or dielectric constant and (b), the imaginary part, or dissipation factor. Within our measure range limit, the relaxation peak seen near the high temperature high frequency range is labeled as the α relaxation and is related to the glass transition temperature of this polymer which was determined to be 125 °C by DSC. Below the glass transition temperature, two sub-glass transition relaxations can be observed where the dielectric constant starts to reduce in the middle (ß relaxation), and another more obvious reduction

towards the low temperature (γ relaxation). These relaxation peaks can be located easier in the dissipation factor plot shown in **Figure 3.8B**.

The relaxation processes of dielectrics are typically analyzed using existing model functions. Various formulas have been suggested to describe the experimentally observed spectra by using the theoretically well-founded Debye function as a starting point. A more general model function was introduced by Havriliak and Negami[125] (NH function) which combines the Cole/Cole-function and the Cole/Davidson-function. The equation is given by **Equation 3.1**

$$\varepsilon(\omega) = \varepsilon_{\infty} + \frac{\Delta\varepsilon}{[1+(i\omega\tau)^{\alpha}]^{\beta}} \tag{3.1}$$

where Δε is the relaxation strength, β and γ are the shape parameters which describe the symmetric and asymmetric broadening of the complex dielectric function.

The glass transition and sub-glass transition dynamics are often studied in a simplified model where a molecule fluctuates in the cage of its neighbors.[126] Its motion is assigned to a relaxation following an Arrhenius-type temperature dependence seen in **Equation 3.2**

$$\boldsymbol{f_{max} = f_{max,\infty} e^{-\frac{E_a}{k_B T}}} \tag{3.2}$$

where E_A is the activation energy, k_B the Boltzmann constant and f_∞ is the relaxation rate at the high temperature limit. The scaling behavior predicted by the Arrhenius equation with log(f) vs. 1/T should yield a straight line, whose slope is proportional to the activation energy. The Arrhenius plot for TDI-EDR148 based on the experimental

result is shown in **Figure 3.8C**. Each data point is the peak relaxation rate (frequency reciprocal) and points related to each relaxation stay well in straight lines. Linear curve fittings are performed and the derived activation energies are 0.145 eV for the γ peak and 0.245 eV for the β peak. These activation energies are considered low, and this suggests that they are easily activated and allowed to move about their local area. The flexible diaminoether within the backbone gives the polymer extra chain movement to increase the dielectric constant, and it helps to drive this relatively low activation energy.[127]

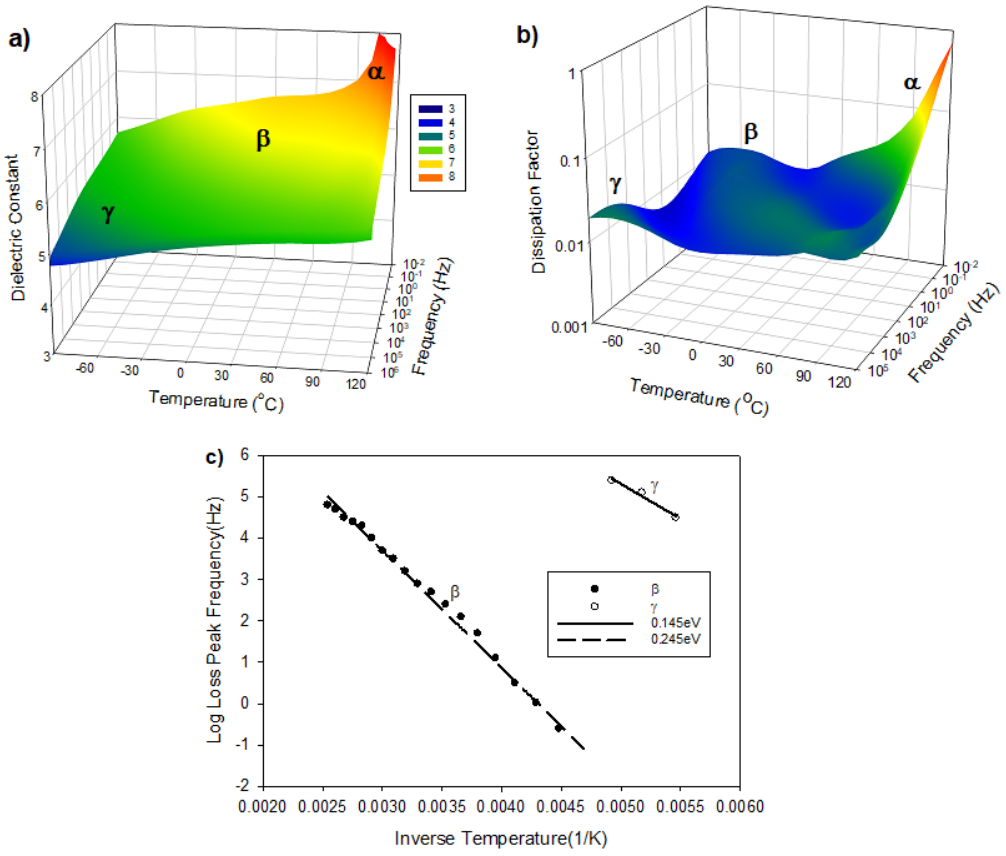

Figure 3.8. Three-Dimensional plots of the real (a) and imaginary (b) parts of the complex dielectric spectroscopy of TDI-EDR148 with the sub-glass transition relaxation peak analysis according to the Arrhenius equation (c).

Since the low temperature dielectric spectroscopy proved to be an important instrument for analyzing the relaxations in TDI-EDR148, a similar system was devised for the University of Connecticut's EIRC for a fraction of the cost. JoAnne Ronzello of the EIRC lead the development of the in-house low temperature setup by attaching a liquid nitrogen tank to an oven and LCR meter while controlling the system with LabVIEW programed by Justin Delarm and Krishnan Sureshkumar. The system, outlined in **Chapter 2**, allowed for samples to be run from -130 °C to 150 °C over the frequency range of 20 Hz to 1 MHz. Since this setup only had an LCR meter attached it was unable to go to the lower frequencies that the Novocontrol provides. Several attempts were made to connect the TDDS to the low temperature sample oven. However, the sensitivity of the TDDS made low temperature measurements too noisy to be of any practical use.

For TDI-EDR148, the polymer film was first metallized with an 80/20 palladium and gold sputter coated metal film to ensure the entire electrode surface was measured throughout the experiment as detailed in **Chapter 2**. The polymer film was then placed inside a specialty-made metal container in order to eliminate interference from the liquid nitrogen stream injected into the sample oven. The sample was run from -130 °C to 130 °C with a step of 10 °C and a hold time of 30 minutes at each temperature to ensure the polymer film was able to equilibrate to each temperature. 10 measurements were taken and averaged for each data point to eliminate any noise that may have been introduced into the system and the data was plotted in **Figure 3.9A** with the dissipation factor plotted in **Figure 3.9B**. The

dielectric constant of the new film measured in the EIRC was slightly lower than those measured at GE with a total dielectric constant at 5.26 at room temperature. The dielectric loss remained below 2% throughout most of the run until the Tg was approached and showed several sub-T_g relaxations.

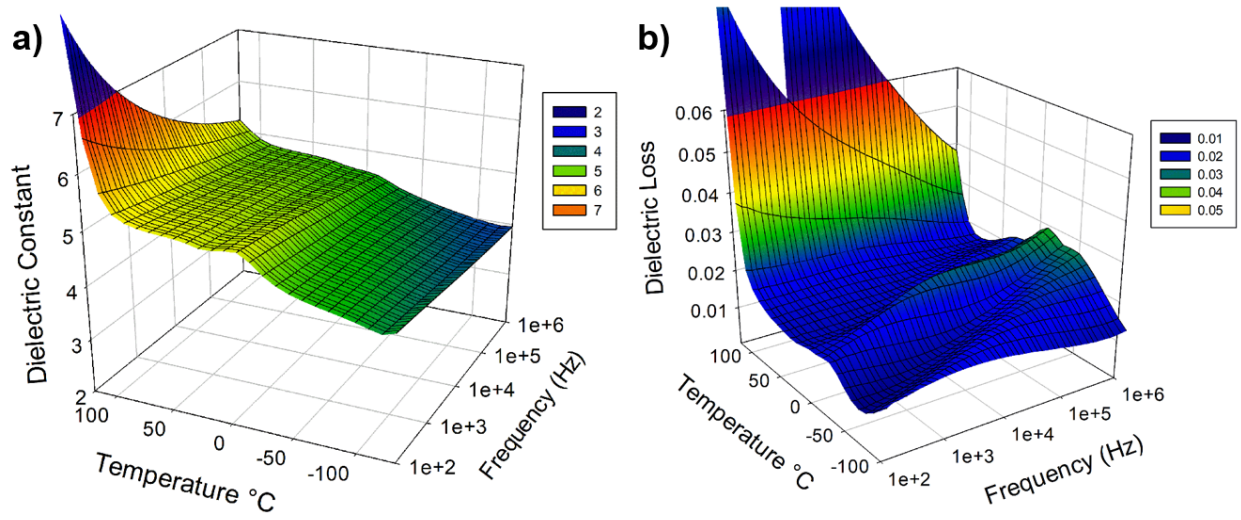

Figure 3.9. Dielectric spectroscopy (A) and Dielectric Loss (B) of TDI-EDR148 from -130 °C to 120 °C carried out on the automated LCR meter in UConn's EIRC.

The dielectric constant is listed for several temperatures in **Table 3.2** below to show the change as TDI-EDR148 was heated. Negative 130 °C was chosen since it was the lowest temperature achievable while using liquid nitrogen in the oven. If liquid helium was used instead the measurement could, in theory, be carried out at much lower temperatures, providing the electronics could withstand those low temperatures. The dielectric constant at -130 °C was seen to be 3.89 which is 1.37 greater than the dielectric constant at 30 °C which is 5.26. At 120 °C the temperature starts to approach the glass transition temperature of TDI-EDR148 of 125 °C, and

therefore the dielectric constant and loss start to drastically increase as segmental mobility increases.

Table 3.2. The measured dielectric constant and loss values for TDI-EDR148 at the extremely low temperature (-130 °C), room temperature (30 °C) and near Tg (120 °C).

Dielectric Constant – TDI-EDR148		
-130 °C	30 °C	120 °C
3.89	5.26	5.71

While it is important to know the dielectric constant and loss at varying temperatures to understand how a dielectric material would perform in a range of environments these numbers by themselves reveal very little about the underlying mechanisms at work. As described in Chapter 1, there are three main polarization mechanisms found in organic polymers without any nanoparticle fillers, the electronic, atomic, and dipolar polarizations which are found from the polarization of electrons, atoms, and dipoles respectively. The electronic dielectric constant is related to the refractive index of a material squared, and so the refractive index of TDI-EDR148 was taken by ellipsometry to be 1.61 at a wavelength 589 nm which is the sodium d line resulting in an electronic dielectric constant of 2.58. Since the atomic polarization is caused by the IR modes in chemical bonds they are expected to be active at any temperature above 0 K. However, the orientational polarization should decrease as the temperature is lowered as temperature moves below their solid-state energy barrier. With -130 °C being the lowest temperature that our current instrument can measure it is taken at the point at which the dipolar polarization is

0 and only the electronic and atomic polarizations contribute to the dielectric constant. By subtracting the electronic portion of 2.58 from 3.89, a value of 1.31 is calculated for the atomic polarization. It is understood that this value for atomic polarization is an overestimated as some dipolar polarization should remain even at -130 °C, however, a more precise value is currently unavailable given the instrumental limitations. Finally, the dielectric constant at -130 °C is subtracted from the dielectric constant room temperature (30 °C) to calculate the portion of the dielectric constant from the dipolar polarization at room temperature which results in a value of 1.37. In order to validate these values, two sets of computational data were used as a comparison. The first was from DFT calculations which determined that TDI-EDR148 had an electronic dielectric constant slightly higher than observed experimentally at 3.02 with an ionic or atomic dielectric constant at 0.87. Similar values were calculated using a machine learning algorithm which is detailed in **Chapter 5 Section 5.7** resulting in an electronic dielectric constant of 2.92 and an atomic dielectric constant of 1.11.[128] These results make sense compared to the experimental results as the contribution to the dielectric constant from the atomic polarization is expected to be lower than 1.31 as our experimental method includes some partial dipolar polarization. These results are all tabulated in **Table 3.3** and outline a path forward to deconvolute the three main polarization mechanisms in polymeric dielectrics to understand which portions yield the greatest benefit. It is my understanding that the dipolar contribution is the polarization mechanism that could

be most improved upon through clever materials design and should, therefore, be the focus of future investigation.

Table 3.3. The breakdown of the dielectric constant into separate polarization mechanisms experimentally and by DFT/DFT-ML. For DFT values, the atomic correlates to the ionic contribution that is calculated.

Type	RI	$E_{electronic}$	E_{atomic}	$E_{dipolar}$	E_{total}	Band Gap
EXP	1.61	2.58	1.31	1.37	5.26	3.9
DFT	1.74	3.02	0.87	N/A	3.89	4.7
DFT-ML	1.71	2.92	1.11	N/A	4.03	4.7

3.6 High Field Characterization

3.6.1 DC Breakdown Analysis

Failure analysis was carried out on 30 samples to determine the DC engineering breakdown field of TDI-EDR148 using two separate film arrangements. The process is described in detail in **Chapter 2**. Measurements were carried out in silicone oil on sample areas 3 mm in diameter in a technique known as ball to plane where the top electrode consisted of a ball bearing pressed against the metalized film and the bottom electrode being the conductive metal oil bath which contacts the opposite side of the film which is also metalized to the same dimensions. The second technique used, referred to as film to film, used a Kapton mask to expose a 2 cm^2 area where conductive metal foils were electrostatically adhered to the polymer film for a larger area measurement. The ball to plan results can be seen in **Figure 3.10A** and the film to film results can be seen in **Figure 3.10B**. The results for both techniques

were analyzed using the Weibull distribution function, F(x) as shown in **Equation 2.4**. By taking a large distribution of data points across several samples, these variations can be averaged out, and a likely breakdown field for a given sample could be determined within acceptable limits, in this case, 63.2% probability. The value measured by ball to plane showed a probabilistic breakdown at 510 MV/m, higher than the value of 308 MV/m for the film to film breakdown field. These results match with the expectation that as the sample measurement area increases from 7.07 mm^2 to 20 mm^2 the number of defects in the sample would increase, raising the probability that the film will undergo premature breakdown. This idea could be extrapolated to breakdown measurements on a smaller electrode size or even at a thinner film thickness below the typical 10 μm thickness used here. Thinner films should have less chance of defects between the two metalized electrodes and could give better breakdown results. However, the areas of the thinner films that contain the defects should be more pronounced and possibly give an even lower breakdown in those areas. However, it should be noted that taking breakdown measurements on extremely thin samples or on extremely small electrodes would offer little insight into how the material would behave in the real world as a wound capacitor. The argument for making small scale measurements would be that processing and sample preparation at the lab scale is not as precise and uniform as industrially produced extruded film which should have fewer defects to cause an early breakdown.

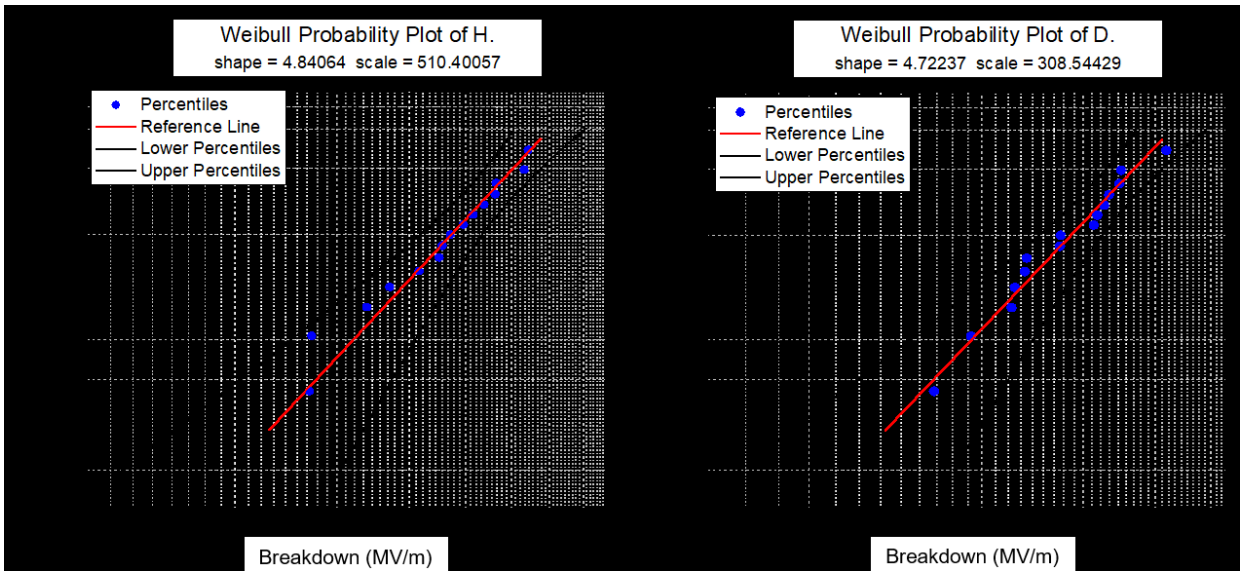

Figure 3.10. Weibull analysis of DC breakdown for TDI-EDR148 by (A) ball to plane in oil and (B) film to film in air methods.

3.6.2 D-E Hysteresis Loop

To determine the energy density, high field polarization measurements of TDI-EDR148 were carried out by a modified Sawyer-Tower polarization loop system as detailed in **Section 2.3.7**. The D-E loop measurement is a great way to measure most of the relevant electrical properties all together within a single measurement. **Figure 3.11** shows the D-E loop result which shows that the polarization behavior is mostly linear, and the small deviation is due to the nonlinear conduction current that increases under higher electric fields. The film can withstand an electric field higher than 630 MV/m before undergoing breakdown. It is important to note that this measurement is taken on a single 3 mm diameter electrode in a ball to plane arrangement under oil and therefore should give a higher value than the probabilistic breakdown measured by DC breakdown and Weibull analysis. The slope of the

charging loop corresponds to the dielectric constant of the sample. A slope of 6.2 was obtained from the linear range which agrees well with the Novocontrol measurement at around 100 Hz.

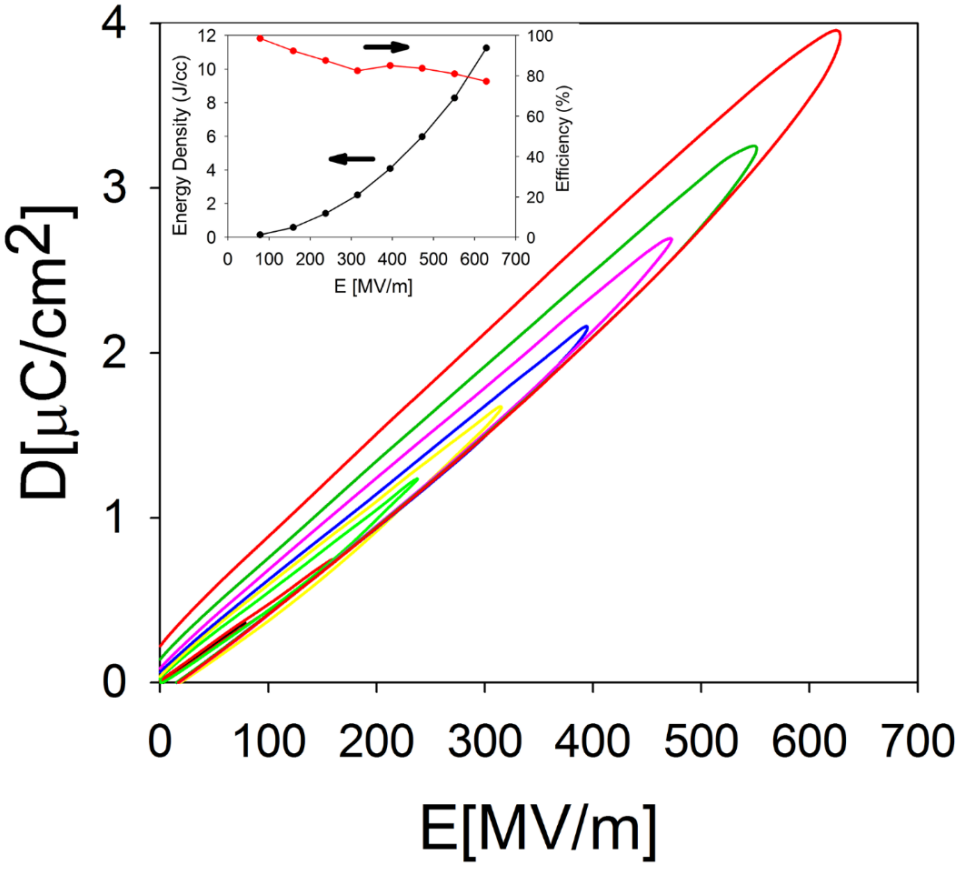

Figure 3.11. D-E loop of TDI-EDR148 with the energy density and efficiency plots as a function of electric field inset.

The area enclosed in the loop is the charge/discharge energy difference during one cycle, and the efficiency is calculated by comparing the input and output energy. As shown in the insert of **Figure 3.11** TDI-EDR148 has an efficiency higher than 80% even under extreme fields. The efficiency can still be improved by more careful processing methods to ensure a homogenous film formation with a smooth surface.

Also, the reduction of any possible impurities or dust can be eliminated through fabrication in a cleanroom environment while remaining solvent can be extracted under longer and more vigorous vacuum oven conditions. The energy density reached 12 J/cc at 600 MV/m which is much higher than most of the commercial capacitor films currently available and over double that of BOPP.

The loss measured in the D-E loop is a combination of polarization loss and conduction loss.[129] The conduction loss can be optimized during processing because it is related more to extrinsic factors such as defects and impurity contaminations than with the structure of the polymer. Polarization loss is due to the intrinsic property of the material, which, is difficult to reduce without changing the molecular structure of the polymer. A high field conduction measurement system was used to measure the conduction current of the sample over an area of 1 cm^2.[116] If a material with high total loss shows a small amount of conduction loss, then that means the material is hard to optimize further due to its intrinsic property.

3.6.3 Pre-Breakdown High Field Conduction

To determine the pre-breakdown conduction at high electric fields, a 300 V/s ramp voltage was applied to the sample up to breakdown and the capacitive charging current was cancelled dynamically to reveal the resistive current as detailed in **Section 2.6.8**. The time constant is much longer than the D-E loop measurement as the measuring takes place over a couple seconds instead of milliseconds, and the polarization current can be ignored compared to conduction current. **Figure 3.11** shows the integrated conduction current of TDI-EDR148 in comparison with two

widely used commercial capacitor films: polystyrene and polypropylene. Full comparison of various polymer films can be found in a related conference paper which will be presented by Zongze Li at IEEE's 2017 Conference on Electrical Insulation and Dielectric Phenomenon (CEIDP) in Fort Worth, TX titled "A novel aromatic polyurea for high energy density capacitors". TDI-EDR148 showed lower conduction current than polystyrene but still had a relatively high low-field conduction loss. According to space-charge-limited current (SCLC) model, under log-log scale, the slope of the current density vs. applied voltage is related to the electron trapping.[116] The slope of TDI-EDR148 is very close to 3 which means it is free of traps, suggesting it has promising high field properties. It should also be noted that the conduction loss has already been decreased by 50% throughout our study through optimization of synthetic and processing parameters. Further processing optimization will continue to improve the film to reach a higher charge/discharge efficiency.

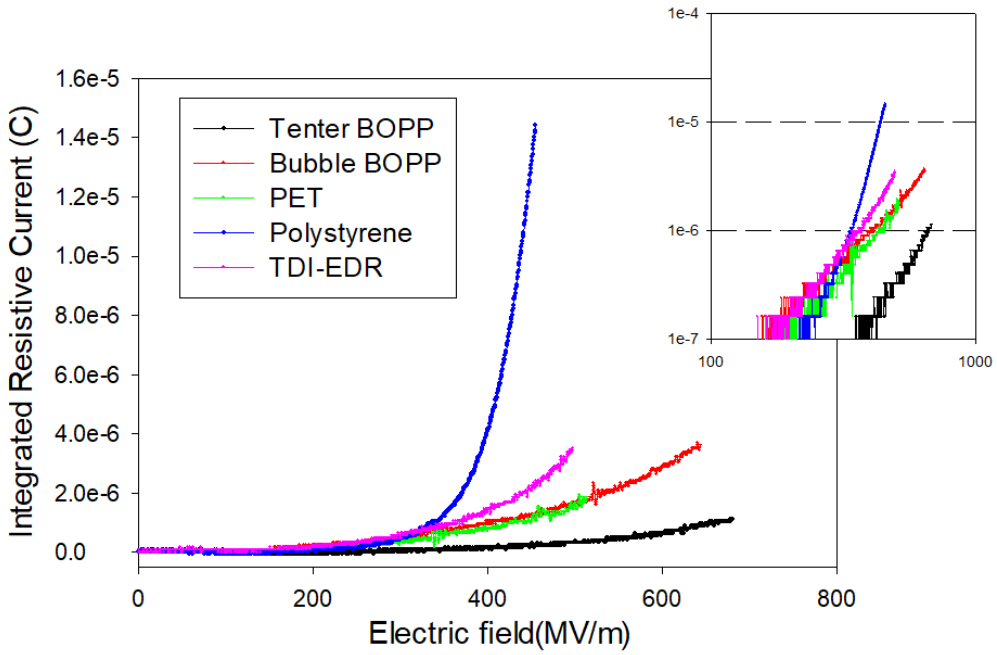

Figure 3.12. High field conduction of TDI-EDR 148 in comparison with two state-of-art capacitor films-polystyrene and bi-axially oriented polypropylene (BOPP). The insert is based on the same set of data under log-log scale with respect to space-charge-limited current (SCLC)model.

This chapter has presented the polyurea TDI-EDR148 as a promising candidate for high energy density dielectrics through careful synthesis and extensive characterized. The measurements indicated that TDI-EDR148 has a dielectric constant from 5 to 6 with a loss factor less than 2%. The energy density can reach 12 J/cc at around 600 MV/m which is more than double the maximum energy density of polypropylene with the ability to operate at higher temperatures due to a Tg of 125 °C. With additional and ongoing processing optimization, the breakdown strength and the energy density can still be further improved. The in-depth dielectric spectroscopy analysis for TDI-EDR148 showed that the different polarization mechanisms in a polymer could be deconvoluted by utilizing a variety of instruments

and carrying out measurements at extremely low temperatures. Potential dipole orientation and dipole moment contribution to the high dielectric constant can be investigated further in a detailed structure-property study in order to devise a polymer system that maximizes the dielectric constant while balancing the other important properties such as mechanical and thermal behavior. By utilizing a polymer containing a benzene ring with a flexible etheramine to form the backbone, high dielectric constants were able to be generated while still maintaining a sufficient thermal operation window.

Chapter 4

4. Synthesis, Characterization, and Modeling of Polythioureas for Dielectric Applications

4.1 Polythioureas as Dielectric Materials

Besides polyureas, a second class of polymers was shown to have both a high dielectric constant and a high band gap, polythioureas. The preliminary work done on polythioureas was described for my Advanced Materials progress report and reiterated here.[56] The first polythiourea synthesized for this work, -NH-CS-NH-C_6H_4-, provided a simple structure for calculations and synthesis; however, the actual synthesized material proved to be insoluble and was seen to melt at or above its degradation temperature, and was therefore not processable into thin films.[68] Ma *et al.* studied polythioureas with longer and more flexible chains, with the idea of improving the processability.[74] By keeping one monomer constant, para-phenylene diisothiocyanate (PDTC), and by varying the diamines between different aromatic, aliphatic, and polyether monomers, structure-property relationships were derived for the dielectric constant of this family of polythioureas. Five different diamines were chosen: 4,4'-oxydianiline (ODA), Bis(4-aminophenyl) methane (MDA), 1,4-Diaminobenzene (PhDA), hexane-1,6-diamine (HDA) and Jeffamine HK511. Further, a thiophosgene reaction was employed to mimic an industrial scale reaction for the polymerization of a related thiourea compound reported by Wu et al.[130] The six

polymers thus studied are listed in **Table 4.1**, and the structures of some of them are shown in **Figure 1.10** in Chapter 1.

Extensive polymer characterization was carried out on these polythioureas; this included obtaining their respective FTIR, XRD and solution NMR spectra to determine the structure. Further computations were performed on these specific polythioureas in order to obtain more accurate property estimates and were compared with experimental results. The low energy polymer configurations obtained as before were subjected to electronic and dielectric property computations.[68,107,108]

Table 4.1. Experimental and computational (shown in brackets) dielectric data for polythioureas. Measured ε_{tot} and $tan\,\delta$ correspond to room temperature (r.t.) and a frequency of 1 kHz; ε_{elec} is reported as the squared value of the measured refractive index.[69]

Polymers	$\varepsilon_{\mathrm{elec}}$	$\varepsilon_{\mathrm{tot}}$	$\tan\delta$	E_{g} (eV)
PDTC-ODA	3.20 (3.86)	4.52 (5.42)	0.0233	3.22 (3.27)
PDTC-MDA	3.28 (3.69)	4.08 (4.59)	0.0348	3.16 (3.41)
PDTC-PhDA	N/A	4.89	0.0144	3.07
PDTC-HDA	2.92 (3.29)	3.67 (4.01)	0.0267	3.53 (3.75)
PDTC-HK511	2.69	6.09	0.0115	3.51
Thiophosgene-MDA	3.03	3.84	0.0226	3.3

The measured $\varepsilon_{\mathrm{tot}}$, E_{g}, and dielectric loss for these polythioureas are shown in **Table 4.1**; the corresponding computed values are shown in brackets for comparison. To determine $\varepsilon_{\mathrm{elec}}$ experimentally, the refractive index was measured by ellipsometry; the square of the refractive index is equivalent to $\varepsilon_{\mathrm{elec}}$, and these values have also been reported in **Table 4.1**.[118] The experimentally determined $\varepsilon_{\mathrm{elec}}$ and $\varepsilon_{\mathrm{tot}}$ are comparable to but lower than the calculated DFT values. These discrepancies are

probably due to calculations being done solely on the crystalline polymer state while experimental measurements are averages over the crystalline and amorphous regions. This is confirmed by comparison of calculated and experimental IR and XRD spectra of both fiber precipitates and solution cast films. While the IR spectra for the synthesized samples and the predicted structures are in close agreement, the XRD patterns of the synthesized fibers were in closer agreement with the XRD spectra of the predicted structures, indicating the larger crystalline content of these samples while the films are generally amorphous. TDDS results for one of these polythioureas, namely PDTC-HDA (the polymer made from 1,4-diisothiocyanatobenzene and hexane-1,6-diamine), are shown in **Figure 4.1A** (this polymer is shown at the top of **Figure 1.10**). While the dielectric constant is shown to increase with operational temperature due to the chains becoming more mobile and thus enhancing dipole alignment, this effect is diminished at high frequencies, as the dipoles are unable to align as quickly.

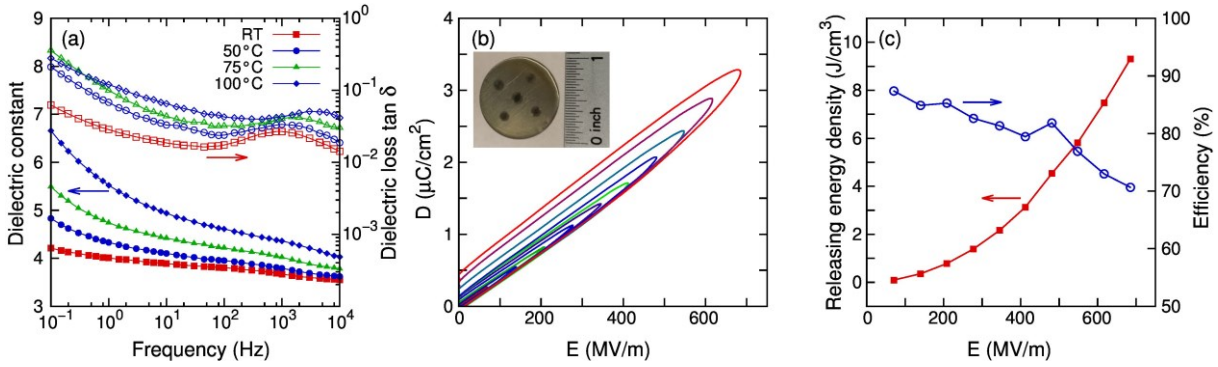

Figure 4.1. "(a) Dielectric constant and dielectric loss $tan\,\delta$ measured at room temperature (RT), 50 °C, 75 °C, and 100 °C, (b) D-E loops, and (c) the releasing energy density and efficiency of PDTC-HDA. A film of PDTC-HDA is also shown in (b) as an inset." Reproduced with permission from[69], Copyright (2014) American Chemical Society.

While the band gap provides a good theoretical substitute for the dielectric breakdown field strength since a higher band gap would imply a higher threshold for impact ionization, access to the breakdown field is possible through either direct breakdown measurements, or electric displacement – electric field (D-E) loop measurements. The latter measurements also provide a pathway to assess linearity and energy recovery and to obtain energy density estimates. Such D-E measurements were done for PDTC-HDA, and this is shown in **Figure 4.1B**. The recoverable energy density as a function of the applied electric field is shown in **Figure 4.1B**. The ability to operate at high electric fields would lead to a significant increase in energy density. For PDTC-HDA, a high energy density of 9.3 J/cm^3 was achieved at a maximum applied field of 685 MV/m, which is a substantial energy density improvement over BOPP (almost double its value).[74] The maximum energy density is expected to further improve with better processing conditions to remove contaminants such as dust impurities and residual solvent as this will lead to higher values of the breakdown field. An important point worth noting is that although the initial computational screening was based just on the dielectric constant and band gap, the directions identified, in terms of materials subclasses to pursue, have led to polymers with acceptable dielectric loss and high breakdown field (and hence, energy density).

PDTC-HK511 showed the highest dielectric constant of 6.09 with a loss of around 1% and a band gap of 3.5 eV setting it apart as a promising material for high-k dielectrics. Of interest was the high polarizability of the polymer to allow it to achieve such high dielectric constants and more in-depth testing was carried out on

PDTC-HK511. The hope of this work was to understand further the underlying mechanism that leads to HK511 giving such high polarizability and then transferring that knowledge to other systems with potentially greater dielectric constants and better overall properties.

4.2 Synthesis and Processing of PDTC-HK511

Para-phenylene diisothiocyanate (PDTC), N-methyl-2-pyrrolidone (NMP), methanol, and dimethylacetamide (DMAc) were used as received from Acros Organics while Jeffamine HK511 was used as received from Huntsman. The reaction scheme and structure of PDTC-HK511 is shown visually in **Scheme 4.1** below. To a dry 50 ml three neck flask, 20 ml of NMP, was first added followed by 1.10 g (5 mmol) of HK511 and stirred under a blanket of nitrogen followed by the addition of 0.961 g (5 mmol) of PDTC. Reactions were carried out at ambient temperature about 20 °C and stirred for 6 hours. The reaction mixture was then precipitated in methanol and washed several times. A yellow-white fiber precipitate was recovered and dried in a vacuum oven at 50 °C for 12 hours.

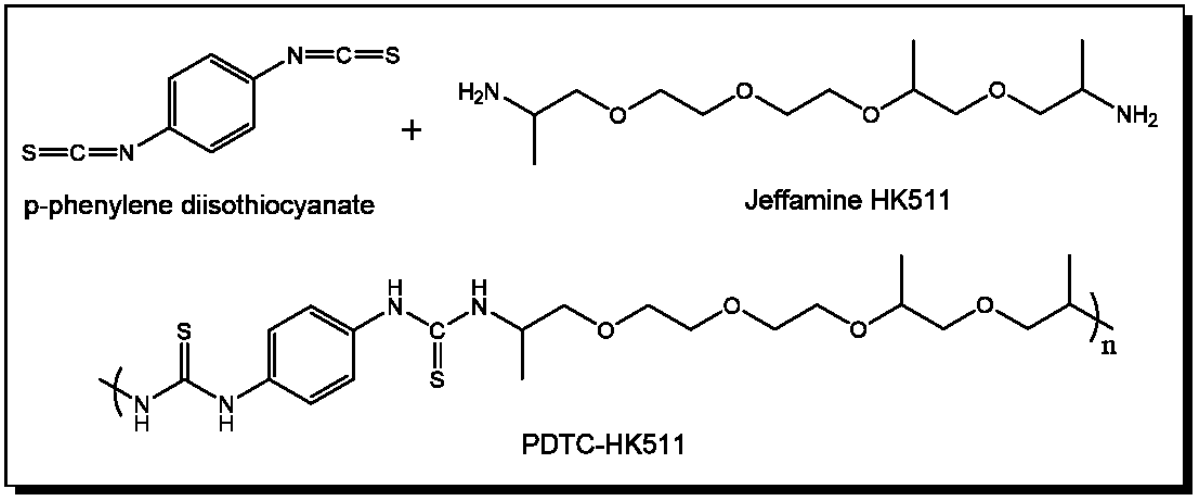

Scheme 4.1 Chemical reaction scheme for PDTC-HK511

4.2.1 Processing of PDTC-HK511

To prepare the polymer to cast, PDTC-HK511 was dissolved in DMAc to form a 10% wt/wt solution which was then filtered through a 0.45 μm PTFE syringe filter. Films were made by two methods: (1) drop cast onto stainless steel shim stocks and (2) free standing films made from film coater on a glass substrate. For method (1) stainless steel shim stocks were purchased from McMaster Carr, placed on a controlled heating plate, and drop cast at 70 °C. The temperature was then raised to 80 °C and allowed to dry for 6 hours before being dried in a vacuum oven at room temperature and then 100 °C for 12 hours. For method (2), a film was cast on a borosilicate glass plate with an Erichsen CoatMaster Film Applicator using a 500 μm blade gap traveling at 10 mm/s at 70 °C. The temperature was then raised to 80 °C and allowed to dry for 6 hours before being dried in a vacuum oven at 100 °C for 12 hours. The freestanding films were then removed from the glass plate and placed in

a PTFE frame and put back in the vacuum oven where they were able to dry for several more hours to remove the remaining solvent. **Figure 4.2** shows a film of polythiourea after it has been removed from the glass substrate measuring roughly 6 inches by 6 inches.

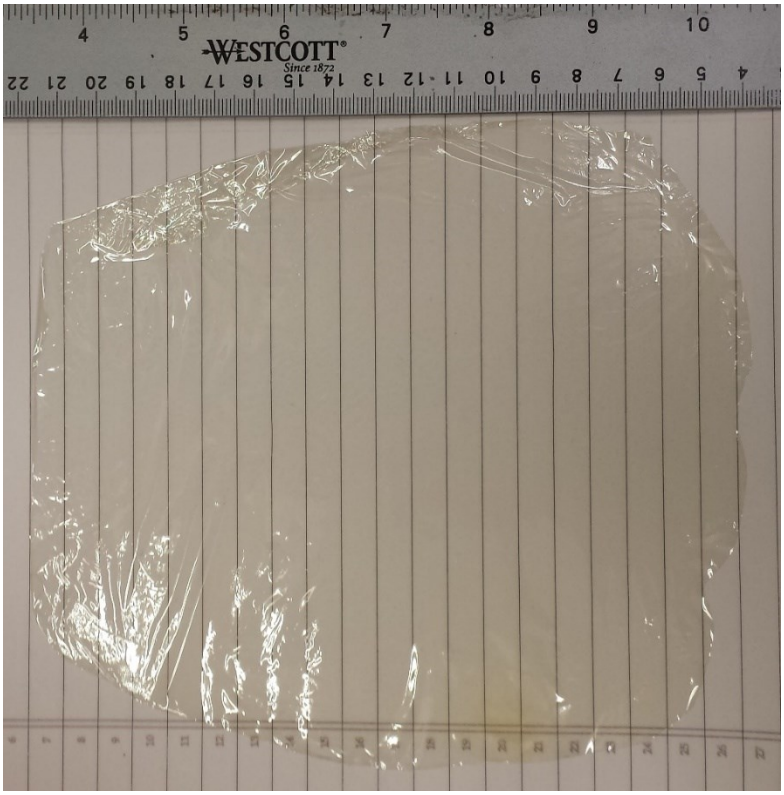

Figure 4.2. Blade cast film of polythiourea after removal from glass substrate

4.3 Structural Characterization

4.3.1 Fourier Transform Infrared Spectroscopy on PDTC-HK511

To verify that the proposed structure was formed during synthesis, Fourier transform infrared (FTIR) spectroscopy was used to verify the structure of the polythiourea produced by transmission mode on thin films of PDTC-HK511. The spectra are shown in **Figure 4.3** below plotted in absorbance verse wavenumber (cm^{-1}). The amide N-H stretching frequency is found at 3230 $cm^{-1,}$ and C-N stretch found at 1310 cm^{-1}. The aromatic peaks are seen at 3040 cm^{-1} for C-H stretching and 1510 cm^{-1} for the C-C frequencies. The thiocarbonyl C=S stretching frequency is seen at 1230 cm^{-1} while the ether stretches C-O-C are found at 1103 cm^{-1} and 1038 cm^{-1}.

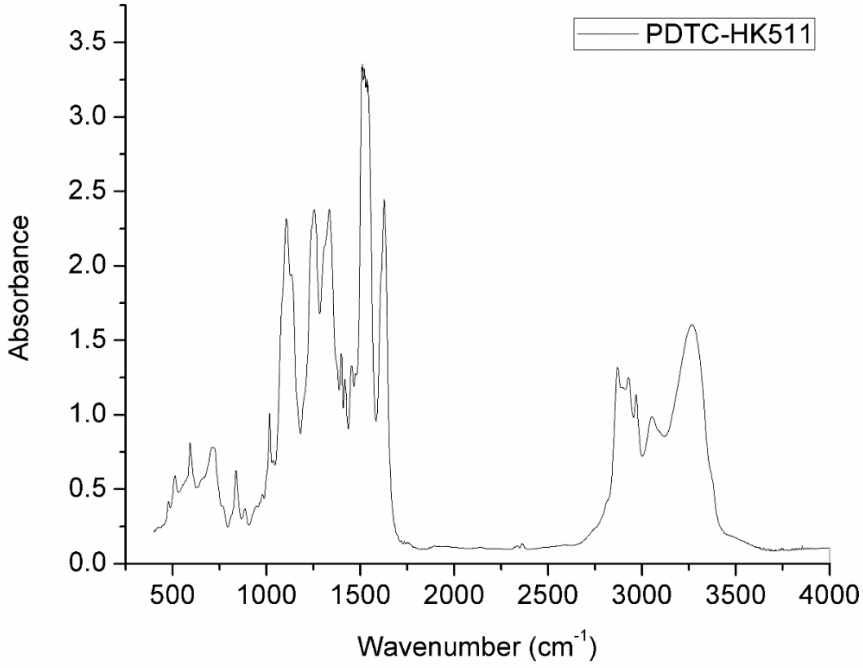

Figure 4.3. FTIR spectra of PDTC-HK511 in transmission mode.

4.3.2 Nuclear Magnetic Resonance on PDTC-HK511

The nuclear magnetic resonance (NMR) spectrum was taken on a Bruker DMX 500 MHz NMR spectrometer, and the signal was analyzed and plotted in **Figure 4.4** below. The ^{1}H NMR was taken in DMSO-d^{6} with 256 scans to give sufficient resolution. All the peaks were labeled alphabetically and correspond to the same letter on the structure of PDTC-HK511 superimposed over the spectra. The peak from 1.06 to 1.13 ppm were assigned to the methyl groups (h) and integrate to 7 protons. The peak at 2.5 ppm was taken as a reference, being residual non-deuterated DMSO in the solution. The peak at 3.52 to 3.56 ppm was assigned to the methylene groups (f,g) and integrated to 12 protons. The peak at 4.49 was assigned to the CH group (d,e) which integrated to 2 protons. The peaks at 7.36 were assigned to the aromatic ring (a) and integrated to 4 protons. The peak at 7.52 was assigned an N-H (c) while 9.44 was assigned the other N-H (b) with each integrating to 2 protons. By observing the amine chain end at 1.27 and integrating that to 0.0641 with 2 protons the number averaged molecular weight was calculated to be 25,975 g/mol. While this molecular weight is a little lower than for other polymers synthesized in this thesis, it proved to be high enough for chain entanglements to produce a free-standing film. The low molecular weight of the final polymer could be caused by the ill-defined structure of the diamine which is a blend of several similar small molecules. Due to this complication, the stoichiometry of the reaction may not have been as close to 1:1 as would be preferred, resulting in a lower polymer molecular weight. While several experimental methods were attempted to increase the molecular weight including

fractionating and titrating the diamine the molecular weight was never able to be substantially increased and only by using a better-defined diamine, such as EDR148 studied in **Chapter 3**, could the molecular weight be increased to about 100,000 g/mol.

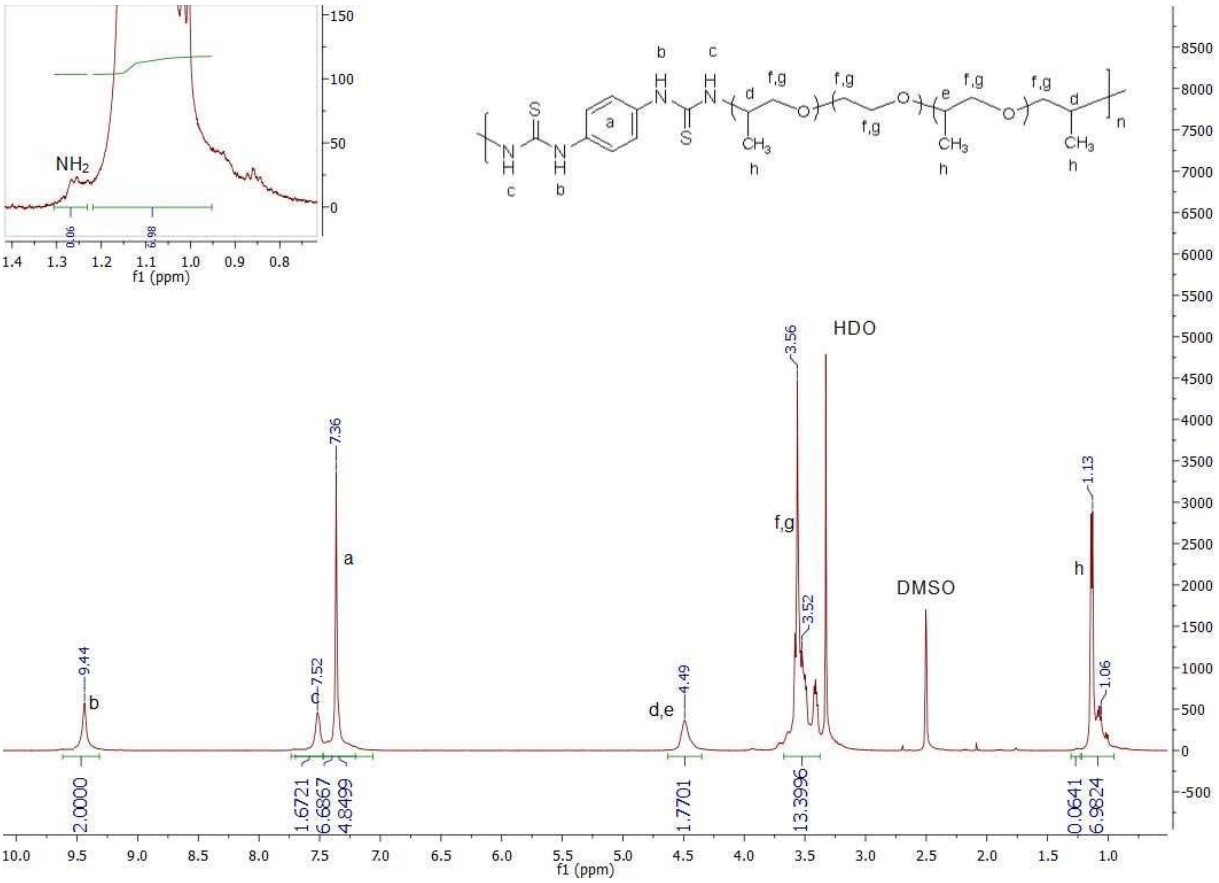

Figure 4.4. NMR spectra and peak assignments for PDTC-HK511 in DMSO-d6

4.3.3 Gel Permeation Chromatography on PDTC-HK511

Gel permeation chromatography (GPC) was run on PDTC-HK511 receive a weight averaged molecular weight (Mw) to compare with the number averaged

molecular weight (Mn) determined by NMR. PDTC-HK511 was used as synthesized in the DMAc solvent which was compatible with the GPC system. Since the polymer was synthesized at a 10% concentration, a small solution was diluted 100x to give a final concentration of 0.1% for the refractive index detector on the DMAc GPC system. The solution was then filtered and placed in a 4 ml sample vial to be run in the GPC auto sampler at a flow rate of 1 ml/min. The Mw was determined to be 48,720 g/mol against a monodisperse PMMA standard and showed a PDI of 1.66 equates to a Mn of 26,830 g/mol.

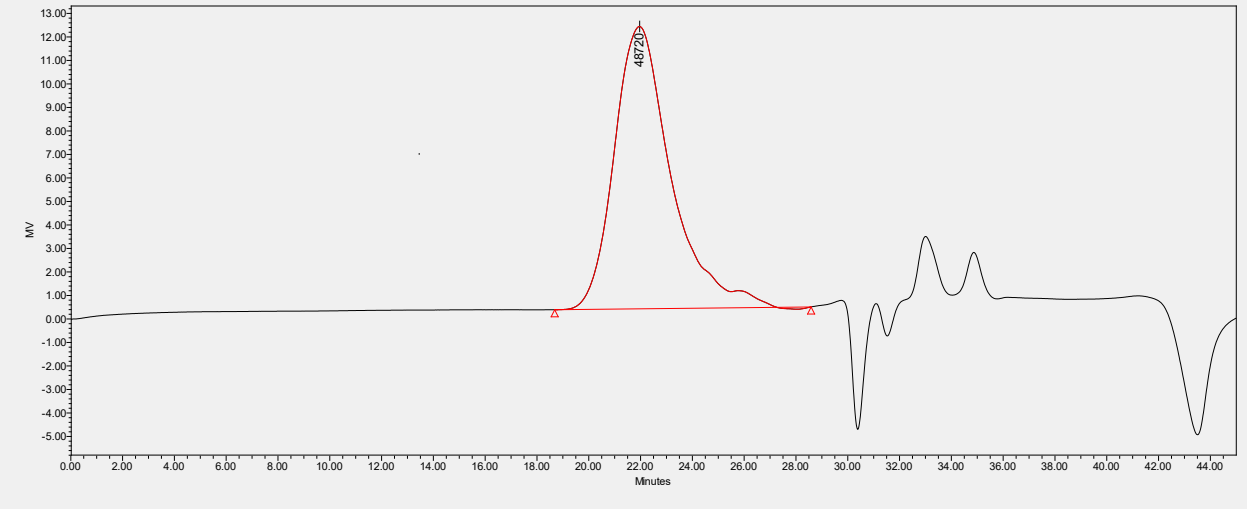

Figure 4.5. GPC trace of PDTC-HK511 in DMAc.

4.3.4 Band Gap Determination by UV-Visible Spectroscopy

The band gap for PDTC-HK511 was determined optically by scanning the UV-Vis spectrum from 800 nm down to 200 nm and observing the onset of UV absorption. Through the Maxwell equation, the optical band gap can be found from taking $1240/\lambda_{onset}$. The UV-Vis spectrum is plotted in **Figure 4.6** with the onset overlaid

graphically. The onset is 353 nm correlating to a band gap of 3.51 eV which is above the threshold of 3 eV initially set up as a screening criterion for high breakdown materials. PDTC-HK511 was predicted by DFT to have a higher band gap of 4.89 eV which would have made it an even more promising candidate for an insulator, however, as previously noted in **Chapter 3**, DFT has shown to over predict the band gaps in the past and this result is not unexpected.

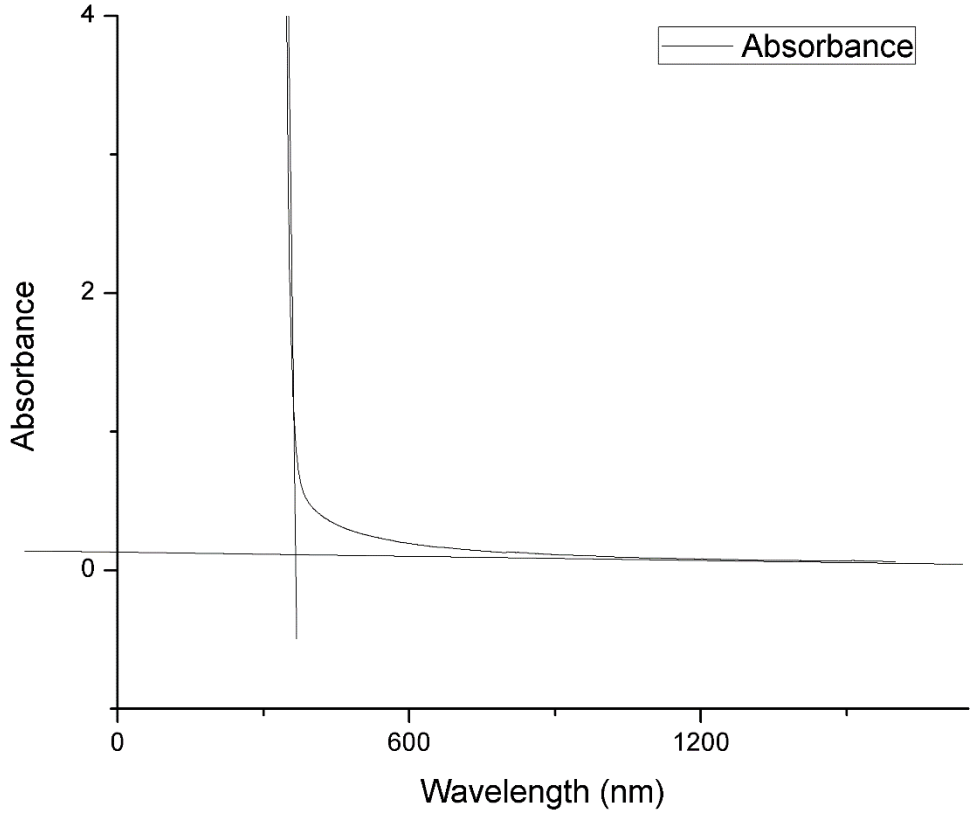

Figure 4.6. PDTC-HK511 UV/Vis spectrum used to determine band gap.

4.4 Thermal Characterization: TGA and DSC

Thermal Gravimetric analysis (TGA) and differential scanning calorimetry (DSC) measurements were run on the polymer film to determine its degradation (T_d), glass transition (T_g), and melt (T_m) temperatures. PDTC-HK511 was found to degrade at 248 °C with an onset at 200 °C as shown in **Figure 4.7** and had undergone its glass transition at 92°C as shown in **Figure 4.8**. A melt transition (T_m) was also observed at 165°C and continued into the degradation of the polymer before it completely melted.

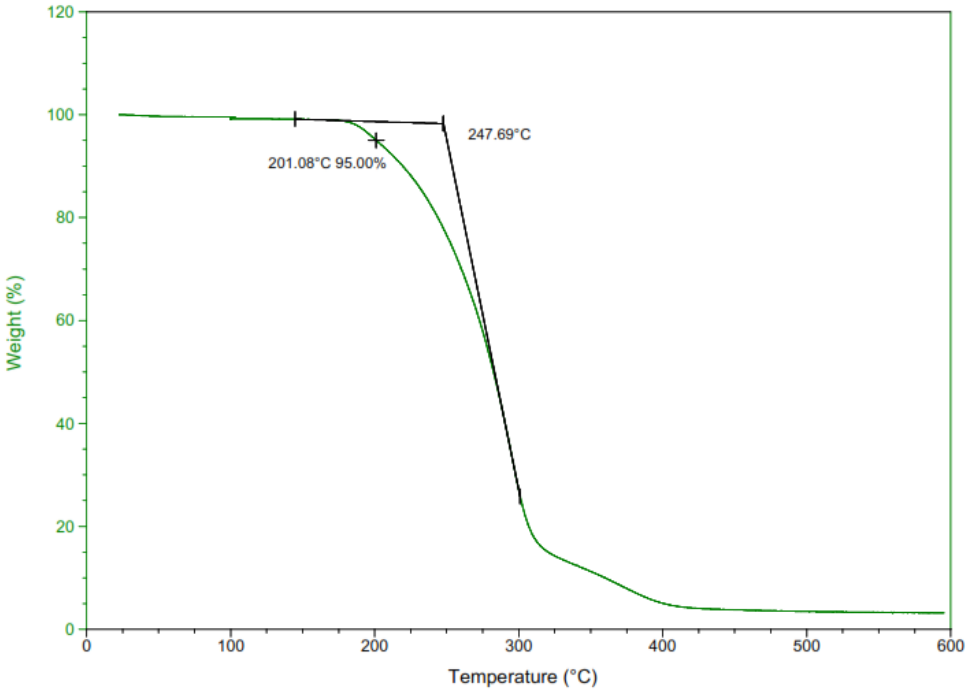

Figure 4.7. Thermal Gravimetric Analysis of PDTC-HK511 under argon.

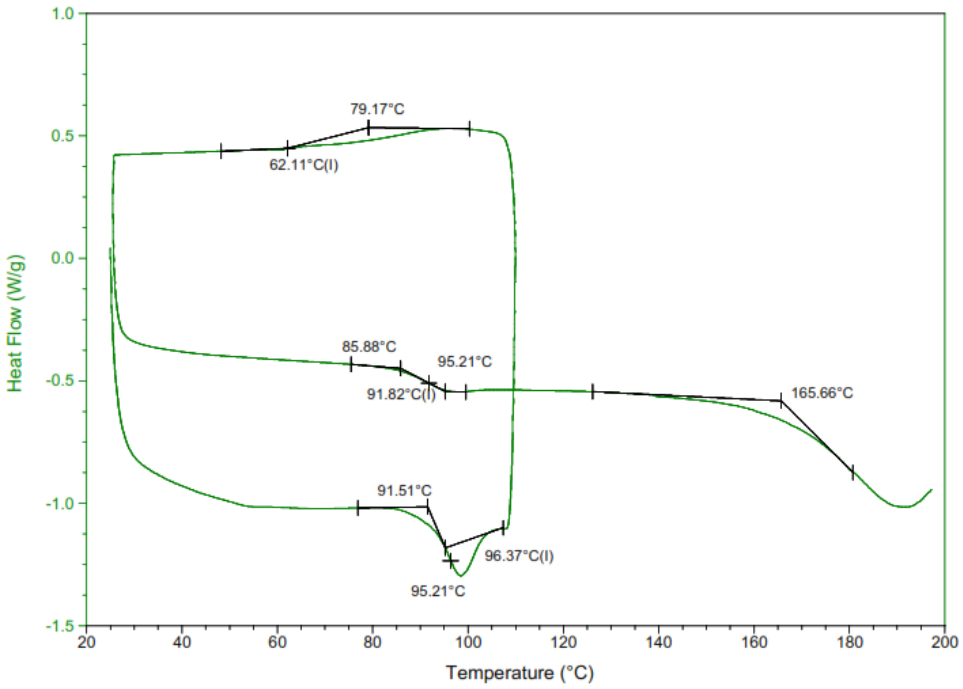

Figure 4.8. Differential Scanning Calorimetry of PDTC-HK511 under argon.

4.5 Dielectric Spectroscopy

Dielectric spectroscopy was carried out on PDTC-HK511 at both General Electric Global Research Center in Schenectady NY and at the Electrical Insulation Research Center (ERIC) at the University of Connecticut and was first detailed in a conference paper published at the 2015 Annual Report Conference on Electrical Insulation and Dielectric Phenomena.[127] The testing for this section was carried out on free standing films of PDTC-HK511 that had been carefully processed to be as uniform in thickness as possible while remaining dust and solvent free. General Electric had access to a Novocontrol dielectric spectrometer which is an industrially produced, complete system that combines a time domain dielectric spectrometer (TDDS) with a frequency domain dielectric spectrometer (LCR meter) and a

temperature controlled environment to scan from 10^{-2} Hz up until 10^{6} Hz across a temperature range of -130 °C to above 200 °C which was used to carry out the initial dielectric spectroscopy mentioned here. **Figure 4.9** shows the dielectric constant and dissipation verse temperature at 20 °C, 30 °C, and 40 °C. PDTC-HK511 was shown to have a high dielectric constant at around 5.5 and a loss about 1.2% at 1 kHz and remained fairly constant until the temperature started approaching the glass transition temperature of 92 °C at which both the dielectric constant and loss increased as is expected.

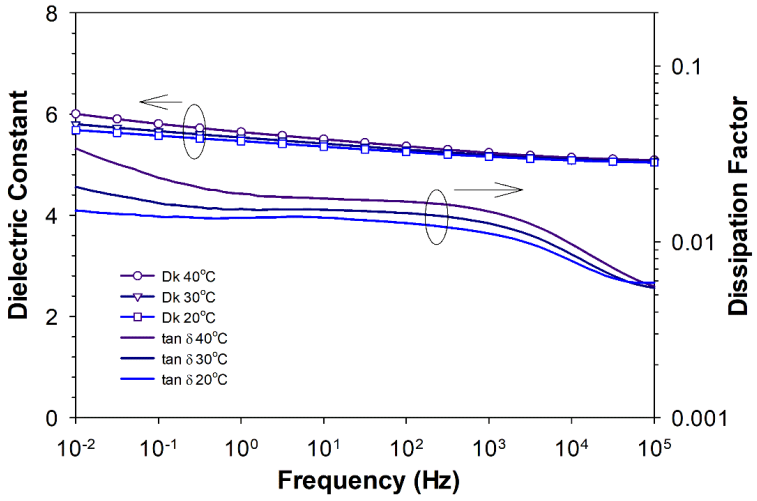

Figure 4.9. Dielectric constant and dissipation factor against frequency as measured on the Novocontrol combined TDDS and LCR meter at GE Global Research. Reproduced with permission from[127], Copyright (2015) IEEE.

The dielectric constant of PDTC-HK511 was seen to be significantly higher than previously reported polythioureas which were based on aromatic diamines compared to the ether containing diamine used in this study.[68,74,130,131] To help understand the polarization mechanism of this polythiourea that contains a rigid

aromatic section and a flexible etheramine segment, a temperature ramp was conducted during dielectric spectroscopy from -130 °C up to 70 °C in the Novocontrol over the frequencies of 0.01 Hz to 10^6 Hz. Two three-dimensional plots were generated from the data measured including a plot of dielectric constant and temperature verse frequency in **Figure 4.10A** and dissipation factor and temperature verse frequency in **Figure 4.10B**. The partial peak seen at the high end of the temperature scan which ends at 70 °C is near the onset of the glass transition as determined by DSC and shown in **Figure 4.8**. By analyzing the dielectric constant and dissipation graphs in **Figure 4.10** it became obvious that there were various sub glass transitions which were labeled in accordance with the Greek alphabet starting with the glass transition as (α), followed by the first lower temperature peak (β), and finally with the low temperature peak of (γ). Starting at the low temperature region, the lowest dielectric constant below the γ peak is seen to be 4 which is almost identical to the dielectric constant for the aromatic polythioureas previously reported.[130] These aromatic polythioureas were seen to derive most of their dielectric constant from the electronic and ionic (atomic) polarization mechanisms as detailed by first principles calculations.[68] Sub glass transition peaks have been attributed to secondary relaxations, often as localized relaxations and local fluctuations of side groups or dipole vectors within a polymer chain.[126] More advanced fluctuations could occur due to steric oscillation of ring structures and crankshaft movements in local chain segments which are not great enough to be considered a glass transition.[126]

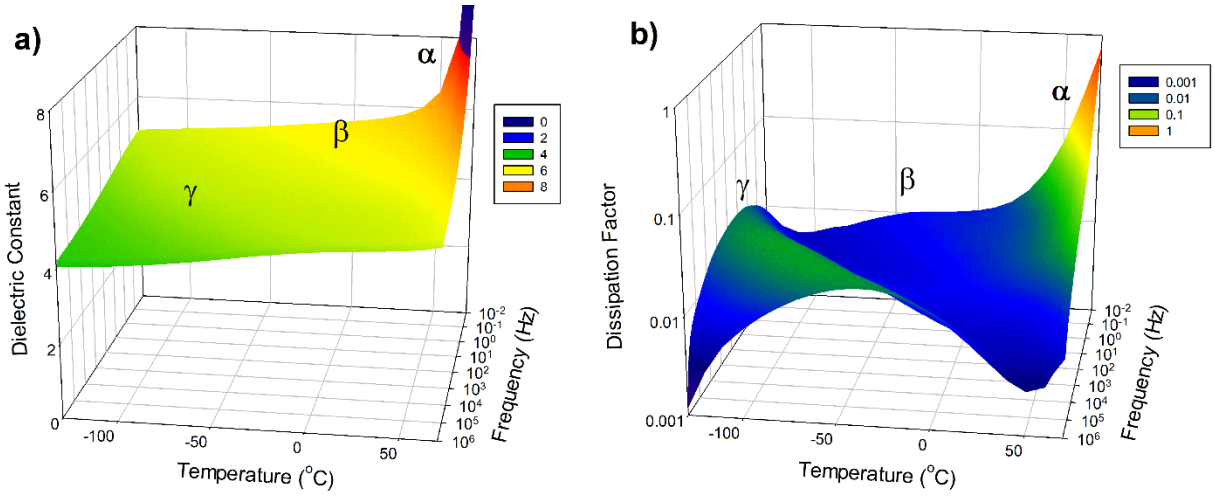

Figure 4.10. "The 3D plots of the real (a) and imagine (b) parts of the complex dielectric spectroscopy for thiourea–etheramine copolymer over a frequency range of 0.01 Hz -10^6 Hz and a temperature range from -130 °C to 70 °C." Reproduced with permission from[127], Copyright (2015) IEEE.

These secondary peaks are much broader than the glass transition peak and have been described by the Havriliak-Negami (HN) function in **Equation 4.1**

$$\boldsymbol{\varepsilon(\omega) - \varepsilon_\infty = \frac{\Delta_\varepsilon}{[1+(i\omega\tau)^\alpha]^\beta}} \quad \textbf{(4.1)}$$

where ω=2πf, Δε being the relaxation strength, α and β being the shape parameters characteristic of the width and symmetry of the loss peak respectively, ϵ_∞ being the unrelaxed optical permittivity, and τ being the relaxation time which is described by the well-known Arrhenius function in **Equation 4.2**

$$\boldsymbol{f_{max} = f_{max,\infty} e^{-\frac{E_a}{k_B T}}} \quad \textbf{(4.2)}$$

where $f_{max,\infty}$ is a dimensional parameter and E_a is the activation energy with k_B being the Boltzmann's constant.[125,126] The isothermal plots of the dielectric spectrum data

as shown in **Figure 4.11A** and **Figure 4.11B** correspond to the ß and γ transitions, respectively. Simple analysis based on the peak relaxation rates of the reciprocal frequency according to the Arrhenius in **Equation 4.2** result in activation energies of 0.45 eV and 0.14 eV for ß and γ transitions, respectively and are plotted in **Figure 4.11C**. While a comprehensive nonlinear, multi-relaxation curve fitting and peak separation as according to the HN function is still underway, the activation energies derived from this first order of accuracy relaxation mapping provide valuable insight into the polarization processes associated with these secondary polarizations.[125,132] The flexible ether linkages in the HK511 segments promote local chain movement such that the ether polar groups can follow the external electric field and contribute to the polarization through localized dipolar orientation. The activation energies for both relaxation peaks are considered to be low, particularly for the relaxation. An activation energy of only 0.14 eV indicates the ease of movement for such local dipole vectors. The high dielectric constant and relatively low dielectric loss for PDTC-HK511 are attributed largely to such secondary relaxations with low activation energies.

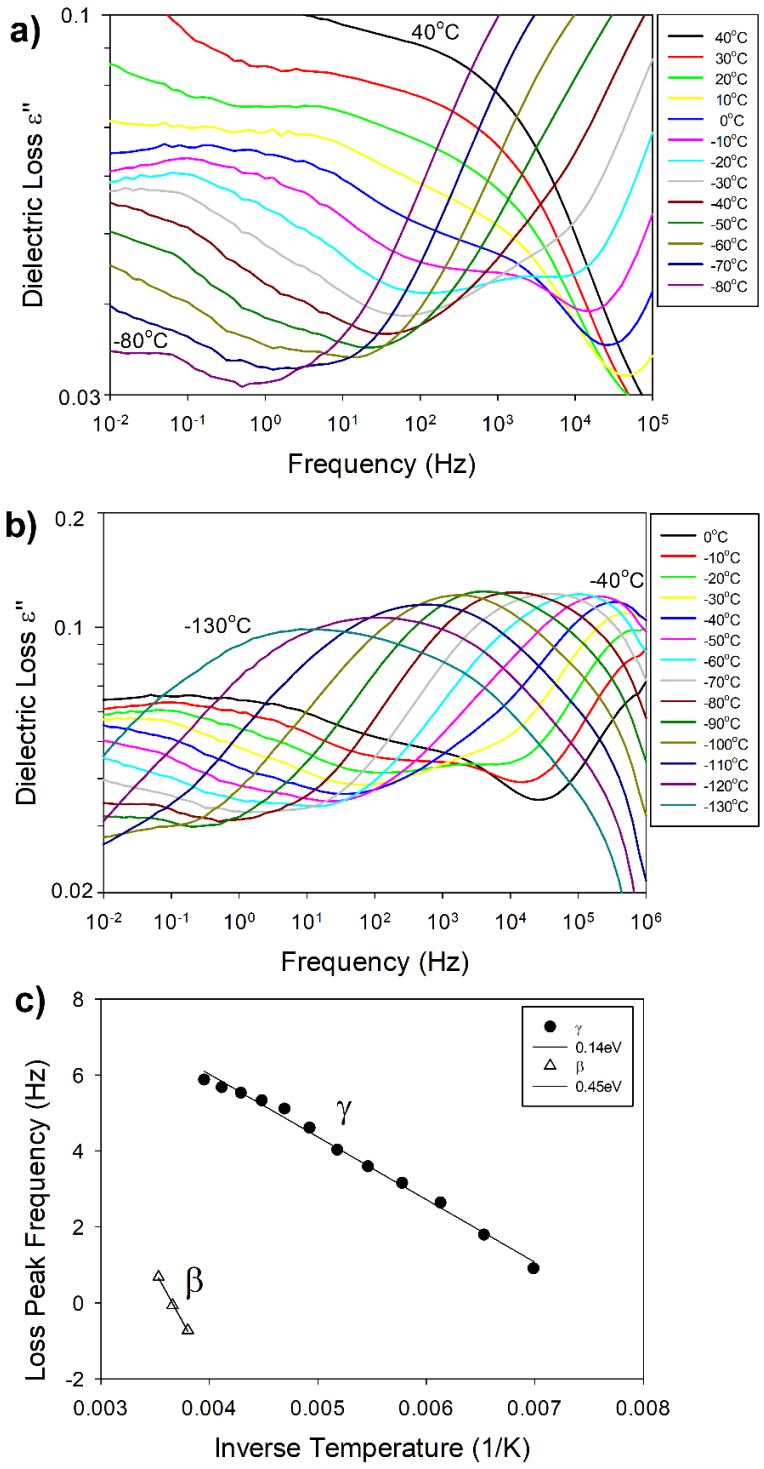

Figure 4.11. "The isothermal plots of the dielectric spectrum data showing the ß transition (a) and γ transition (b), as well as the corresponding relaxation map (c) for both ß and γ transitions as according to Arrhenius equation. Compared with the α relaxation peak, these secondary relaxation peaks are much broader and often nonsymmetrical."[127]

As outlined in **Chapter 2** and discussed for polyurea in **Chapter 3**, a low temperature system was developed at the University of Connecticut's EIRC to conduct similar measurements to the Novocontrol. JoAnne Ronzello of the EIRC lead the development of the in-house low temperature setup by attaching a liquid nitrogen tank to an oven and LCR meter while controlling the system with LabVIEW programed by Justin Delarm and Krishnan Sureshkumar. The system, outlined in Chapter 2, allowed for samples to be run from -130 °C to 150 °C over the frequency range of 20 Hz to 1 MHz. Since this setup only had an LCR meter attached it was unable to go to the lower frequencies that the Novocontrol provides. Several attempts were made to connect the TDDS to the low temperature sample oven. However, the sensitivity of the TDDS made low temperature measurements too noisy to be of any practical use. The film of PDTC-HK511 was prepared as previously mentioned for the low temperature setup and was run from -130 °C to 100 °C with a step of 10 °C and a hold time of 30 minutes at each temperature to ensure the polymer film was able to equilibrate to each temperature. 10 measurements were taken and averaged for each data point to eliminate any noise that may have been introduced into the system and the data was plotted in **Figure 4.12A** with the dissipation factor plotted in **Figure 4.12B**. The dielectric constant was seen to be about the same as previously reported with a value of 5.6 at room temperature and a dielectric loss below 2% prior to approaching the Tg of the polymer near 90 °C when the dielectric constant and loss both drastically increased as expected. Several sub-Tg relaxations were also observed similar to the case of TDI-EDR148 and are being investigated further.

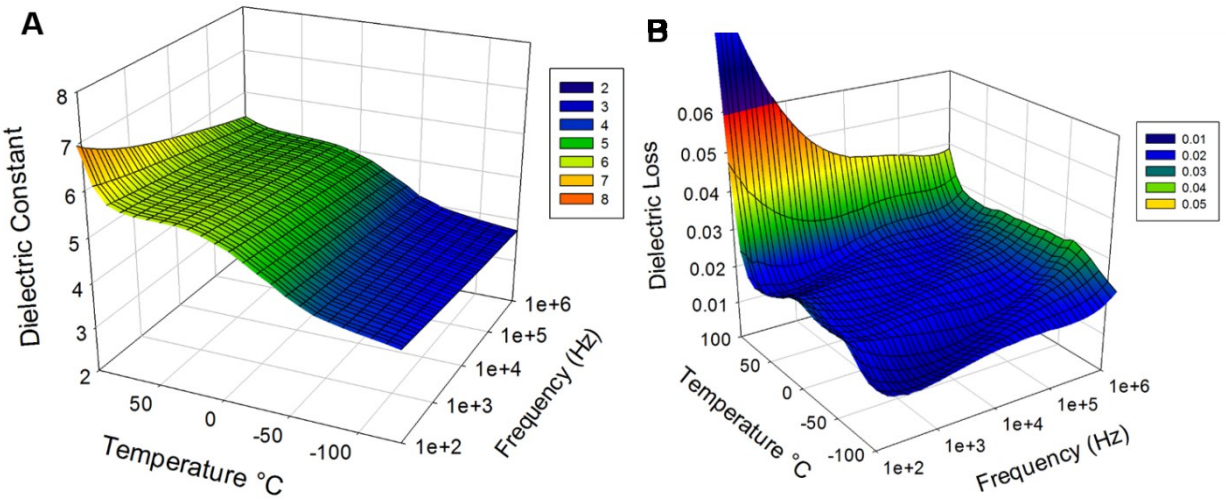

Figure 4.12. Dielectric spectroscopy (A) and Dielectric Loss (B) of PDTC-HK511 from -130 °C to 100 °C carried out on the automated LCR meter in UConn's EIRC.

A similar treatment of the data was carried out for PDTC-HK511 as had been carried out for TDI-EDR148 in **Chapter 3**. The dielectric constant at -130 °C was taken to be the experimentally determined value for $\varepsilon_{electronic} + \varepsilon_{atomic}$, which came to 3.89. It is understood, as previously mentioned, that this value is an overestimate since even at -130 °C there should still be some dipolar polarization occurring in the polymer films which is being included here. The refractive index was measured as described in **Chapter 2** to be 1.64 for PDTC-HK511, which was converted to an $\varepsilon_{electronic}$ of 2.69. Subtracting 2.69 from 3.89 gave a εatomic of 1.20, which again is really ε_{atomic} + a small contribution of $\varepsilon_{dipolar}$. By taking the room temperature dielectric constant of 5.62 and subtracting the -130 °C dielectric constant of 3.89 the $\varepsilon_{dipolar}$ is calculated to be 1.74 for PDTC-HK511.

This value makes sense in comparison to TDI-EDR148, which, had a $\varepsilon_{dipolar}$ of 1.37, and PDTC-HK511 was expected to have a higher amount of dipolar polarization due to the structure of the HK511 unit in the backbone. The tabulated results from experiments and three types of computational predictions are shown in Table **4.2**.

Table **4.2**. The breakdown of the dielectric constant into separate polarization mechanisms experimentally and by DFT, DFT-ML, and MD. For DFT values, the atomic correlates to the ionic contribution that is calculated. *The ε_{total} given for MD combines the $\varepsilon_{electronic}$ from DFT with the $\varepsilon_{dipolar}$ for MD which includes ε_{atomic}.

Type	**RI**	$\boldsymbol{\varepsilon_{electronic}}$	$\boldsymbol{\varepsilon_{atomic}}$	$\boldsymbol{\varepsilon_{dipolar}}$	$\boldsymbol{\varepsilon_{total}}$	**Band Gap**
EXP	1.64	2.69	1.20	1.73	**5.62**	3.51
DFT	1.74	3.04	0.99	N/A	4.03	4.89
DFT-ML	1.72	2.95	0.99	N/A	3.94	4.89
MD	N/A	N/A	N/A	2.72	**5.76***	N/A

In addition to the DFT computations and machine learning predictions based on the total DFT database, molecular dynamics simulations were carried out by Dr. Mayank Misra in Dr. Sanat Kumar's group at Columbia. More in-depth MD simulations are currently being run on PDTC-HK511, similar to the simulations carried out on the copolyimides in **Chapter 5** and will be reported at a later date. Molecular dynamics is not able to calculate the refractive index or electronic portion of the dielectric constant and DFT/DFT-ML cannot predict the dipolar polarization as the simulations take place in a crystalline system at 0 K. Therefore, to get a total simulated value for the dielectric constant, the $\varepsilon_{electronic}$ from DFT was combined with

the $\varepsilon_{dipolar}$ from MD, which is known to also include the ε_{atomic} contribution to give a value of 5.76, which is extremely close to the experimentally determined value of 5.62. These results help to show that the overall approach taken in this thesis to deconvolute the contributions to the dielectric constant from the total measured dielectric constant going in the correct direction even if the approach hasn't been perfected yet. The combination of the ε_{atomic} and $\varepsilon_{dipolar}$ are very close to the values predicted by MD. However, the procedure needs to be improved to remove the remainder of the $\varepsilon_{dipolar}$ from ε_{atomic} to bring the values in line with prediction. From the simulations, it is estimated that a dielectric constant of 0.2 extra is being attributed to ε_{atomic} rather than $\varepsilon_{dipolar}$, meaning that the contribution from the dipolar polarization is actually larger than shown. It is my belief that a better understanding of the polarization mechanisms at work in dielectric polymers, through low temperature investigation and computational modeling, will enable the creation of improved materials by maximizing the ionic and dipolar polarizations to the limit where they do not negatively impact the dielectric loss.

4.6 High Field Characterization

4.6.1 DC Breakdown Analysis

Failure analysis was carried out on 30 samples to determine the DC engineering breakdown field of PDTC-HK511. The process is described in detail in **Section 2.3.6**. Measurements were carried out in silicone oil on sample areas 3 mm in diameter and analyzed using the Weibull distribution function, F(x) as shown in

Equation 2.4. Film quality including surface roughness and impurities are known to reduce the measured breakdown and is taken into account with a Weibull analysis. Ideally, a Weibull distribution will have all the tested points failing at the same value, in this case, the breakdown field. However, impurities such as dust, small molecules like solvent, local crystallization, and other phenomena exist to cause early breakdown. By taking a large distribution of data points across several samples, these variations could hopefully be averaged out, and a likely breakdown field for a given sample could be determined within acceptable limits, in this case, 63.2% probability. For PDTC-HK511, the characteristic 63.2% probability breakdown field was found to be 603 MV/m over 30 measurements as shown in **Figure 4.12**. To get the maximum potential energy density of PDTC-HK511, the engineering DC breakdown strength and the dielectric constant determined by TDDS was used to get a maximum energy density of 9.82 J/cc at breakdown. These results give nearly double the maximum energy density of the commercial dielectric capacitor film, BOPP and show that PDTC-HK511 could be a promising candidate for dielectric films in pulse powered applications.

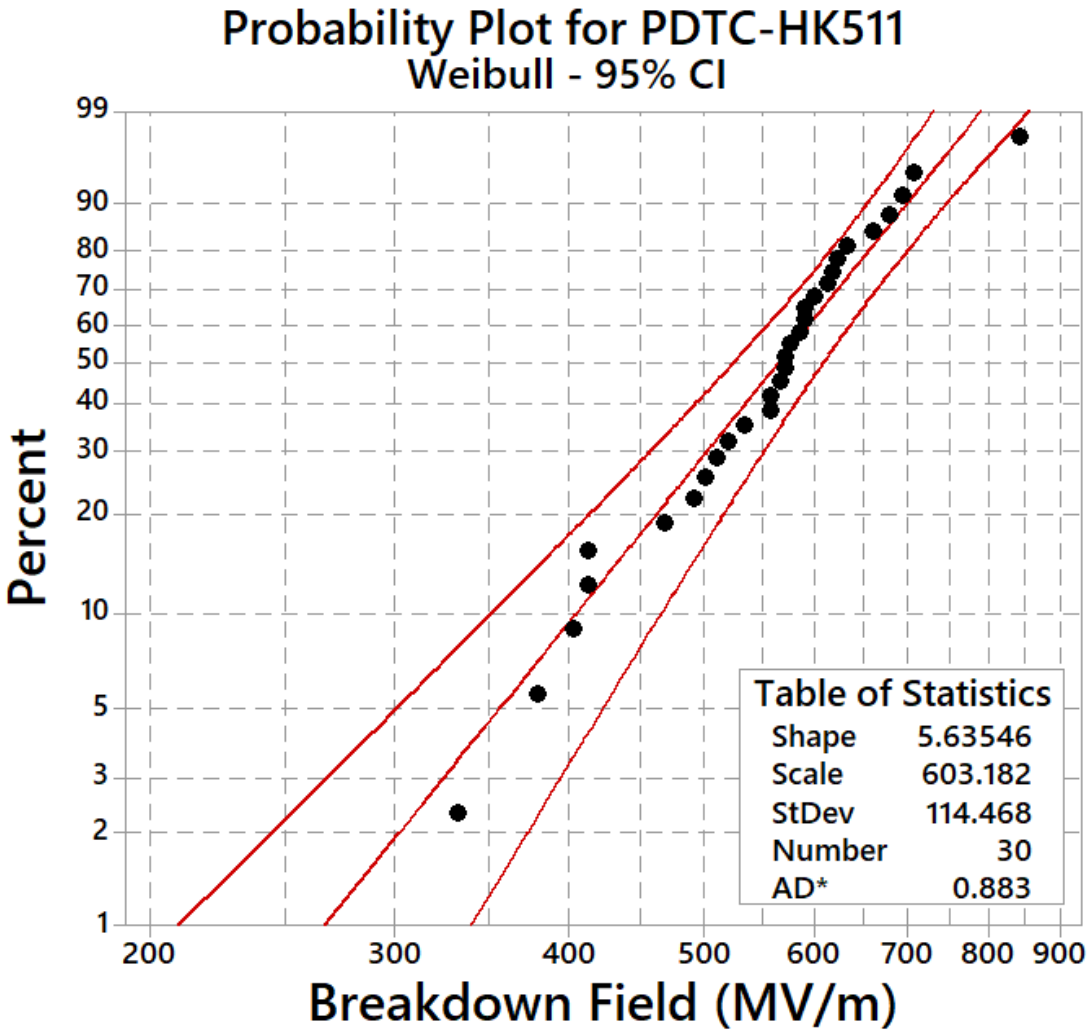

Figure 4.12. Weibull analysis of the DC breakdown for PDTC-HK511[127]

4.6.2. AC D-E Hysteresis Loop

To study the AC the high field polarization behavior of PDTC-HK511, a modified Sawyer-Tower polarization loop tester was used to characterize the polymer film as described in **Section 2.3.7** using metalized electrodes with a diameter of 3 mm in a ball to plane setup. As shown in **Figure 5.13**, a linear polarization behavior is observed for PDTC-HK511 with a breakdown strength higher than 530 MV/m. The

exact breakdown strength is unknown by this method as the large step size means the sample could have endured a slightly higher field. The slope of the D/E loop indicates a dielectric constant of about 5.7, which agrees very well with the low field broadband dielectric spectrum data. The sample actually demonstrated a high breakdown strength of about 600 MV/m prior to failure. However, that final loop exhibited a much higher loss. The area enclosed within the D/E loops (hysteresis) corresponds to the total loss during this high field polarization test, which is the summation of dipolar loss with the conduction loss under high electrical field. Such high field conduction loss may be associated with the residual solvents, chemical residues, and reaction by-products, as well as other impurities and thin film imperfections. With improvements to the reaction chemistry and thin film fabrication processing, it is expected that such conduction loss can be significantly reduced. As shown in the insert of **Figure 4.13**, the discharge efficiency is obtained by computing the ratio of released energy to the total stored energy density. By integrating the D/E curve, the released energy density is 7 J/cc at 525 MV/m with an efficiency of 88%. The discharge efficiency will improve along with the reduction of conduction loss.

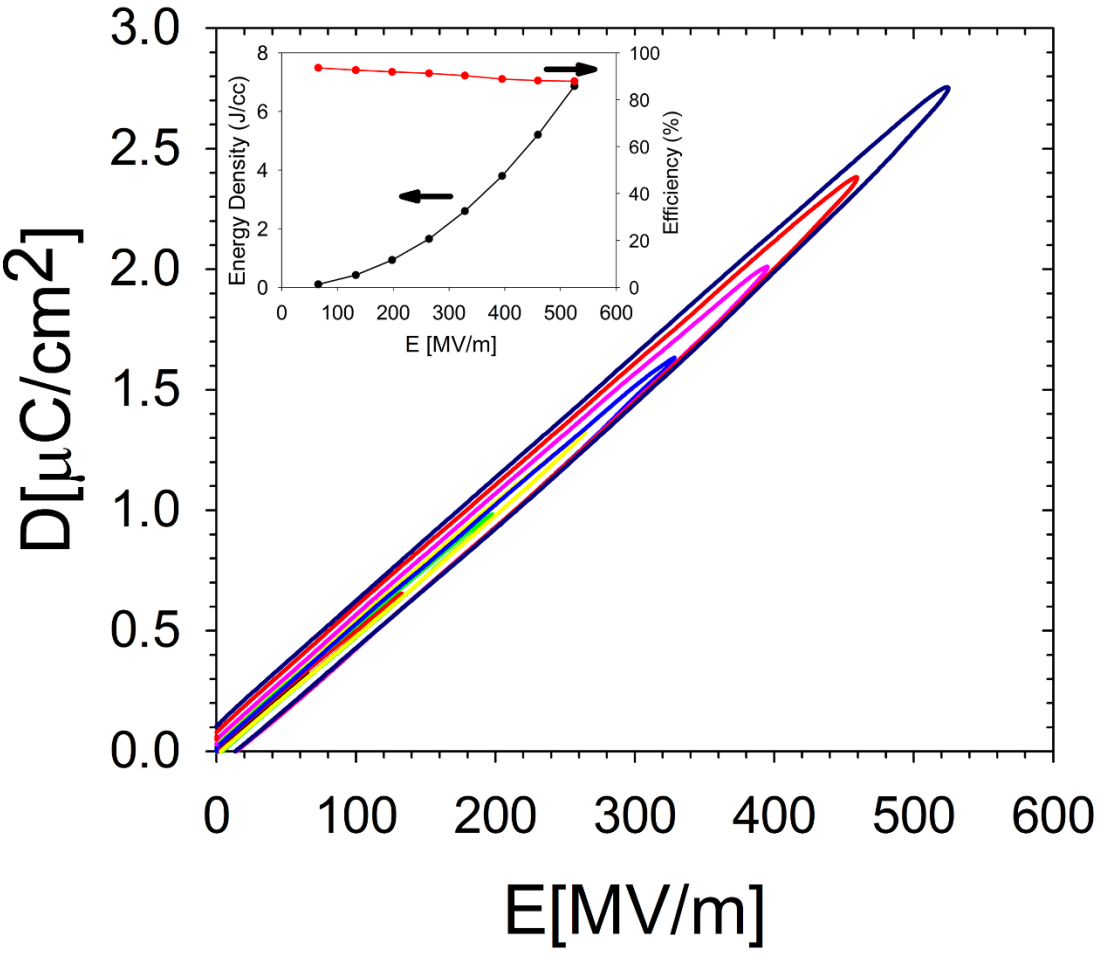

Figure 4.13. D/E loop for thiourea–etheramine copolymer tested at 100 Hz and the corresponding energy density and discharge efficiency in the insert. The breakdown strength of the sample is ~600 MV/m and the slope of the D/E loop indicates a dielectric constant of 5.7 which agrees very well with the low field broadband dielectric spectrum measurement. The released energy density is as high as 7 J/cc at 500 MV/m. Reproduced with permission from[127], Copyright (2015) IEEE.

Chapter 5

5. Synthesis, Characterization, and Modeling of Copolyimides for Dielectric Applications

5.1 Polyimides and their Copolymers as Dielectric Materials

Polyimides have traditionally been used in high temperature applications and as low K dielectric materials for electronic packaging but have not been heavily investigated for their use as high K dielectrics for pulsed powered applications. The initial screening of polymer classes yielded the imide structure as a favorable repeat unit to achieve both high dielectric constant and a high band gap.[68] Rui Ma, et al., carried out a systematic study by looking at four dianhydrides and 4 diamines to produce 10 polymers which could be processed into free standing films for electrical characterization.[69] The preliminary studies on polyimides were detailed in my Advanced Materials Progress Report and reproduced in the introduction here.[56]

Polyimides are attractive for dielectric applications due to their high thermal stability, which allows them to have a higher operational temperature than traditional polymers such as BOPP. Inspired by the identification of polyimides as an attractive subclass in the initial computation-based screening, Ma *et al.*[69] synthesized ten polyimides by choosing four different rigid aromatic dianhydrides, namely Pyromellitic dianhydride (PMDA), 3,3',4,4'-Benzophenone tetracarboxylic dianhydride (BTDA), 4,4'-Oxydiphthalic anhydride (OPDA) and 4,4'-

Hexafluoroisopropylidene phthalic anhydride (6FDA), along with two flexible diamines with aliphatic chains of different lengths, propane-1,3-diamine (DAP) and hexane-1,6-diamine (HDA). Also chosen were two different ethers containing Jeffamines (D230 and HK511), based on previous positive results. In this fashion, 10 polyimides were studied, some of which are shown in **Figure 1.10.** The measured band gap, dielectric constant and dielectric loss of these polymers are shown in **Figure 5.1**

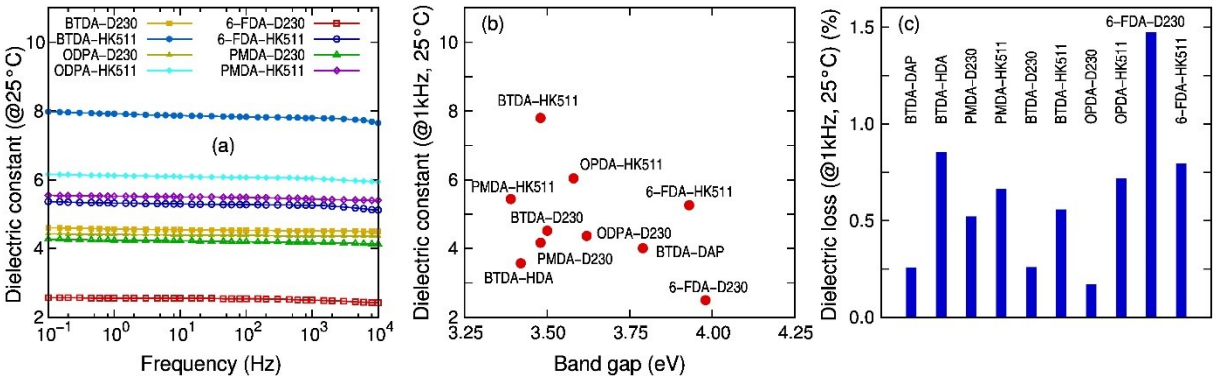

Figure 5.1. (a) The dielectric constant measured for all the polyimides at room temperature (25 °C) given as a function of frequency, (b) dielectric constants measured at 1 kHz plotted against the band gaps, and (c) dielectric losses measured at 1 kHz. Reproduced with permission from[69], Copyright (2015) American Chemical Society.

The dipolar polarizability of the imide functional group leads to all the polyimides having higher dielectric constants than BOPP. It can be seen from **Figure 5.1** that the polyimide BTDA-HK511 showed the highest ε_{tot} of 7.8, which is in large part due to orientational polarization imparted by the polyether section. BTDA-HK511 was also seen to have one of the lowest dielectric loss values of all the

polyimides shown in **Figure 5.1**C, around 0.5%, while being able to operate at temperatures up to 75 °C. Large scale free standing films could be made out of this polymer (as shown in **Figure 5.2A**). Results of TDDS measurements performed at increasing temperatures on BTDA-HK511 are plotted in **Figure 5.2B**, and a Weibull plot of the breakdown measurements for BTDA-HK511 is shown in **Figure 5.2C**. It was concluded that while the dielectric constant decreases with frequency due to slower orientation of the dipoles with alternating electric fields, dielectric loss increases because of chain relaxations. The Weibull analysis was used to determine a characteristic breakdown field of 676 MV/m, as shown in **Figure 5.2**C. For a straight comparison, the same exercise was performed for the polyimide that formed the best films, namely, BTDA-HDA, which displayed the highest breakdown field (among all polyimides considered here) of 812 MV/m, although with a modest dielectric constant of less than 4. The respectable breakdown field of BTDA-HK511 along with its high dielectric constant of 7.8 corresponds to a potential energy density of 15.77 J/cm^3. This is nearly three times that of BOPP. The co-design approach has thus lead to a number of polymer dielectrics that could potentially surpass BOPP in actual applications.

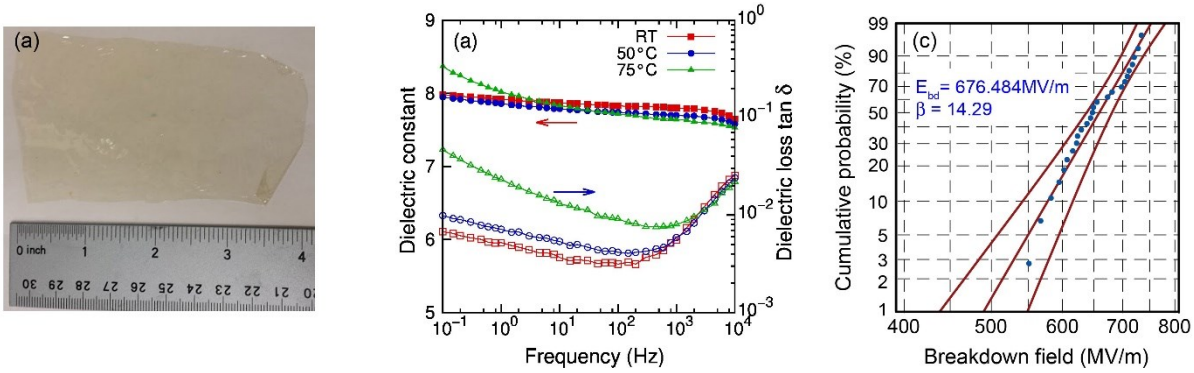

Figure 5.2. (a) A solvent casted free-standing film of BTDA-HK511 with a thickness of 12 microns, (b) the dielectric constant and loss at the room temperature (RT), 50°C, and 75°C, (c) Weibull plot of dielectric breakdown, with the characteristic breakdown field and the slope parameter indicated. Reproduced with permission from[69], Copyright (2015) American Chemical Society.

The two most promising polymers, BTDA-HDA and BTDA-HK511 were further studied to try and optimize their properties. The flexible ether containing HK511 segment is able to impart dipolar polarization when an electric field is applied to increase the dielectric constant (K) higher than the typically K of about 4 found in most polyimides. The penalty for this large polarization potential is a reduced glass transition (Tg) temperature and subsequently a lowered operational temperature for a finished capacitor. The loss in polymer dielectrics greatly increases above the Tg as the rubbery state allows for heightened chain mobility and slower relaxations. To further investigate how the role of HK511 and dipolar polarization on the high energy density, HDA was incorporated into the polyimide. Since HDA is aliphatic in nature it does not impart any dipolar polarization beyond the two nitrogen atoms used in the imide bond. BTDA-HDA, having been previously studied, was shown to have a K of 3.5 and a breakdown strength of 812 MV/m as determines by Weibull analysis on 25

samples resulting in an energy density of ca. 10 J/cc. Copolyimides of the dianhydride BTDA and the two diamines, HDA and Jeffamine HK511, were made in an attempt to balance the dielectric constant and breakdown strength to maintain high energy densities > 10 J/cc with throughout all three copolymer compositions.

5.2 Synthesis and Processing of Polyimide Copolymers

5.2.1 Synthesis of Polyimide Copolymers

Synthesis of the polyimide copolymers was changed from the method previously reported by Rui Ma in order to improve processability. In this work, the monomers were first reacted to form the polyamic acid, cast as a film, and then finally imidized after drying as shown in **Scheme 5.1**. Three copolymers were produced in mole ratios, containing 25% HK511 and 75% HDA for (HK25), 50% HK511 and 50% HDA for (HK50), and 75% HK511 and 25% HDA for (HK75). In a round bottom flask, an equivalent amount of BTDA was dissolved in DMAc to a 10% solution by weight and stirred magnetically. In a separate flask, the molar ratio of an equivalent molar number of diamines was mixed and dissolved in DMAc to a 10% solution by weight and then slowly added dropwise to the reaction flask while stirred. The diamines were added slowly to the dianhydride to account for any differences in reactivity between the primary amine of the HDA and the secondary amine of the HK511 to try and ensure as random of a copolymer as possible was formed. The reaction was then left to stir for 24 hours at 40 °C to ensure complete polyamic acid formation.

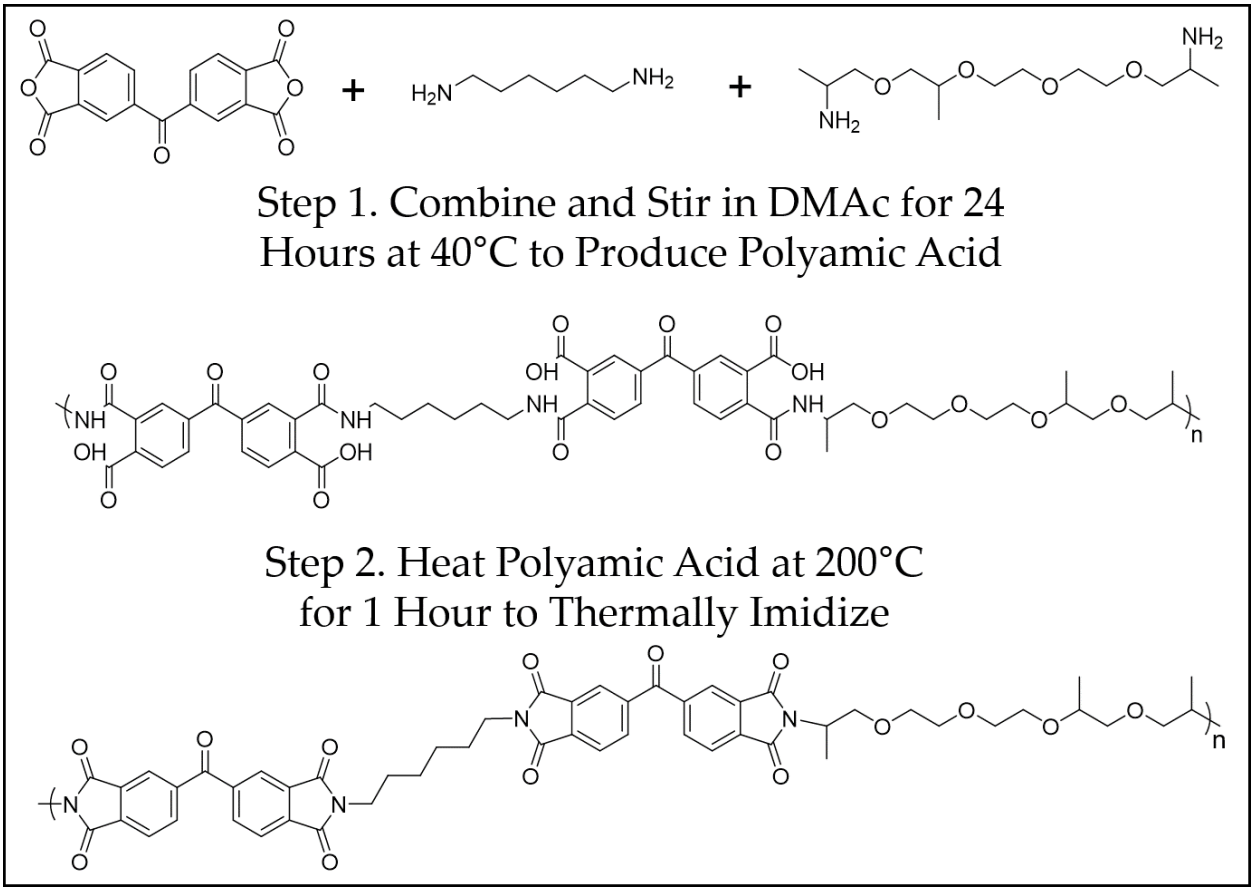

Scheme 5.1 Reaction of PAA to Polyimide

5.2.2 Processing of Polyimide Copolymers

The polyamic acid was processed in a similar manner to the rest of the polymers explained in detailed in **Chapter 2** and utilized in **Chapter 3** and **Chapter 4**. Numerous substrates were used to cast on including borosilicate glass, quartz microscope slides, stainless steel shim stocks, and silica wafers. For the majority of the samples, free standing films were cast from a 5% by weight solution of copolyimide in DMAc passed through a 0.45 μm syringe filter. An ideal condition was found to be using an Erichsen CoatMaster film applicator with a blade height of 380

μm traveling at 10 mm/s on a glass substrate and a drying temperature of 40 °C for 24 hours. A film roughly 6 inches by 6 inches square was produced on the glass substrate which was then dried in a vacuum oven at increasing temperatures up to 100 °C for 24 hours to ensure complete removal of the solvent. After the solvent was removed from the film, the glass plate was placed in a furnace at 100 °C and increased 50 °C every hour until 250 °C where the film remained for 1 hour to ensure complete imidization of the polyamic acid film. The film was then placed in a bath of distilled water for up to 48 hours to aid in removal from the glass plate with the assistance of a razor blade. The copolyimide film was then cut down to remove the edges that were not uniform, and the reduced film was then placed in a Teflon frame and dried under vacuum in an oven at 110 °C for 24 hours to ensure complete removal of water. A 4 x 4-inch free-standing film was ultimately produced that had a thickness of 10-12 μm. The film can be seen in **Figure 5.3** where it is placed next to a ruler for scale.

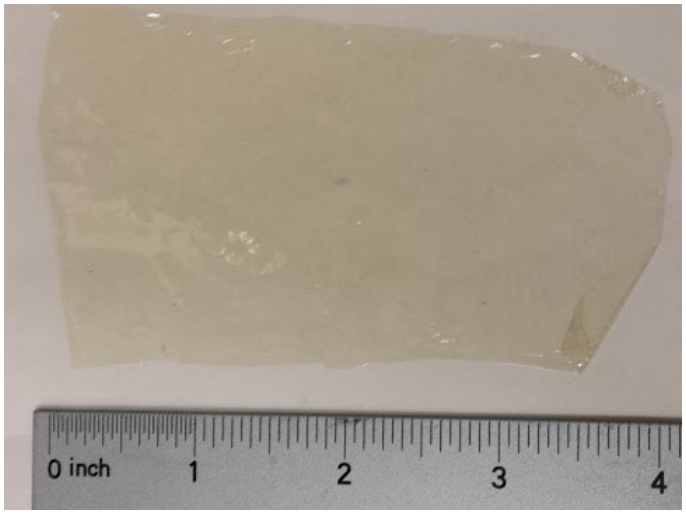

Figure 5.3. An example of a film of BTDA-HK511 cast from DMAc and thermally imidized in the solid state.

5.3 Structural Characterization

5.3.1 Fourier Transform Infrared (FTIR) Spectroscopy

Since this new technique for producing polyimides entailed first producing a polyamic acid film and then thermally imidized in an oven, FTIR was used to ensure that the imidization was carried through until completion. For this temperature optimization study, eight 1-inch by 1-inch glass slides were prepared from microscope slides and cleaned to use as a film substrate. Polyamic acid was then drop cast on each microscope slide at the same time, and they were left to dry for 24 hours at 40 °C to ensure minimal imidization took place. The glass slide labeled R.T. was then set aside and kept at room temperature while the remaining films were placed in the furnace at 50 °C for 1 hour. After an hour passed the slide labeled 50 °C was removed from the oven, and the temperature was increased to 100 °C for 1 hour. This process continued to increase the temperature by 50 °C each hour, removing the next slide as the temperature was increased until the last slide was cured at 350 °C for the final hour. After all films were removed from the furnace they were left to cool and photographed to show their visual characteristics as shown in **Figure 5.4**.

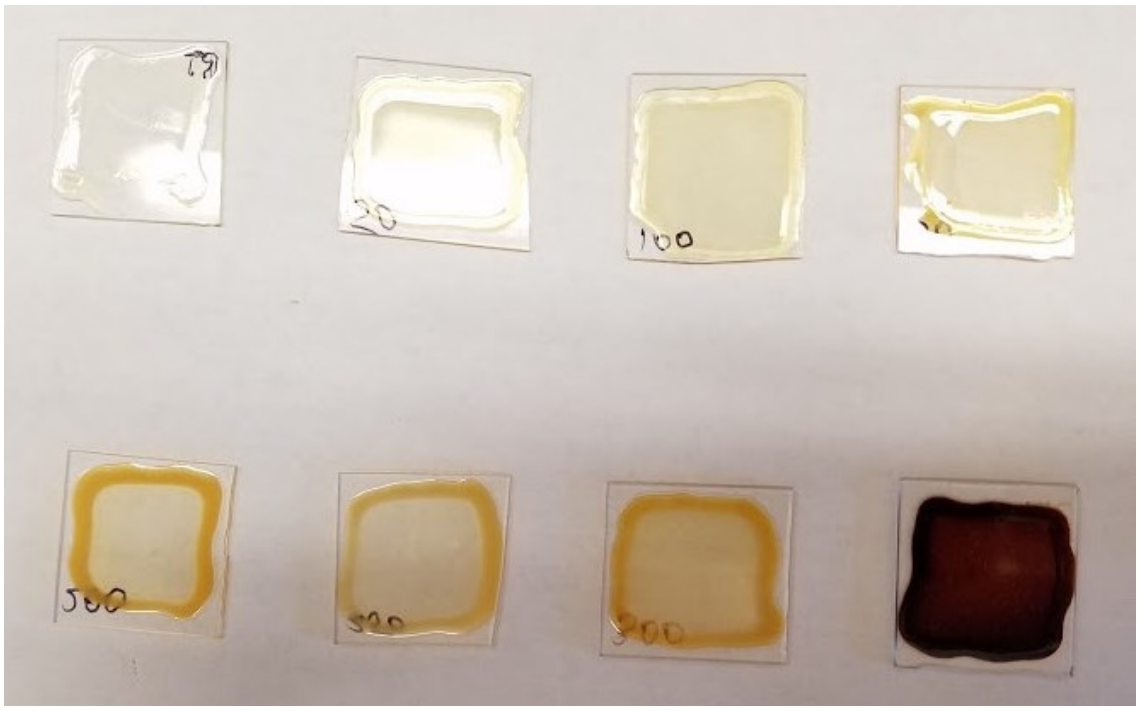

Figure 5.4. Polyamic acid films of BTDA-HDA cast on borosilicate glass and thermally cured at increasing temperatures in the furnace for imidization.

The films were then analyzed by FTIR in transmission mode with a blank glass slide used to cancel out the background, and the spectra from 1900 cm^{-1} to 1500 cm^{-1} were overlaid and analyzed as seen in **Figure 5.5.** At about 1780 cm^{-1} the in-phase -CO- stretching of the imide group is seen to increase as the temperature increased and saturated at 200 °C. At about 1720 cm^{-1} the out of phase -CO- stretching of the imide group is shown to increase again nearly saturating at 200 °C but increasing ever so slightly at 300 °C but then reducing at 350 °C. This reduction is most likely due to an onset of degradation which starts to occur around 350 °C to 400 °C for BTDA-HDA as shown by Dr. Rui Ma et al.[69] The vibration for -C-NH- found at about 1550 cm^{-1} was shown to decrease as the temperature decreased and saturated at 250

°C. These findings were used to set our maximum curing temperature at 250 °C to ensure complete imidization after 1 hour increments of 50 °C from 100 °C upwards.

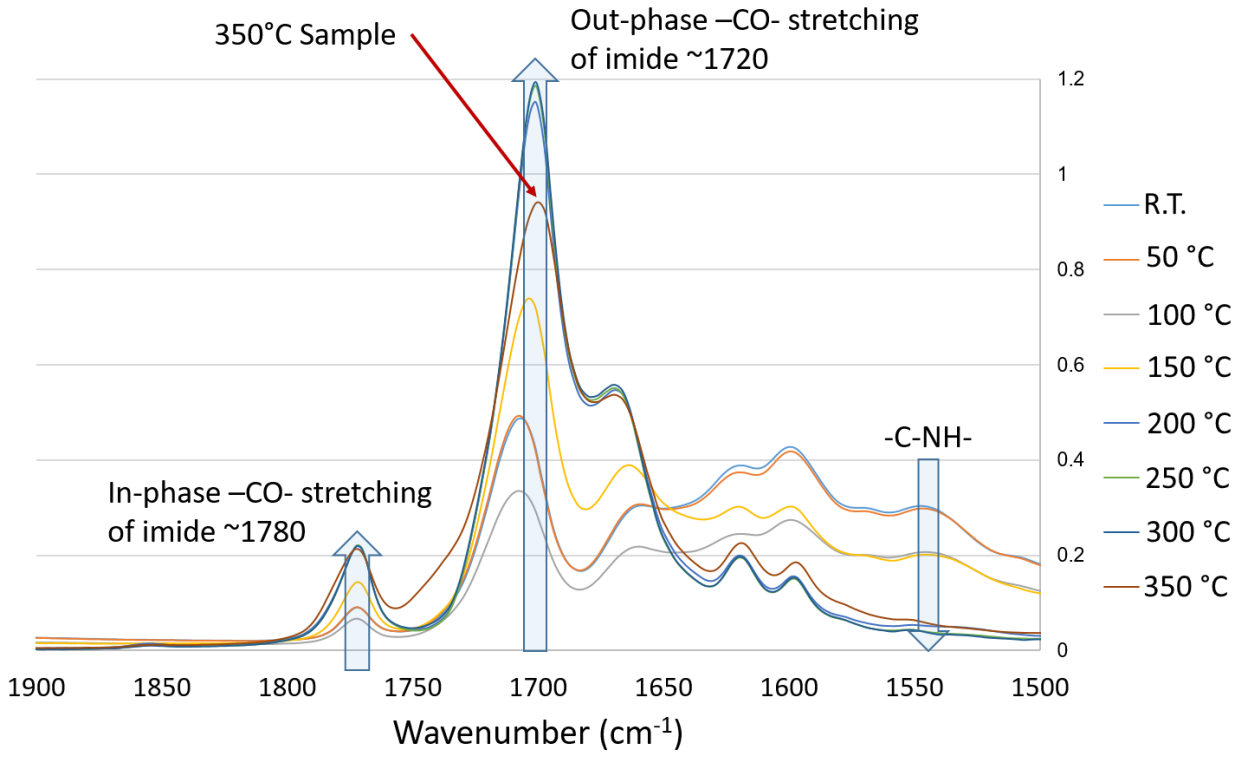

Figure 5.5. FTIR spectra of several films of BTDA-HDA taken to observe the thermal imidization of the polyamic acid film at varying temperatures in the furnace.

5.3.2 Density Measurements

Density measurements were taken by suspending the polyimide and copolyimide films in water and adding sodium iodide until the density of the solution matched the density of the films as previously reported by Lei Zhu et al.[133] To ensure that the measurements were accurate after each addition of salt the solution was vortex stirred for 5 minutes to facilitate complete dissolution followed by bath

sonication for 5 minutes to remove any air bubbles adsorbed onto the films. Once the film was observed to stay suspended in place for 5 minutes, away from the edges of the vial, a 5 ml aliquot was removed via a volumetric pipette and masses on a microbalance. The aliquot was then replaced into the vial, and 4 more aliquots were separately removed, weighted, and averaged to give an average density of the film. This process was then repeated on two more films of similar composition to give the three data points used to give error bars in **Figure 5.6.** Since this process was very time intensive and density values were needed for all 5 polyimide compositions, only three data points were recorded per polyimide. I am very thankful to my undergraduate researcher, Sydney Scheirey, for carrying out the majority of these density measurements which took the better part of two weeks to complete. **Figure 5.6** shows the experimental results overlaid on a plot with results from DFT and MD simulations. The results appear as expected, with DFT producing the densest polymers at about 1.6 g/cm^3 due to the computations having been run at a crystalline 0 K. Molecular Dynamics (MD) simulation gave the lowest density at about 1.2 g/cm^3 due to a preconditioning stage which consisted of heating the polymer to 1000 K followed by a fast cooling to 300 K over about 90 nanoseconds which is extremely fast compared to experimental timescales. The density of real polyimides was found to be only slightly higher than MD calculations at about 1.3 g/cm^3. An increase in free volume, which, along with the decrease in density, has been attributed to reduce dipole constraints and subsequently increase the dielectric constant.[134] At about 1.3

g/cm^3 these copolyimides are less dense than most polyimides which could help account for their higher dielectric constant and energy density.

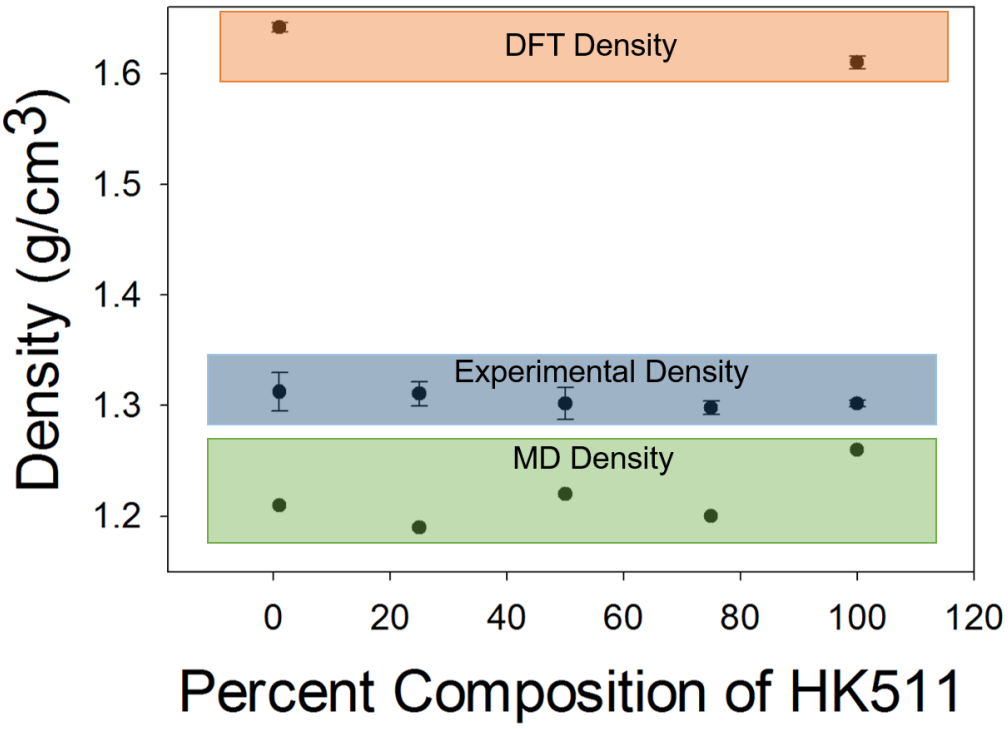

Figure 5.6. Copolyimide densities taken from DFT, MD, and experimental methods.

5.3.3 Band Gap Determination by UV-Visible Spectroscopy

The energy of the band gaps in the polyimide films was determined by UV-Visible spectroscopy as detailed in **Chapter 2**. The absorbance was recorded as the light source scanned from 1600 nm down to 200 nm and the sudden onset of absorption was taken graphically as the intercept between the base line and the vertical line. Through the Maxwell equation, the optical band gap can be found from taking $1240/\lambda_{onset}$. For BTDA-HDA the onset was at 362 nm which corresponds to a band gap

of 3.42 eV, and for BTDA-HK511 the onset was at 356 nm corresponding to a band gap of 3.48 eV as shown in **Figure 5.7**. The band gap energies for the copolymers fell between these two values as would be expected. Since the structures of these polymers are so large they are difficult and computationally expense to run on DFT. Instead, a machine learning algorithm was used.[128] BTDA-HK511 was estimated to have a band gap of 4.79 eV by this method and BTDA-HDA was expected to havea band gap of 3.7 eV, the latter being closer to the observed value but neither being too far off for computational predictions. An important note here is that the training data for the machine learning model did not contain a significant number of similar polyimide systems and therefore it is expected that the machine learning prediction would at best be a close approximation. As mentioned previously, the target of these polar polymers is to have a band gap greater than 3 eV which has previously been shown to be sufficient to act as a dielectric medium in pulse powered applications such as capacitors.[68]

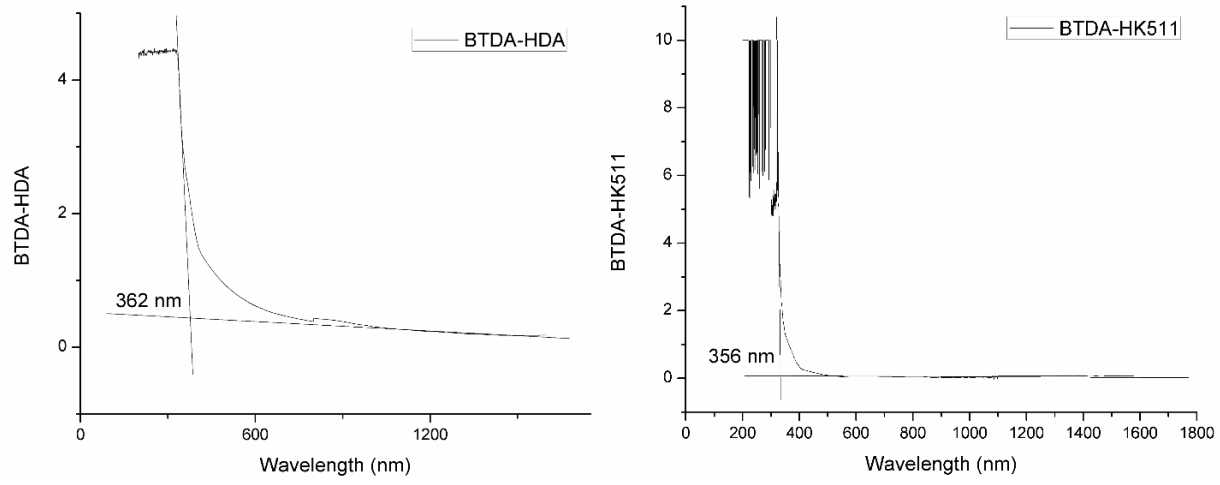

Figure 5.7. UV-Vis spectra of BTDA-HDA and BTDA-HK511 polymer films plotted as absorbance verse wavelength.

5.4 Thermal Characterization

5.4.1 Thermal Gravimetric Analysis

The thermal behavior of the polyimides was studied by Thermal Gravimetric Analysis (TGA) and Differential Scanning Calorimetry (DSC) to determine their onset of degradation and glass transition temperatures respectively. The TGA was utilized as laid out in **Chapter 2** for both polymer powders and the polymer films that were cast from DMAc. In order to analyze the polymer films, specially made lids had to be placed over the platinum TGA pans to ensure the films wouldn't blow away as the furnace was being purged with argon. All polyimide samples displayed similar thermal behavior by TGA as seen in **Figure 5.8** where representative TGA plots were overlaid for each of the polymer samples to show the onset temperature for degradation to be above 300 °C with minimal degradation until roughly 400 °C for all samples. This temperature is well above any expected use of these polymers as thin film capacitor dielectrics which is promising. The stable baseline before degradation also indicates that the polymer films were free of the majority of solvent, however, trace solvent and impurities could still remain in amounts too small to be noticed or trapped until degradation.

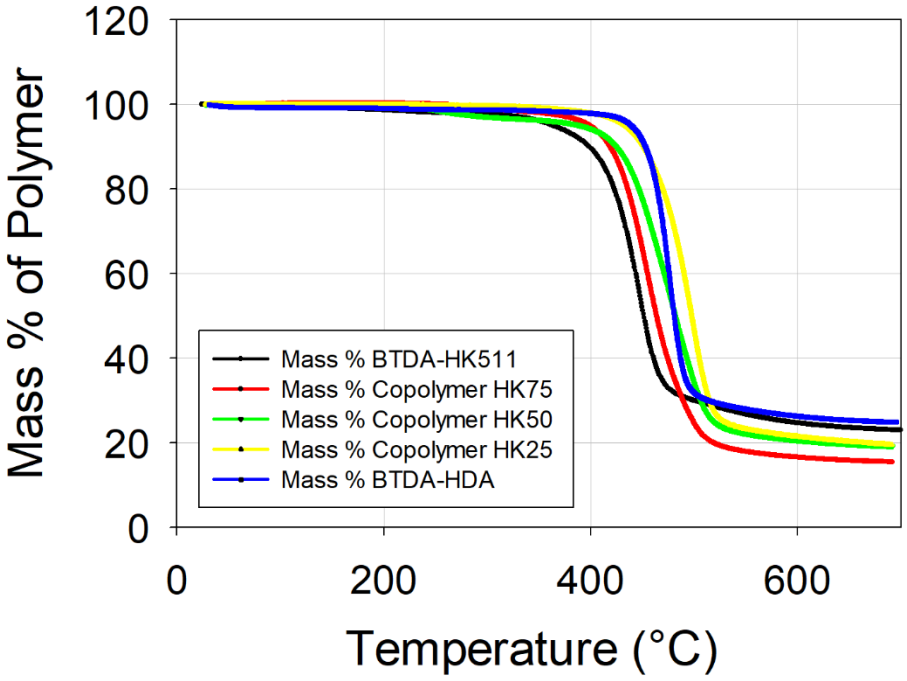

Figure 5.8. Thermal Gravimetric Analysis for the 2 polyimide homopolymers and 3 copolymers showing an onset temperature of degradation around 300 °C to 400 °C.

5.4.2 Differential Scanning Calorimetry

DSC was used to investigate the polyimide films for any thermal transitions that could affect processing parameters and electrical testing conditions. The DSC plots and associated glass transition temperatures (Tg) are overlaid and labeled on **Figure 5.9**. The two homopolymers have Tg values of 78 °C for BTDA-HK511 and 150 °C for BTDA-HDA. The well-known Fox equation is shown in **Equation 5.1**

$$\frac{1}{T_g(K)} = \frac{w_1}{T_{g,1}(K)} + \frac{w_2}{T_{g,2}(K)} \qquad \textbf{(5.1)}$$

relates the Tg of miscible copolymers by a rule of mixtures between their homopolymers using temperature in Kelvin and the weight fraction of each portion.

The thermal properties of the homopolymers and copolymers listed in **Table 5.1**. The similarity in Tg between predicted values and DSC values help to confirm that copolymers with the correct concentration of each diamine were produced. Unfortunately, this is insufficient evidence to say that truly random copolymers were synthesized as even miscible blends would exhibit the same trend in Tg. However, there is little reason to suggest at this time that the slight variations in arrangements of polymer repeat units should affect the electrical properties in any substantial way and the method of dropwise addition of diamines to the reaction vial suggest that a somewhat random copolymer should have been formed as intended.

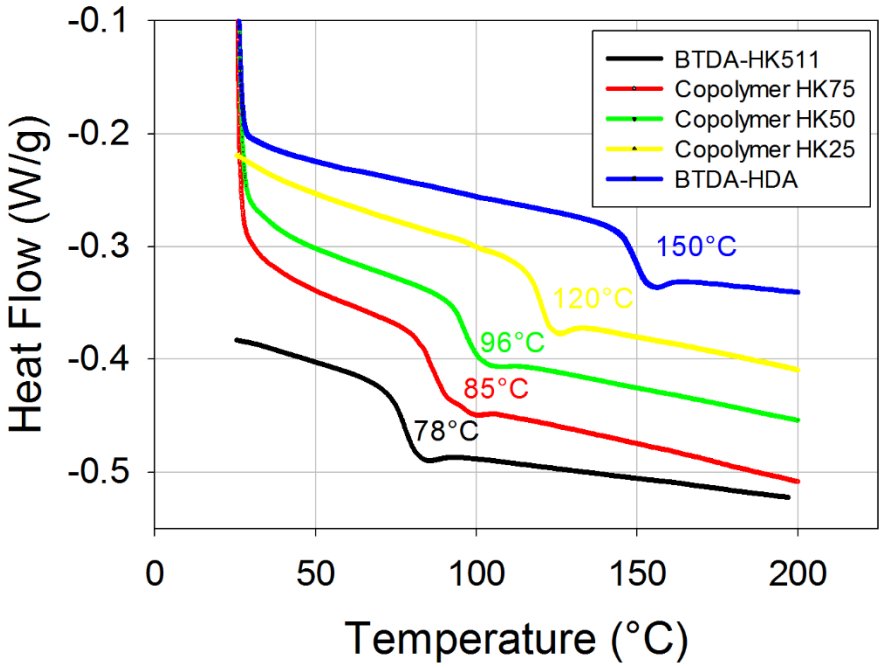

Figure 5.9. Differential Scanning Calorimetry plots for the 2 polyimide homopolymers and 3 copolymers showing glass transition temperatures ranging from 78 °C for BTDA-HK511 to 150 °C for BTDA-HDA.

Table 5.1. Experimental thermal data for polyimides with Fox Equation predictions.

Copolymers	T_g (°C)	Calculated T_g (°C)	T_o(°C)	T_d(°C)
BTDA-HK511	78	N/A	311	447
BTDA-HK75	85	86.71	324	438
BTDA-HK50	96	99.05	342	453
BTDA-HK25	120	117.85	366	476
BTDA-HDA	150	N/A	338	482

5.5 Dielectric Spectroscopy

Dielectric spectroscopy for all five polyimides was initially investigated by time domain dielectric spectroscopy in order to probe low frequencies down to $1x10^{-3}$ Hz, and the results were plotted as dielectric constant and loss against frequency at room temperature as shown in **Figure 5.10**. The dielectric constants fit the expected trend, with reported values taken at 1 kHz and BTDA-HK511 having the highest at 7.8, followed by HK75 at 5.6, HK50 at 5.34, HK25 at 4.42, and BTDA-HDA at 3.57 with all showing loss below 1% at 1 kHz. The three copolymers were also subjected to a temperature ramp which showed stable results until the Tg where both K and loss drastically increased as seen in **Figure 5.11** The Tg observed via dielectric spectroscopy was similar to the value found by DSC, however it was not exact as the temperature steps where 25 °C increments compared to the near continuous sampling with DSC. The Tg values correlated with the **Equation 5.1** which is used to predict the Tg of copolymers. The presence of a single Tg for the copolymers indicates that

both segments are miscible and that a random copolymer was formed during polymerization in a ratio very close to the feed ratio.

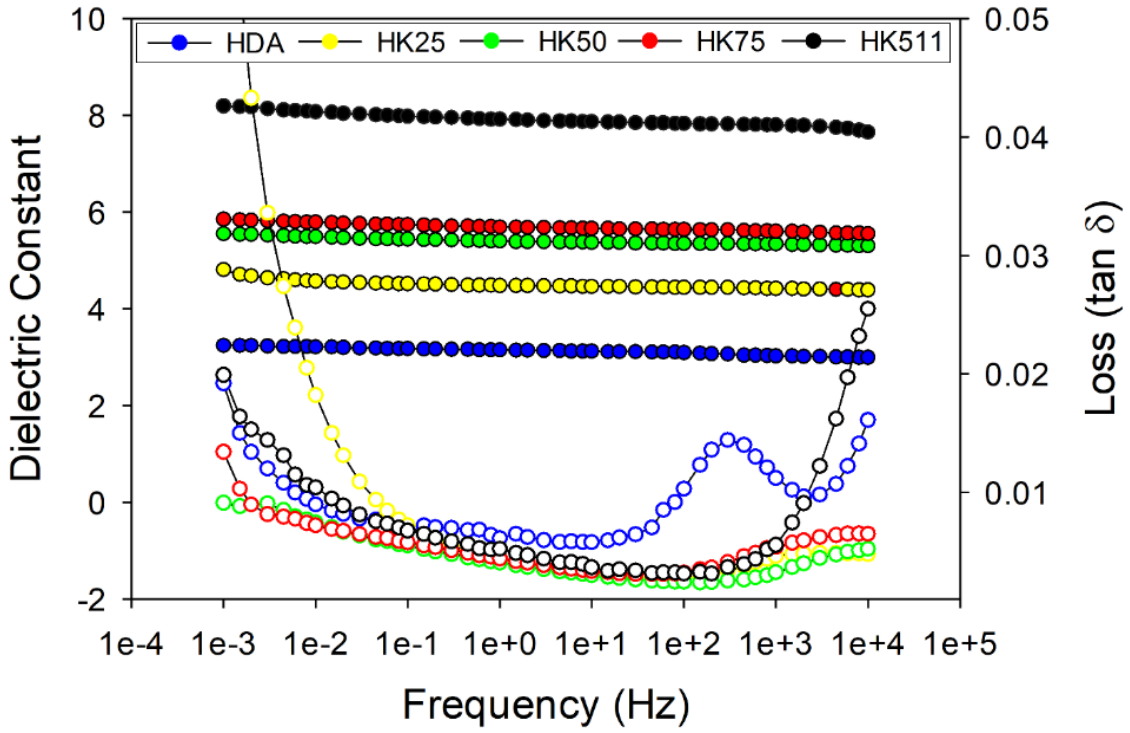

Figure 5.10. Dielectric constant and loss for all five polyimide systems from TDDS at room temperature.

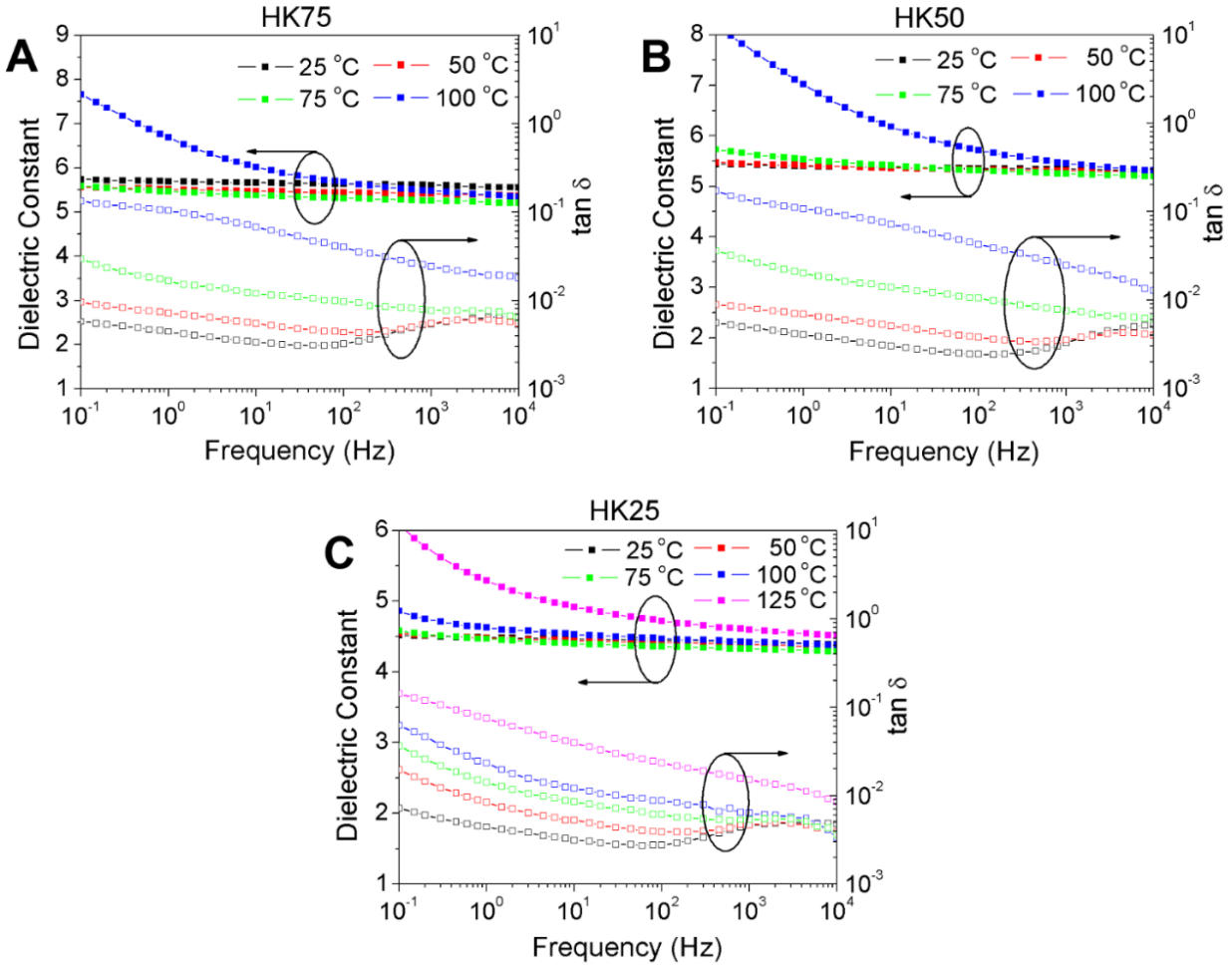

Figure 5.11. TDDS of polyimide copolymers with a temperature ramp for (A) HK75, (B) HK50, and (C) HK25.

5.6 High Field Characterization

5.6.1 DC Breakdown Analysis

Failure analysis was carried out on 25 samples for each polyimide to determine the DC engineering breakdown field of the polymers. The process is described in detail in **Section 2.3.6**. Measurements were carried out in a ball to plane setup in silicone oil on samples 3 mm in diameter and analyzed using the Weibull distribution

function, F(x) as shown in **Equation 2.4.** Film quality, including surface roughness and impurities, is known to reduce the measured breakdown and is taken into account with a Weibull analysis. Ideally, a Weibull distribution will have all the tested points failing at the same value, in this case, the breakdown field. However, impurities such as dust, small molecules like solvent, local crystallization, and other phenomena exist to cause early breakdown. By taking a large distribution of data points across several samples, these variations could hopefully be averaged out, and a likely breakdown field for a given sample could be determined within acceptable limits, in this case, 63.2% probability. For the most part, the breakdown values matched expectations with higher breakdown fields reported for copolymers with a higher concentration of HDA. However, HK25 has the highest breakdown field of 868 MV/m as seen in **Figure 5.12**. It has been suggested that short range ordering combined with strong dipoles can lead to extremely high dielectric breakdown strengths (ca. 1.1 GV/m).[135] The ability of BTDA-HDA to induce short range ordering and minor crystallization and has been studied extensively by Dr. Cakmak et al., as part of this research effort and the addition of 25% HK511 may impart enough dipolar character to bring the breakdown strength above that of BTDA-HDA. The results of that work, led by Dr. Cakmak's group, will be published in two papers shortly.

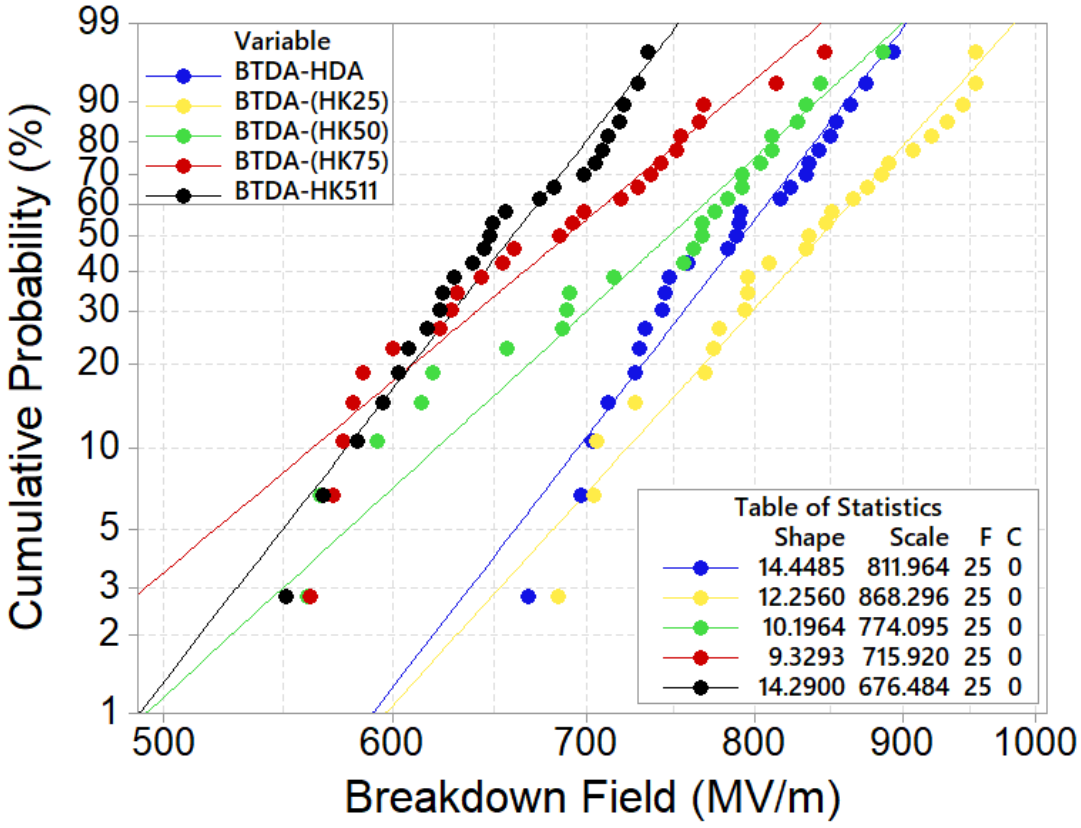

Figure 5.12. Weibull distribution for each of the copolyimides and the two homopolymer films calculated from 25 separate breakdown measurements each.

5.6.2 AC D-E Polarization Loop Analysis

The AC breakdown field was also determined by use of a D-E loop as discussed in **Section 2.3.7** on samples 3 mm in diameter with a ball to plane setup. The D-E Loop is a useful measurement for testing dielectric materials as it can determine dielectric constant, breakdown field, energy storage, and energy loss all at once. The D-E loop charges and discharges the polymer film as a capacitor dielectric while increasing across a set voltage ramp. Typically, the higher the electric field that is applied, the larger the hysteresis loss that is observed. Especially at high fields,

conduction losses can lead to high hysteresis loss and low efficiency in the material despite a high energy storage. The D-E hysteresis loops for the three copolymers are shown below in **Figure 5.13** with their respective energy density and efficiency graphs plotted against the applied electric field in the insert.

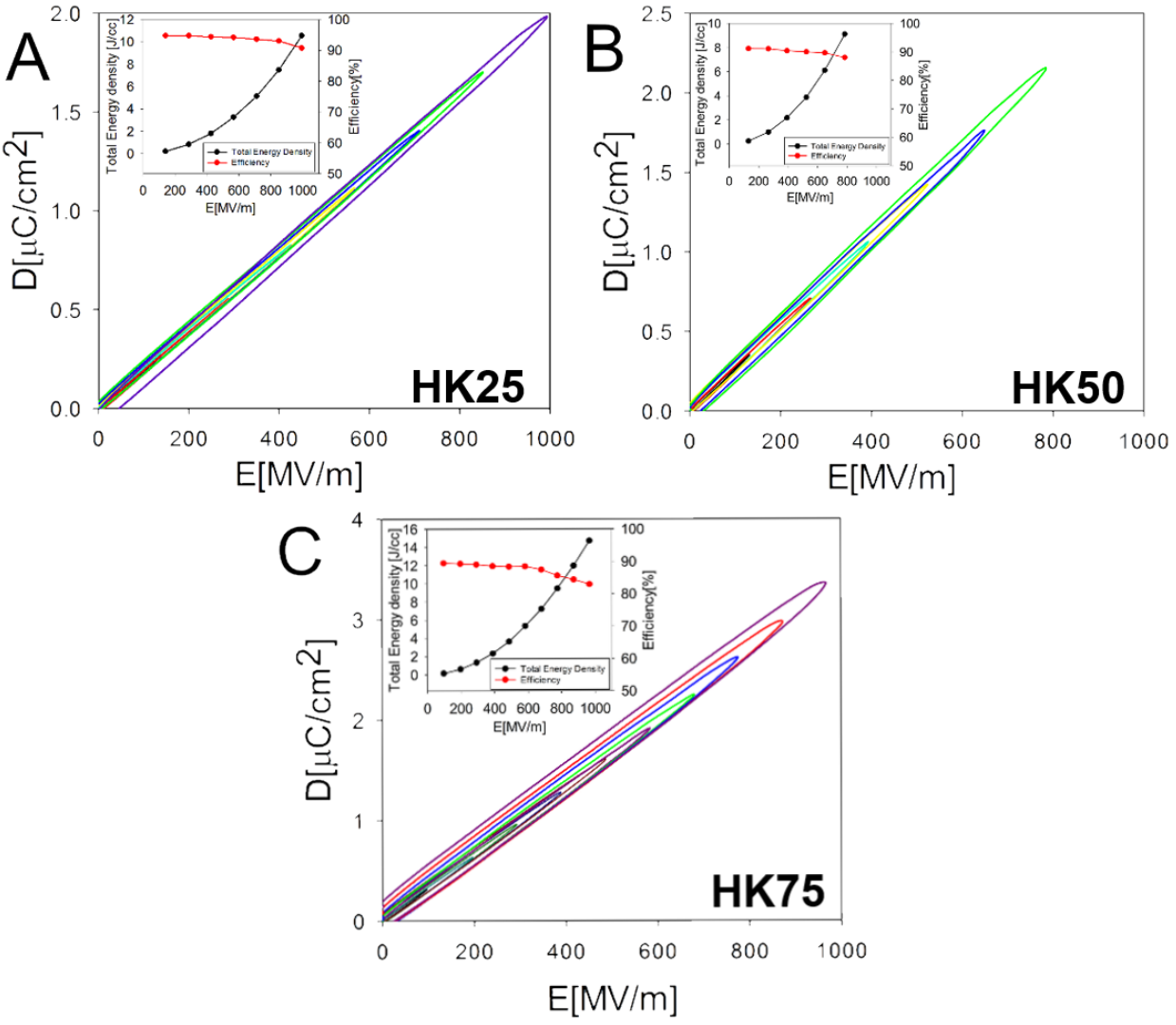

Figure 5.13. Charge discharge D-E hysteresis loops for the copolyimides showing an energy density of (A) HK25 9.58 J/cc, (B) HK50 8.03 J/cc, and (C) HK75 14.72 J/cc.

The energy density values from D-E loops can be compared to the energy density values from DC Weibull breakdown plots by incorporating the dielectric

constant measured by TDDS with the DC breakdown values. By using **Equation 1.9,** the maximum theoretical energy density can be calculated by taking half the dielectric constant of the material determined by TDDS, the permittivity of a vacuum, and the square of the electric field at DC breakdown as determined through Weibull analysis. This value can be compared to the total energy density value given by the D-E hysteresis loop. This analysis gives similar but different results for both AC and DC values. For the copolymer HK25, the energy density from the Weibull (868 MV/m) and TDDS (4.42) give a maximum energy density at the breakdown of 14.76 J/cc compared with a maximum measured energy density of 9.58 J/cc as determined by D-E loops. For the copolymer HK50, the energy density from the Weibull (774 MV/m) and TDDS (5.34) give a maximum energy density at the breakdown of 14.16 J/cc compared with a maximum measured energy density of 8.03 J/cc as determined by D-E loops. For the copolymer HK75, the energy density from the Weibull (716 MV/m) and TDDS (5.6) give a maximum energy density at the breakdown of 12.71 J/cc compared with a maximum measured energy density of 14.72 J/cc as determined by D-E loops.

Table 5.2. Electrical properties for polyimides and copolyimides

Copolymers	$\epsilon_{1\text{kHz}}$	Tan $\delta_{1\text{kHz}}$	DC Breakdown (MV/m)	DC Energy Density (J/cc)	AC Energy Density (J/cc)
BTDA-HDA	3.57	0.85%	812	9.97	N/A
BTDA-(HK25)	4.42	0.46%	868	14.74	9.58
BTDA-(HK50)	5.34	0.33%	774	14.16	8.03
BTDA-(HK75)	5.6	0.54%	716	12.71	14.73
BTDA-HK511	7.8	0.55%	676	15.77	N/A

5.7 Simulation Results

Dr. Arun Kumar Mannodi Kanakkithodi from Dr. Ramprasand's group at the University of Connecticut was able to assist with two forms of computational predictions consisting of density functional theory (DFT) and a DFT based machine learning (DFT-ML) high speed prediction system. The DFT computations were performed using the projector augmented-wave (PAW) formalism as implemented in Vienna Ab Initio Simulation Package (VASP). The polymer chains were first set up as a repeating unit, and the Minima Hopping Algorithm was implemented to find the low energy structures which the computations were then carried out on. Due to these computationally intensive tasks required to prepare the polymer for calculations, the simulations get increasingly resource intensive as more atoms are added to the simulation and the polyimides studied here pushed the boundaries of what was possible on our resources. The smaller polyimide BTDA-HDA, the minimization, and computations were able to be carried out fully. However, the larger polyimide BTDA-HK511 proved to be too large to be completed in a reasonable timeframe. As a result, the DFT values were only available for BTDA-HDA at time of publishing since the copolymers would be even larger and more complicated. This problem will be overcome in the near future as programs with more optimized code are developed and as Moore's Law drastically improves the computational resources available to an academic researcher.

To overcome these computational limitations, we moved to a recently developed and validated method that has been gaining increasingly usefulness which

is the practice of using machine learning to predict with reasonable certainty the properties of a polymer in a fraction of the time needed to carry out traditional DFT computations. To do this, DFT results from hundreds of computations were feed into an algorithm which produced a fingerprint of the polymers and mapped those fingerprints to computed properties. After many optimization and validation stages, the machine learning algorithm was optimized to give similar results on new polymers as expensive DFT results. To get the DFT-ML predictions for the polyimides and their copolymers the structures were fed into the premade program to generate their unique fingerprint, which was then run through the ML algorithm to generate the DFT-based predictions. By this technique, the DFT-ML properties of all 5 polyimides were able to be generated in less than 10 minutes, including the time needed to create the polymer structures, compared to the months or years of time that would have been required to carry out traditional DFT calculations on all the copolyimides. There is one large drawback for the ML predictions that is inherent in all ML datasets which is that the data used to train the ML algorithm needs to be sufficiently similar to the data that is attempting to be predicted. This is an obvious drawback with the current dataset being used, as the reason the DFT-ML approach was used is because it was difficult to get the DFT results for these and similar polyimides due to their large dependence on aromatic rings which contain tens of atoms each. As such, there is not a large database of DFT results on polyimide systems from which the ML algorithm could be trained on. Of course, this is a relatively new technique being used in our collaboration, and as these research efforts

progress, more and more DFT computations will be added to the database, including polyimides, which will lead to substantial improvements in the DFT-ML predictions generated. As such, it would be important to revisit the results presented in this chapter in several years when computational power and polyimide dataset have increased to make these predictions more accurate. As it currently stands, these polyimides were shown to have their refractive index, and thus electronic dielectric constant, drastically overestimated compared to what was experimentally determined by ellipsometry. As long as these limitations are understood and considered when viewing the results, the DFT-ML predications still serve as a useful technique for analysis and comparison in the absence of any better options.

As a compliment to the DFT and DFT-ML predictions from Dr. Ramprasad's group Dr. Mayank Misra from Dr. Sanat Kumar's group at Columbia University was able to lend his expertise to help carry out property predictions by the technique of molecular dynamics. This technique is able to handle large polymer chains, in this case, 50 repeat units in length, and as such was able to simulate both the homopolymers as well as the three copolymers if they are taken as idealized perfectly alternating copolymers. This system serves as a great basis for research to study the dielectric constant, dielectric loss, and breakdown strength which are three of the most important electrical properties for dielectric polymers. After construction of the polymer chain, each system was heated to 1000 K for 5 ns which allowed the chain to achieve an amorphous state before being cooled down to 700 K at a rate of 50 K/ns. Afterwards, the samples were cooled to 300 K at a slower rate of 5 K/ns. The slow

cooling phase starts at a relatively higher 700 K than is often used for polymers, such as polypropylene, which is typically slowly cooled after 500 K since the Tg of polyimides is typically higher. It is desirable to start the slow cooling processes well above the Tg of the polymer to allow the chains time to relax. Continuing to cool the polymers rapidly through the glass transition would force a very amorphous state that would be unrepresentative of the real polymer chains, this would compound the problem facing molecular dynamics where timescales are already much more accelerated than they would be in the lab. The sample is then equilibrated at 300 K for 10 ns and then tested for static dielectric permittivity over 20 ns in a production run. The results for dielectric permittivity, labeled at ionic are plotted against the experimental results by TDDS labeled as total in **Figure 5.14** and the complete tabulated values from both DFT-ML and MD are shown in **Table 5.3** for all copolyimides.

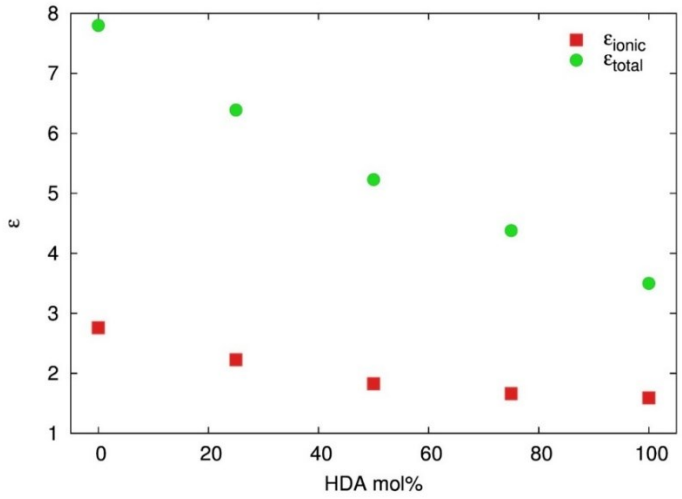

Figure 5.14. The static dielectric permittivity for all the copolymers. The red squares represent the ionic component of dielectric permittivity calculated from simulations. The green circles are the total dielectric permittivity measured for the sample experimentally by TDDS.

Table 5.3. DFT-ML and MD computational data for copolyimides with the Total ε (Simu)* results taken as the Electronic ε (DFT-ML) + Ionic ε (MD) results.

Copolymers	Electronic ε (DFT-ML)	Ionic ε (DFT-ML)	Ionic ε (MD)	Total ε (Simu)*	Band gap (DFT-ML)
BTDA-HDA	3.60	1.24	1.60	5.20	3.69
BTDA-(HK25)	3.50	1.17	1.70	5.20	4.02
BTDA-(HK50)	3.40	1.11	1.80	5.20	4.32
BTDA-(HK75)	3.40	1.05	2.20	5.60	4.57
BTDA-HK511	3.30	1.00	2.80	6.10	4.79

The dielectric loss was also probed by molecular dynamics to compare to the experimentally determined dielectric loss by TDDS. After the 20 ns run to determine the dielectric constant the samples were still determined to be between 50 and 70% unrelaxed and an additional time temperature superposition approach was required the produce a relaxed system. The samples were heated to 350, 400, 450, 500, 550, and 600 K with a constant number of chains, volume, and temperature or NVT. The simulations were run for 25 ns with the final 20 ns of each used to calculate the dipole correlation, with all the functions plotted in **Figure 5.15A**. The curves were than analyzed using a stretched exponential function to produce the data shown in Table 5.X, with relaxation time τ (ns) stretching exponent (b) and average relaxation time τ_{avg} (ns). The addition of HDA drastically reduces the relaxation time of the polymer chain which could be due to the increase in separation and spatial distribution of the HK511 units throughout the samples. These fitting parameters were then used to plot the frequency dependent dielectric loss and loss peaks which are overlaid on the

plot of experimental loss from TDDS in **Figure 5.15B**. The measurements only allow for a small area of overlap between the experimental results and the computational results due to the difficulty of achieving low frequency loss values in MD simulations. However, the area of overlap shows comparable results. By using time temperature superposition, the loss at MHz frequencies was able to be probed computationally, which, was previously unable to be reached through traditional MD.

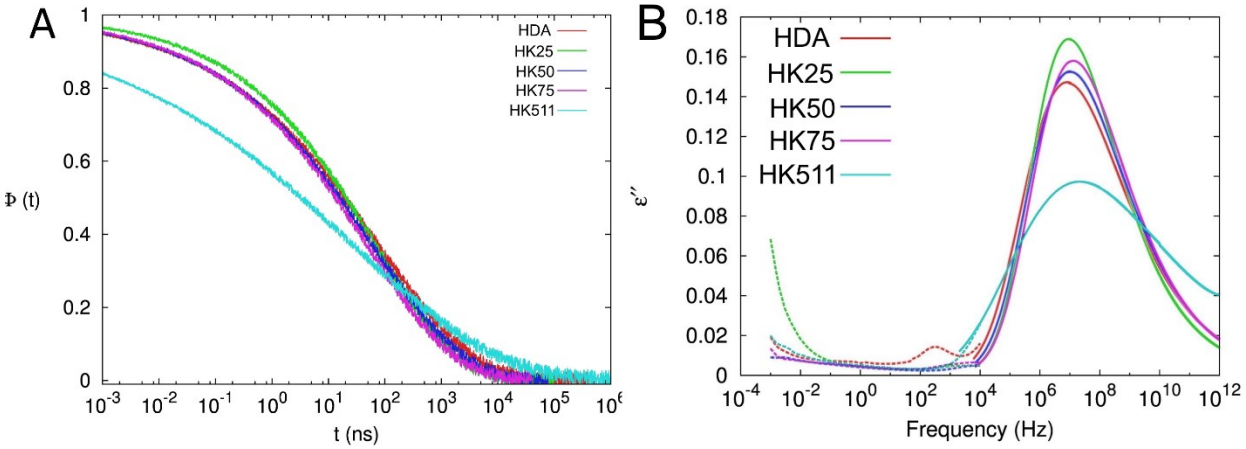

Figure 5.15. (A) The master curve for dipole correlation function and (B) dielectric loss for the copolymers. The dotted lines in the loss curve are dielectric loss data obtained from experiments, and the solid lines are from molecular dynamics.

Table 5.4 Stretched exponential fitting parameters for the dipole moment correlation function for the copolyimides from MD.

Copolymers	τ (ns)	β	τ_{avg} (ns)
BTDA-HDA	78.53	0.26	1.50E+03
BTDA-(HK25)	70.24	0.3	6.51E+02
BTDA-(HK50)	61.55	0.27	9.55E+02
BTDA-(HK75)	49.54	0.28	6.37E+02
BTDA-HK511	28.81	0.17	1.67E+04

In general, all five polymer systems were still determined to be amorphous in nature after the cooling period. However, some of the localized structures were notable. The polymer repeat segment that was produced from the diamine Jeffamine Etheramine HK511 was shown to often exhibit a characteristic bend around where the two isopropyl oxy groups are found. This bend is consistent with the helical nature of polyethylene oxide (PEO) and polypropylene oxide (PPO) which are homopolymers of the two-different ether containing entities inside HK511. **Figure 5.16** shows this helical twist in a snapshot of the copolymer HK50 where a BTDA unit is attached to HDA, in turn, which is attached to another BTDA which is attached to the bend HK511 which is connected to another BTDA to repeat along the polymer chain. It is important to note that this helical bend doesn't happen to the same magnitude at every repeat unit however it does occur often enough to be considered significant upon visual observation. This HK511 is attributed to causing an increase in free volume and density which matches the predicted results seen in **Figure 5.6** above. The fact that DFT predicted a lower density for BTDA-HK511 than for BTDA-HDA shows that the low energy crystalline structures at 0 K that DFT uses to carry out computations may be misrepresenting the actual structure of any polymer containing HK511 or a similar ether containing unit.

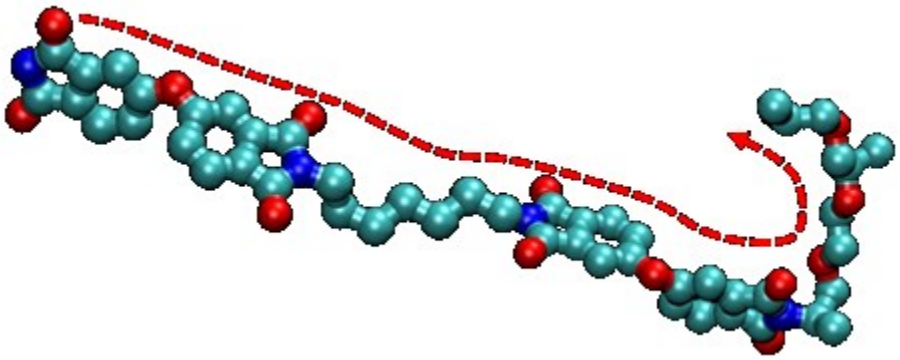

Figure 5.16. Simulation snapshot of a characteristic bend in the HK511 ether containing polymer segment shown in BTDA-HK50.

5.8 Low Temperature Dielectric Spectroscopy

A similar low temperature dielectric study was performed on the copolyimides as was done for the polyurea and polythiourea in **Chapter 3** and **Chapter 4** respectively. This system was developed at the University of Connecticut's EIRC to conduct similar measurements to the Novocontrol. JoAnne Ronzello of the EIRC lead the development of the in-house low temperature setup by attaching a liquid nitrogen tank to an oven and LCR meter while controlling the system with LabVIEW programed by Justin Delarm and Krishnan Sureshkumar. The system, outlined in Chapter 2, allowed for samples to be run from -130 °C to 150 °C over the frequency range of 20 Hz to 1 MHz. The polymer samples for BTDA-HDA, HK25, and HK50 were carried out on freestanding films between 10 μm and 30 μm thick. For HK50, a thicker film was required as thin films were too brittle to be subjected to the pressure exerted by the spring-loaded sample holder. In the case of HK25, the film was cast onto a polished silica wafer that measured 2" in diameter, which acted

as a support substrate. Copolymer films were prepared with deposited electrodes as previously mentioned for the low temperature setup in **Chapter 2** and was run from -130 °C to 150 °C with a step of 10 °C and a hold time of 30 minutes at each temperature to ensure the polymer film was able to equilibrate to each temperature. 10 measurements were taken and averaged for each data point to eliminate any noise that may have been introduced into the system. The data for HK25 was plotted in **Figure 5.17A** with the dissipation factor plotted in **Figure 5.17B** to show a visual sample of the copolyimides spectra.

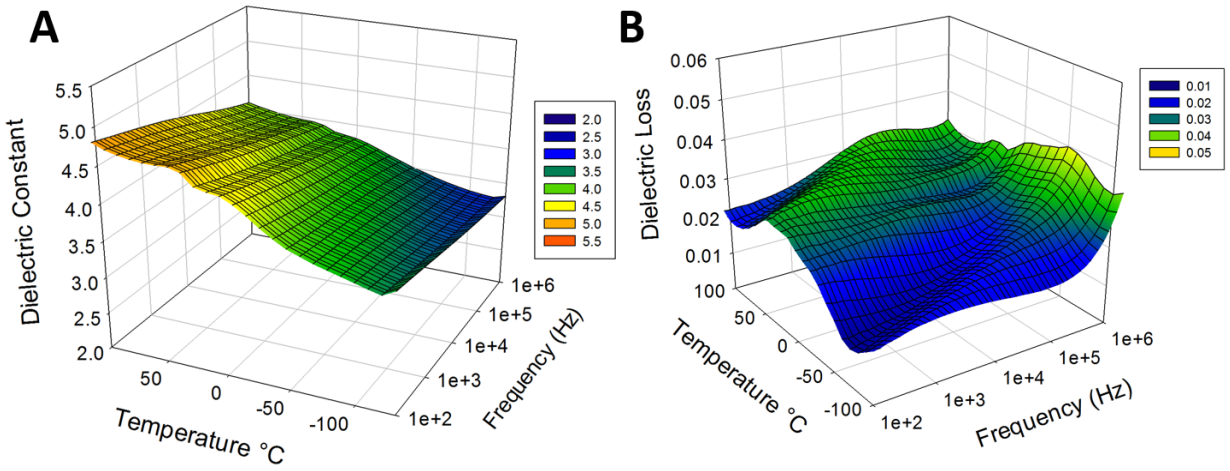

Figure 5.17. Dielectric spectroscopy (A) and Dielectric Loss (B) of HK25 from -130 °C to 100 °C carried out on the automated LCR meter in UConn's EIRC.

The experimental data for all the copolymers besides BTDA-HK511 are shown in **Table 5.5** with the DFT-ML predictions and MD simulations shown in (parenthesis). The experimental data for the copolyimides were broken into three dielectric constants with the aid of computational predictions as in previous chapters. The square of the refractive index of the polymer films was taken as $\varepsilon_{electronic}$ and was

subtracted from the -130 °C dielectric constant to give an estimated ε_{atomic}. The -130 °C dielectric constant ($\varepsilon_{electronic} + \varepsilon_{atomic}$) was subtracted from the room temperature dielectric constant to give an estimated value for $\varepsilon_{dipolar}$. The value of $\varepsilon_{dipolar}$ was shown to increase as the content of HK511 was increased in the copolyimides as would be expected due to previous results. The value for ε_{atomic} was also shown to increase as HK511 content was increased, however, as mentioned previously, a portion of this atomic polarization could be attributed to the $\varepsilon_{dipolar}$ that was not fully frozen in the polymer films at -130 °C. These results show the importance of both the ε_{atomic} and $\varepsilon_{dipolar}$ in next generation dielectric materials and the addition of monomers such as HK511, which are polarizable while increasing free volume, in enhancing the dielectric constant of organic polymers.

Table 5.5 Experimental breakdown of the three main polarization mechanisms taken from the low temperature dielectric spectroscopy for the copolyimides with the DFT-ML and MD computational data for copolyimides shown in (parenthesis) with the Total ε (Simu)* results taken as the Electronic ε (DFT-ML) + Ionic ε (MD) results.

Polymer	Tg	$\varepsilon_{electronic}$ (DFT-ML)	ε_{atomic} (DFT-ML)	$\varepsilon_{dipolar}$ (MD)	ε_{total} (Simu)*
HK511	78	2.7 (3.3)	(1.00)	(2.8)	7.8 (6.1)
HK75	85	2.7 (3.4)	1.94 (1.05)	0.97 (2.2)	5.6 (5.6)
HK50	96	2.7 (3.4)	1.94 (1.11)	0.94 (1.8)	5.6 (5.2)
HK25	120	2.7 (3.5)	0.88 (1.17)	0.85 (1.7)	4.4 (5.2)
HDA	150	2.7 (3.6)	0.57 (1.24)	0.15 (1.6)	3.4 (5.2)

Chapter 6

6. Organotin Polymers for Dielectric Applications

6.1 Rational Co-Design of Metal Containing Polymers

There are several aspects that drive the performance of dielectric materials including dielectric constant and breakdown which, when combined, determine the energy density of a given material which we ultimately desire to be increased. A theoretical approximation for the maximum intrinsic breakdown strength of a polymer is band gap as previously discussed, leaving us with the desire to maximize both band gap and dielectric constant. As was previously described in the introduction and shown in **Figure 1.8**, for most organic polymers the electronic portion of the dielectric constant was shown by Density Functional Theory (DFT) computations to be inversely proportional to the band gap and posed a problem for increasing both values simultaneously. Thankfully, those same calculations showed that the ionic portion of the dielectric constant had no relationship with band gap and there existed polymers with both high ionic dielectric constants and large band gaps. To increase the ionic portion of the dielectric constant, a few strategies were imposed in this thesis and in this chapter, we focus on the addition of metal atoms.

Metal atoms have often been used as a way to achieve high dielectric constants in polymers. In the introduction, the use of $BaTiO_3$ in ceramic MLCC was discussed as being implemented in the early 1920s due to its ultra-high dielectric constant of

over 1,000. These metals later made their way into film capacitor research as nanocomposites utilizing interfacial polarization to increase their dielectric constant to somewhere between the low dielectric of the organic polymer and the ultrahigh dielectric of the ceramic. Despite the high dielectric constants, nanocomposites have some drawbacks such as dispersion and adhesion issues within the polymer matrix as well as high field failure and instability of dielectric constant over a large frequency range. To combat some of these difficulties, the idea arose that incorporation of the metal atom directly into the main chain of an organic polymer could produce desirable properties. Several computational studies were carried out to down select which metals should be first investigated. The addition of chemical intuition helped refine the search to include practical systems that could actually be produced in the lab. In the end, tin was chosen to be the first element incorporated into the main chain resulting in successful synthesis and testing of a range of organotin polyesters culminating in the report of a metal containing polymer with high dielectric constant, high band gap, and a theoretical energy density on par with BOPP, a good starting point for a new class of dielectrics.

6.1.1 Metal Containing Polymers

To realize the benefits that dispersed metal atoms have for dielectrics, without the drawbacks of aggregate metal atoms and clusters, polymers with metal atoms directly and discreetly incorporated into the backbone were envisioned. The initial idea was to have a single metal atom spaced throughout a polymer chain; this would give increased polarization over the typical carbon-hydrogen moieties found in

polyethylene or polypropylene. Since there are currently 118 known elements, with most of them being some type of metal, a better approach had to be devised than simple trial and error to determine the best elements for incorporation for dielectric applications. Since these metal atoms would replace the carbon in a polymer, group 14 elements were chosen for initial studies. Dr. Ramprasad's group expertize in DFT computations helped start the rational search by investigating carbon, silicon, germanium, tin, and lead as XY_2 compounds where X is the metal and Y_2 is either two hydrogens, chlorines, or fluorenes.[136] Some group 14 elements could also exhibit XY_4 structures. However, this was ignored during the first steps for simplicity of calculations and analysis. The overall results of this study are shown in **Figure 6.1** with dielectric constant plotted against band gap showing both the electronic and total dielectric constants of the crystalline compounds. From that work, it was shown that the halogen containing units $SnCl_2$, GeF_2, and PbF_2 resulted in the highest dielectric constants and band gaps of the studied materials and that these heavier group 14 elements showed a strong promise to replace carbon and silicon for dielectric materials.

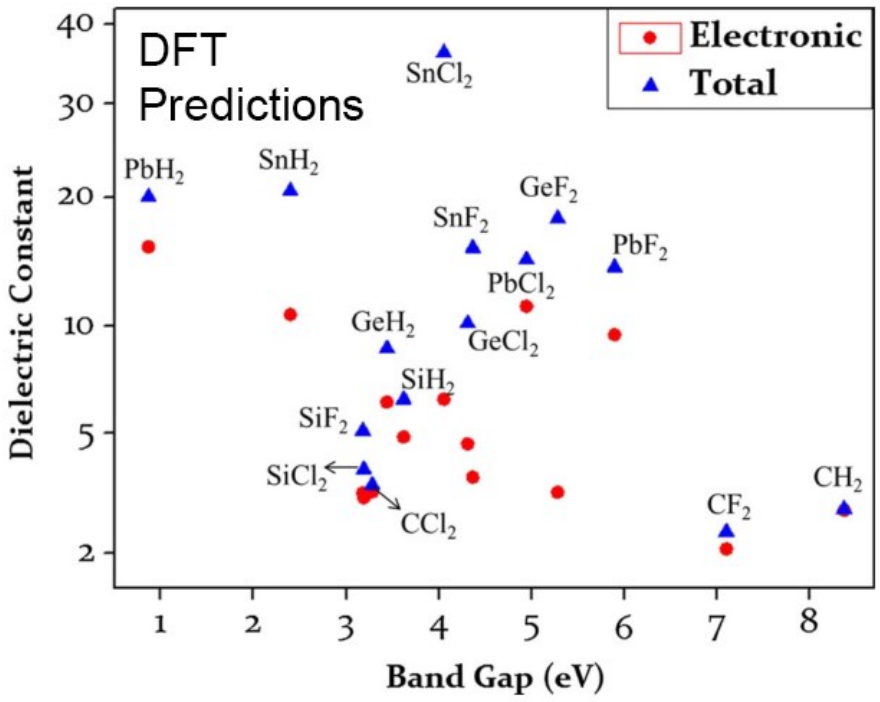

Figure 6.1. "Dielectric constant versus band gap for the 15 systems. The electronic component is seen to correlate inversely with the band gap. The total dielectric constant goes very high in cases with large ionic components" Reproduced with permission from reference [136]. Copyright (2014) Springer US.

6.1.2 Tin-Containing Polymers

The first computational systems that were investigated for dielectric properties as part of this collaboration were based on the polyethylene chain for simplicity of calculations. In this case, group 14 elements in the similar XY_2 form where Y_2 was two chlorines or fluorenes were chosen to replace CH_2 groups along the polyethylene backbone, and numerous calculations were then carried out through DFT. The dielectric constant was then plotted against band gap and shown in **Figure 6.2** with the inset depicting a cartoon of the modified polyethylene chains used for

simulations. By replacing carbon units with higher order elements, the band gap is seen to decrease linearly. However, the improvement in dielectric constants, specifically with the addition of SnF_2 units, provides promise for future work. However, several of these computationally derived polymers would be difficult to synthesize in the laboratory as stringing multiple GeF_2 and SnF_2 units together is a lot harder with known chemistry.

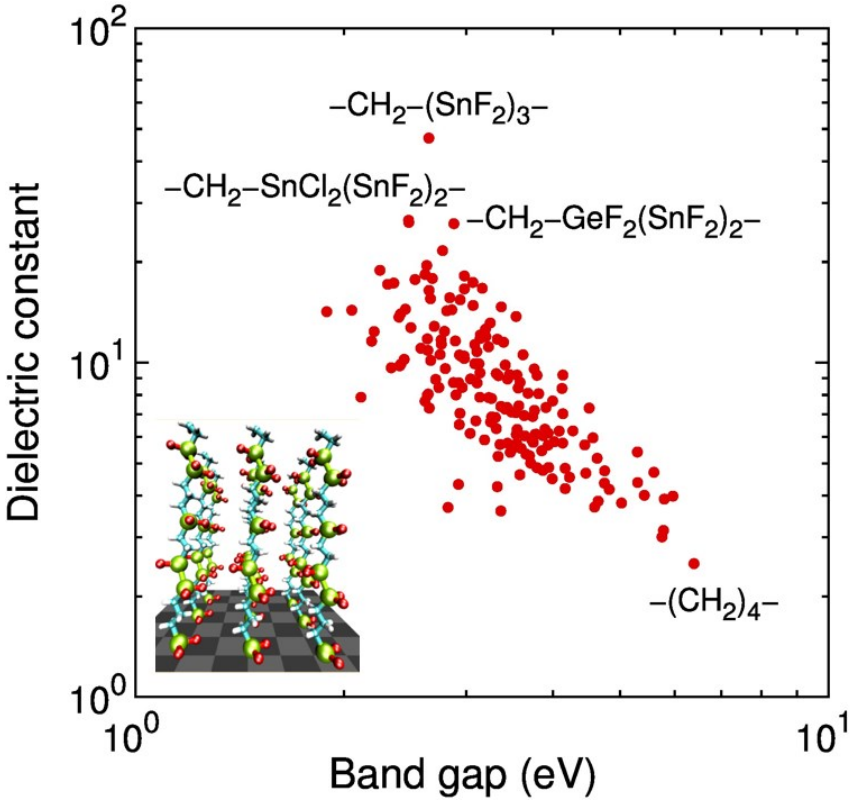

Figure 6.2. "Total dielectric permittivity as a function of the computed DFT band gap for the 175 systems with an artistic rendition of the stacked polymer chains in the inset. Reproduced with permission from reference [137]. Copyright (2013) American Chemical Society.

Other insights gained from that work are proved to be of equal value for synthetic efforts such as the study of dielectric constant and band gap verse XY_2

fraction as shown in **Figure 6.3**. For initial design parameters guidance was sought by our electrical engineer collaborators Dr. Steve Boggs and Dr. Yang Cao resulting in a constraint of dielectric constant greater than 5 and band gap greater than 3 for this preliminary search. It became evident that as the atomic mass increased, a lower fraction was needed to achieve comparable, or even better, results. By moles we would require 55% SiF_2, 33% GeF_2, or 17% SnF_2 showing that not only did SnF_2 crystals yield the highest dielectric constants[136] they also required the least amount in the polyethylene backbone and thus would be most amenable to synthesis.

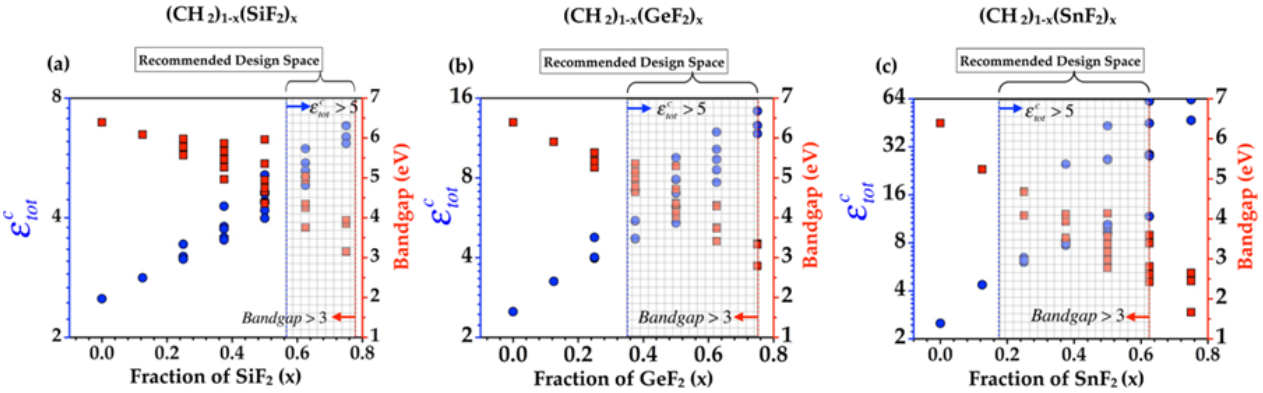

Figure 6.3. "Variation between the total dielectric constant and the band gap as a function of composition x for three classes of systems as predicted by the property expansion approach." Reproduced with permission from reference [137]. Copyright (2013) American Chemical Society.

Several methods for incorporating the SnF_2 into a polyethylene backbone were attempted by Dr. Aaron Baldwin including ADMET and some doping procedures. It was determined that these methods were either too hard to carry out or yielded too low of a molecular weight to be of any use and other synthetic routes were investigated. Dr. Charles Carraher ran numerous studies in the 1960s on the

incorporation of tin into low molecular weight polyesters through an interfacial reaction where the tin atom was bound to the oxygens of the deprotonated acids, forming a link between chains.[138–140] In those reactions, a dialkyl dichloro tin was dissolved in an organic phase, typically carbon tetrachloride although many organic solvents were reported, and a diacid was dissolved in an aqueous solution and neutralized with a base, typically sodium hydroxide or triethylamine, stirred at high speeds in a blender the organic phase was separated out and water or acetone was added to induce precipitation.[138] This reaction was expanded by Dr. Carraher to diols, diamines, and dithiols with mixed success.[141] Dr. Baldwin modified this reaction by using tetrahydrofuran (THF) as the dimethyl dichloro tin solvent resulting in a single-phase reaction carried out at much lower stirring speeds as is typical in most traditional condensation polymerizations.[71] Through this revised method, much higher molecular weight organotin polyesters were able to be synthesized, moving one step closer towards a polymer with tin in the backbone for dielectric applications.

3.1.3 Aliphatic, Aromatic, and Chiral Organotin Polyesters

The synthesis scheme for the new organotin polyesters as devised by Dr. Baldwin is laid out in **Scheme 6.1.** By choosing these diacids, several fundamental properties of tin polyesters were able to be probed and understood for further experimental design. Using aliphatic acids with an increasing number of CH_2 spacers between the acid end groups, from 1 to 8, the tin content was able to be varied. In changing the nature of the aromatic ring through the introduction of heteroatoms, the effect of electron donating and withdrawing groups adjacent to the oxygens bound

to tin was able to be studied. And finally, by adding chirality to the polymer repeat unit, the effects of crystallinity were able to be monitored.

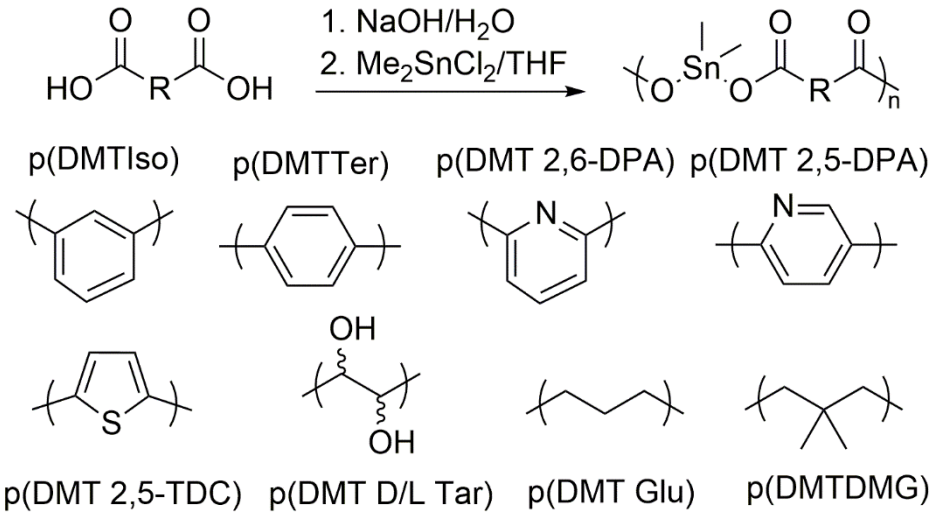

Scheme 6.1 Synthesis scheme for aliphatic, aromatic, and chiral organotin polyesters. Reproduced with permission from[56], Copyright (2016) John Wiley and Sons, Inc.

These first polymers all exhibited solubility issues and were, for the most part, only soluble in acetic acid, trifluoroacetic acid, or meta-cresol. This caused issues in producing a good quality film for dielectric measurements as the acids evaporated too quickly to give smooth films and m-cresol, having a high boiling point of 212 °C, proved difficult to remove from the cast films completely. As a result, dielectric measurements were carried out on pressed pellets to keep all results comparable. Thermally, all tin organotin polyesters showed no signs of degradation until ca. 235 °C and no thermal transitions were found through DSC investigations.

The aliphatic polymers were investigated experimentally as well as through DFT predictions to gain insight into their structure as well as their electronic

properties. The of structures of various tin polyesters had been suggested in 1969 by Peruzzo et al.,[142] and subsequently reported by Carraher[139] in 1973. However, the molecular weights reported were closer to oligomers in nature. Several important regions of the IR spectrum include the Sn-O, or tin carboxylate, mode between 630 – 643 cm^{-1}. The C-O carboxylate asymmetric bridging and nonbridging modes are seen at 1550-1580 cm^{-1} and 1635 – 1660 cm^{-1} respectively, while the symmetric bridging and nonbridging are found at 1410 – 1430 cm^{-1} and 1350 – 1370 cm^{-1} respectively. These peaks were experimentally confirmed by Baldwin et al. and predicted in DFT calculations by Dr. Ramprasad's group.[71,72] The end result of the predictions were three low energy structural motifs that the poly(dimethyltin esters) were able to arrange into depending on the bonding of the carboxylates. These three motifs, as well as various aliphatic chain conformations, are shown in **Figure 6.4** below for the poly(dimethyltin suberate) p(DMTSub), a polyester containing 6 aliphatic CH_2 spacers. All of these motifs were proven to be present in the poly(dimethyltin esters) through FTIR characterization and initially lead to processing difficulties as large coordination networks lead to semi crystalline films, however, these difficulties were later overcome.

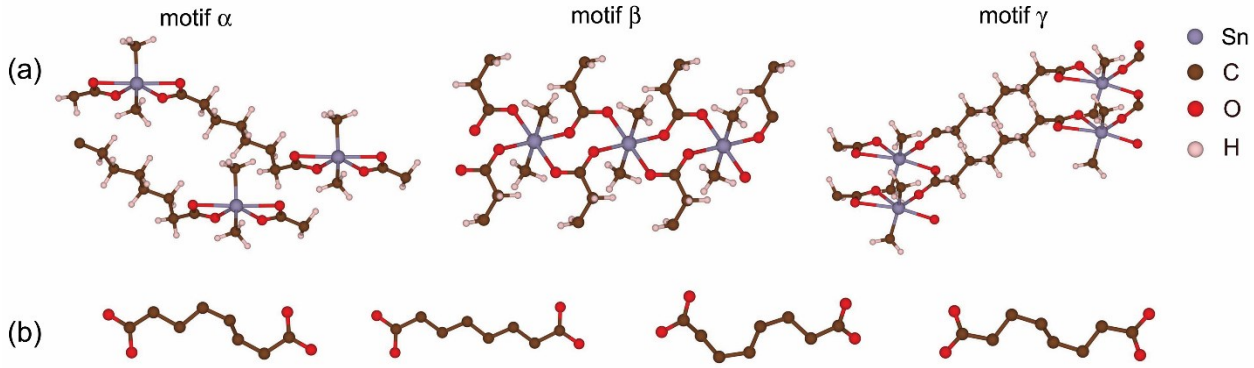

Figure 6.4. (a) Three low energy structural motifs predicted through DFT computations on poly(dimethyltin suberate) with α being intrachain, ß being interchain, and γ being a hybrid of both. (b) Four possible chain conformations of the aliphatic linkers. Reproduced with permission from reference[72]. Copyright (2015) American Chemical Society.

The coordination network formation due to the interchain and hybrid motifs posed film processing difficulties, and some of the polyesters also exhibited solubility issues in similar solvents. To remove any processing variations from the results, all the aliphatic polymers were electrically characterized as pressed pellets for dielectric spectroscopy. The dielectric constant and band gap verse the number of CH_2 units in the aliphatic spacer in were experimentally determined and plotted alongside the calculated values for each of the three different motifs in **Figure 6.5**. In general, the experimental and computational results followed a similar trend and were closely related, with the dielectric constant decreasing as aliphatic spacers were added. This made sense as less metal content gave rise to a lower ionic contribution to the dielectric constant. In addition, the band gaps were mostly around 4 to 5 eV which has been previously considered acceptable for an insulator in this study. However, it appeared that 5 - 7 aliphatic spacers were ideal for high dielectric constants as it was

a secondary plateau in the results. In the case of p(DMTSub), the tin polyester exhibited a dielectric constant of 6.6 with a band gap of 6.7 eV proving to be an exceptionally promising material.[72] In order to validate these computational results, the refractive index was taken for some of the tin polyesters, which when squared gives the electronic portion of the dielectric constant, and correlated well with the results predicted by DFT.[71]

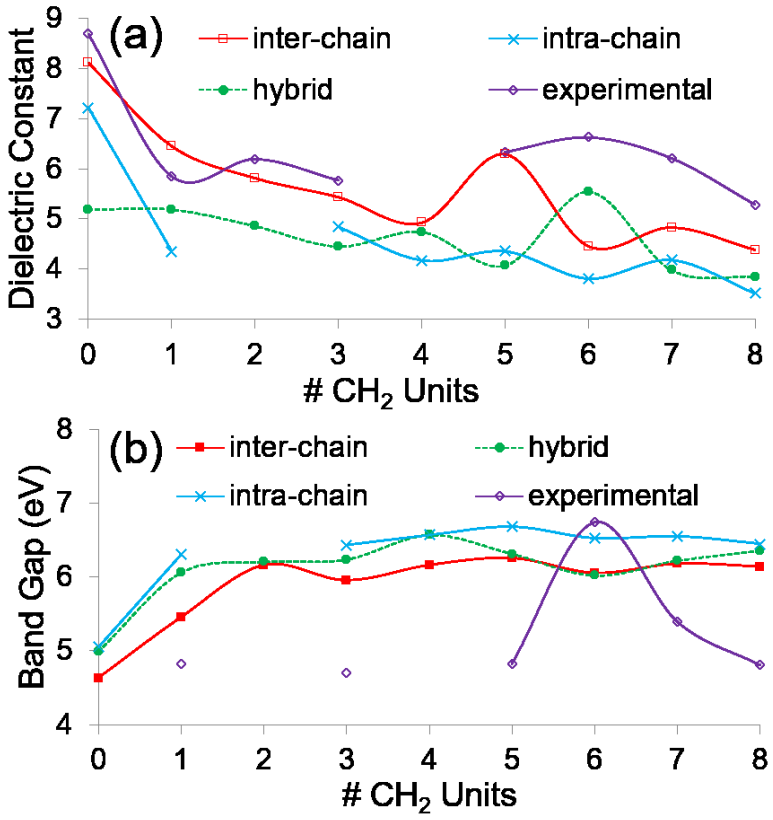

Figure 6.5. Dielectric constant and band gap verse number of aliphatic CH_2 spacers for tin polyesters with experimental values alongside predicted DFT values. Reproduced with permission from reference[72]. Copyright (2015) American Chemical Society.

Aromatic and chiral organotin polyesters were also studied by Baldwin et al., consisting of the building blocks shown in **Scheme 6.1**. Of the aromatic systems,

three types were chosen, two neutral, two electron-withdrawing, and one electron donating ring based on benzene, pyridine, and thiophene respectively. The systems with meta attachments to the main chain were found to have higher dielectric constants of around 5.5 while then ortho and para connected polymers had slightly lower dielectric constants than 5. The aromatic rings also gave an increased thermal stability to these polymers, and no degradation was recorded before 250 °C while dielectric losses were all less than three percent and one as low as 0.39%. By modifying the chirality in the polymer backbone and incorporating D- and L- forms of tartaric acid the crystallinity was able to be tuned to a degree. Using a racemic mixture of D- and L- tartaric acid the crystallinity of the polymers increased while using either enantiomer by themselves resulted in a more amorphous structure as determined by X-ray diffraction. Unfortunately, the addition of hydroxyl groups in the tartaric acid lead to an increase in loss which was attributed to an increased affinity for water, a highly polar molecule with a high dielectric constant, that can migrate in the electrical fields created during dielectric testing.[73]

6.2 Optimization of Organotin Polyesters[143]

In order for a polymer to serve as a dielectric for energy storage applications, it needs to be able to survive in an electric field without breaking down. High field characterization techniques require a high-quality film that is mostly free from defects and impurities. In addition, a thin film, on the order of 10 microns, is required due to limitations in the power source. Previously almost all the organotin polyesters

were tested as pressed pellets to provide a uniform testing environment as only a few could be cast as thin films. Among the few that could be cast as thin films, such as p(DMTGlu) and p(DMTSub), a high degree of crystallinity was observed due to the strong tendency for interchain coordination during the drop cast process. In general, organotin polyesters with longer aliphatic linkers showed a larger degree of crystallinity and longer crystalline branches. To disrupt the interchain networks that lead to crystallizations, a new diacid was introduced, 3,3-dimethylglutarate (DMG), which has two methyl groups in the aliphatic spacer. This DMG group imparted enough steric hindrance that large interchain networks between the tin centers and nearby oxygens could be suppressed to a point where amorphous films were produced by a solvent cast method.

6.2.1 Material and Synthesis of Organotin Copolymers

In order to understand the network formation process and the effect that it has on dielectric properties, a systematic study was devised to form blends and copolymers of the new diacid DMG with the non-hindered diacid with the same number of aliphatic spacers, Glu, and the diacid that resulted in the highest dielectric constant and band gap as a pressed pellet, Sub, with 6 aliphatic spacers. The synthesis was carried out following **Scheme 6.1** where homopolymers of p(DMTGlu), p(DMTSub), and p(DMTDMG) were each individually prepared to be characterized independently and then blended together. The blend ratios were all prepared with at least 50% by weight p(DMTDMG) to ensure an amorphous film and then increased in increments of 10% until the concentration was 90% p(DMTDMG) by weight with

10% of the other organotin polyester. For example, a blend with 20% of the diacid being Glu and 80% being DMG would be named as poly(dimethyltin glutarate)20-*b*-(dimethyltin 3,3-dimethyl glutarate)80] or p(Glu20-*b*-DMG80). The blends were then dissolved in meta-cresol and stirred for an hour to ensure complete dissolution. Prior to being drop cast, the blends were filtered through a 0.45 micron PTFE syringe filter to remove any laboratory containments that may have entered the solution. Copolymers were synthesized in the same weight percent ratios between diacids as was used for the blends. This resulted in a range of copolymer compositions with the following naming scheme. For example, the synthesis of a copolymer with 20% of the diacid being Glu and 80% of the diacid being DMG the resultant copolymer would be named poly[(dimethyltin glutarate)20-*co*-(dimethyltin 3,3-dimethylglutarate)80] or p(Glu20-*co*-DMG80). Solutions of the copolymers were prepared similarly to the blends with the copolymer dissolved in meta-cresol for 1 hour while stirring and then filtered through a 0.45 micron PTFE syringe filter.

3.2.2 Structural Characterization: FTIR and XRD

While p(DMTGlu) had previously been characterized in-depth by Dr. Baldwin, p(DMTSub) and p(DMTDMG) was structurally studied by FTIR and XRD for this work.[71] The experimental and predicted FTIR are shown in **Figure 6.6** for p(DMTDMG) in (a) and (b) with p(DMTSub) in (c) and (d). The FTIR of the homopolymers are shown to be a mixture of the predicted DFT results for the Intra, Inter, and Hybrid motifs as have previously been found and are consistent with the predictions made by Puruzzo et. al.[142] The presence of both symmetrical and

asymmetrical carboxylate stretching frequencies is possible since tin is able to take on both a tetrahedral and octahedral configuration.

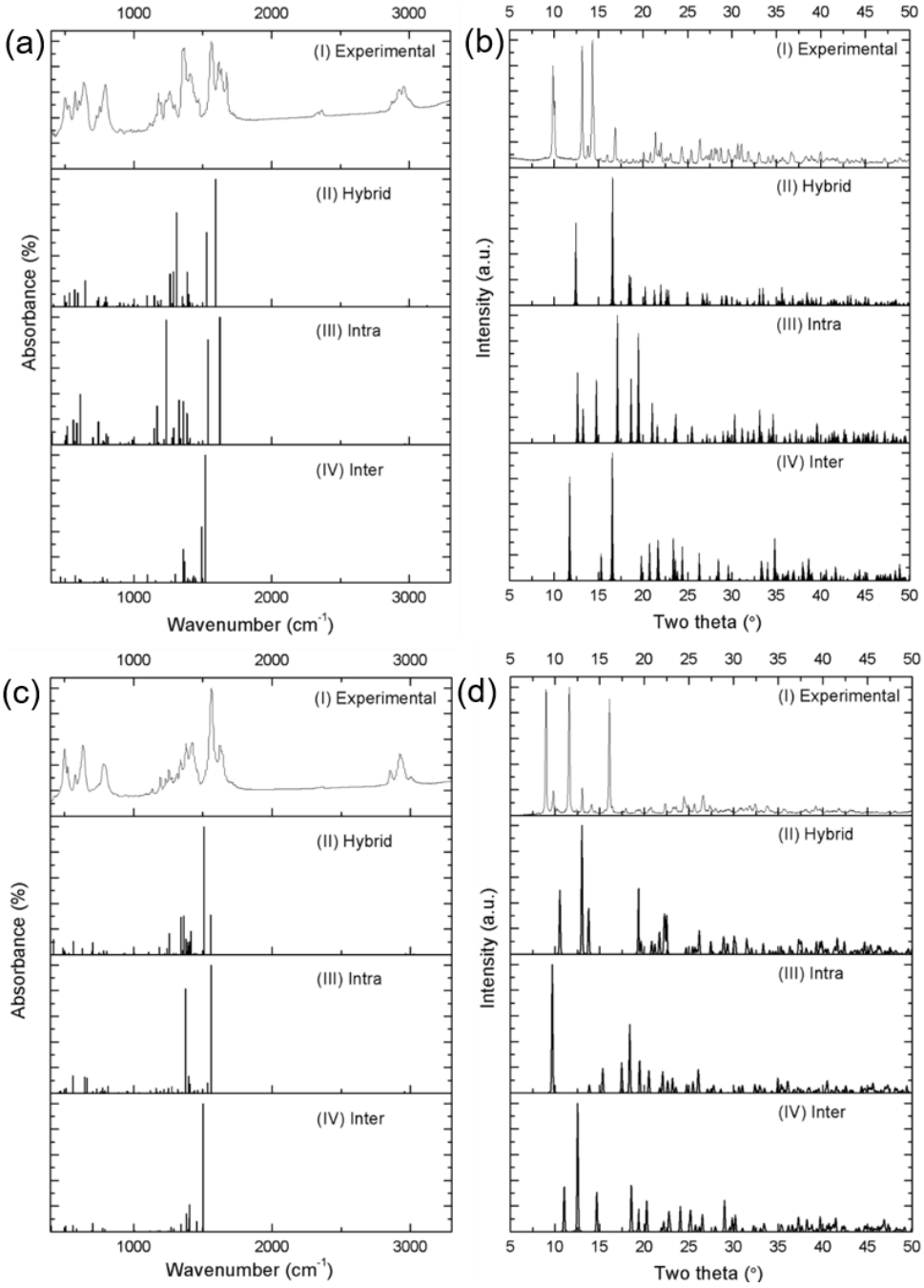

Figure 6.6. "Comparison of p(DMTDMG) (a) FTIR and (b) powder XRD spectra alongside p(DMTSub) (c) FTIR and (d) powder XRD spectra. DFT results for the three different motifs are compared beneath the experimental results." Copyright (2016) American Chemical Society.[143]

The FTIR analysis of the copolymers showed a similar result as would be expected and are found in **Figure 6.7** and the copolymers of p(DMTGlu) are omitted due to the fact that they show a similar result. FTIR analysis of the blends was not carried out as it would be a mixture of the spectra found from both homopolymers. To process the polymer powders into films for structural analysis, several techniques were tested. Glass microscope slides were chosen as the substrate so that it would not interfere with the x-ray diffraction measurements. While a spin coating procedure was carried out using 1,1,1,3,3,3-Hexafluoro-2-propanol (HFIP) the resultant films were on the order of 10s of nanometers thick and too thin for any electrical characterization. To ensure that the XRD was carried out on films as similar to the ones used for electrical measurements as possible, a 10% by weight solution of homopolymers, blends, and copolymers were prepared in m-cresol and drop cast onto glass 1 inch by 1-inch glass microscope slides after passing through a 0.45 micron PTFE syringe filter. The films were dried at 100 °C for one hour under the fume hood to evaporate the solvent before being transferred to a vacuum oven to be dried at 150 °C for 24 hours. The cast films were unable to be removed from the glass substrate after drying and were measured as prepared in a poly(methyl methacrylate) sample holder. The bottom of the glass slide was secured to the sample holder by a small amount of putty in such a way that it would not interfere with the measurement.

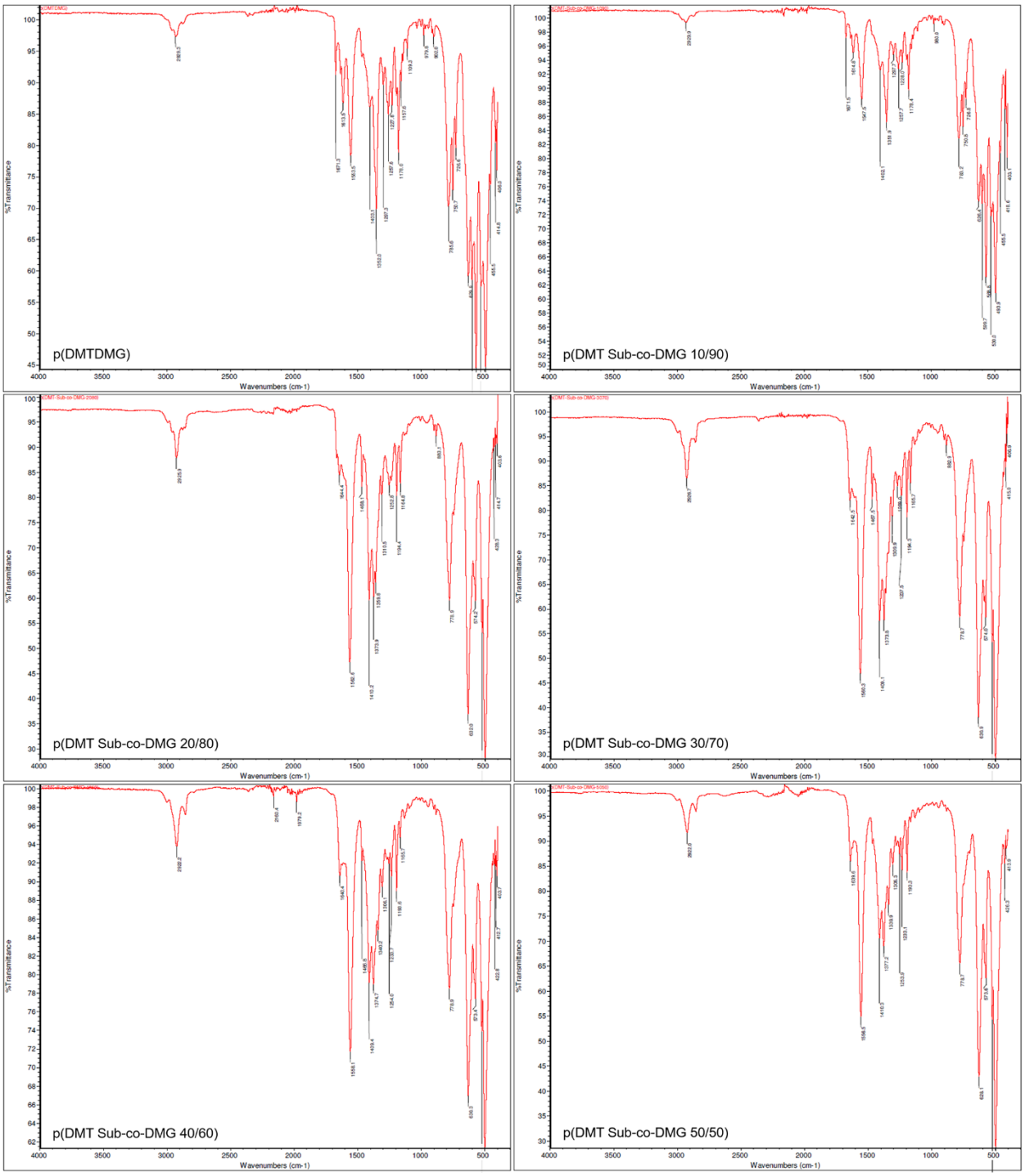

Figure 6.7. FTIR spectrum from p(DMTDMG) alongside all of the copolymers with p(DMTSub) to show the tin oxygen bonds necessary for the formation of an organotin polyester. Copyright (2016) American Chemical Society.[143]

Blends of p(DMTSub) with p(DMTDMG) were shown to be amorphous, both by visual inspection and by XRD as seen in **Figure 6.8.**

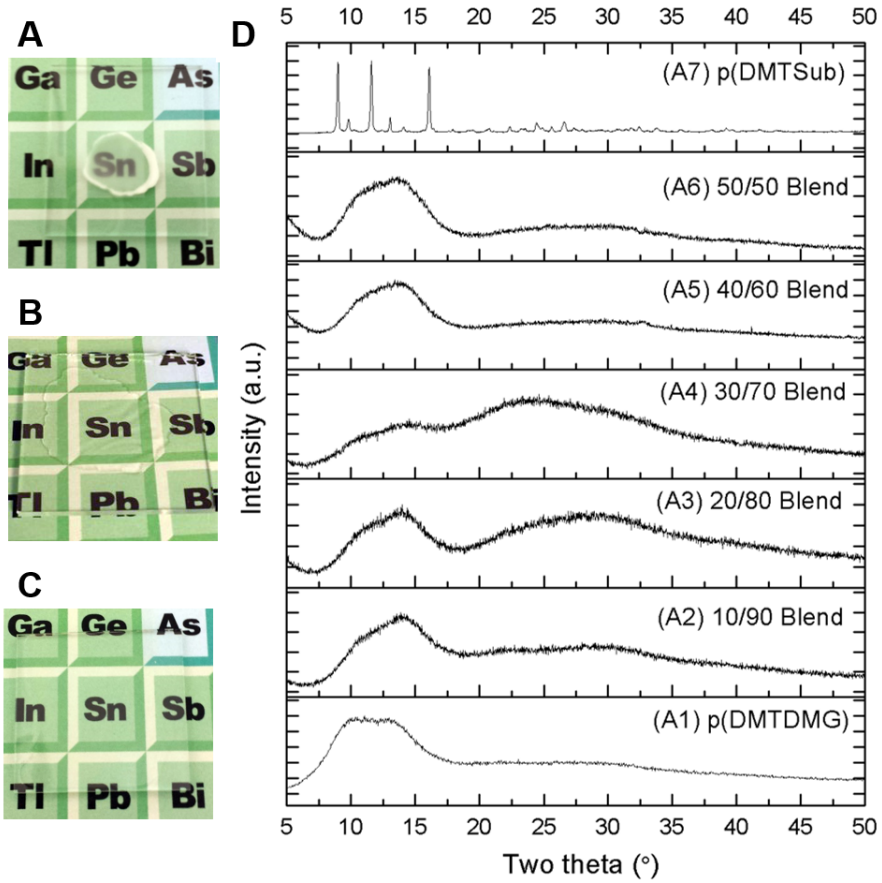

Figure 6.8. Film photos of (A) p(DMTSub), (B) p(Sub30-*b*-DMG70), and (C) p(DMTDMG) cast on glass microscope slides with (D) x-ray diffraction spectra of homopolymers and blends of p(DMTSub) and p(DMTDMG). Copyright (2016) American Chemical Society.[143]

To demonstrate the difference between the crystalline powder XRD pattern and the amorphous film XRD the copolymers of p(DMTSub) with p(DMTDMG) and their respective homopolymers were plotted together in **Figure 6.9.** For both comparisons, the XRD pattern for p(DMTSub) was taken from the powder as it was very difficult to get a homogenous film from p(DMTSub) that was noticeably different

from the powder pattern. The left column in **Figure 6.9A** shows the powder XRD pattern of p(DMTDMG) at the bottom, with copolymers of increasing p(DMTSub) content in them as the plot continues upward and the patterns indicate a clear shift from one homopolymer to the other. The second column in **Figure 6.9B** shows that the copolymers produced amorphous films up to 30% by weight Sub and then the resulting copolymers produced opaque and crystalline films. The crystalline films produced from the copolymers were different from the homopolymers as they were homogeneous throughout and lacked any significant branching patterns that both p(DMTGlu) and p(DMTSub) produced.

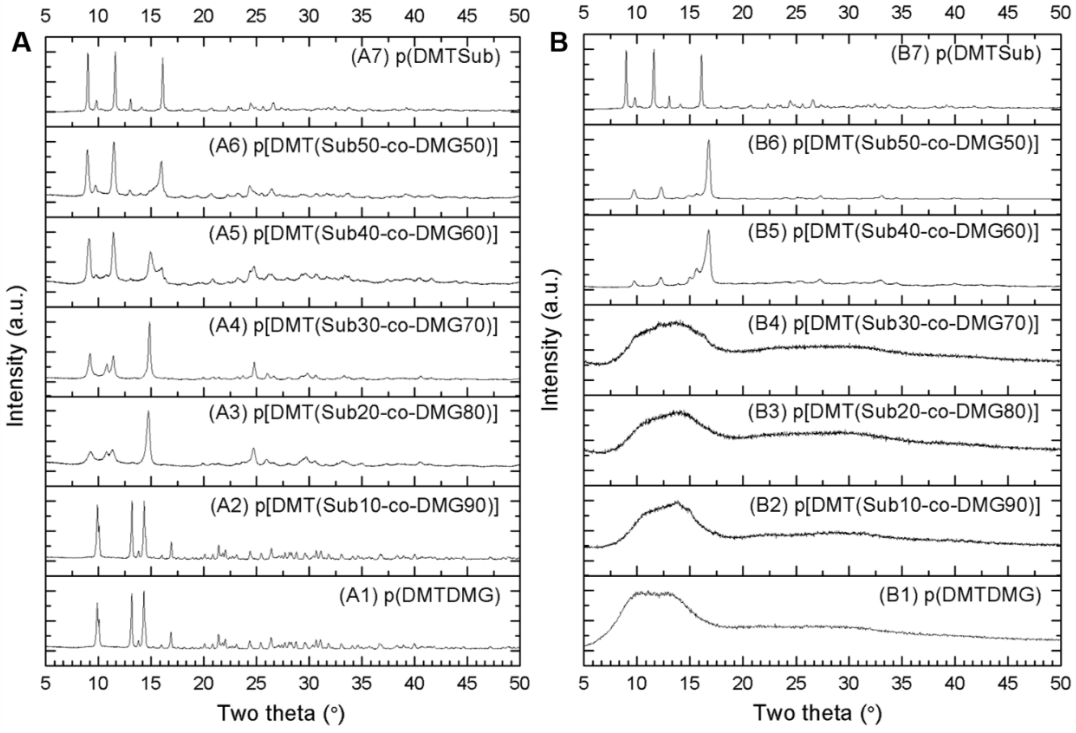

Figure 6.9. X-ray different patterns of (A) powder homopolymers and copolymers of p(DMTSub) and p(DMTDMG) along films cast from those same polymer compositions (B). Copyright (2016) American Chemical Society.[143]

6.2.3 Thermal Characterization

The thermal characterization for p(DMTSub) had previously been carried out by Dr. Baldwin et al., and so the results are omitted from the following figures and can be found in the references. However, it did not vary significantly from the other organotin polyesters.[72] The TGA results are shown in **Figure 6.10** with the onset of degradation found to be between 245 °C and 260 °C which is sufficient for most dielectric applications. The DSC results in **Figure 6.11** show no thermal transitions for any of the organotin copolymers below their degradation temperature.

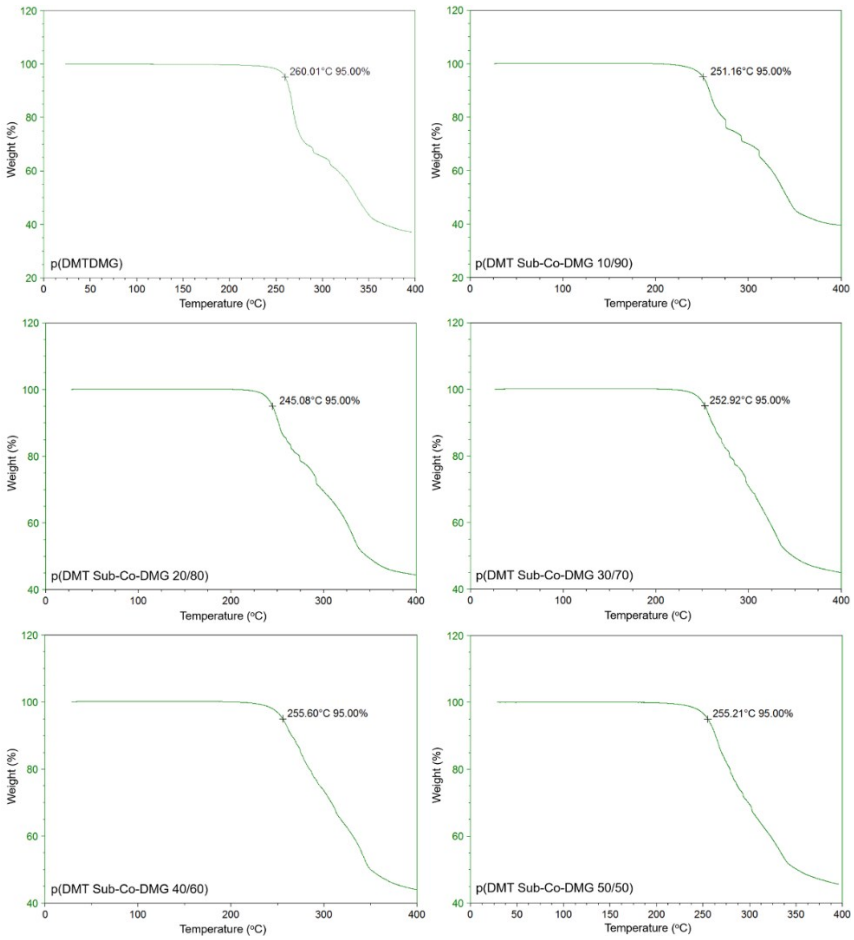

Figure 6.10. Thermal gravimetric analysis (TGA) of the homopolymer p(DMTDMG) and copolymers produced with p(DMTSub) run in a nitrogen environment. Copyright (2016) American Chemical Society.[143]

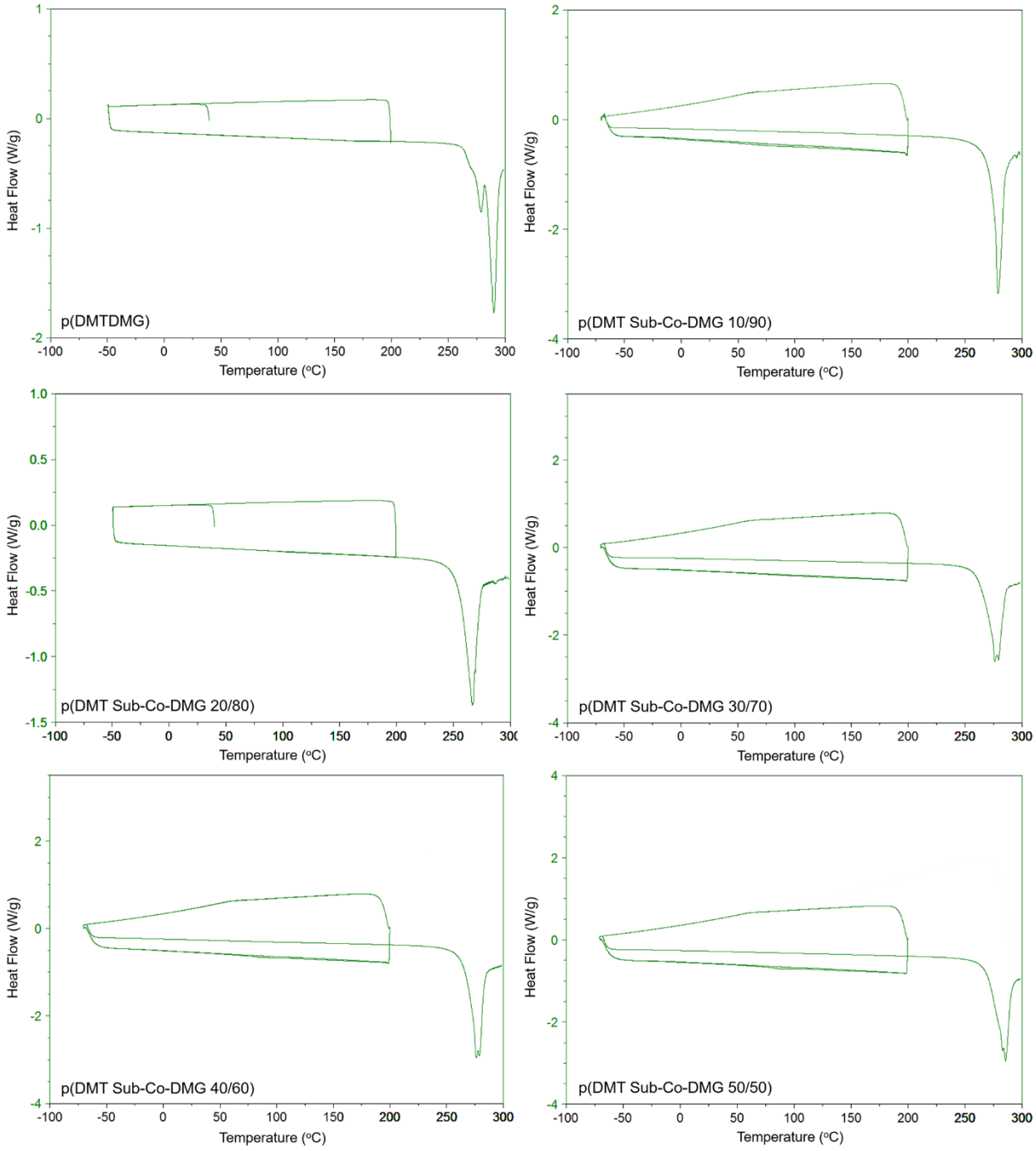

Figure 6.11. Differential scanning calorimetry of the homopolymer p(DMTDMG) and copolymers produced with p(DMTSub) run in a nitrogen environment. Copyright (2016) American Chemical Society.[143]

6.2.4 Band Gap Determination by UV-Vis Spectroscopy

The band gaps for p(DMTDMG) and the copolymers were determined optically by scanning the UV-Vis spectrum from 800 nm down to 200 nm and observing the onset of UV absorption. Through the Maxwell equation, the optical band gap can be found from taking $1240/\lambda_{onset}$. Films were drop cast onto quartz microscope slides, transparent to UV light, from a 10% m-cresol solution. The UV-Vis spectra are plotted in **Figure 6.12** with the onset overlaid graphically. The band gap for p(DMTSub) was the highest of all the organotin polyesters at 6.7 eV. However, the band gap for p(DMTDMG) was lower at 4.8 eV. Due to the nature of a copolymer's band gap, the portion with the lowest band gap is going to dominate the overall result and a rule of mixtures does not apply. As a result, all of the copolymers had band gaps between 4.8 eV and 4.9 eV which is greater than the threshold of 3 eV initially set up as a screening criterion for high breakdown materials. P(DMTDMG) was predicted by DFT to have a higher band gap of 5.9 eV which would have made it an even more promising candidate for an insulator. However, DFT over predicted the band gaps for the aliphatic organotin polyesters except for p(DMTSub), so the results are not surprising.[72]

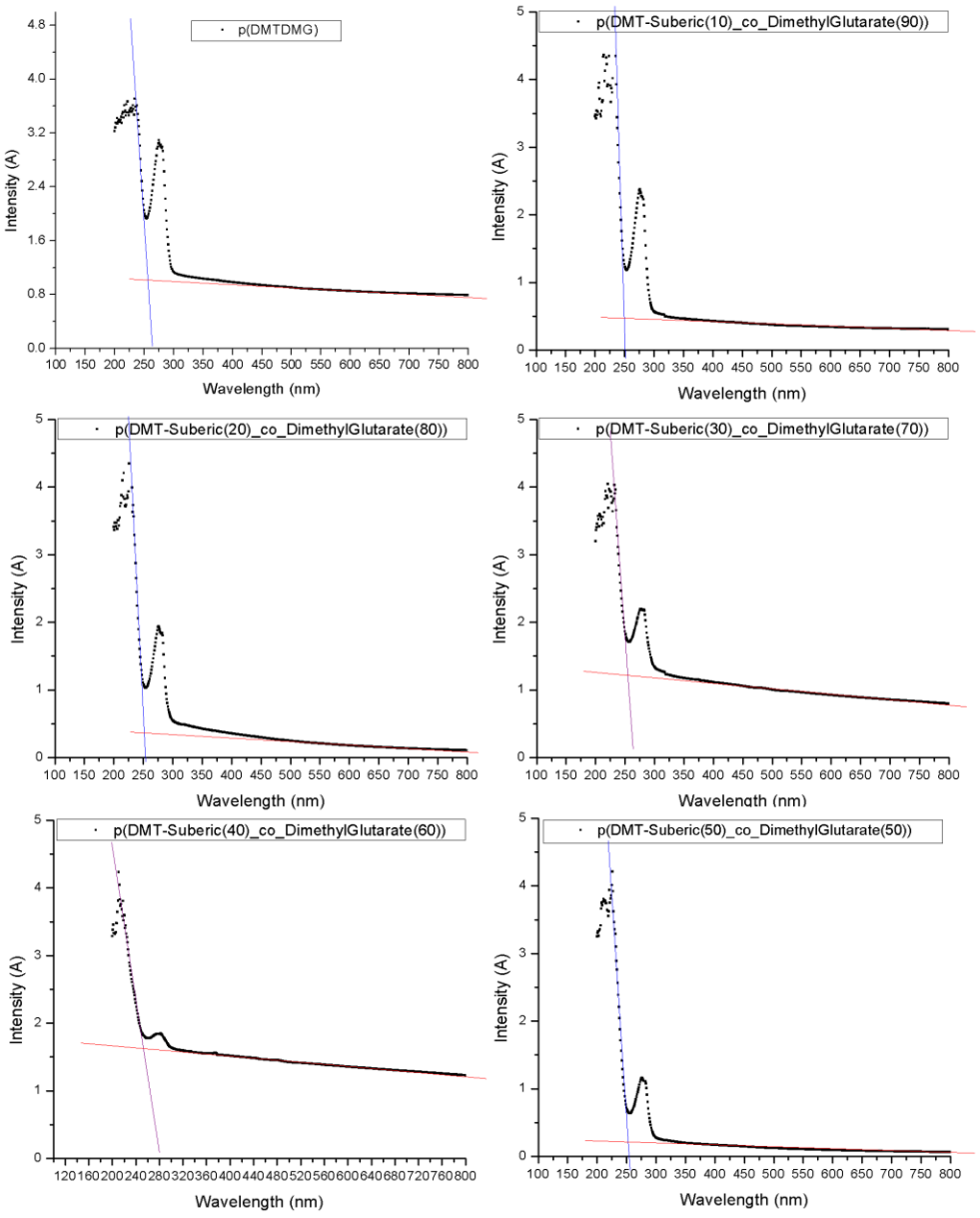

Figure 6.12. UV-Vis spectra for p(DMTDMG) and copolymers with p(DMTSub) taken from scanning 800 nm down to 200 nm. Copyright (2016) American Chemical Society.[143]

6.2.5 Dielectric Properties

The dielectric properties of organotin polyesters were characterized by dielectric spectroscopy over the range of 20 Hz to 1 MHz on an LCR meter as outlined in Chapter 2. The electronic properties including dielectric constant (K), loss, and band gap for the homopolymers, blends, and copolymers of p(DMTSub) and p(DMTDMG) are listed in **Table 6.1.** The naming convention used to save space in the table is as follows. Different blends were named as BP10, BP20, BP30, BP40 and BP50 for 10%, 20%, 30%, 40% and 50% of p(DMTSub), respectively, with the remainder being p(DMTDMG). The copolymers were named as CP10, CP20, CP30, CP40, and CP50 for 10%, 20%, 30%, 40%, and 50% of the suberic acid moiety, respectively, with the corresponding 3,3-dimethyl glutaric acid. Overall, the organotin polyesters had band gaps above 4.8, dielectric constants above 5, and losses below 2%. An important note for why the values of p(DMTSub) listed here are different from those provided by Dr. Baldwin are due to previous measurements being conducted on pressed pellets while these current measurements were taken on drop cast films on stainless stain shim stocks. In doing so it was noted that the dielectric constant dropped from 6.6 to 5.6 at 10 kHz which matched the predicted value of 5.5 by DFT.

Table 6.1. Dielectric constant and loss values are taken at 10 kHz for tin polyesters and their band gaps. DFT results shown in (parenthesis) are calculated from the average of the three motifs. [143]

Polymer	p(DMTSub)	p(DMTDMG)	BP10	BP20	BP30	BP40	BP50	CP10	CP20	CP30	CP40	CP50
K (10 kHz)	5.6 (5.5)	6.3 (5.3)	6.8	6.6	6.2	5.7	5.1	6.7	6.6	6.4	6.0	5.9
Loss (10 kHz)	1.7	1.2	0.9	0.8	0.7	0.9	0.5	1.8	1.0	1.0	1.4	1.8

Band gap (eV)	6.7 (6.2)	4.8 (5.9)	4.8	4.8	4.8	4.8	4.8	4.8	4.9	4.9	4.9	4.9

Figure 6.13A and Figure 6.13B shows the dielectric constant and loss as a function of frequency for the homopolymers and blends of p(DMTSub) with p(DMTDMG). For the homopolymers p(DMTDMG) had the higher dielectric constant of 6.3 compared to 5.6 for p(DMTSub). However, two of the blends had a higher dielectric constant than either. BP10 had the highest dielectric constant of 6.8 while BP20 was next highest at 6.6, both at 10 kHz. Both of these blends had loss values below 1% making them promising candidates for further characterization. The remaining blends had dielectric constants less than p(DMTDMG) with BP30 at 6.2, BP40 at 5.7 and finally, lower than p(DMTSub) is BP50 at 5.1. With a decrease in p(DMTDMG) content, the free volume of the system would drop which could explain the reduced dielectric constant. The reason that BP was found to be below p(DMTSub) could be due to a micro or nano segregation between the different homopolymers which would lead to reduced film quality and higher permittivity.

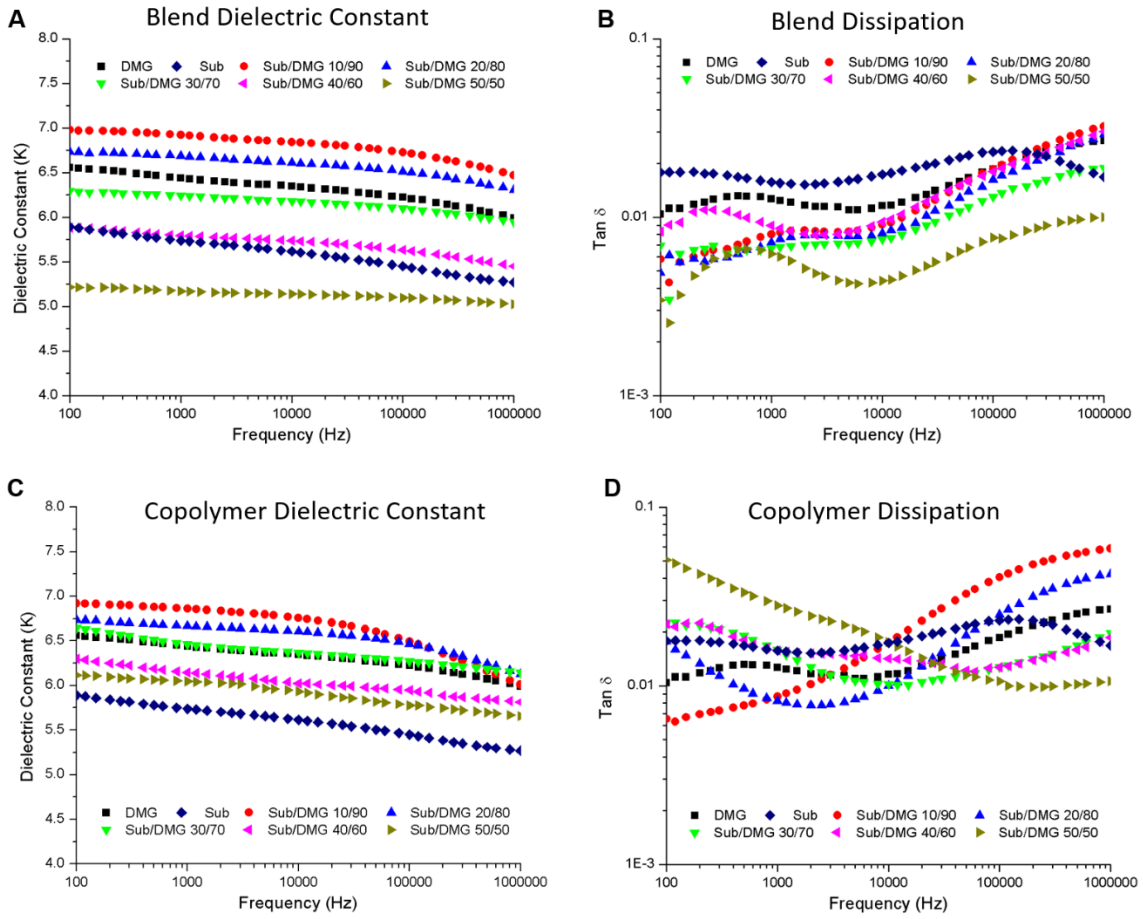

Figure 6.13. Dielectric constant (A) and loss (B) plotted against frequency for homopolymer and blends, and dielectric constant (C) and loss (D) plotted against frequency for homopolymers and copolymers of p(DMTSub) and p(DMTDMG) drop cast from m-cresol onto stainless steel shim stocks. Copyright (2016) American Chemical Society.[143]

Figure 6.13C and Figure 6.13D shows the similar dielectric spectroscopy for copolymers of p(DMTSub) and p(DMTDMG) with a similar decrease in dielectric constant as the DMG content was decreased. One notable difference, however, is that the lowest copolymer, CP50, has a dielectric constant of 5.9 which is higher than p(DMTSub) at 5.6. This evidence gives credence to the suggestion that micro or nano

phase segregation could be occurring in the blends with reduced amount of p(DMTDMG). Since CP50 is a random copolymer, the likelihood of phase segregation would be much reduced and the homogenous film, despite being somewhat crystalline, gives a better electronic performance. While CP10 had the highest dielectric constant of 6.7, slightly lower than BP10, it is interesting that CP20 had the same dielectric constant of 6.6 as BP20. This provides a good comparison between blends and copolymers as they both also have similar loss values of 0.8% and 1%. For this reason, both BP20 and CP20 were chosen for high field characterization by D-E loop hysteresis.

6.2.6 Energy Density

All energy density measurements here were carried out in a modified Sawyer-Tower circuit in a ball to plane configuration using 3 mm diameter electrodes as detailed in **Section 2.3.6**. Previously, Dr. Baldwin carried out D-E hysteresis loops on a blend of p(Glu20-b-DMG80) and reported a maximum field of 400 MV/m with an energy density of 4 J/cc.[71] Following that result, the similar blend was measured for p(DMTSub), or BP20, and found to have a lower maximum field of 300 MV/m, but due to a higher dielectric constant had a similar energy density of 4 J/cc.[72] The copolymer, CP20, was recently studied for this optimization study and was found to withstand a higher electric field with a breakdown of 500 MV/m and a resulting energy density of 6 J/cc with an efficiency at breakdown of around 85% as shown in **Figure 6.13.**[143]

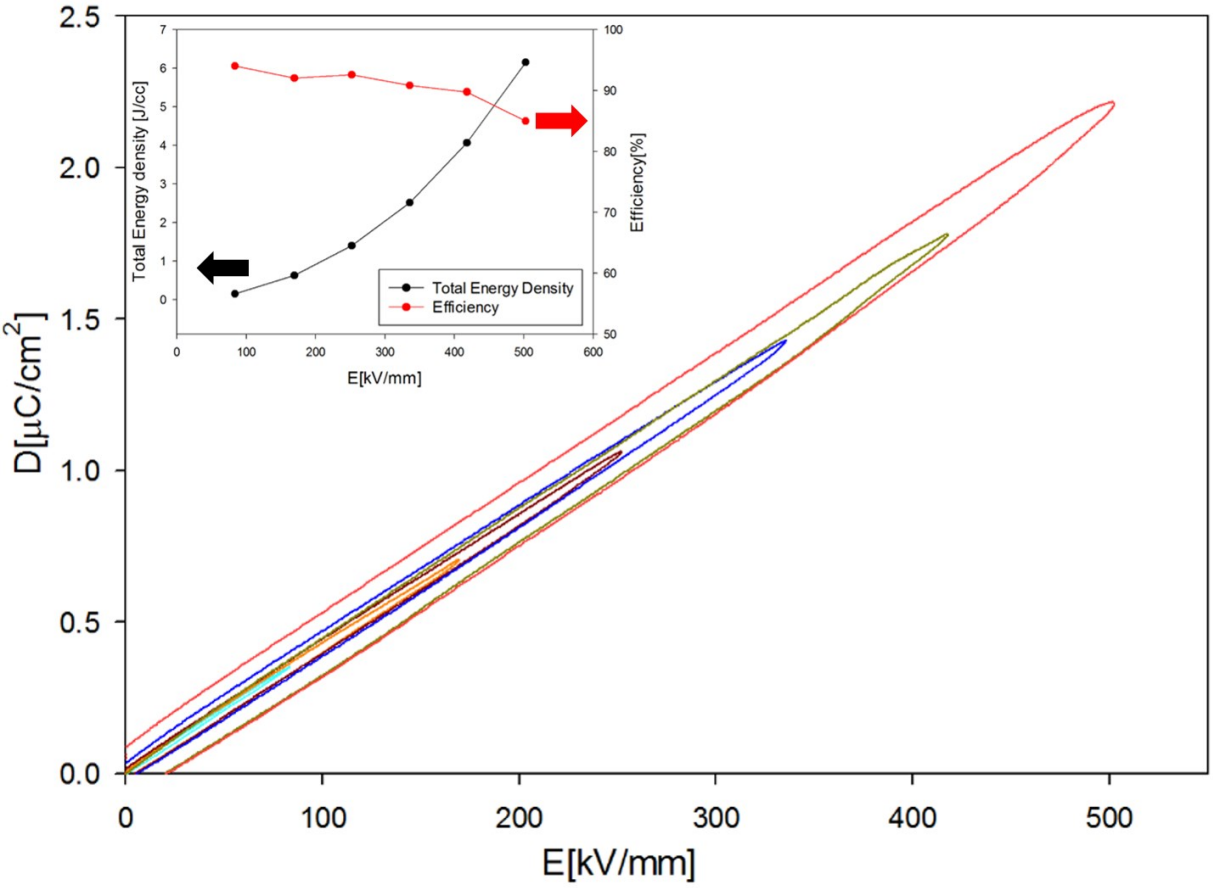

Figure 6.14. D−E hysteresis loop for p(Sub20-*co*-DMG80) or CP20 along with an inset showing the corresponding total energy density and efficiency plot. Copyright (2016) American Chemical Society.[143]

The work in Section 3.2 details the optimization of organotin polyesters for dielectric applications aided by density functional theory in a rational co-design search. By working in tandem with theorists to provide computational guidance along the way, new and promising polymers such as those containing tin could be discovered. While their development is only a few years old, organometallic polymers are proving to be a promising candidate for in the field of energy storage where their energy density has been improved from 4 J/cc to 6 J/cc which is over the all-important 5 J/cc

maximum energy density of BOPP. Despite this being a mostly symbolic barrier, it shows that with further optimization and refinement, organotin polyesters, or other metal containing polymers, could fill a niche between low-field ceramic dielectrics and high-field organic polymer dielectrics.

Chapter 7

7. Approaching the Band Gap of Metal Oxides in Metal Organic Frameworks of Cadmium and Zinc

7.1 Rational Design of Zinc and Cadmium Polyesters

The successful incorporation of dimethyl tin into a polymer backbone to produce a library of dielectric materials with tunable properties encouraged us to look towards more metals for a similar purpose. Tin is considered a post transition metal since it is placed between the transition metals to the left and the metalloids to the right. Previously Dr. Aaron Baldwin investigated silicone polymers without much success, while germanium and lead had cost issues associated with their use, effectively eliminating the rest of the group 14 elements. Transition metals are one of the most populated categories on the periodic table with about 38 elements, depending on which authority is asked and similar enough to tin that comparable chemistry could be considered. Tin is well known to exist in both the Sn(II) state with a coordination number of 4 and as Sn(IV) with a coordination number of 6 depending on the environment tin is subjected to. To better understand the structure property relationships between the metals chosen and their dielectric properties it was important to understand the effect of coordination number if any existed, which would allow better prediction of which of the 38 transition metal elements should be investigated. Zinc(II) and Cadmium(II) were chosen as a starting point since they are

close in proximity to Tin on the periodic table and each has a strong tendency to form either a 4-coordination environment in the case of Zn(II) and a 6-coordination environment in the case of Cd(II). To allow for a direct comparison to the previously studied Tin systems a series of aliphatic polyesters were synthesized for each metal with the number of CH_2 spacers varied from 1 CH_2 to 8 CH_2. This chapter will discuss the synthesis and characterization of these metal ester polymers and their relation to computationally predicted properties resulting in polymers that approach the dielectric constant of their respective metal oxides while nearly doubling their band gaps.

7.2 Experimental Synthesis of Zinc and Cadmium Polyesters

The synthesis of Zinc and Cadmium polyesters proceeded in a similar manner to the reaction adapted from Carraher for tin polyesters with some minor modifications as shown in **Scheme 7.1A** with proposed binding modes shown in **Scheme 7.1B**. Previously the diacids were deprotonated in an aqueous base, and the metal was dissolved in a miscible organic solvent, THF, which allowed for a single-phase reaction. Here, Zinc and Cadmium chlorides were soluble in the aqueous phase, and the diacids were dissolved in 1,2-dichloroethane (1,2-DCE) and deprotonated by triethylamine (TEA). The organic phase was rapidly stirred in a round bottom flask while the aqueous phase was added in a 1:1 stoichiometric amount and allowed to react at room temperature. Depending on the metals and diacids used the reaction

time varied, with the completed reaction time taken as the time precipitation occurred in the solution. The precipitate was separated out by vacuum filtration and washed with deionized water and 1,2-DCE to remove any unreacted monomers. The recovered powder was then dried under vacuum and heat to remove all remaining solvent before being massed to calculate percent yield and used for further characterization. To facilitate a concise discussion about the 16 synthesized polymers, a generic naming scheme was employed using a letter and a number. The letter designated if the polymer is Zinc (Z) or Cadmium (C) based, while the number denotes how many CH2 linkers are present between the diacids. For example, **Z2** refers to the zinc polyester created with succinic acid and **C4** refers to the cadmium polyester created with adipic acid. The complete reaction schemes can be found in the supporting information of the published manuscript.

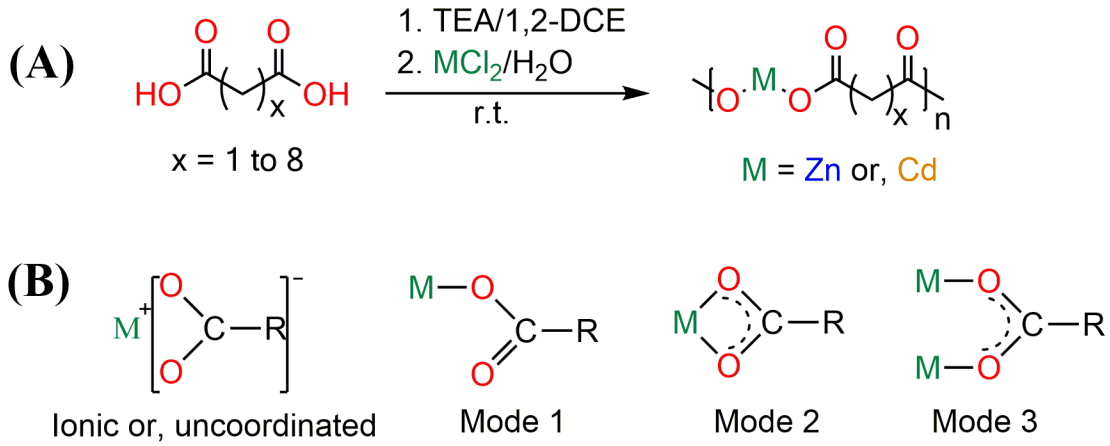

Scheme 7.1. **(A)** General reaction scheme for the Zn- and Cd-systems with different di-acids. **(B)** Possible modes of interaction between carboxylate group (COO^-) and metal, M; ionic or uncoordinated form (left), unidentate coordination (Mode 1), bidentate bridging coordination (Mode 2) and bidentate chelating coordination (Mode 3).

The reaction time and percent yield were shown to change as a function of the number of CH_2 spacers and plotted in **Figure 7.1**. **Z1** and **C1** took the longest to react, before precipitate formed, between 10 to 20 hours, with yields around 50%. For the rest of the metal polyester systems, the reaction time then dropped to below 5 hours and continued to decrease in time as the number of CH_2 spacers increased. The decrease in reaction time was shown to correlate with an increase in percent yield which leveled off at 90%. The decrease in reaction time is thought to be due to the more accessible carboxylates on attached to longer aliphatic chains. In a similar manner, an increased reaction speed could allow for higher yields as the step growth reaction would stay in solution longer to fully react before precipitating out with unreacted chain ends and effectively throwing off the stoichiometric balance in the reaction solution.

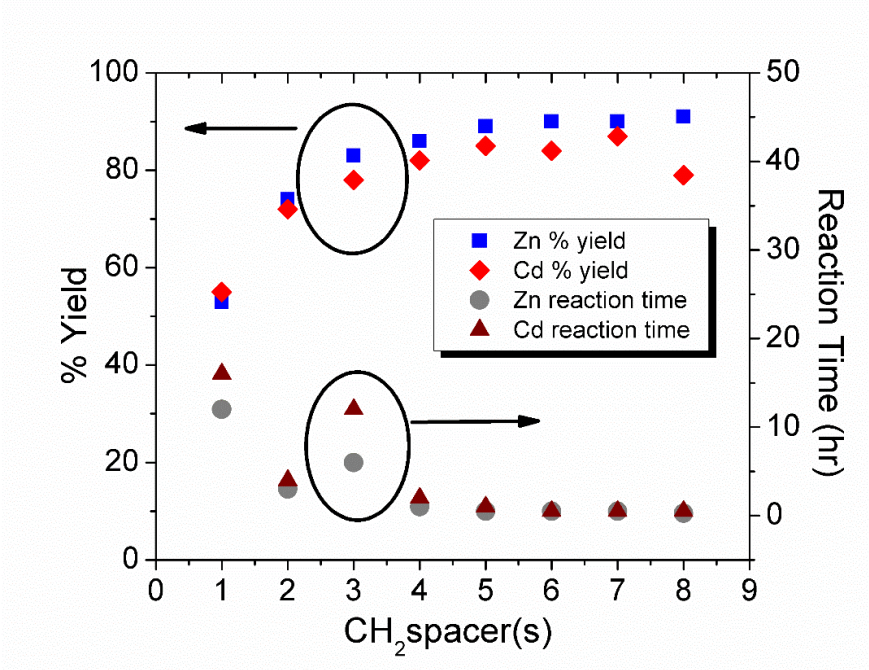

Figure 7.1. Effect of methylene (-CH_2-) unit spacers of diacids on the % yield and reaction time (hour) of the Zn(II)- and Cd(II)-polymers.

7.2.1 Density Functional Theory (DFT) on Transition Metal Polyesters

For the most part, the DFT calculations were carried out by Dr. Arun K. Mannodi-Kanakkithodi from Dr. Ramamurthy Ramprasad's group in close coordination with both myself and Shamima Nasreen from Dr. Gregory Sotzing's group to determine the structure, coordination, density, and other parameters. As in earlier chapters, the starting point for DFT computations are the low energy crystalline structures of the material so that a stable and repeating unit cell can be created. The Minima Hopping Algorithm was used to systematically explore low energy structures from the randomly chosen structure initially entered into the program since no constraints are placed on the position of atoms of the shape of the unit cells.[144,145] After an extensive search of all 16 metal polyesters was complete, the 8 lowest energy structures were saved and further analyzed. To determine coordination number, any oxygens with 2.5 angstroms of the zinc metal center and within 2.6 angstroms of the cadmium metal center were taken as coordinated to the metal. By following that procedure, Zinc appears predominantly in a 4-fold coordination environment, and cadmium mainly existed in a 6-fold coordination environment with minor exceptions which will be discussed in later sections, correlating well with the known properties of zinc and cadmium oxides. The predicted structures showed similar motifs for cadmium and zinc as they did for tin polyesters with the carboxylates forming either two or three-dimensional networks seen in **Figure 7.2**.

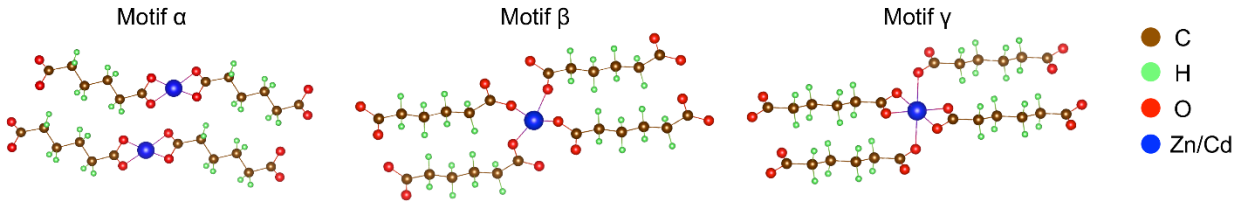

Figure 7.2. The three kinds of motifs observed for the Zn- and Cd-systems. Motif α shows a 2D motif for a 4-fold coordination, Motif ß shows a 3D motif with a 4-fold coordination, and Motif γ shows a 3D motif with a 6-fold coordination of metal.

After the low energy structures were found, the remaining properties could be computed by a variety of techniques. The dielectric constants were calculated using Density Functional Perturbation Theory (DFTP) as implemented in Vienna ab-initio Software Package (VASP).[103] The dielectric tensors corresponding to the electronic and ionic contributions to the dielectric constant were obtained from the DFPT computation. The reported (electronic and ionic) dielectric constant values were the traces of these tensors, while the total dielectric constant values were obtained as the sum of the two components. The dielectric constant was seen to depend on the structural motif, and the final values reported for each system was an average of the overall low energy structures. Furthermore, the FTIR spectra for the structures were also computed for a direct comparison with the experimentally obtained spectra. For any given structural motif, FTIR intensities for different frequency modes were calculated utilizing the DFT computations, given as a function of Born effective charge tensors and phonon mode eigenvectors for all the atoms in the system.[106] The band gap energies were estimated using the Heyd–Scuseria–Ernzerhof (HSE) electronic exchange-correlation functional for purely crystalline representation,

which offers more reliable results at sufficiently higher computational cost. While the dielectric constants were found to range from 4 to 6, which is double that of PE or PP, the band gaps were seen to be greater than 5 eV for all metal systems. DFT-predicted ground-state structures are expected to be stable at room temperatures as well, and thus, the computed values are expected to be consistent at higher temperatures as well with slight differences. Most notably, the lack of orientational motion, as restricted by DFT, would reduce or nearly eliminate any dipolar polarization that could exist in these systems from being predicted by these computational methods.

7.3 Characterization of Zinc and Cadmium Polyesters

7.3.1 Structural Characterization: FTIR, NMR, and XRD

To confirm the structure of these new metal polyesters, FTIR analysis was carried out on all 16 systems, both experimentally on a diamond ATR and computationally by DFT. The experimental FTIR spectra were plotted next to the computationally predicted FTIR which showed a reasonable correlation and are available in the supporting information of the published manuscript. Instead, a table of the FTIR spectral analysis is shown here in the interest of space in **Table 7.1**. The expected strong absorption bands were observed for C-O and in all cases were found to be in the range of 1525-1560 cm^{-1}, while symmetric bridging and non-bridging occurred at 1410-1453 cm^{-1} and 1322-1398 cm^{-1}, respectively.[146] Uncoordinated carboxylic acid (C-O) typically shows peaks around 1725–1700 cm^{-1} and was not

found in any spectra, confirming that nearly all carboxylic acids were coordinated to metals. The sharp peaks in the region 454-411 cm^{-1} were attributed to the Zn-O bond[147], while the peaks at 584-517 cm^{-1} were associated with the Cd-O bond.[148] A slight shifting of these peaks was observed in the experimental spectra compared to the predicted spectra since the predicted structures are calculated from perfectly crystalline morphologies at zero Kelvin. Four different kinds of interactions are shown for metal to oxygen bonding in **Scheme 7.1B** that are identifiable by FTIR. Symmetric and asymmetric band separation values have been shown to follow a trend where uncoordinated acid > unidentate coordination > bi-dentate (bridging>chelating) coordination.[149] The FTIR spectral analysis in **Table 7.1** showed the presence of a bidentate bridging or -inter chain motif (Mode 2) and a chelation (Mode 3), or intra chain motif, the interaction between the metal carboxylate groups for all of the Zn(II) and Cd(II) coordination polymers. The C-H stretching band was found in the region of 2850-2950 cm^{-1}, and the intensity increased as the number of -CH_2- spacers increased from **Z1** to **Z8** and **C1** to **C8** due to the sp^3 hybridized methylene unit(s). With the incorporation of more -CH_2- spacers, a three-dimensional network was possible due to the flexibility of the aliphatic chain within the coordination environment. This network was also found in the DFT modeling as 4-fold and 6-fold coordination within the possible 2D (α motif) or 3D (ß and/or, γ motifs) network. Zn(II)-polymers favored an orientation of 4-fold coordination, whereas, Cd(II)-polymers showed a preference for a 6-fold coordination environment which again matched the predicted DFT results. The larger size of the metal center of 4d-

block Cd(II), compared to that of 3d-block Zn(II), enables it to bind to this additional ligand in a 6-fold coordination environment.[150]

Table 7.1. FTIR determined binding mode of Zn(II)-coordination complex polymers and Cd(II)-coordination complex polymers with different diacids. MO = mode of coordination.

Polymer	**Z1**	**Z2**	**Z3**	**Z4**	**Z5**	**Z6**	**Z7**	**Z8**
ν_{as} COO^- (cm^{-1})	1525	1535	1527	1528	1528	1530	1527	1529
ν_{as} COO^- (cm^{-1})	1443, 1389	1445, 1386	1441, 1402	1444, 1399	1451, 1398	1446, 1398	1450, 1397	1453, 1398
$\Delta\nu$ (cm^{-1})	82, 136	90, 149	84, 124	84, 129	77, 130	84, 132	77, 130	76, 131
MO	C, B	C, B	C, B	C, B	C, B	C, B	C, B	C, B
Polymer	**C1**	**C2**	**C3**	**C4**	**C5**	**C6**	**C7**	**C8**
ν_{as} COO^- (cm^{-1})	1547	1549	1531	1527	1525	1535	1534	1535
ν_{s} COO^- (cm^{-1})	1434	1445, 1367	1395	1427, 1408	1463, 1409	1418, 1391	1423, 1398	1424, 1392
$\Delta\nu$ (cm^{-1})	113	104, 182	136	66, 119	62, 116	117, 144	111, 136	111, 143
MO	B	C, B	B	C, B	C, B	C, B	C, B	C, B

The morphology of all 16 metal polyester systems was investigated by Powder X-Ray Diffraction on the D2 Phaser to get XRD patterns for each system which are plotted in **Figure 7.3**. A general trend is seen where by an addition of CH_2 spacers results in a shift to lower angles in the first peak found between 5 and 15 2θ for **Z3** to **Z8** and **C4** to **C8**. The resultant d-spacing is shown to increase with a similar increase in CH_2 spacers, and the values are plotted in **Table 7.2**. **Z1** and **Z1** showed slightly more amorphous nature compared to systems with more CH_2 spacers.

Similarly, **C1**, **C2**, and **C3** are shown to be even more amorphous than their Zinc counterparts with broad peaks present in the XRD patterns. These results suggest that a critical number of CH_2 units is needed, depending on the metal system, to allow for proper alignment of polymers chains, and with it, an increase in crystallinity. It stands to reason that the smaller the metal atom, the less CH_2 spacers would be needed as the steric interactions caused by that metal center would be reduced.

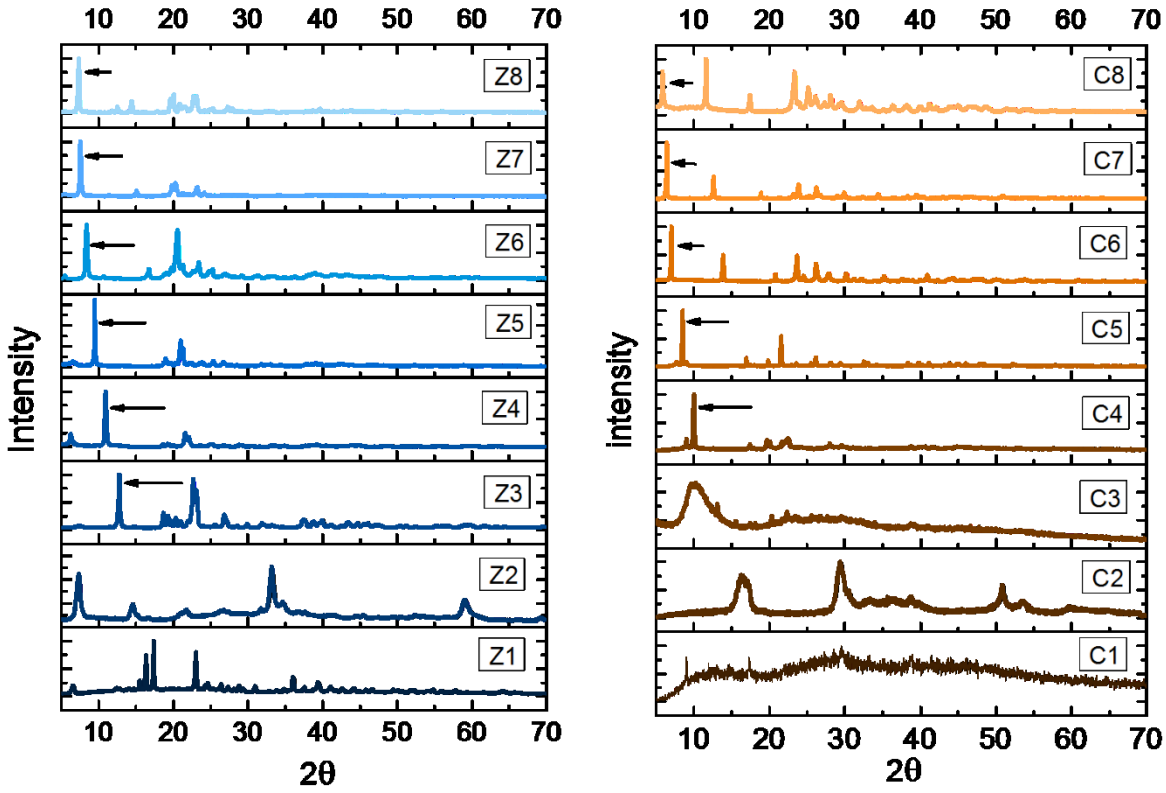

Figure 7.3. X-Ray diffraction (XRD) patterns for the Zn(II) (left) and Cd(II) (right) polymers with aliphatic spacers ranging from 1 to 8 -CH_2- units.

Table 7.2. Tabulated d-spacing with a corresponding angle in theta (θ) for the most intense peak of the Zn(II) and Cd(II) polymers, showing their trend of d-spacing with increasing number of aliphatic -CH_2- spacer.

Unit spacer		1 -CH_2-	2 -CH_2-	3 -CH_2-	4 -CH_2-	5 -CH_2-	6 -CH_2-	7 -CH_2-	8 -CH_2-
Zn(II)	Angle (θ)	8.6913	16.6013	6.3648	5.4646	4.7363	4.1799	3.7855	3.6539
	d-spacing	10.1619	5.3336	13.8702	16.1530	18.6351	21.1142	23.3134	24.1521
Cd(II)	Angle (θ)	14.7705	14.7299	5.0903	4.9993	4.2609	3.5022	3.1889	2.5994
	d-spacing	5.9904	6.0067	17.3399	17.6553	20.7132	25.1983	27.6736	33.9481

NMR was taken using acetic acid-d4. The integration per proton is calculated from the sum of the acid chain ends divided by the number of protons from the chain end. The number of repeat units, n, is determined by dividing the integral of the triplet at δ = 2.457 ppm by the number of protons, 4, and dividing by the integration per proton. Mn is then calculated from the sum of the FWchain end + (FWrepeat unit) (n). **Figure 7.4** and **Figure 7.5** show the NMR spectra for Z3 and C3 with peaks assigned. Polymer **Z3** had a chain end ratio of 0.015/4 or 0.00375 resulting in a degree of polymerization of n = (3.964/4)x(1/0.00375) = 264 repeat units. Using the repeat unit formula weight of 195 g/mol and accounting for end groups, the molecular weight came out to 52,744 g/mol. Polymer **C3** had a chain end ratio of 0.015/4 or 0.00375 as well, resulting in a degree of polymerization of n = (4.043/4)x(1/0.00375) = 270 repeat units. Using the repeat unit formula weight of 248 g/mol and accounting for end groups, the molecular weight came out to 67,145 g/mol. Both these molecular weights are sufficiently long to allow for chain entanglements and can be considered polymers.

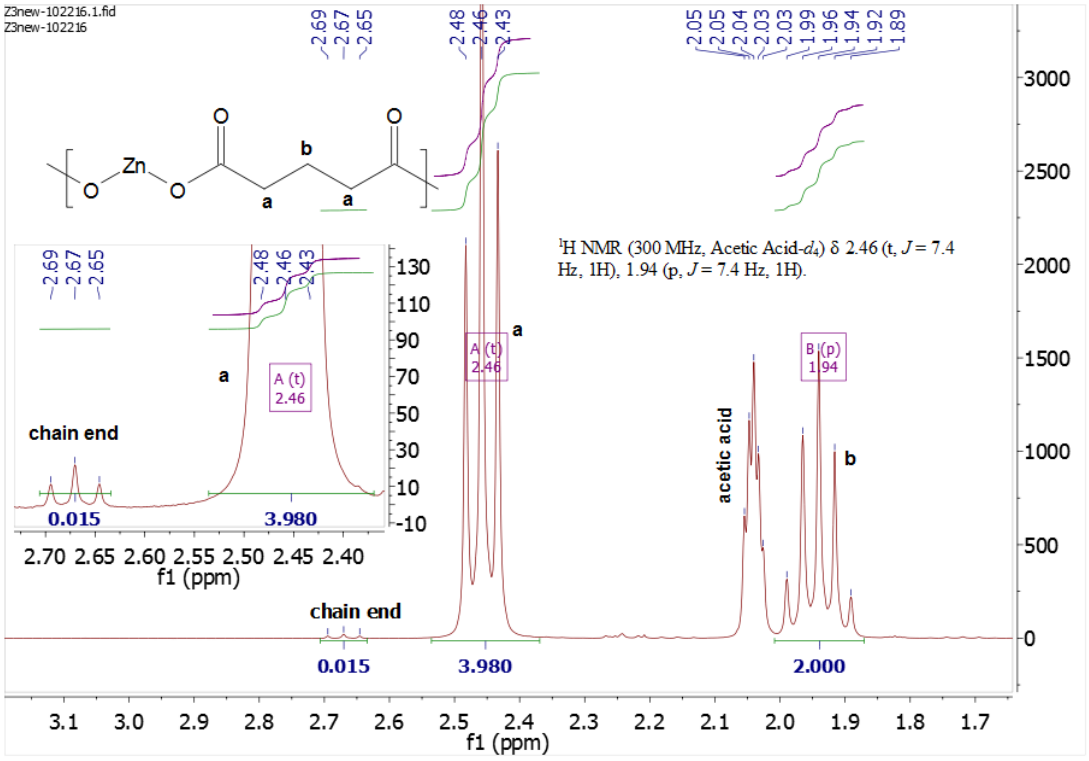

Figure 7.4. [1]H-NMR of **Z3** showing a molecular weight of 52,744 g/mol.

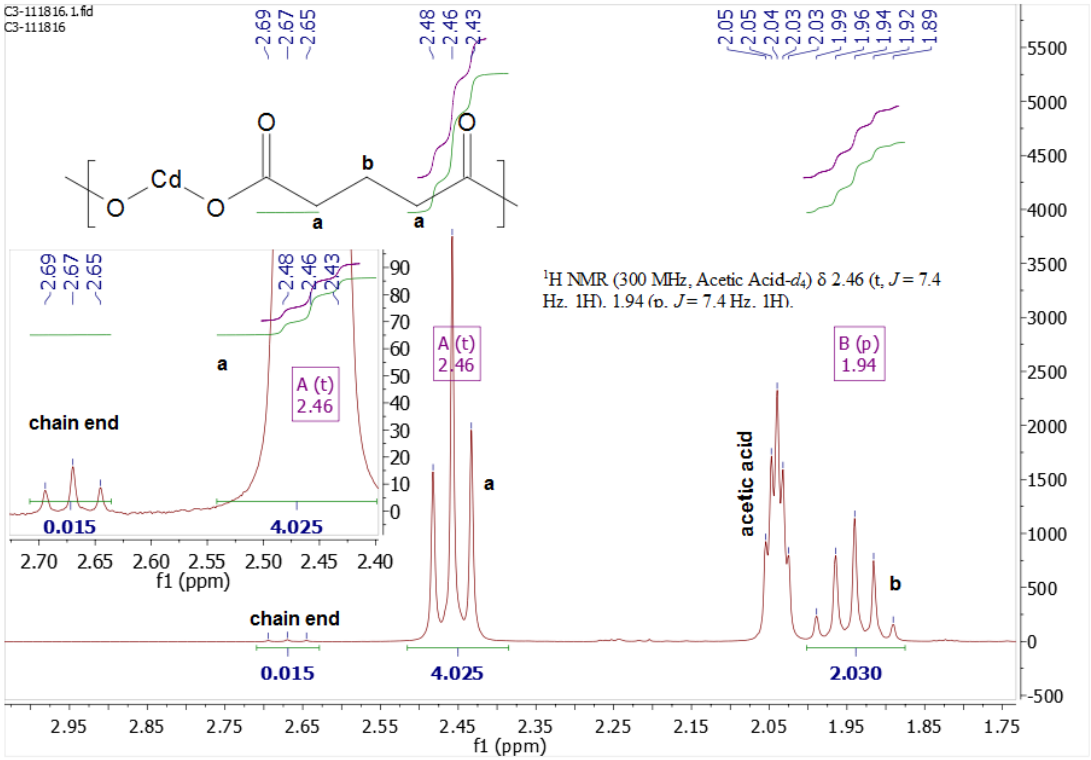

Figure 7.5. [1]H-NMR of **C3** showing a molecular weight of 67,148 g/mol.

7.3.2 Thermal Characterization

Thermal characterization was carried out by Thermogravimetric Analysis (TGA) to determine the onset of degradation (T_d) and by Dynamic Scanning Calorimetry (DSC) to determine thermal transitions such as glass transition temperature (T_g) and melting temperature (T_m). No thermal transitions were seen in the DSC below the degradation temperature of the metal polymers, and as such the DSC traces are not shown, however, they can be viewed in the supporting information of the published manuscript. The TGA traces are shown in **Figure 7.6** with the metal polyesters with the same number of CH_2 spaces overplayed on the same plot. Two separate degradation temperatures are reported in **Table 7.3**, the first one being the onset temperature (T_d) as calculated by the intersection of the two slopes, and the second being the temperature at 5% weight loss ($T_{5\%}$). The thermal analysis shows that the zinc polyesters are stable until roughly 300 °C while the cadmium polyesters are stable at a lower temperature, around 250 °C.

Table 7.3. Thermal data from TGA showing temperature at onset of degradation (T_d) and temperature at 5% weight loss ($T_{5\%}$)

Zn(II) polymer(s)	**Z1**	**Z2**	**Z3**	**Z4**	**Z5**	**Z6**	**Z7**	**Z8**
T_d (°C)	164	327	315	326	332	327	303	311
$T_{5\%}$ (°C)	215	419	360	370	355	361	345	333
Cd(II) polymer(s)	**C1**	**C2**	**C3**	**C4**	**C5**	**C6**	**C7**	**C8**
T_d (°C)	263	317	310	245	233	293	273	280
$T_{5\%}$ (°C)	271	196	210	279	296	328	293	301

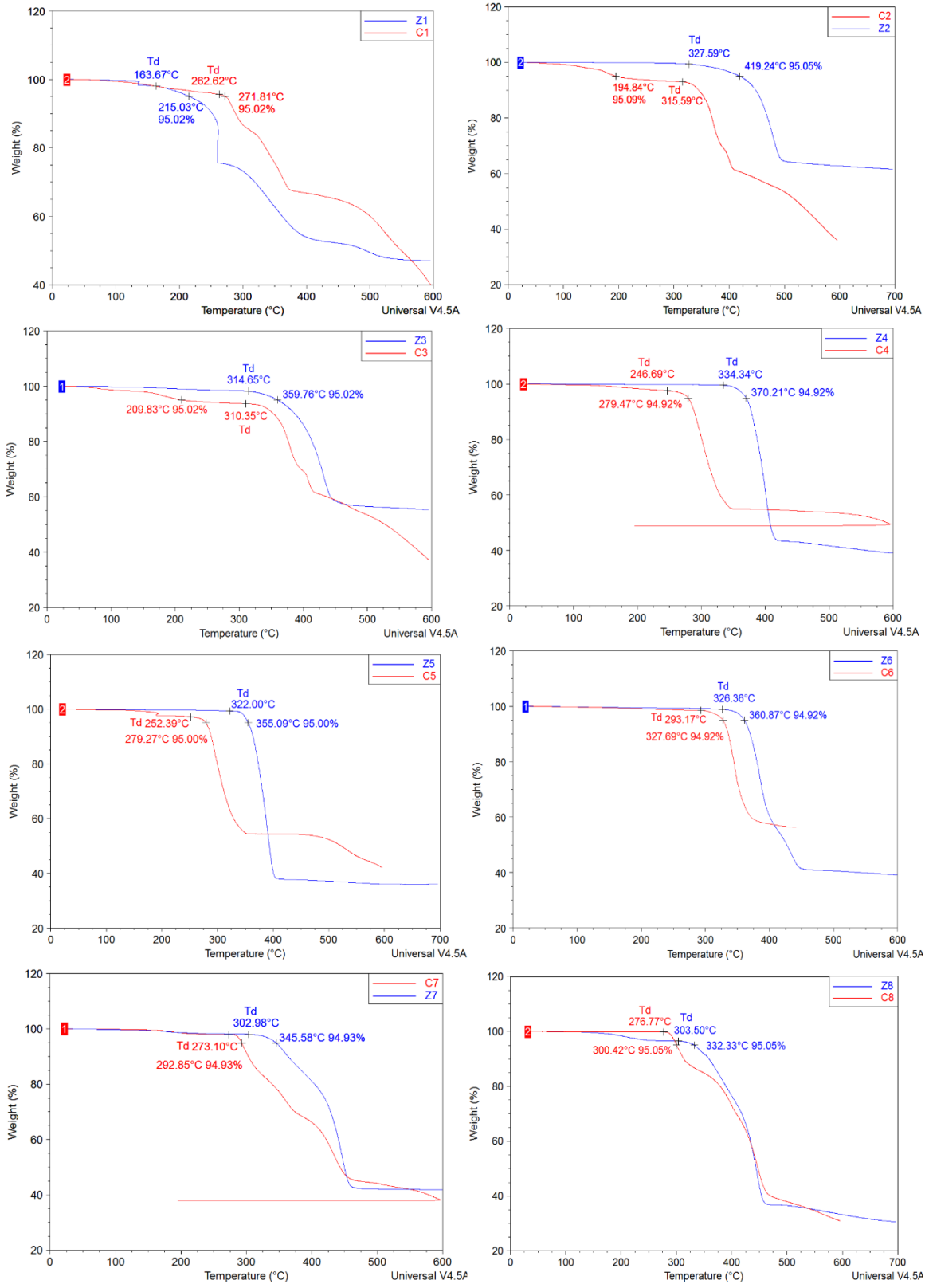

Figure. 7.6. TGA plots for **Z1-Z8** and **C1-C8** polymers showing the onset of degradation (T_d) and degradation temperature ($T_{5\%}$) at 5% weight loss.

7.3.3 Dielectric Properties

Dielectric spectroscopy was carried out on all sixteen metal polyesters as pressed pellets due to their limited solubility. After the pellets were pressed, they were dried under vacuum overnight to ensure removal of water before testing. Dielectric constant and loss were analyzed as a function of frequency for all pressed polymer and pressed pellets of their respective metal oxides for comparison and plotted in **Figure 7.7**. The zinc polyesters had a comparably lower dielectric constant than the cadmium polyesters with **Z1** having the highest dielectric constant of 4.69 and about 2% loss while **Z8** had the lowest dielectric constant of 3.61 and a loss up to 4%. For comparison, ZnO has a dielectric constant of 8.61 as measured here with a loss over 25% making it unsuitable for nearly all dielectric applications in its natural state. Coordination of zinc within the carboxylate backbone network of the polymer was shown to greatly reduce the loss exhibited and bring the materials into a useable range. The experimental dielectric constant was then plotted against the predicted dielectric constant from DFT calculations against the number of CH_2 spacers in **Figure 7.7C**. The results show good correlation between real and predicted values with two outliers at 4 CH_2 spacers and 8 CH_2 spacers.

Cadmium polyesters were plotted in **Figure 7.5D** for dielectric constant and **Figure 7.7E** for dielectric loss alongside CdO for comparison. Cadmium showed a similar trend to Zinc but with a higher dielectric constant across all polymers. **C1** showed the highest dielectric constant at 1 kHz of 6.61, only slightly lower than the value for CdO which was recorded to be 6.95. In the case of **C1**, the loss could be

drastically reduced from 27% to about 4% while maintaining a similar dielectric constant to the metal oxide. As the number of CH_2 spacers increased, the dielectric constant continued to drop to a minimum value of 3.97 for **C8** with a low loss of 0.5%. This trend is also shown in **Figure 7.7F** where the real and DFT values are plotted together in great correlation. The density of the metal polyesters was used to determine the metal volume percent for each polymer system and plotted with dielectric constant for both the experimental results and DFT predictions in **Figure 7.8**. It was seen that the volume of the metal had more of an impact on dielectric properties than the weight of the metal fraction and differences in predicted results can be attributed to differences in experimental density.

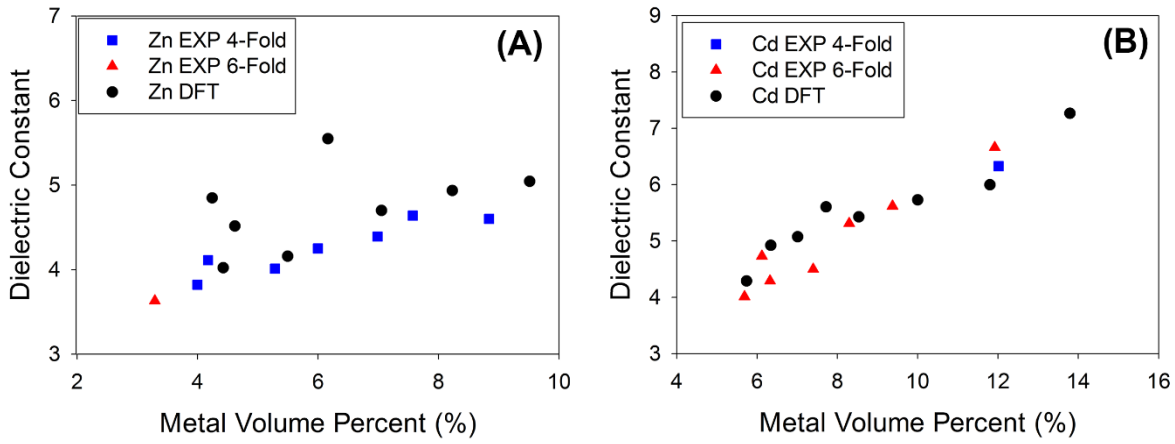

Figure 7.7. Plots generated from experimental and calculated data by DFT of dielectric constant versus metal volume fraction for 4-fold and 6-fold coordination of (A) zinc and (B) cadmium systems.

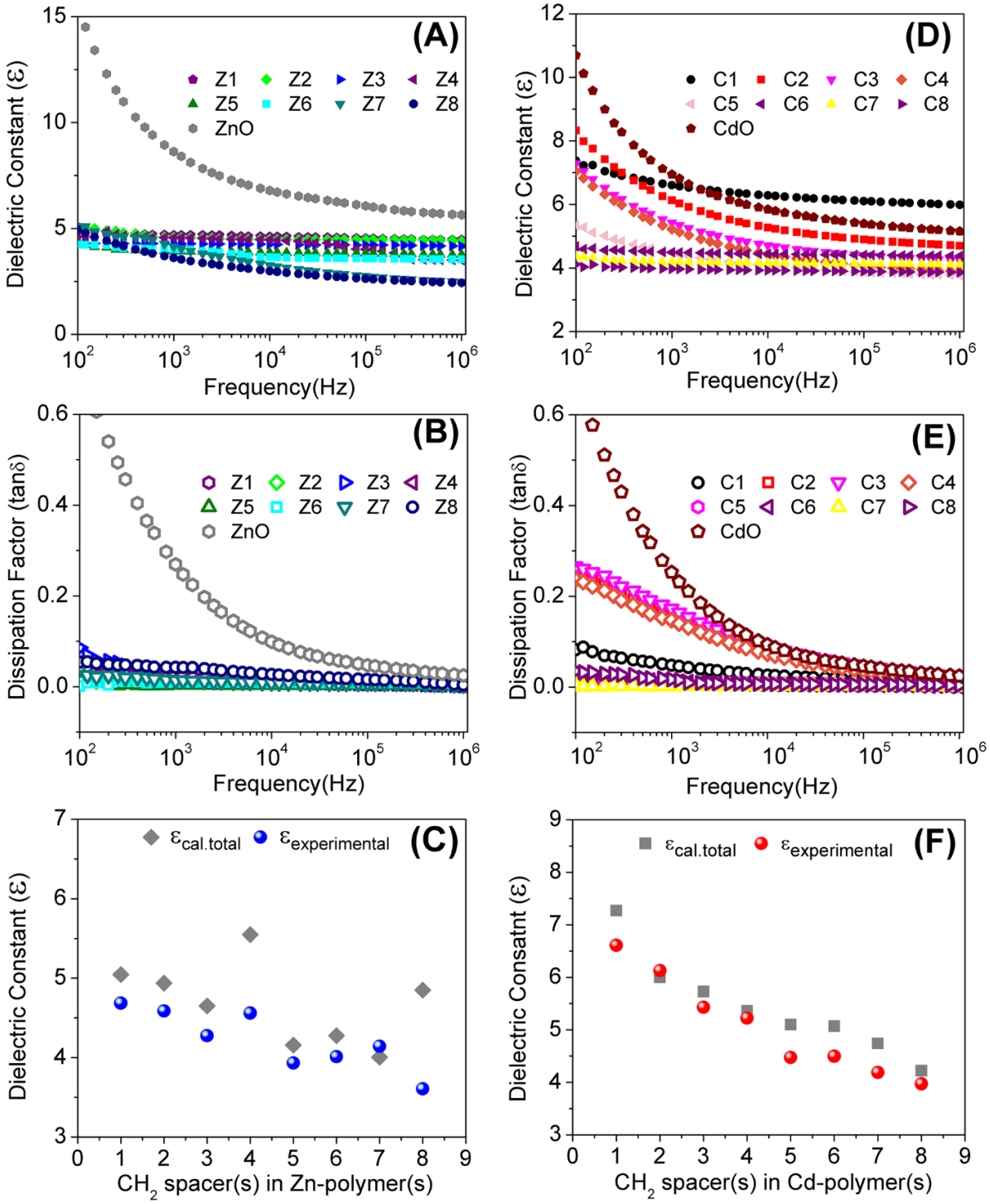

Figure 7.8. (A) Dielectric constant of Zn(II) polymers and ZnO**, (B)** corresponding dissipation of Zn (II) polymers with ZnO, **(D)** dielectric constants of Cd(II) polymers with CdO, **(E)** corresponding dissipation of Cd(II) polymers with CdO, calculated total dielectric constants compared to the experimental measurements as a function of number of CH_2 spacers for **(C)** Zn and **(F)** Cd-polymers.

7.3.4 Optical Band Gap Determination

Band gap determination was carried out by UV-Vis spectroscopy and determined by the onset of absorbance in the UV region as shown in **Figure 7.9**. The complete procedure and theory behind the optical band gap measurements can be found in **Chapter 2** of this thesis. All of the metal polyesters showed a band gap higher than 5 eV, mostly around 5.5 eV, which is indicative of a high intrinsic breakdown. **Table 7.4** shows the experimental and predicted dielectric constants, loss values, band gaps, and metal volume fractions tabulated for all metal polyesters. The respective metal oxides have a band gap of 3.37 for ZnO and 2.28 for CdO, which in the case of CdO, has been doubled by complexation of cadmium between aliphatic carboxylates. While no breakdown measurement could be carried out on these metal polyester systems in this preliminary study, the drastic increase in band gap indicated that a variation of these metal containing polymer systems could be useful for dielectric applications.

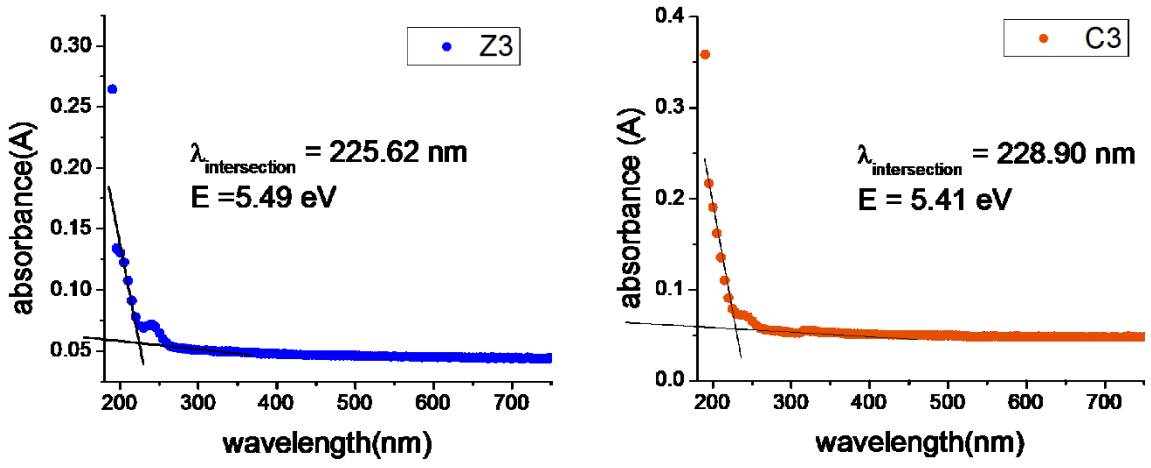

Figure 7.9. UV-Vis spectra of Z3 (blue left) and C3 (red right) for optical band gap.

Table 7.4. Measured dielectric constants (ε_{exp}), calculated total dielectric constants (ε_{calc}), measured dissipation factors (tan δ), measured band gap energies (BG_{exp}), and calculated band gap energies (BG_{calc}), calculated metal volume fraction ($MV_{calc.}$) and measured metal volume fraction ($MV_{exp.}$) and calculated coordination numbers ($CN_{calc.}$) for **Z1**-**Z8** polymers on top and **C1-C8** polymers below.

Zn(II) polymers	**Z1**	**Z2**	**Z3**	**Z4**	**Z5**	**Z6**	**Z7**	**Z8**
ε_{exp} at 1kHz	4.69	4.59	4.28	4.56	3.93	4.01	4.14	3.61
ε_{calc}	5.05	4.94	4.70	5.55	4.16	4.28	4.02	4.85
tan δ_{exp} at 1kHz	0.023	0.014	0.027	0.021	0.005	0.010	0.013	0.042
BG_{exp} (eV)	5.67	5.47	5.49	5.51	5.42	5.21	5.53	5.57
BG_{calc} (eV)	6.38	6.89	6.36	6.31	6.53	6.19	6.41	6.35
MV_{calc} (%)	9.51	8.23	7.05	6.16	5.50	4.62	4.42	4.24
MV_{exp} (%)	8.84	7.57	6.01	6.98	5.28	4.17	4.01	3.29
$CN_{calc.}$	4	4	4	4	4	4	4	6
Cd(II) polymers	**C1**	**C2**	**C3**	**C4**	**C5**	**C6**	**C7**	**C8**
εexp at 1kHz (r.t)	6.61	6.13	5.43	5.22	4.47	4.50	4.19	3.97
εcalc	6.90	6.00	5.73	5.42	5.88	5.07	4.90	4.29
tan δexp at 1kHz (r.t)	0.041	0.155	0.171	0.145	0.006	0.012	0.002	0.016
BGexp (eV)	5.49	5.55	5.41	5.50	5.52	5.81	5.47	5.54
BGcalc (eV)	5.29	5.31	5.53	5.91	5.88	5.75	5.25	5.54
MVcalc (%)	13.79	11.80	10.00	8.53	7.72	7.01	6.34	5.74
MVexp. (%)	11.92	12.01	9.37	8.29	6.12	7.39	6.32	5.69
CNcalc.	4	6	6	6	6	6	6	6

7.4 Expansion of Metal-Containing Polymers Conclusion

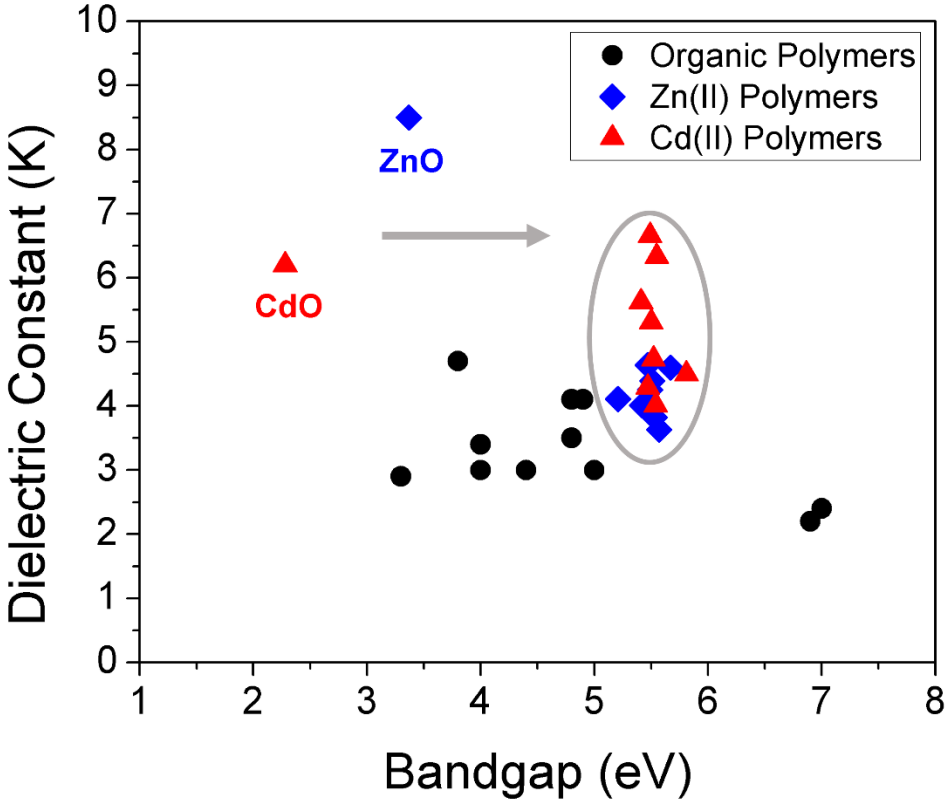

Figure 7.10. Dielectric constant verse band gap for metal oxides, metal containing polyesters, and several common organic polymers including polyethylene (PE) and polypropylene (PP).

Figure 7.10 above serves as a visual conclusion for this chapter. After an in-depth investigation of group 14 metals for dielectric applications, cadmium and zinc were chosen as two initial transition metals to investigate. Through complexation with carboxylates into a polymer backbone, new dielectric materials with similar dielectric constants could be synthesized and characterized. More importantly, the dielectric loss could be drastically reduced by an order of magnitude, and the band gap could be doubled in several cases. In accordance with the ideas of the Materials

Genome Initiative and the Rational Co-Design Process suggested by our research group, all experiments were carried out in close collaboration with computational simulations. The idea to investigate not just the metal weight fraction but also the metal volume fraction came from discussions with the simulation team when a discrepancy between the experimental and predicted results were discovered. Through validation of the DFT predictions by experiments for these two transition metals, the remaining 36 transition metals can be predicted with increased accuracy and confidence that the results are meaningful and predictive of the real results. Since the transitions metal represents the largest elemental block on the periodic table, it is essential to thoroughly screen the metals and their potential polymers for dielectric applications in a comprehensive search.

Chapter 8

8. Conclusion and Future Impact of the Polymer Genome as a Part of the Materials Genome Initiative

8.1 Recap of Rational Co-Design Process

This work has outlined the approach and benefits of the use of a rational co-design process for the exploration of new materials as initially laid out in recent publications on the topic and reiterated here.[56,151] Often times, materials discovery is carried out in small groups with a few experimentalists working together or by an isolated computationalists making predictions without the ability to test them in the real world. I have tried to convince the reader of the practicalities of coupling computations, synthesis, and characterization to aid in the discovery and optimization of new materials. This co-design paradigm may be more powerful, efficient, cost-effective, insightful, and rewarding than just computational or experimental approaches and can significantly extend the reaches of purely Edisonian attempts. The basic outline of the technique is shown in **Figure 1.4** to demonstrate how different teams can work together to continuously improve each other's work and bring various viewpoints and expertise that wouldn't have otherwise been available. Through the continuation of this rational co-design loop, new polymers with targeted properties can be rapidly synthesized and characterized to screen for desirable properties and speed up the development of next-generation

materials. It should be noted that while this method was used for the exploration of dielectric polymers, it can be applied to any field of study where material properties can be predicted computationally. This outlook is consistent with the charter of the Materials Genome Initiative, which mandates the community to surpass traditional (but valuable) Edisonian and intuition-driven approaches adopted to date.

8.2 Comparison of Experimentations to Simulations

Computational simulations were carried out on a wide range of polymeric materials by following known dielectric in literature and the intuition of polymer chemists. In looking to expand the bounds of dielectric materials, two classes of polymers were studied. The first class consists of traditional organic polymers such as polypropylene, polyureas, polythioureas, and polyimides. These organic polymers can be readily made into films for electrical characterization. The second class consists of metal containing polymers where a metal atom is incorporated directly into the backbone such as the tin, zinc, and cadmium polyesters in **Chapter 6** and **Chapter 7**. This group also contains new, unexplored metals in similar frameworks and is called metal organic polymers, not to be confused with organometallic polymers where carbon is bonded to a metal atom. A comprehensive plot of the simulated results are shown below in **Figure 8.1** with the red squares denoting the organic polymers and the other symbols denoting the metal organic polymers.[152]

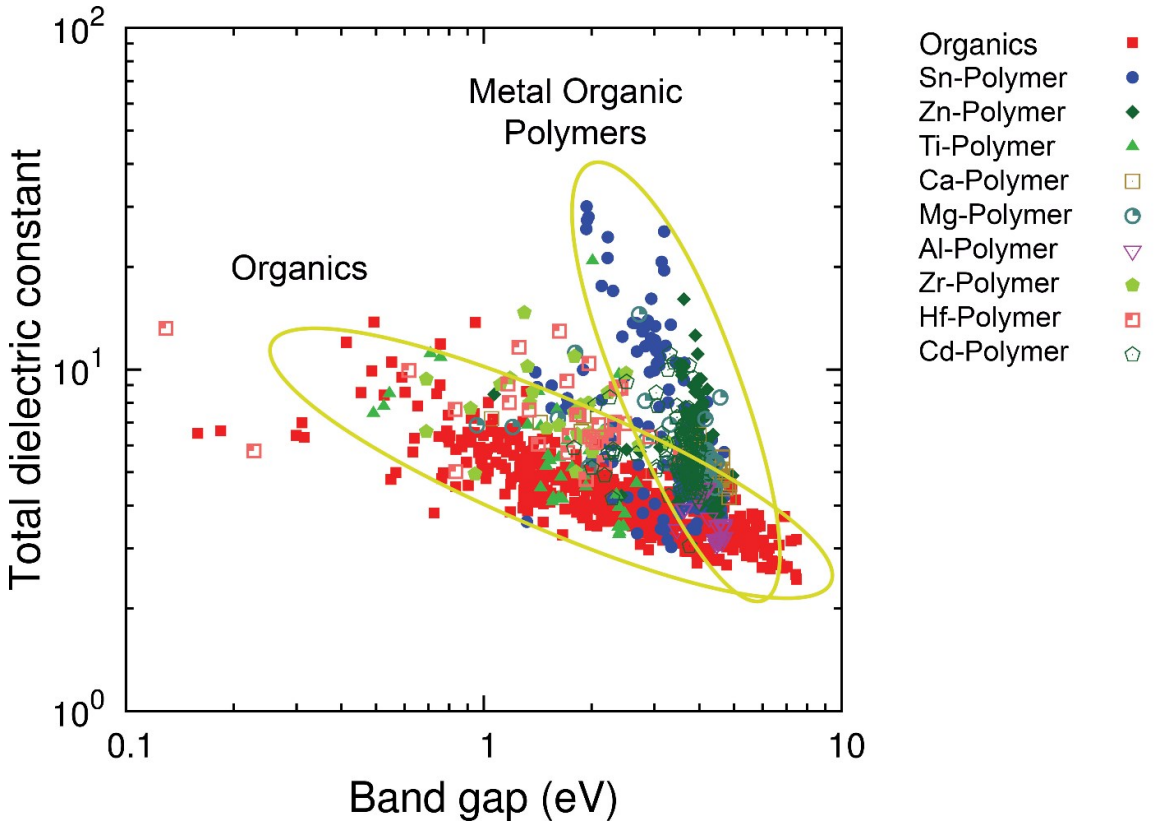

Figure 8.1. Computed dielectric constant of more than one thousand organic and organometallic materials, shown against their computed bandgap. Two ovals are used to indicate the different regions occupied by the organic and organometallic materials. Reproduced with permission from reference.[152] Copyright (2016) Macmillan Publishers.

By carrying out systematic studies into the experimental properties of polyimides, polythioureas, and metal containing tin and cadmium polymers, an experimental data set was established.[69,71,73,74,127,143] The experimental results are plotted as dielectric constant against band gap in **Figure 8.2** along with some common organic polymers used in dielectrics and an overlay of the original organic polymers studied by DFT. The graph shows that, while many high dielectric constant organic polymers have been made, the only way to expand the property subspace to include band gaps above 4 eV and dielectric constants above 5 requires the use of

metal containing polymers and their large contribution to the ionic portion. This experimental data was compared to the results from DFT to validate that the data being generated was within an acceptable error range to give a reasonable prediction for experimentalists. The machine learning algorithms were trained and validated on the DFT data, so it was essential to ensure that the DFT values represented reality. Otherwise, the machine learning results would be deceiving.

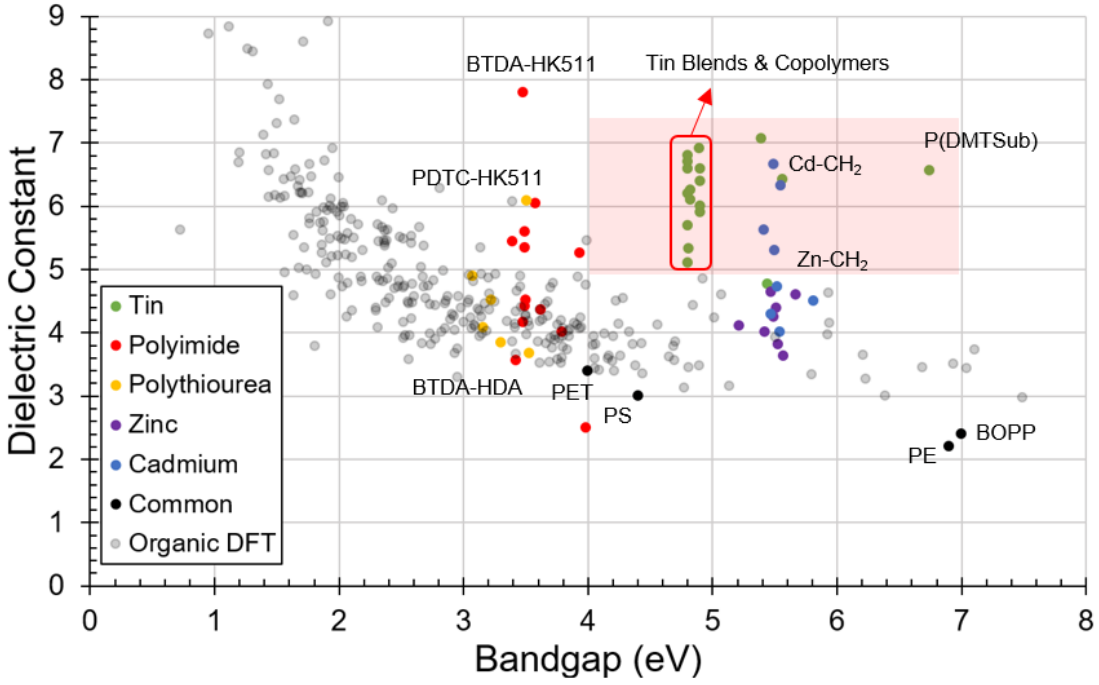

Figure 8.2. Dielectric constant and band gap data for synthesized polymers in the Sotzing Research Group at the University of Connecticut with the original simulated organic polymers overlaid.

Another way to represent the experimental data set is a series of bar graphs to show more properties than just dielectric constant and band gap. **Figure 8.3** shows those values with the addition of dielectric loss, glass transition temperature, and the

important value of breakdown strength. A few things are immediately evident when viewing the data in this way. The first is that the metal polymers do not show thermal transitions such as a glass transition below their degradation temperature as is evident by the large lack of data in that area. In addition, many of the polymers do not have breakdown strengths listed. This is due to the difficulty in producing high-quality films on which these sensitive measurements can be carried out. As the experimental methods and procedures have improved, both in our own lab and Dr. Cao's lab, the number of polymers with breakdown strengths recorded have increased and should continue to increase.

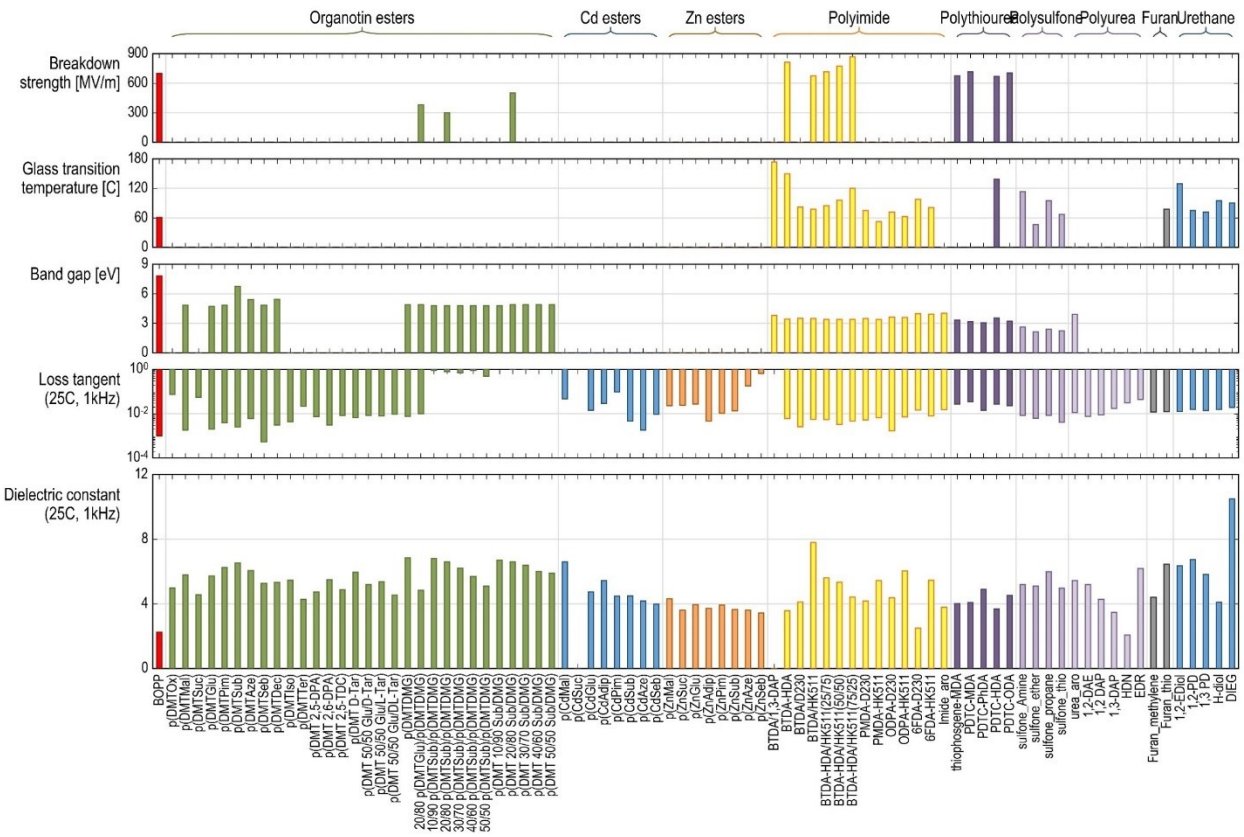

Figure 8.3. Plot of most of the next generation dielectric polymers synthesized in the Sotzing Research Group and Characterized in collaboration with the University of Connecticut's EIRC for their electrical properties.

8.3 Polymer Genome as a Part of the Materials Genome Initiative

The Materials Genome Initiative was launched by the United States Government under a directive from the White House in 2011 to find ways to discover and utilize new materials faster and cheaper than ever before. The initiative realizes that in the current industrial age of our country, advanced materials are an integral part of our society. They serve as the means to improve our environment, health, safety, and security. The benefit of this initiative has been the investment of hundreds of millions of dollars in federal money to fund programs dedicated to pursuing and understanding the material genome. In a similar way to how the human genome was analyzed, the initiative hopes to fully understand the processing-structure-property relationships in materials and devise the perfect material for any given situation with relative ease. To accomplish this, a large amount of experimental and computational data has to be collected and organized in an accessible and useful way. Only with all of this data catalogued properly can machine learning algorithms, and eventually artificial intelligence, make use of all of our knowledge to give the blueprints of the desired material.

Over the years, numerous polymer databases have popped up online, some of which have even been used in this work in an attempt to catalog all known materials data.[80,82,153–155] At the University of Connecticut, Dr. Ramprasad's group has constructed their own polymer data repository in an effort to understand the polymer genome. This database, called Khazana, which can be found at Khazana.uconn.edu,

has stored all the computational and experimental data that has been generated as part of the Multidisciplinary University Research Initiative (MURI) that has funded the majority of this work. In addition to our own data, the database contains numerous related publications, and the volume continues to grow daily. The data repository can be searched in a number of ways including IUPAC name, trade name, formula, polymer class, or even SMILES string to make searching as intuitive as possible. A unique feature of Khazana is that the machine learning algorithm is baked directly into the website for anyone to use. As a result, if a polymer is searched for that has no experimental or computational data, the machine learning algorithm will automatically determine the predicted properties and display them to the user in real time. This allows any researcher around the world to make use of the machine learning at any time. In addition, as new data is added to the data repository, the machine learning can retrain itself to improve its prediction.

The flowchart for the polymer genome is shown in **Figure 8.4**, and a view of the initial search results for a polythiourea in Khazana is shown in **Figure 8.5** where experimental data, DFT data, and machine learning data are all displayed. In addition, when a single polymer is selected, more data will be displayed such as any experimental thermal and solubility data. The categories of data will continue to expand as the database continues to grow. Once a critical mass of any type of data is entered, such as glass transition temperature, the machine learning algorithm can be trained by experimental data and predict properties that would be difficult or impossible to predict with current DFT. It should be apparent by now that there is a

great potential to humanity if the goals of the material genome are realized. In a few short years since the initiative began, a data repository is already able to carry out machine learning predictions on experimental and computational data to produce on-the-fly results to anyone in the world. As computational power continues to increase in a near-exponential way, computer modeling is going to become ever cheaper and faster. This will allow for a great growth in the amount of computational data available to carry out predictions. As the amount of data increases, the accuracy of the results should continue to improve. By carrying out cross-functional research between chemists, engineers, and computationalists, the goal of the materials genome has come closer to realization.

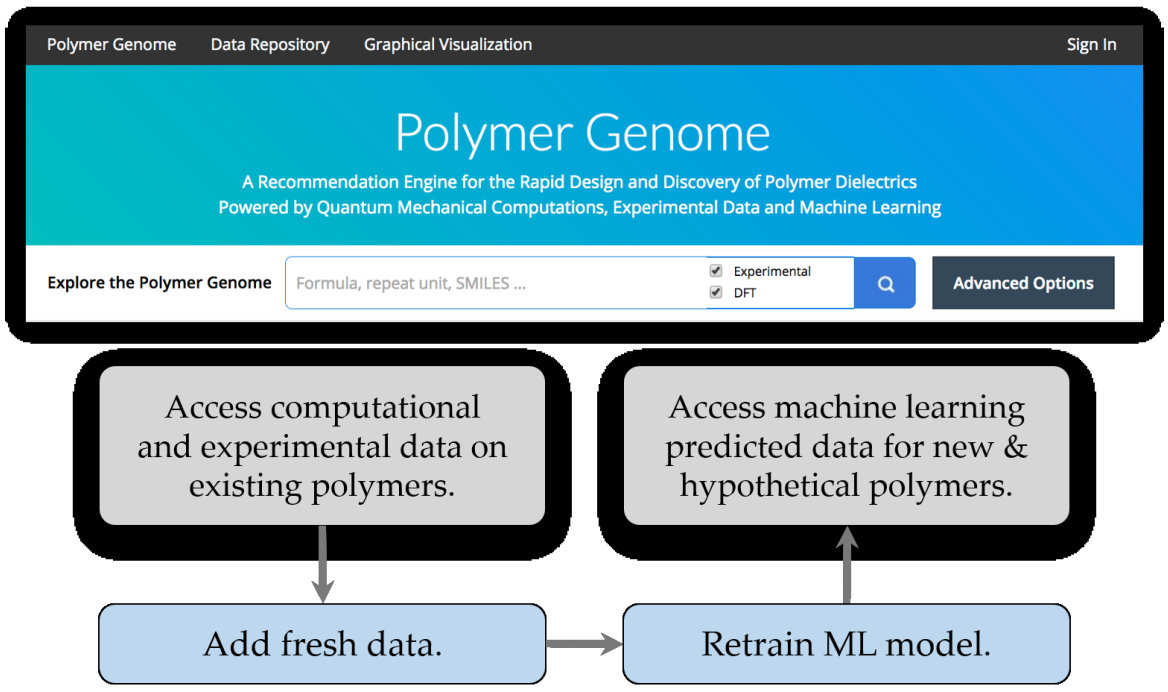

Figure 8.4. Graphical depiction of how the Polymer Genome can be used and expanded on in the future, which can be found online at http://khazana.uconn.edu/polymer_genome/

Formula Unit	Repeat Unit SMILES	Polymer Name or Class	Band Gap (eV)	Dielectric Constant	Refractive Index	Electron Affinity (eV)	Ionization Energy (eV)	DFT Results
$C_7H_6N_2S$ (ID: E0003)	NH-CS-NH-C6H4 NC(=S)NC(C=C1)=CC=C1	Polythiourea	3.10 (2.92)	6.70 (5.46)	(2.05)	(2.74)	(5.43)	343
$C_{20}H_{16}N_4OS_2$ (ID: E0023)	NH-CS-NH-C6H4-NH-CS-NH-C6H4-O-C6H4 NC(=S)NC(C=C1)=CC=C1NC(=S)NC(C=C2)=CC=C2OC(C=C3)=CC=C3	Polythiourea	3.22 (3.16)	4.52 (4.93)	1.79 (1.96)	(2.49)	(5.56)	0319 0320 0321 0322 0323
$C_{21}H_{18}N_4S_2$ (ID: E0024)	NH-CS-NH-C6H4-NH-CS-NH-C6H4-CH2-C6H4 NC(=S)NC(C=C1)=CC=C1NC(=S)NC(C=C2)=CC=C2CC(C=C3)=CC=C3	Polythiourea	3.16 (3.43)	4.08 (4.66)	1.81 (1.92)	(2.36)	(5.54)	0324 0325 0326
$C_{14}H_{12}N_4S_2$ (ID: E0025)	NH-CS-NH-C6H4-NH-CS-NH-C6H4 NC(=S)NC(C=C1)=CC=C1NC(=S)NC(C=C2)=CC=C2	Polythiourea	3.07 (2.92)	4.89 (5.46)	(2.05)	(2.74)	(5.43)	N/A
$C_{14}H_{20}N_4S_2$ (ID: E0026)	NH-CS-NH-C6H4-NH-CS-NH-(CH2)6 NC(=S)NC(C=C1)=CC=C1NC(=S)NCCCCCC	Polythiourea	3.53 (3.92)	3.67 (4.35)	1.71 (1.82)	(2.13)	(5.39)	0327 0328 0329 0330

Figure 8.5. Example of the Polymer Genome database being put to use to search for polythioureas, resulting in a display of experimental and machine learning properties with links to references.

References

(1) Omar, M. *Elementary Solid State Physics: Principals and Applications*, 4th ed.; Addison-Wesley, 1994.

(2) Xu, K. Nonaqueous Liquid Electrolytes for Lithium-Based Rechargeable Batteries. *Chem. Rev.* **2004**, *104* (10), 4303–4417.

(3) Simon, P.; Gogotsi, Y. Materials for Electrochemical Capacitors. *Nat. Mater.* **2008**, *7* (11), 845–854.

(4) Kao, K. C. 2 - Electric Polarization and Relaxation. In *Dielectric Phenomena in Solids*; Kao, K. C., Ed.; Academic Press: San Diego, 2004; pp 41–114.

(5) Ku, C. C.; Liepins, R. *Electrical Properties of Polymers: Chemical Principles*; Hanser Publishers: New York, 1989; Vol. 30.

(6) Sun, Y.; Bealing, C.; Boggs, S.; Ramprasad, R. 50+ Years of Intrinsic Breakdown. *IEEE Electr. Insul. Mag.* **2013**, *29* (2), 8–15.

(7) Ho, J.; Jow, T. R.; Boggs, S. Historical Introduction to Capacitor. *IEEE Electr. Insul. Mag.* **2010**, *26* (1), 20–25.

(8) Tiku, D. Modular Multilevel MMI (HB) Topology for Single-Stage Grid Connected PV Plant. In *11th Irence on AC and DC PoweET International Confer Transmission*; IEEE: London, UK, 2015.

(9) Xue, Y.; Divya, K. C.; Griepentrog, G.; Liviu, M.; Suresh, S.; Manjrekar, M. Towards Next Generation Photovoltaic Inverters. In *Energy Conversion Congress and Exposition (ECCE)*; IEEE: Phoenix, AZ, 2011; pp 2468–2474.

(10) Lu, J.; Moon, K.; Xu, J.; Wong, C. P. Synthesis and Dielectric Properties of Novel High- K Polymer Composites Containing in-Situ Formed Silver Nanoparticles for Embedded Capacitor Applications. *J. Mater. Chem.* **2006**, *16*, 1543–1548.

(11) Page, R. M. *The Origin of Radar*; Greenwood Publishing Group: Westport, CT, 1979.

(12) Doyle, M. R.; Samuel, D. J.; Conway, T.; Klimowski, R. R. Electromagnetic Aircraft Launch System - EMALS. *IEEE Transcations Magn.* **1995**, *31*, 528–533.

(13) Rourke, R. O. *Navy Ford (CVN-78) Class Aircraft Carrier Program: Background and Issues for Congress*; 2013.

(14) Beach, F.; McNab, I. Present and Future Navel Applications for Pulsed Power. In *IEEE Conference on Pulsed Power*; Monterey, CA, 2005.

(15) Walls, W. A.; Weldon, W. F.; Pratap, S. B.; Palmer, M.; Adams, L. D.

Applications of Electromagnetic Guns to Future Navel Platforms. *IEEE Transcations Magn.* **1999**, *35* (1), 262–267.

(16) Moses, E. I.; Boyd, R. N.; Remington, B. A.; Keane, C. J.; Moses, E. I.; Boyd, R. N.; Remington, B. A.; Keane, C. J. The National Ignition Facility: Ushering in a New Age for High Energy Density Science. *Phys. Plasmas* **2009**, *16* (41006).

(17) Lindl, J. Development of the Indirect-Drive Approach to Inertial Confinement Fusion and the Target Physics Basis for Ignition and Gain. *Phys. Plasmas* **1995**, *3933* (2), 3933–4024.

(18) Fleurot, N.; Cavailler, C.; Bourgade, J. L. The Laser Megajoule (LMJ) Project Dedicated to Inertial Confinement Fusion: Development and Construction Status. *Fusion Eng. Des.* **2005**, *74* (1–4), 147–154.

(19) Dummer, G. W. A. *Electronic Inventions and Discoveries*, 4th ed.; UK: Institute of Physics Publishing: Bristol, 1997.

(20) Cohen, I. B. *Dictionary of Scientific Biography*; Gillispie, C. C., Ed.; Charles Scribner's Sons: New York, 1972.

(21) Fitzgerald, D. G. Improvements in Electrical Condensers or Accumulators. 3466/1876, 1876.

(22) Mclean, D. A. Metallized Paper for Capacitors. *Proc. IRE* **1950**, *38* (9), 1010–1014.

(23) Mclean, D. A.; Wehe, H. G. Miniature Lacquer Film Capacitors. *Proc. IRE* **1954**, *42* (12), 1799–1805.

(24) Cozens, J. H. Development of Plastic Dielectric Capacitors. *IRE Trans. Compon. Parts* **1959**, *CP-6* (2), 114–118.

(25) Sarjeant, W. J.; Zirnheld, J.; MacDougall, F. W. Capacitors. *IEEE Trans. Plasma Sci.* **1998**, *26* (5), 1368–1392.

(26) Picci, G.; Rabuffi, M. Status Quo and Future Prospects for Metallized Polypropylene Energy Storage Capacitors. *IEEE Trans. PLASMA Sci.* **2002**, *30* (5), 1939–1942.

(27) Laghari, J. R.; Sarjeant, W. J. Energy-Storage Pulsed-Power Capacitor Technology. *IEEE Trans. Power Electron.* **1992**, *7* (1), 251–257.

(28) Longo, C.; Savaris, M.; Zeni, M.; Brandalise, R. N.; Grisa, A. M. C. Degradation Study of Polypropylene (PP) and Bioriented Polypropylene (BOPP) in the Environment. *Mater. Res.* **2011**, *14* (4), 442–448.

(29) Ho, J.; Jow, R. *Characterization of High Temperature Polymer Thin Films for Power Conditioning Capacitors*; Adelphi, MD, 2009.

(30) Zhu, L.; Wang, Q. Novel Ferroelectric Polymers for High Energy Density and

Low Loss Dielectrics. *Macromolecules* **2012**, *45* (7), 2937–2954.

(31) Chu, B.; Zhou, X.; Ren, K.; Neese, B.; Lin, M.; Wang, Q.; Bauer, F.; Zhang, Q. M. A Dielectric Polymer with High Electric Energy Density and Fast Discharge Speed. *Science.* **2006**, *313* (5785), 334–336.

(32) Wu, S.; Lin, M.; Lu, S. G.; Zhu, L.; Zhang, Q. M. Polar-Fluoropolymer Blends with Tailored Nanostructures for High Energy Density Low Loss Capacitor Applications. *Appl. Phys. Lett.* **2011**, *99* (13), 7–10.

(33) Guan, F.; Pan, J.; Wang, J.; Wang, Q.; Zhu, L. Crystal Orientation Effect on Electric Energy Storage in Poly(vinylidene Fluoride-Co-Hexafluoropropylene) Copolymers. *Macromolecules* **2010**, *43* (1), 384–392.

(34) Luo, H.; Zhang, D.; Jiang, C.; Yuan, X.; Chen, C.; Zhou, K. Improved Dielectric Properties and Energy Storage Density of Poly(vinylidene Fluoride- *Co* -Hexafluoropropylene) Nanocomposite with Hydantoin Epoxy Resin Coated $BaTiO_3$. *ACS Appl. Mater. Interfaces* **2015**, *7* (15), 8061–8069.

(35) Hoque, N. A.; Thakur, P.; Bala, N.; Kool, A.; Das, S.; Ray, P. P. Tunable Photoluminescence Emissions and Large Dielectric Constant of the Electroactive Poly(vinylidene Fluoride–hexafluoropropylene) Thin Films Modified with SnO_2 Nanoparticles. *RSC Adv.* **2016**, *6* (36), 29931–29943.

(36) Smith, O. L.; Kim, Y.; Kathaperumal, M.; Gadinski, M. R.; Pan, M. J.; Wang, Q.; Perry, J. W. Enhanced Permittivity and Energy Density in Neat Poly(vinylidene Fluoride-Trifluoroethylene-Chlorotrifluoroethylene) Terpolymer Films through Control of Morphology. *ACS Appl. Mater. Interfaces* **2014**, *6* (12), 9584–9589.

(37) Zhang, Z.; Chung, T. C. M. Study of VDF / TrFE / CTFE Terpolymers for High Pulsed Capacitor with High Energy Density and Low Energy Loss. *Macromolecules* **2007**, *40* (4), 783–785.

(38) Zhang, X.; Shen, Y.; Shen, Z.; Jiang, J.; Chen, L.; Nan, C. W. Achieving High Energy Density in PVDF-Based Polymer Blends: Suppression of Early Polarization Saturation and Enhancement of Breakdown Strength. *ACS Appl. Mater. Interfaces* **2016**, *8* (40), 27236–27242.

(39) Li, W.; Jiang, L.; Zhang, X.; Shen, Y.; Nan, C. High-Energy-Density Dielectric Films Based on the Polyvinylidene Fluoride and Aromatic Polythiourea for Capacitors. *J. Mater. Chem. A* **2014**, *2* (38), 15803–15807.

(40) Dang, Z. M.; Yuan, J. K.; Zha, J. W.; Zhou, T.; Li, S. T.; Hu, G. H. Fundamentals, Processes and Applications of High-Permittivity Polymer-Matrix Composites. *Prog. Mater. Sci.* **2012**, *57* (4), 660–723.

(41) Arlt, G.; Hennings, D.; De With, G. Dielectric Properties of Fine-Grained Barium Titanate Ceramics. *J. Appl. Phys.* **1985**, *58* (4), 1619–1625.

(42) Thakur, V.; Kessler, M. Polymer Nanocomposites: New Advanced Dielectric Materials for Energy Storage Applications. In *Advanced Energy Materials*; Tiwari, A., Valyukh, S., Eds.; John Wiley & Sons, Inc.: Hoboken, NJ, USA., 2014; pp 207–257.

(43) Zhu, J. L.; Lin, S.; Feng, S. M.; Wang, L. J.; Liu, Q. Q.; Jin, C. Q.; Wang, X. H.; Zhong, C. F.; Li, L. T.; Cao, W. Pressure Tuned Ferroelectric Reentrance in Nano-BaTiO3 Ceramics. *J. Appl. Phys.* **2012**, *112* (12).

(44) Barber, P.; Balasubramanian, S.; Anguchamy, Y.; Gong, S.; Wibowo, A.; Gao, H.; Ploehn, H. J.; zur Loye, H.-C. Polymer Composite and Nanocomposite Dielectric Materials for Pulse Power Energy Storage. *Materials (Basel).* **2009**, *2* (4), 1697–1733.

(45) An, A. L.; Boggs, S. A.; Calame, J. Energy Storage in Polymer Films with High Dielectric Constant Fillers. **2006**, 466–469.

(46) Riggs, B. C.; Elupula, R.; Rehm, C.; Adireddy, S.; Grayson, S. M.; Chrisey, D. B. Click-In Ferroelectric Nanoparticles for Dielectric Energy Storage. *ACS Appl. Mater. Interfaces* **2015**, *7* (32), 17819–17825.

(47) Tang, H.; Zhou, Z.; Sodano, H. A. Relationship between BaTiO3 Nanowire Aspect Ratio and the Dielectric Permittivity of Nanocomposites. *ACS Appl. Mater. Interfaces* **2014**, *6* (8), 5450–5455.

(48) Wen, F.; Xu, Z.; Tan, S.; Xia, W.; Wei, X.; Zhang, Z. Chemical Bonding-Induced Low Dielectric Loss and Low Conductivity in High-K Poly(vinylidenefluoride-Trifluorethylene)/graphene Nanosheets Nanocomposites. *ACS Appl. Mater. Interfaces* **2013**, *5* (19), 9411–9420.

(49) Gowdhaman, P.; Antonyraj, K.; Annamalai, V. An Effective Approach on Physical and Dielectric Properties of PZT- PVDF Composites. *Int. J. Adv. Sci. Res. Int. J. Adv. Sci. Res. J.* **2015**, *1* (8), 322–328.

(50) Xiao, X.; Xu, N.; Jiang, Y.; Zhang, Q.; Yu, E.; Yang, H. TiO $_2$ @Ag/P (VDF-HFP) Composite with Enhanced Dielectric Permittivity and Rather Low Dielectric Loss. *RSC Adv.* **2016**, *6* (73), 69580–69585.

(51) Xu, X. ling; Yang, C. jin; Yang, J. hui; Huang, T.; Zhang, N.; Wang, Y.; Zhou, Z. wan. Excellent Dielectric Properties of Poly(vinylidene Fluoride) Composites Based on Partially Reduced Graphene Oxide. *Compos. Part B Eng.* **2017**, *109*, 91–100.

(52) Cui, Z.; Cao, Z.; Ma, R.; Dobrynin, A. V.; Adamson, D. H. Boron Nitride Surface Activity as Route to Composite Dielectric Films. *ACS Appl. Mater. Interfaces* **2015**, *7* (31), 16913–16916.

(53) Cui, Z.; Martinez, A. P.; Adamson, D. H. PMMA Functionalized Boron Nitride Sheets as Nanofillers. *Nanoscale* **2015**, *7* (22), 10193–10197.

(54) Li, Q.; Chen, L.; Gadinski, M. R.; Zhang, S.; Zhang, G.; Li, H.; Haque, A.; Chen, L. Q.; Jackson, T.; Wang, Q. Flexible High-Temperature Dielectric Materials from Polymer Nanocomposites. *Nature* **2015**, *523* (7562), 576–579.

(55) Diaham, S.; Saysouk, F.; Locatelli, M. L.; Lebey, T. Huge Improvements of Electrical Conduction and Dielectric Breakdown in polyimide/BN Nanocomposites. *IEEE Trans. Dielectr. Electr. Insul.* **2016**, *23* (5), 2795–2803.

(56) Mannodi-Kanakkithodi, A.; Treich, G. M.; Huan, T. D.; Ma, R.; Tefferi, M.; Cao, Y.; Sotzing, G. A.; Ramprasad, R. Rational Co-Design of Polymer Dielectrics for Energy Storage. *Adv. Mater. Prog. Rep.* **2016**, *28* (30), 6277–6291.

(57) Friedel, R. D.; Israel, P.; Finn, B. S. *Edison's Electric Light: Biography of an Invention*; Rutgers University Press, 1987.

(58) T.P., H. Edison's Method. In *Technology at the Turning Point*; Pickett, W. P., Ed.; San Francisco Press: San Francisco CA, 1977; pp 5–22.

(59) Jandeleit, B.; Schaefer, D. J.; Powers, T. S.; Turner, H. W.; Weinberg, W. H. Combinatorial Materials Science and Catalysis. *Angew. Chemie - Int. Ed.* **1990**, *38*, 2494–2532.

(60) Opel, M.; Geprägs, S.; Althammer, M. Combinatorial Solid State Materials Science and Technology. *Sci. Tech. Adv. Mater.* **2000**, *1*, 1–10.

(61) Takeuchi, I.; Dover, R. B. Van. Combinatorial Synthesis and Evaluation of Functional Inorganic Materials Using Thin-Film Techniques. *MRS Bull.* **2002**, No. April, 301–308.

(62) Ceder, G.; Persson, K. The Stuff of Dreams. *Nat. Publ. Gr.* **2013**, *309* (6), 36–40.

(63) Ceder, G.; Sadoway, D. R.; Aydinol, M. K.; Huang, B. Identification of Cathode Materials for Lithium Natteries Guided by First-Principles Calculations. *Nature* **1998**, *392*, 694–696.

(64) Peng, H.; Zakutayev, A.; Lany, S.; Paudel, T. R.; Avezac, M.; Ndione, P. F.; Perkins, J. D.; Ginley, D. S.; Nagaraja, A. R.; Perry, N. H.; Mason, T. O.; Zunger, A. Li-Doped Cr2 MnO4: A New P-Type Transparent Conducting Oxide by Computational Materials Design. *Adv. Funct. Mater.* **2013**, *42*, 5267–5276.

(65) Gautier, R.; Zhang, X.; Hu, L.; Yu, L.; Lin, Y.; Sunde, T. O. L.; Chon, D.; Poeppelmeier, K. R.; Zunger, A. Prediction and Accelerated Laboratory Discovery of Previously Unknown 18-Electron ABX Compounds. *Nat. Chem.* **2015**, *7* (4), 308–316.

(66) Jung, V.; Fecher, G. H.; Balke, B.; Fecher, G. H.; Kandpal, H. C.; Wurmehl, S.; Picozzi, S.; Freeman, A. J.; Balke, B.; Wurmehl, S.; Fecher, G. H.; Felser, C.

Rational Design of New Materials for Spintronics: Co2FeZ (Z = Al, Ga, Si, Ge). *Adv. Mater.* **2008**, *9*, 14102.

(67) Nørskov J.K.; Bligaard T.; J., R.; C.H., C. Towards the Computational Design of Solid Catalysts. *Nat. Chem.* **2009**, *1*, 37–46.

(68) Sharma, V.; Wang, C.; Lorenzini, R. G.; Ma, R.; Zhu, Q.; Sinkovits, D. W.; Pilania, G.; Oganov, A. R.; Kumar, S.; Sotzing, G. A.; Boggs, S. A.; Ramprasad, R. Rational Design of All Organic Polymer Dielectrics. *Nat. Commun.* **2014**, *5*, 4845–4852.

(69) Ma, R.; Baldwin, A. F.; Wang, C.; Offenbach, I.; Cakmak, M.; Ramprasad, R.; Sotzing, G. A. Rationally Designed Polyimides for High-Energy Density Capacitor Applications. *ACS Appl. Mater. Interfaces* **2014**, *6* (13), 10445–10451.

(70) Lorenzini, R. G.; Kline, W. M.; Wang, C. C.; Ramprasad, R.; Sotzing, G. A. The Rational Design of Polyurea & Polyurethane Dielectric Materials. *Polymer.* **2013**, *54* (14), 3529–3533.

(71) Baldwin, A. F.; Ma, R.; Mannodi-Kanakkithodi, A.; Huan, T. D.; Wang, C.; Tefferi, M.; Marszalek, J. E.; Cakmak, M.; Cao, Y.; Ramprasad, R.; Sotzing, G. A. Poly(dimethyltin Glutarate) as a Prospective Material for High Dielectric Applications. *Adv. Mater.* **2014**, *27* (2), 346–351.

(72) Baldwin, A. F.; Huan, T. D.; Ma, R.; Mannodi-Kanakkithodi, A.; Tefferi, M.; Katz, N.; Cao, Y.; Ramprasad, R.; Sotzing, G. A. Rational Design of Organotin Polyesters. *Macromolecules* **2015**, *48* (8), 2422–2428.

(73) Baldwin, A. F.; Ma, R.; Huan, T. D.; Cao, Y.; Ramprasad, R.; Sotzing, G. A. Effect of Incorporating Aromatic and Chiral Groups on the Dielectric Properties of Poly(dimethyltin Esters). *Macromol. Rapid Commun.* **2014**, *35* (24), 2082–2088.

(74) Ma, R.; Sharma, V.; Baldwin, A. F.; Tefferi, M.; Offenbach, I.; Cakmak, M.; Cao, Y.; Ramprasad, R.; Sotzing, G. A. Rational Design and Synthesis of Polythioureas as Capacitor Dielectrics. *J. Mater. Chem. A* **2015**, *3*, 14845–14852.

(75) Pablo, J. J. De; Jones, B.; Lind, C.; Ozolins, V.; Ramirez, A. P. The Materials Genome Initiative , the Interplay of Experiment , Theory and Computation. *Curr. Opin. Solid State Mater. Sci.* **2014**, *18* (2), 99–117.

(76) Materials Genome Initiative (Online 2011) https://www.mgi.gov.

(77) *Integrated Computational Materials Engineering: A Transformational Discipline for Improved Competitiveness and National Security*; The National Academies Press: Washington DC, 2008.

(78) Belsky, A.; Hellenbrandt, M.; Karen, V. L.; Luksch, P. Research Papers New

Developments in the Inorganic Crystal Structure Database (ICSD): Accessibility in Support of Materials Research and Design Research Papers. *Acta Cryst.* **2002**, *B58*, 364–369.

(79) Khzana (Online 2017).

(80) Saal, J. E.; Kirklin, S.; Aykol, M.; Meredig, B.; Wolverton, C. Materials Design and Discovery with High-Throughput Density Functional Theory: The Open Quantum Materials Database (OQMD). *JOM* **2013**, *65* (11), 1501–1509.

(81) Taylor, R. H.; Rose, F.; Toher, C.; Levy, O.; Yang, K.; Buongiorno, M.; Curtarolo, S. A RESTful API for Exchanging Materials Data in the AFLOWLIB.org Consortium. *Comput. Mater. Sci.* **2014**, *93*, 178–192.

(82) Jain, A.; Ong, S. P.; Hautier, G.; Chen, W.; Davidson, W.; Jain, A.; Ong, P.; Hautier, G.; Chen, W.; Gunter, D.; Skinner, D.; Ceder, G.; Persson, K. A. Commentary: The Materials Project: A Materials Genome Approach to Accelerating Materials Innovation. *APL Mater.* **2013**, *1*, 11002.

(83) Nalwa, H. S. *Handbook of Low and High Dielectric Constant Materials and Their Applications*; Academic Press, 1999.

(84) Ennis, J. B.; Macdougall, F. W.; Yang, X. H.; Cooper, R. A.; Seal, K.; Naruo, C.; Spinks, B.; Kroessler, P.; Bates, J. Recent Advances in High Voltage, High Energy Capcitor Technology. In *16th IEEE International Pulsed Power Conference*; Albuquerque, NM, USA, 2007; pp 282–285.

(85) MacDougall, F.; Ennis, J.; Yang, X.; Cooper, R.; Gilbert, J.; Bates, J.; Naruo, C.; Schneider, M.; Keller, N.; Joshi, S.; Ho, J.; Scozzie, C.; Yen, S. High Energy Density Capacitors for Pulsed Power Applications. In *IEEE Conference on Pulsed Power*; Washington DC, 2009.

(86) Bluhm, H. *Pulsed Power Systems: Principles and Applications*; Springer, 2006.

(87) Yang, L.; Ho, J.; Allahyarov, E.; Mu, R.; Zhu, L. Semicrystalline Structure − Dielectric Property Relationship and Electrical Conduction in a Biaxially Oriented Poly (Vinylidene Fl Uoride) Film under High Electric Fields and High Temperatures. *ACS Appl. Mater. Interfaces* **2015**, *7*, 19894–19905.

(88) Zhang, Q. M.; Bharti, V.; Zhao, X. Giant Electrostriction and Relaxor Ferroelectric Behavior in Electron-Irradiated Poly(vinylidene Fluoride-Trifluoroethylene) Copolymer. *Science.* **1998**, *280*, 2101–2104.

(89) Jiang, L.; Li, W.; Zhu, J.; Huo, X.; Luo, L.; Zhu, Y. Great Reduction of Loss at High Electric Field in the Polyvinylidene Fluoride / Aromatic Polythiourea Blend Films along with an Irreversible Phase Transition. *Appl. Phys. Lett.* **2015**, *106*, 52901.

(90) Zhang, S.; Zou, C.; Kushner, D. I.; Zhou, X.; Jr, R. J. O.; Zhang, N.; Zhang, Q. M. Semicrystalline Polymers with High Dielectric Constant , Melting

Temperature , and Charge-Discharge Efficiency. *IEEE Trans. Dielectr. Electr. Insul.* **2012**, *19* (4), 1158–1166.

(91) Gadinski, M. R.; Han, K.; Li, Q.; Zhang, G.; Reainthippayasakul, W.; Wang, Q. High Energy Density and Breakdown Strength from β and γ Phases in Poly(vinylidene Fluoride-Co-Bromotrifluoroethylene) Copolymers. *ACS Appl. Mater. Interfaces* **2014**, *6*, 18981–18988.

(92) Shen, Y.; Lin, Y.; Zhang, Q. M. Polymer Nanocomposites with High Energy Storage Densities. *MRS Bull.* **2017**, *40*, 753–759.

(93) An, A. L.; Boggs, S. A. What Is " Nano" in the Context of a Filled Dielectric? In *IEEE International Symposium on Electrical Insulation*; Toronto, Ont, 2006; pp 273–276.

(94) Carr, J. M.; Mackey, M.; Flandin, L.; Schuele, D.; Zhu, L.; Baer, E. Effect of Biaxial Orientation on Dielectric and Breakdown Properties of Poly(ethylene terephthalate)/Poly(vinylidene Fluoride- O-Tetrafluoroethylene) Multilayer Films. *J. Polym. Sci. Part B Polym. Phys.* **2013**, *51* (11), 882–896.

(95) Zhou, Z.; Carr, J.; Mackey, M.; Yin, K.; Schuele, D.; Zhu, L.; Baer, E. Interphase/Interface Modification on the Dielectric Properties of Polycarbonate/Poly(vinylidene Fluoride-Co-Hexafluoropropylene) Multilayer Films for High-Energy Density Capacitors. *J. Polym. Sci. Part B Polym. Phys.* **2013**, *51* (12), 978–991.

(96) Wolak, M. A.; Pan, M.; Wan, A.; Shirk, J. S.; Mackey, M.; Hiltner, A.; Baer, E.; Flandin, L.; Wolak, M. A.; Pan, M.; Wan, A.; Shirk, J. S.; Mackey, M.; Hiltner, A.; Baer, E.; Flandin, L. Dielectric Response of Structured Multilayered Polymer Films Fabricated by Forced Assembly. *Appl. Phys. Lett.* **2008**, *92*, 113301.

(97) Tseng, J.; Tang, S.; Zhou, Z.; Mackey, M.; Carr, J. M.; Mu, R.; Flandin, L.; Schuele, D. E.; Baer, E.; Zhu, L. Interfacial Polarization and Layer Thickness Effect on Electrical Insulation in Multilayered Polysulfone/poly(vinylidene Fluoride) Films. *Polymer.* **2014**, *55* (1), 8–14.

(98) Mackey, M.; Schuele, D. E.; Zhu, L.; Flandin, L.; Wolak, M. A.; Shirk, J. S.; Hiltner, A.; Baer, E. Reduction of Dielectric Hysteresis in Multilayered Films via Nanoconfinement. *Macromolecules* **2012**, *45* (4), 1954–1962.

(99) Huan, T. D.; Boggs, S.; Teyssedre, G.; Laurent, C.; Cakmak, M.; Kumar, S.; Ramprasad, R. Advanced Polymeric Dielectrics for High Energy Density Applications. *Prog. Mater. Sci.* **2016**, *83*, 236–269.

(100) Wang, C. C.; Pilania, G.; Boggs, S. A.; Kumar, S.; Breneman, C.; Ramprasad, R. Computational Strategies for Polymer Dielectrics Design. *Polymer.* **2014**, *55* (4), 979–988.

(101) Hohenberg, P.; Kohn, W. Hohenberg, P.; Kohn, W. *Phys. Rev.* **1964**, *136*, B864–B871.

(102) Kohn, W.; Sham, L. J. Self-Consistent Equations Including Exchange and Correlation Effects. *Phys. Rev.* **1965**, *140* (4A), A1133–A1138.

(103) Baroni, S.; De Gironcoli, S.; Dal Corso, A.; Giannozzi, P. Phonons and Related Crystal Properties from Density-Functional Perturbation Theory. *Rev. Mod. Phys.* **2001**, *73* (2), 515–562.

(104) McPherson, J.; Kim, J.; Shanware, A.; Mogul, H.; Rodriguez, J. Proposed Universal Relationship Between Dielectric Breakdown and Dielectric Constant. In *Digest. International Electron Devices Meeting*; IEEE: San Francisco CA, 2002; pp 633–636.

(105) Heyd, J.; Scuseria, G. E.; Ernzerhof, M. Hybrid Functionals Based on a Screened Coulomb Potential. *J. Chem. Phys.* **2003**, *118* (18), 8207–8215.

(106) Wang, C. C.; Pilania, G.; Ramprasad, R. Dielectric Properties of Carbon-, Silicon-, and Germanium-Based Polymers: A First-Principles Study. *Phys. Rev. B* **2013**, *87* (3), 35103.

(107) Zhu, Q.; Sharma, V.; Oganov, A. R.; Ramprasad, R. Predicting Polymeric Crystal Structures by Evolutionary Algorithms. *J. Chem. Phys.* **2014**, *141* (2014), 154102.

(108) Zhu, Q.; Artem, R.; Glass, C. W.; Stokes, H. T. Constrained Evolutionary Algorithm for Structure Prediction of Molecular Crystals: Methodology and Applications. *Acta Cryst.* **2012**, *B68*, 215–226.

(109) Nicolet, T.; All, C. Introduction to Fourier Transform Infrared Spectrometry. *A Thermo Electron Bussines* **2001**, 1–8.

(110) Range, T.; Temperature, R.; Weight, S.; Pans, P. S.; Q-, T. G. A.; Selection, G.; Preferences, I.; Bunsen, T. Operation Manual for the TA Instruments TGA Q-500 : 7–9.

(111) C, T. R. C. Operation Manual for the TA Instruments DSC Q-100 and Q-20 : 2–4.

(112) Edition, S. Hp 4284a Precision Lcr Meter Operation Manual. **1998**, No. 4284.

(113) Mopsik, F. I. Precision Time-Domain Dielectric Spectrometer. *Rev. Sci. Instrum.* **1984**, *55* (1), 79–87.

(114) Millikan, R. A. A Direct Photoelectric Determination of Planck's "h." *Phys. Rev.* **1916**, *7* (3), 355–388.

(115) Dissado, L. A.; Fothergill, J. C. *Electrical Degradation and Breakdown in Polymers*; Stevens, G. C., Ed.; The Institution of Engineering and Technology: London, 1992.

(116) Li, Z.; Xu, C.; Uehara, H.; Boggs, S.; Cao, Y. Transient Characterization of Extreme Field Conduction in Dielectrics. *AIP Adv.* **2016**, *6* (11).

(117) Isabell, T. C.; Fischione, P. E.; O'Keefe, C.; Guruz, M. U.; Dravid, V. P. Plasma Cleaning and Its Applications for Electron Microscopy. *Microsc. Microanal.* **1999**, *5* (2), 126–135.

(118) Fujiwara, H. Ellipsometry. In *Handbook of Optical Metrology: Principles and Applications*; CRC Press: Boca Raton, Florida, 2009; pp 641–660.

(119) Simpson, J.; St.Clair, A.; Fundamental Insight on Developing Low Dielectric Constant Polyimides. *Thin Solid Films* **1997**, *308–309*, 480–485.

(120) Hwang, H. J.; Li, C. H.; Wang, C. S. Dielectric and Thermal Properties of Dicyclopentadiene Containing Bismaleimide and Cyanate Ester. Part IV. *Polymer.* **2006**, *47* (4), 1291–1299.

(121) Wang, Y.; Zhou, X.; Lin, M.; Zhang, Q. M. High-Energy Density in Aromatic Polyurea Thin Films. *Appl. Phys. Lett.* **2009**, *94* (20), 1–4.

(122) Wu, S.; Lin, M.; Burlingame, Q.; Zhang, Q. M. Meta-Aromatic Polyurea with High Dipole Moment and Dipole Density for Energy Storage Capacitors. *Appl. Phys. Lett.* **2014**, *104* (7).

(123) Wang, Y.; Zhou, X.; Lin, M.; Lu, S. G.; Lin, J.; Furman, E.; Zhang, Q. M. Nonlinear Conduction in Aromatic Polyurea Thin Films and Its Influence on Dielectric Applications over a Broad Temperature Range. *IEEE Trans. Dielectr. Electr. Insul.* **2010**, *17* (1), 28–33.

(124) Cheng, Z.; Lin, M.; Wu, S.; Thakur, Y.; Zhou, Y.; Jeong, D.-Y.; Shen, Q.; Zhang, Q. M. Aromatic Poly(arylene Ether Urea) with High Dipole Moment for High Thermal Stability and High Energy Density Capacitors. *Appl. Phys. Lett.* **2015**, *106* (20), 202902.

(125) Havriliak, S.; Negami, S. A Complex Plane Representation of Dielectric and Mechanical Relaxation Processes in Some Polymers. *Polymer.* **1967**, *8*, 161–210.

(126) McCrum, N. G.; Read, B. E.; Williams, G. *Anelastic and Dielectric Effects in Polymeric Solids*; Dover Books on Engineering; Dover Publications, 1967.

(127) Tefferi, M.; Ma, R.; Treich, G.; Sotzing, G.; Ramprasad, R.; Cao, Y. Novel Dielectric Films with High Energy Density. *Electr. Insul. Dielectr. Phenom. (CEIDP), 2015 IEEE Conf.* **2015**, 451–454.

(128) Mannodi-Kanakkithodi, A.; Pilania, G.; Ramprasad, R. Critical Assessment of Regression-Based Machine Learning Methods for Polymer Dielectrics. *Comput. Mater. Sci.* **2016**, *125*, 123–135.

(129) Li, Z.; Uehara, H.; Ramprasad, R.; Boggs, S.; Cao, Y. Dynamics of Nonlinear

Charge Injection in Polymeric Films. **2016**, 3–6.

(130) Wu, S.; Li, W.; Lin, M.; Burlingame, Q.; Chen, Q.; Payzant, A.; Xiao, K.; Zhang, Q. M. Aromatic Polythiourea Dielectrics with Ultrahigh Breakdown Field Strength, Low Dielectric Loss, and High Electric Energy Density. *Adv. Mater.* **2013**, *25* (12), 1734–1738.

(131) Wu, S.; Burlingame, Q.; Cheng, Z.-X.; Lin, M.; Zhang, Q. M. Strongly Dipolar Polythiourea and Polyurea Dielectrics with High Electrical Breakdown, Low Loss, and High Electrical Energy Density. *J. Electron. Mater.* **2014**, *43* (12), 4548–4551.

(132) Schlosser, E.; Schönhals, A. Recent Development in Dielectric-Relaxation Spectroscopy of Polymers. *Colloid Polym. Sci.* **1989**, *267*, 963–969.

(133) Treufeld, I.; Wang, D. H.; Kurish, B. a.; Tan, L.-S.; Zhu, L. Enhancing Electrical Energy Storage Using Polar Polyimides with Nitrile Groups Directly Attached to the Main Chain. *J. Mater. Chem. A* **2014**, *2* (48), 20683–20696.

(134) Thakur, Y.; Zhang, B.; Dong, R.; Lu, W.; Iacob, C.; Runt, J.; Bernholc, J.; Zhang, Q. M. Generating High Dielectric Constant Blends from Lower Dielectric Constant Dipolar Polymers Using Nanostructure Engineering. *Nano Energy* **2017**, *32* (September 2016), 73–79.

(135) Burlingame, Q.; Wu, S.; Lin, M.; Zhang, Q. M. Conduction Mechanisms and Structure-Property Relationships in High Energy Density Aromatic Polythiourea Dielectric Films. *Adv. Energy Mater.* **2013**, *3* (8), 1051–1055.

(136) Mannodi-Kanakkithodi, A.; Wang, C. C.; Ramprasad, R. Compounds Based on Group 14 Elements: Building Blocks for Advanced Insulator Dielectrics Design. *J. Mater. Sci.* **2014**, *50* (2), 801–807.

(137) Pilania, G.; Wang, C. C.; Wu, K.; Sukumar, N.; Breneman, C.; Sotzing, G.; Ramprasad, R. New Group IV Chemical Motifs for Improved Dielectric Permittivity of Polyethylene. *J. Chem. Inf. Model.* **2013**, *53* (4), 879–886.

(138) Carraher Jr., C. E.; Dammeier, R. L. Production of Organometallic Polymers by the Interfacial Technique. *Die Makromol. Chemie* **1970**, No. 135, 107–112.

(139) Carraher Jr., C. E. Comparative Infrared Spectroscopy of Group IV a Polyesters and Polyoxides. *Die Angew. Makromol. Chemie* **1973**, *31* (1), 115–122.

(140) Carraher Jr., C. E. Comparative Synthesis of Oligomeric Group IV Polyesters. *J. Polym. Sci. Part A-1 Polym. Chem.* **1972**, *10* (2), 413–417.

(141) Carraher Jr., C. E. Organotin Polymers. In *Macromolecules Containing Metal and Metal-Like Elements, Volume 4, Group IVA Polymers*; Abd-El-Aziz, A. S., Carraher Jr., C. E., Pittman, C. U., Zeldin, M., Eds.; John Wiley & Sons, 2005;

pp 263–309.

(142) Peruzzo, V.; Plazzogna, G.; Tagliavini, G. Electrochemical Preparation of Trimethyltin Carboxylates. *J. Organomet. Chem.* **1969**, *18* (1), 89–94.

(143) Treich, G. M.; Nasreen, S.; Mannodi-Kanakkithodi, A.; Ma, R.; Tefferi, M.; Flynn, J.; Cao, Y.; Ramprasad, R.; Sotzing, G. A. Optimization of Organotin Polymers for Dielectric Applications. *ACS Appl. Mater. Interfaces* **2016**, *8* (33), acsami.6b04091.

(144) Goedecker, S. Minima Hopping: An Efficient Search Method for the Global Minimum of the Potential Energy Surface of Complex Molecular Systems. *J. Chem. Phys.* **2004**, *120* (21), 9911–9917.

(145) Amsler, M.; Goedecker, S. Crystal Structure Prediction Using the Minima Hopping Method. *J. Chem. Phys.* **2010**, *133* (22), 224104.

(146) Peruzzo, V.; Plazzogna, G.; Tagliavini, G. The Preparation and Properties of Some Allyltin carboxylates:R3SnOOCR′ (R′ = CH3, CH2Cl), R2Sn(OOCR′)2 (R′ = CH2Cl, CHCl2) and [R2Sn(OOCR′)]2O (R′ = CH2Cl, CHCl2, CCl3). *J. Organomet. Chem.* **1972**, *40* (1), 129–133.

(147) Sowri Babu, K.; Reddy, A. R.; Sujatha, C.; Reddy, K. V.; Mallika, A. N. Synthesis and Optical Characterization of Porous ZnO. *J. Adv. Ceram.* **2013**, *2* (3), 260–265.

(148) Ristić, M.; Popović, S.; Musić, S. Formation and Properties of Cd(OH)2 and CdO Particles. *Mater. Lett.* **2004**, *58* (20), 2494–2499.

(149) Palacios, E. G.; Juárez-López, G.; Monhemius, A. J. Infrared Spectroscopy of Metal Carboxylates: II. Analysis of Fe(III), Ni and Zn Carboxylate Solutions. *Hydrometallurgy* **2004**, *72* (1–2), 139–148.

(150) Kimblin, C.; Parkin, G. Comparison of Zinc and Cadmium Coordination Environments in Synthetic Analogues of Carbonic Anhydrase: Synthesis and Structure of {[PimPri,But]Cd(OH2)(OClO3)}(ClO4). *Biochemistry* **1996**, *1669* (15), 6912–6913.

(151) Treich, G. M.; Tefferi, M.; Nasreen, S.; Mannodi-kanakkithodi, A.; Li, Z.; Ramprasad, R.; Sotzing, G. A.; Cao, Y. A Rational Co-Design Approach to the Creation of New Dielectric Polymers with High Energy Density. *IEEE Trans. Dielectr. Electr. Insul. Spec. Issue Dielectr. Mater. Electr. Energy Storage* **2017**.

(152) Huan, T. D.; Mannodi-Kanakkithodi, A.; Kim, C.; Sharma, V.; Pilania, G.; Ramprasad, R. A Polymer Dataset for Accelerated Property Prediction and Design. *Sci. Data* **2016**, *3*, 160012.

(153) Curtarolo, S.; Setyawan, W.; Wang, S.; Xue, J.; Yang, K.; Taylor, R. H.; Nelson, L. J.; Hart, G. L. W.; Sanvito, S.; Buongiorno-nardelli, M.; Mingo, N.;

Levy, O. AFLOWLIB . ORG : A Distributed Materials Properties Repository from High-Throughput Ab Initio Calculations. *Comput. Mater. Sci.* **2012**, *58*, 227–235.

(154) Pizzi, G.; Cepellotti, A.; Sabatini, R.; Marzari, N.; Kozinsky, B. AiiDA : Automated Interactive Infrastructure and Database for Computational Science. *Comput. Mater. Sci.* **2016**, *111*, 218–230.

(155) Bligaard, T. The Computational Materials Repository. *Comput. Sci. Eng.* **2012**, *14* (6), 51–57.